Chair of Structural and Functional Ceramics

Doctoral Thesis

Understanding the fracture behaviour of 2D/3D ceramic architectures with tailored microstructures

Dipl.-Ing. Josef Christian Schlacher, BSc

May 2024

MONTANUNIVERSITÄT LEOBEN
www.unileoben.ac.at

AFFIDAVIT

I declare on oath that I wrote this thesis independently, did not use any sources and aids other than those specified, have fully and truthfully reported the use of generative methods and models of artificial intelligence, and did not otherwise use any other unauthorized aids.

I declare that I have read, understood and complied with the "Good Scientific Practice" of the Montanuniversität Leoben.

Furthermore, I declare that the electronic and printed versions of the submitted thesis are identical in form and content.

Date 02.05.2024

Signature Author
Josef Christian Schlacher

Funding for this research was provided by the European Research Council (ERC) excellent science grant “CERATEXT” through the Horizon 2020 program under contract 817615.

Acknowledgements

First of all, I would like to express my sincerest gratitude to my supervisor Univ.-Prof. Dr. Raul Bermejo, head of the Chair of Structural- and Functional Ceramics, for his trust, advice and the continuous encouragement during my PhD-time. I am very grateful to him for giving me the opportunity to perform my thesis within his group and for the excellent guidance throughout the entire project.

Furthermore, I would like to thank Univ.-Prof. Dipl.-Ing. Dr.mont. Daniel Kiener from the Chair of Materials Physics for being my mentor.

My sincere gratitude is expressed to Dr. Tamas Csanádi from the Institute of Materials Research (Slovak Academy of Sciences) and to Dr. Zdenek Chlup from the Institute of Physics of Materials (Czech Academy of Sciences) for their support and the friendly environment during my research stays in Košice as well as in Brno. Especially, I want to thank them both for the fruitful collaboration.

Special thanks goes also to Sebastian Geier, Dr.-Ing. Serkan Nohut and Dr. Martin Schwentenwein from Lithoz GmbH for the great collaboration.

I would like to thank all my colleagues at the Chair of Structural- and Functional ceramics for the great working environment and for all the help during my research. Especially, I want to thank my office mates Ing. Roman Papšík and Dipl.-Ing. Abdullah Jabr, as well as my former colleague Dipl.-Ing. Dr. mont. Anna-Katharina Hofer for their valuable support and for the great time together.

Many thanks goes also to my former students Isabel Gavalda-Velasco, Luisa Bastos Mateus, MSc. and Dipl.-Ing. Fabian Stücklberger. It was really great working with you together.

Last but not least, I would like to express my deepest gratitude to my family, especially my parents Josef and Hermine Schlacher, for their continuous support and for always believing in me.

Abstract

Layered ceramic architectures with alternating material layers with tailored microstructures have been demonstrated as effective approach for optimizing the mechanical behaviour of advanced ceramics. Due to the different coefficients of thermal expansions within the combined multi-material layer regions, alternating tensile as well as compressive residual stresses are generated after cooling down from the sintering temperature. For instance, in designs where the compressive residual stresses are located within the top surface layer regions, a significant increase in the strength can be achieved. In cases where damage tolerance is pursued, the in-plane compressive residual stresses may be embedded within the ceramic architecture aiming to provide "crack arrest" of propagating surface cracks. In addition to the architectural design approach for layered ceramic systems (laminates), recent research has demonstrated that orienting the microstructure ("texturing") along the [0001] basal directions within specific layer regions may further improve the fracture resistance of alumina-based laminates through energy-dissipating deflection mechanisms during the fracture process. This approach resembles some natural systems, as in seashells and is often referred to as bioinspired design concept.

The fracture behaviour and the underlying mechanisms of such textured alumina-based ceramic laminates have not been fully understood yet. In this thesis, the micro-scale fracture toughness of individual textured alumina grain and grain boundaries is investigated through micro-cantilever bending tests. The investigation on the micro-scale level may be used for better understanding the macroscopic fracture behaviour of layered alumina-based laminates with textured microstructures. Furthermore, the Hertzian contact damage behaviour of alumina-based laminates with internal textured regions is assessed and the corresponding surface as well as sub-surface damage are studied in detail. In addition, the high-temperature fracture behaviour of layered alumina ceramics with textured microstructures are explored by performing (uniaxial) bending tests up to temperatures of 1200 °C, which may be paramount for assessing their potential for high-temperature applications.

Another important aspect is that although such alumina-based 2D-architectures (planar structures fabricated through tape casting) may show high potentials in designing mechanical resistant or damage-tolerant systems, the application of the multi-material design concepts with residual stresses on more complex-shaped components has not been investigated yet. Therefore, the potentials of designing alumina-based 3D-multi-material architectures through stereolithographic printing and their mechanical performance is studied. Firstly, the mechanical

strength of 3D-printed alumina is tailored by embedding alumina-zirconia layers between outer pure alumina surface layers with significant compressive residual stresses. Secondly, the thermal shock behaviour of 3D-printed multi-material ceramics with embedded alumina (protective) regions under compressive residual stresses is explored. Based on the damage-tolerant design concept, a first demonstrator component (i.e. ceramic turbine blade) with complex shapes is designed through the multi-material design approach and its effectiveness for arresting thermal shock cracks is demonstrated.

Keywords: Alumina, Laminates, Residual stress, 3D-printing, Fracture behaviour

Kurzfassung

Keramische Schichtarchitekturen mit abwechselnden Materialien und gezielt eingestelltem internen Gefüge haben sich als besonders effektiv hinsichtlich der Optimierung des mechanischen Verhaltens von Hochleistungskeramiken erwiesen. Aufgrund der unterschiedlichen thermischen Ausdehnungskoeffizienten zwischen den kombinierenden Multi-Material-Regionen, werden abwechselnde Zug- als auch Druckeigenspannungen nach dem Abkühlen von der Sintertemperatur eingestellt. In Schichtdesigns mit maßgeschneiderten Druckeigenspannungen an den Oberflächenregionen kann eine wesentliche Erhöhung der mechanischen Festigkeit erzielt werden. In Anwendungen wo hingegen eine hohe Schadenstoleranz gefragt ist, können die Schichten die unter Druckeigenspannungen stehen in der Schichtarchitektur eingebettet werden, sodass es zu einem erwünschten Rissstopp von fortschreitenden Oberflächenrissen kommen kann. Zusätzlich zu den Designstrategien von Architekturen keramischer Laminate, konnte in neueren Forschungsarbeiten eine gezielte Verbesserung der Schadenstoleranz von Aluminiumoxid-basierenden Laminaten durch Texturierung des Gefüges in die [0001] Basal-Richtung, welche auf energiefreisetzenden Ablenkungsmechanismen der Risse während des Bruchvorganges zurückzuführen ist, nachgewiesen werden. Dieser Ansatz ermöglicht es die Bauweise von natürlichen Materialien, wie dieser einer Muschel, nachzuahmen und kann dem bioinspirierten Designkonzept zugeordnet werden.

Jedoch wurde das Bruchverhalten und die dahinterstehenden Mechanismen von keramischen Aluminiumoxid-basierenden texturierten Laminaten noch nicht vollständig verstanden. In dieser Arbeit, wurden die Bruchzähigkeiten von individuellen texturierten Aluminiumoxid-Körnern und Korngrenzen in der Mikroebene durch Cantilever-Biegeversuchen weitgehend untersucht. Diese Untersuchungen können wesentlich zum Verständnis des makroskopischen Bruchvorganges von Aluminiumoxid-basierenden Laminaten mit texturiertem Gefüge beitragen. Des Weiteren wurde das Hertz'sche Kontaktschädigungsverhalten von solchen keramischen texturierten Schichtarchitekturen mit den damit verbunden oberflächennahen Schädigungsmechanismen erforscht. Das Hochtemperaturbruchverhalten von keramischen Laminaten mit texturiertem Gefüge wurde im Rahmen von uniaxialen Biegeversuchen bis zu Temperaturen von 1200 °C studiert, welches sehr wesentlich für die Anwendung solcher im Hochtemperatursektor wäre.

Ein weiterer wichtiger Aspekt ist, dass solch Aluminiumoxid-basierende 2D-Schichtarchitekturen (plane Schichten hergestellt mittels Tape Casting) zwar sehr hohes Potential hinsichtlich dem Design von mechanisch-resistenten oder schadenstoleranten Systemen aufweisen, die Erweiterung des Multi-Material-Konzeptes mit Eigenspannungen an Komponenten mit komplexer Geometrie wurde bis dahingehend noch nicht erreicht. Deshalb wird in weiterer Folge das Potential zum Designen von Aluminiumoxid-basierenden 3D-Multi-Material-Architekturen mittels stereolithographischem Druck und deren mechanische Performance weitgehend beurteilt. Die Erhöhung der mechanischen Festigkeit von 3D-gedrucktem Aluminiumoxid durch das Einbetten von Aluminiumoxid-Zirkonoxid-Schichten zwischen Aluminiumoxid-Außenschichten unter Druckeigenspannungen in einem Multi-Material-Laminat wird erforscht. Des Weiteren wird das Thermoschockverhalten von Multi-Material-Keramiken mit internen Aluminiumoxid-(Schutz)schichten unter Druckeigenspannungen untersucht. Basierend auf dieses schadenstolerante Konzept, kann erstmalig ein geometrisch-komplexer Demonstrator (Keramik-Turbinenschaufel) unter Anwendung der Multi-Materialtheorie entwickelt und eine Effektivität zum Stoppen von Thermoschockrissen nachgewiesen werden.

Schlüsselwörter: Aluminiumoxid, Laminate, Eigenspannungen, Additive Fertigung, Bruchverhalten

List of abbreviations

CTE	Coefficient of thermal expansion	ppm/°C
ZTA	Zirconia-toughened alumina	-
TGG	Templated grain growth	-
2D	Tape-casted (planar structures)	-
3D	Additive-manufactured	-
LCM	Lithography-based Ceramic Manufacturing	-
[0001]	Crystallographic orientation normal to the basal planes	-
t	Plate thickness	m
∂W	Mechanical work	J/m^2
∂U_{el}	Stored elastic energy	J/m^2
G_c	Fracture energy or critical energy release rate	J/m^2
∂A	Fracture surfaces	m^2
σ_f	Strength	MPa
G	Energy release rate	J/m^2
K	Stress intensity factor	MPa $m^{1/2}$
σ	Applied stress	MPa
a_c	Critical “Griffith” defect size	m
$P(\sigma, V)$	Probabilities of failures	-
V	Volume	m^3
σ_0^*	Scale parameter (3-parameter distribution)	MPa
m^*	Weibull modulus (3-parameter distribution)	-
V_0	Scaling volume	m^3
σ_u	Lower bound of strength	MPa
σ_0	Characteristic strength	MPa
m	Weibull modulus	-
a	Contact radius	m
P	Applied load	N
R	Radius of the spherical indenter	m
E^*	Combined elastic modulus	GPa
E'	Elastic modulus of indenter	GPa
ν'	Poisson’s ratio of indenter	-

E	Elastic modulus of specimen	GPa
v	Poisson's ratio of specimen	-
σ_z	Axial stress	MPa
p_m	Mean contact pressure	MPa
σ_{max}	Maximum tensile stresses	MPa
τ_{max}	Maximum shear stresses	MPa
ε	Total strain	-
ε_{th}	Thermal strain	-
ε_{el}	Elastic strains	-
σ_{th}	Thermal stresses	MPa
σ_{ts}	Maximum thermal stresses	MPa
B	Biot number	-
h	Heat transfer coefficient	W m^{-2} K^{-1}
λ	Thermal conductivity	W m^{-1} K^{-1}
d	Characteristic length of the specimen	m
σ^*	Dimensionless normalized stress	-
ΔT_c	Critical temperature difference	°C
R	First thermal shock parameter	°C
$\sigma_{res,i}$	Residual stresses in i^{th} layer	MPa
E_i	Young's modulus of each i^{th} layer	GPa
α_i	Coefficient of thermal expansion of each i^{th} layer	ppm/°C
v_i	Poisson's ratio of each i^{th} layer	-
ΔT	Temperature difference	°C
T_0	Room temperature	°C
T_{ref}	Reference temperature	°C
$\bar{\alpha}$	Average coefficient of thermal expansion	ppm/°C
V_A	Total volume of material A	m^3
V_A	Total volume of material B	m^3
T_A	Total thickness of material A	m
T_B	Total thickness of material A	m
t_A	Layer thickness of material A	m
t_B	Layer thickness of material B	m
K_R	Apparent fracture toughness	MPa $m^{1/2}$
a	Crack length	m

K_{tip}	Stress intensity factor at the crack tip	MPa $m^{1/2}$
K_{res}	Stress intensity factor considering the contribution of the residual stresses	MPa $m^{1/2}$
K_{appl}	Applied stress intensity factor	MPa $m^{1/2}$
σ_{appl}	Applied stress field	MPa
Y	Geometry factor	-
K_{Ic}	Fracture toughness	MPa $m^{1/2}$
K_0	(Intrinsic) fracture toughness of each layer region	MPa $m^{1/2}$
$\sigma_{res}(x)$	Residual stress field at the distance x	MPa
$h(x,a)$	Weight function	m
R	Crack growth resistance	-
ESC	Laminates with external compressive residual stresses	-
K_{Rpeak}	Highest peak in the apparent fracture toughness	MPa $m^{1/2}$
σ_{min}	Threshold strength (lower bound)	MPa
$CaCO_3$	Aragonite	-
PMMA	Poly(methyl methacrylate)	-
CVD	Chemical Vapour Deposition	-
G_d	Critical energy release rate for deflection	J/m^2
G_p	Critical energy release rate for penetration	J/m^2
Γ_i	Interfacial fracture resistance	J/m^2
G_c	Fracture resistance of the single platelet	J/m^2
η_{res}	Non-dimensional length parameters	-
FIB	Focus Ion Beam technique	-
σ_c	Fracture stress	MPa
F_{max}	Maximum fracture load	N
a, b, m_a, L, x_1, x_2 and z_0	Cantilever dimensions	m
α	Notch depth	m
I_x	Second moment of area	m^4
WOF	Work of fracture	J/m^2
σ_f	Flexural strength	MPa
F	(Maximum) fracture force	N
S_1	Outer span	m
S_2	Inner span	m

b	Specimen width	m
h	Specimen height	m
ε	Flexural (outer fibre) strain	-
δ	Displacement	m
B3B	Ball-On-Three Balls test	-
f	Pre-factor	-
t	Specimen thickness	m
R	Specimen radius	m
R_a	Support ring radius	m
SEM	Scanning electron microscopy	-
AE	Acoustic Emission	-
eu	Energy unit	$10^{-14}V^2s$
$\Delta T_c'$	(Second) temperature difference	°C
FE	Finite Element	-

Content

General Part

1. Introduction and motivation

Designing structural components for many demanding fields (i.e. medical sector, space engineering, high temperature application, etc.) requires the use of exceptional materials. Advanced ceramics show a variety of attractive properties, such as corrosion resistance, high-temperature stability, biocompatibility, and the high-stiffness-to-weight-ratio, which are paramount for their application in modern sectors [1,2].

One limitation on the use of ceramic components is the lack of reliability and damage tolerance upon mechanical loading associated with the absence of plasticity. The inherent brittleness (low fracture toughness) and the scatter in mechanical strength of advanced ceramics are the main limiting factors for preventing their use in applications where high safety is sought [3]. One strategy to overcoming this lack of plasticity may be provided by mimicking the "brick-mortar" structure as found in seashells [4,5]. Following the "bio-inspired" design concept may lead to tougher and more reliable ceramic architectures, as presented in "nacre-like" alumina ceramics [6]. Such nacre-like alumina ceramics exhibit enhanced fracture toughness; however, the strength may be compromised by the rather weak secondary phases, especially at elevated temperatures. Another promising strategy has been demonstrated by designing layered architectures of different ceramic regions with "strong" interfaces, leading to alternating residual stresses through the differences of the thermal expansion coefficients (CTE) by cooling down from the sintering temperature [7]. Depending on the final application, the compressive residual stresses can be either located in the top-surface layers (mechanical-resistant design) or within the embedded layer regions (damage-tolerant system), to provide crack shielding mechanisms [8,9]. The first approach may increase the strength of ceramic parts by the magnitude of the corresponding in-plane compressive residual stresses in the surface region [10–13]. In the second design concept, the strategy of embedding barriers against crack propagation reduces significantly the strength variability and enhances their fracture resistance, yielding an increased damage tolerance of the ceramic part [8,14–17].

To improve the mechanical properties of ceramic laminates, microstructure tailoring of each layer region has been established as additional strategy. For instance, the addition of zirconia to alumina (zirconia-toughened alumina (ZTA)) combined with alumina layers, allows the tailoring of the mismatch of thermal expansion coefficient, which is paramount for adjusting the magnitude of corresponding residual stresses [18]. In recent research, orienting the microstructure ("texturing") by "templated grain growth (TGG)" exploited in the embedded

layer regions has been pursued to further improve the fracture resistance (damage tolerance) of ceramic architectures, associated with energy-dissipating deflection mechanisms [19–21]. Besides the major advances in the field of "textured" ceramic laminates, there is still open research for assessing their potential in special applications. For instance, the link from the micro- to the macro-scale level has to be explored for understanding the fracture process of layered textured alumina ceramics. Another important factor is assessing the damage tolerance of textured alumina laminates under severe conditions (i.e. high-temperature environment).

Although these positive impacts of architectural designing of ceramic laminates together with microstructure tailoring on its mechanical response have been reported [18,22], the breakthrough of multi-material systems with tailored residual stresses as structural components for industrial application may be hindered by the planar-structures (no design complexity) given by the 2D-fabrication processes (i. e. tape casting). To overcome many limitations factors of designing complex-ceramic-parts or components, the mechanical properties of alumina ceramics fabricated by stereolithographic 3D-printing, such as Lithography-based Ceramic Manufacturing (LCM) [23–25] was investigated in a previous work [26]. Beyond these research activities, novel 3D-printing techniques may be also employed to enable designing of multi-material-based concepts with high complexity [27]. Therefore, another question in this thesis addresses whether it is possible to combine the architectural approach with tailored residual stresses together with the advantages of novel LCM 3D-printing to design ceramic components with superior mechanical properties.

The overarching goal of this thesis is to (i) deepen the understanding of the fracture behaviour and the corresponding damage mechanisms under distinct loading scenarios as well as testing conditions and (ii) assess the potential of design concepts with residual stresses for enhancing the structural integrity of 3D-printed components. The effect of residual stresses and tailored microstructures on the mechanical response of *2D* (tape-casted) as well as *3D* (additive manufactured) ceramic architectures are studied under distinct loading scenarios (i.e. contact loading, thermal shock, among others). As *2D*-architectures, (i) laminates with alternating (equiaxed) alumina-zirconia (or pure alumina) and textured alumina regions have been investigated, whereas (ii) multi-material ceramics combining alumina and alumina-zirconia layers have been considered for *3D*-architectural designing (Fig. 1).

The main results of this doctoral thesis are discussed as an extended summary of the author's recent publications. A schematic overview of the research activities within the thesis is shown in Fig. 1.

The first design concepts are based on microstructure regions of randomly distributed alumina-zirconia (or pure alumina) grains (euqiaxed) and textured alumina layer regions (elongated grains oriented along [0001]-direction). To better understand the macroscopic fracture behaviour of layered alumina-based ceramics with textured microstructures, the (localized) micro-scale fracture toughness of individual textured alumina grains and grain boundaries are compared in **Publication A**. From the macroscopic viewpoint, spherical indentation tests are conducted to investigate the contact damage behaviour of alumina-based architectures with textured layer regions (**Publication B**). Furthermore, the macroscopic fracture behaviour of these architectures is investigated under uniaxial bending tests over a wide temperature range (up to 1200°C) for assessing their structural integrity under severe conditions (**Publication C**). The micro- and macro-scale results are correlated in Chapter **5.1** and **5.2**, which may enhance the understanding of the acting mechanisms within textured alumina laminates during the fracture process.

Chapter **5.3** deals with the potentials of the stereolithographic 3D-printing for designing and fabricating novel alumina-based multi-material ceramics with exceptional mechanical resistance or damage tolerance. For these research studies multi-materials architectures are designed based on alumina and alumina-zirconia (zirconia-toughened alumina (ZTA)) layer regions. In **Publication D**, the feasibility of 3D-printing alumina with superior strength is demonstrated by using the multi-material approach with compressive residual stresses in the surface layers. **Publication E** discusses the effectiveness of the multi-material design to enhance the reliability of 3D-printed ceramics by embedding protective regions, acting against crack propagation. As final step, the first 3D-printed multi-material component of complex-shaped geometry with outstanding damage tolerance is presented in **Publication E,** which may open new pathways for novel industrial applications.

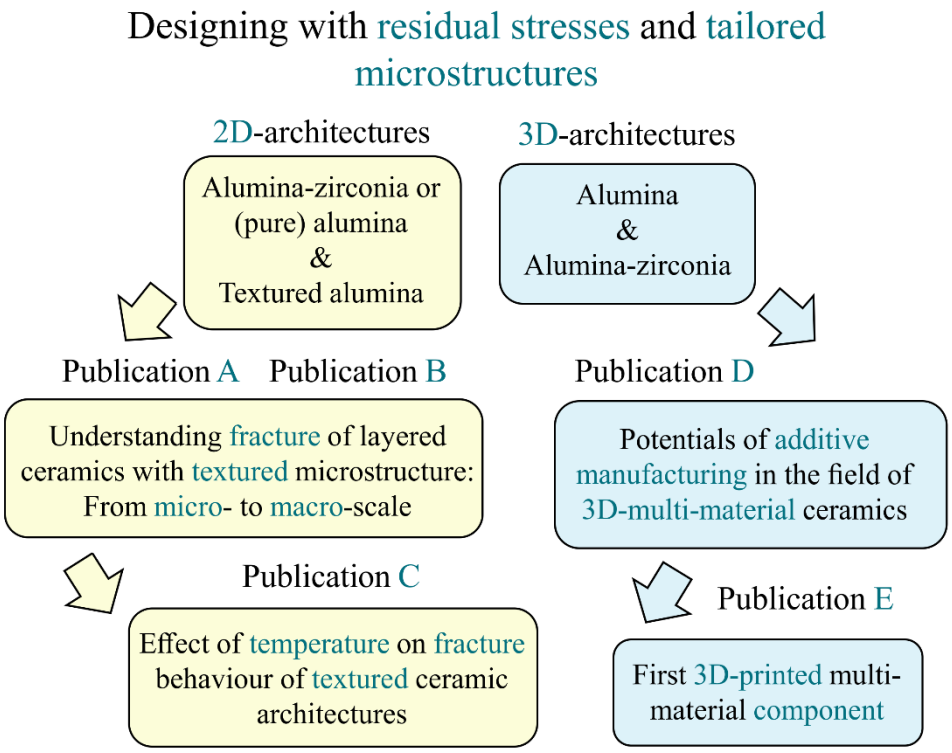

Fig. 1: Schematic overview of the research activities on layered alumina-based ceramics with tailored residual stresses and microstructures.

2. Theoretical background

In this Chapter, the theoretical background of the thesis is given, aiming to provide the reader a comprehensive yet short overview on assessing the mechanical behaviour of ceramic materials. The main focus here is on (i) the theory of brittle fracture and (ii) the contact damage as well as (iii) thermal shock behaviour of advanced ceramics. Furthermore, the state of the art of concepts for designing layered ceramic architectures as a strategy for improving their mechanical properties is discussed in detail.

2.1. Mechanical behaviour of advanced ceramics

2.1.1. Fracture and strength of brittle materials

In general, the fracture of advanced ceramics initiates from rather small defects distributed within the component or at its surface. Although these defects may exhibit an infinite volume, they can be described as sharp cracks according to the Linear-elastic fracture mechanics [1,3].

Based on the fundamental work of Griffith [28], where the brittle fracture behaviour is described using an energy approach, it is shown that an existing crack a under applied stress σ may extend to $(a + \partial a)$ within a plate of thickness t, when the mechanical work done through the crack growth (∂W) is equal or exceeds the contribution of changes in the stored elastic energy (∂U_{el}) and that in the fracture energy (G_c) for creating new fracture surfaces $(\partial A = t\partial a)$ [1,29,30]:

$$\partial W \geq \partial U_{el} + G_c t \partial a \,. \tag{1}$$

Assuming an edge crack within a fixed (infinite) plate, the corresponding strength σ_f can be derived from the relation as [30]:

$$\sigma_f = \sqrt{\frac{G_c E}{\pi a}}, \tag{2}$$

where E is the Young's modulus of the material and G_c the critical energy release rate. In general, depending on the loading condition and the geometry of the crack as well as the specimen, a so-called geometry factor Y can be defined and the strain energy release rate G may be calculated as [30]:

$$G = \left(Y^2\sigma^2/E\right)\pi a, \tag{3}$$

In any case where the G exceeds G_c, fracture might occur, which is known as failure criterion [30]:

$$G \geq G_c, \tag{4}$$

In the year 1957, Irwin [31] introduced the concept of the stress intensity factor $K = \sqrt{GE}$ (plane stress condition) or $K = \sqrt{\frac{GE}{1-\nu^2}}$ (plane strain condition). An important loading mode in ceramics takes place when the applied forces are perpendicular to the crack planes. In such case, the well-known Griffith/Irwin failure criterion can be defined as [1,29,30]:

$$K_I = \sigma Y\sqrt{\pi a} \geq K_{Ic}, \tag{5}$$

where σ is the applied stress, a is the crack size and K_{Ic} the "critical" stress intensity factor or fracture toughness of the material. In this regard, the stress at failure (fracture strength), σ_f, may be calculated from the failure criterion, with a_c as the critical "Griffith" defect size, as follows [30]:

$$\sigma_f = \frac{K_{Ic}}{Y\sqrt{\pi a_c}}\ . \tag{6}$$

In the fracture analysis (fractography [32]) of ceramics, it might be helpful to estimate the critical sizes of flaws (i.e. pores, agglomerates, surface cracks, etc.) distributed within the volume or at the surface. Therefore, Eq. 6 can be rearranged as follows [30]:

$$a_c = \frac{1}{\pi}\left(\frac{K_{Ic}}{Y\sigma_f}\right)^2. \tag{7}$$

Since the strength of ceramics mainly depends on defect distributions, fracture statistics has to be applied for evaluating their strength parameters [33]. A statistical fracture theory for brittle materials with homogenous defect densities, was proposed by Weibull [34,35], based on the "weakest-link" hypothesis, where fracture initiates from a single critical flaw. The Weibull distribution in its original 3-parameter form of the probabilities of failures (P), which is depending of the volume (V) and the applied stress state (σ), can be written as:

$$P(\sigma, V) = 1 - \exp\left[-\frac{V}{V_0}\left(\frac{\sigma - \sigma_u}{{\sigma_0}^*}\right)^{m^*}\right] \tag{8}$$

where ${\sigma_0}^*$ and m^* are materials parameters and V_0 the scaling volume, and σ_u is a lower bond of the strength [36]. In cases of small sample sets and where σ_u is unknown, the fitting of the 3-parameter distribution may remain unstable [37]. It is important to emphasize; however, that the effect of residual stresses on the mechanical behaviour of ceramic laminates can be described using the 3-parameter form for the statistical evaluation, where the total stress state can be determined as superposition of the applied stress and the contribution of residual stress, so that the lower bound is well known ($\sigma_u = -\sigma_{res}$) [13].

Nevertheless, in most of the practical cases, the lower bound can be set to zero ($\sigma_u = 0$), leading to the well-known 2-parameter Weibull distribution [36]:

$$P(\sigma, V) = 1 - \exp\left[-\frac{V}{V_0}\left(\frac{\sigma}{\sigma_0}\right)^m\right] \tag{9}$$

where σ_0 is the characteristic strength and m the Weibull modulus of the material. In this regard, the Weibull modulus (m) describes the width of the distribution (scatter of strength data) and the characteristic strength (σ_0) is related to the stress state, where the probability of failure P is approx. 63 % with the specimen volume (V) equal to a reference volume V_0 ($V=V_0$) [36]. Noteworthy to mention, Danzer [36] stated that this well-known 2-parameter Weibull distribution can be considered as special case of a more general distribution function of inhomogeneous defects.

2.1.2. Contact damage in ceramics

In 1881, H. Hertz [38] first reported a work about the contact scenarios between elastic bodies, which was the beginning of the scientific field of contact mechanics. In the Hertz theory, the following assumptions were made [39,40]:

(i) Both contacting bodies may be considered as half elastic-space. Therefore, the curvatures of the solids are relatively large compared to the contact radius a.

(ii) The contact radius a is relatively small compared to the dimensions of the contacting solids.

(iii) The contact between the two bodies can be considered as frictionless [39,40].

A prominent contact scenario may be the one of a rigid sphere (i.e. spherical indenter) on a flat (specimen) surface, which is also from high interest in this work. According to Hertz, the contact radius a can be determined as [39,40]:

$$a = \left(\frac{3PR}{4E^*}\right)^{1/3} \tag{10}$$

where P is the applied load, R the radius of the spherical indenter, and E^* is the combined elastic modulus taking into account the elastic moduli as well as Poisson's ratio of the indenter (ν', E') and the specimen (ν, E), respectively [39,40]:

$$\frac{1}{E^*} = \frac{(1-\nu^2)}{E} + \frac{\left(1-\nu'^2\right)}{E'} \tag{11}$$

In the contact region, the (normalized) surface pressure distribution can be written as [39,40]:

$$\frac{\sigma_z}{p_m} = -\frac{3}{2}\left(1-\frac{r^2}{a^2}\right)^{1/2} \qquad r \leq a \tag{12}$$

with σ_z as the axial stress and p_m as the mean contact pressure ($p_m = P/\pi a^2$) for spherical indentation [39,40]. Details about the Hertzian stress fields, the resulting contours of equal principal stresses as well as the corresponding stress trajectories, can be found in the book of Fischer-Cripps [39].

According to the Hertzian theory, the maximum tensile stress (i.e. first principal radial stress) associated with crack initiation at the contact region can be calculated as [39]:

$$\sigma_{max} = (1-2\nu)\frac{P}{2\pi a^2} \tag{13}$$

Furthermore, the maximum shear stresses τ_{max}, occurring in the sub-surface region (depth ~ 0.5 × a), can be correlated with the mean contact pressure as follows [41]:

$$\tau_{max} \approx 0.48\, p_m \tag{14}$$

In general, two main damage patterns can be distinguished under spherical indentation, namely (i) the classical Hertzian ring and cone cracking (see Fig. 2a) as typically found in homogenous polycrystalline ceramics or glasses and (ii) the quasi-plastic damage within the sub-surface (Fig. 2b) of specific ceramics with controlled microstructures [41,42]. In case of the former damage mode, it is interesting to note that the propagation of deleterious cone cracks is favoured along

the stress trajectory of the “third” principal stress due to its orthogonality to the “first” principal stress in radial direction [39].

The formation of the quasi-plastic sub-surface damage zones can be explained by shear-fault/wing crack mechanisms within microstructural features (micro-cracks) of tailored ceramics [41]. Many researchers have reported the successful introduction of quasi-plastic shear faulting within ceramic architectures with tailored microstructures, yielding increased contact damage resistance. For instance, grain coarsening [43,44] or increasing the level of porosities [45] within polycrystalline ceramic microstructures could favour the quasi-plastic damage pattern. In addition, interface designing has been reported as exceptional approach for micro-crack formation within sub-surface damage zones. Belmonte et al. [46] found micro-cracking as main mechanisms along the weak interfaces of second phases trough adding graphene nanofillers in silicon carbide ceramics (Fig. 2d). In the work of Cai et al. [47], sub-surface shear faulting through sliding mechanisms along mica/glass interfaces is also an interesting way for triggering quasi-plasticity (Fig. 2c). Based on the multi-layer concept, alumina systems with embedded calcium-hexaluminate interfaces [48,49] or the design with brittle coatings [50,51] have been investigated in literature for enhancing their contact damage resistance.

It is worth highlighting that the formation of quasi-plastic damage is associated with the maximum shear stresses (see Eq. 14) acting within the sub-surface zone, whereby its location (centre) has to be taken into account for designing multi-layer systems.

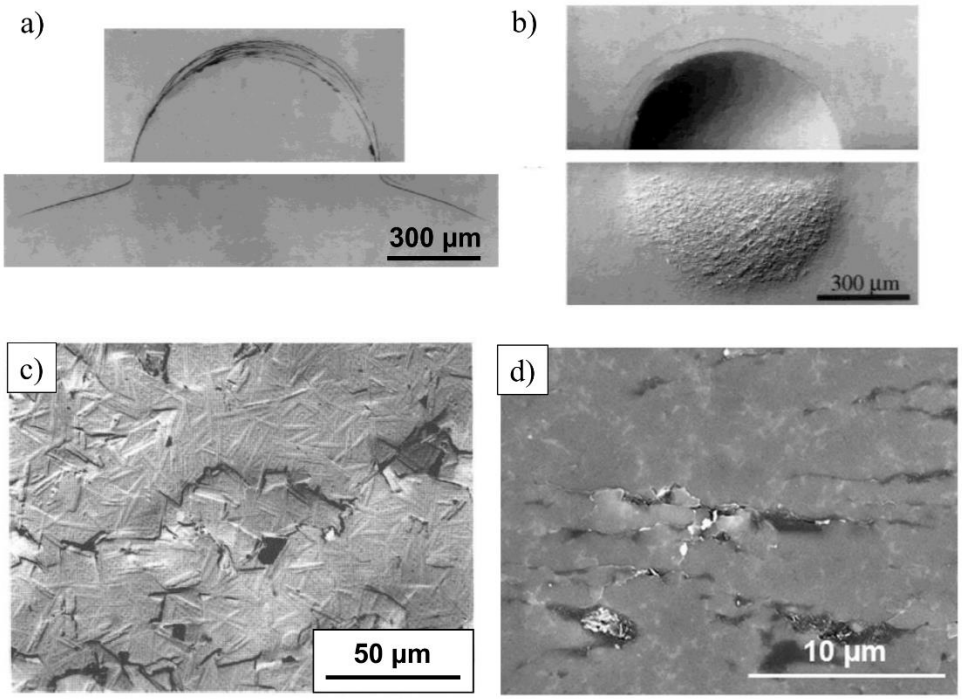

Fig. 2: (a) Classical Hertzian ring/cone cracking in fine-grained as well as (b) quasi-plastic damage zone within rather coarse-grained silicon nitride ceramics. Adapted from [44] with permission from Wiley. (c) Sub-surface shear faulting in mica-glass ceramics. Reproduced with permission from Springer Nature [47]. (d) Micro-crack formation along the matrix/graphene interface of silicon carbide composites. Adapted from [46] with permission from Elsevier.

2.1.3. Thermal shock behaviour

Thermal shock associated with rapid heating or cooling has been found to be one of the most critical loading conditions in ceramic materials. The corresponding thermals stresses generated due to the sudden temperature changes could lead to severe degradation and/or failure of the ceramic part or component [1,52].

Assuming a ceramic bar with heating from the temperature T_0 to T_1 fixed on its ends (constrained), the total strain ε becomes zero with the compensation of thermal strains ε_{th} through the development of elastic strains ε_{el} within the bar, so that it may be written [1]:

$$\varepsilon = \varepsilon_{el} + \varepsilon_{th} = 0 \tag{15}$$

where the thermal strains ε_{th} can be expressed with α as the thermal expansion coefficient (CTE), as follows [1]:

$$\varepsilon_{th} = \alpha(T_1 - T_0) \tag{16}$$

The constraint in the thermal expansion may cause the elastic strains ε_{el} responsible for the creation of stresses. By assuming E as the elastic constant, the thermal stress σ_{th} can be written as [1]:

$$\sigma_{th} = E\varepsilon_{el} = -E\varepsilon_{th} = -E\alpha(T_1 - T_0) = -E\alpha\Delta T \tag{17}$$

The magnitude of these thermal stresses are strongly affected by many physical materials properties, such as elastic constants, thermal expansion coefficients, thermal conductivity, among others. These physical properties are also considered in the thermal shock parameters, which may allow the design of thermal shock resistant ceramics [1,53].

Assuming a plate geometry, the maximum thermal stresses σ_{ts} arising from rapid cooling (T_0 to T_1) within a medium, under consideration of the Poisson's ratio ν may be written as [1,29]:

$$\sigma_{ts} = -\frac{\alpha E}{1-\nu}\Delta T = -\frac{\alpha E}{1-\nu}(T_1 - T_0) \tag{18}$$

Considering the Biot concept, the heat transfer coefficient h between cooling medium and sample may be included in the Biot number B as [1]:

$$B = \frac{h\,d}{\lambda} \tag{19}$$

where λ is the thermal conductivity and *d* is the characteristic length of the specimen. The Biot-modulus *B* may be expressed in a dimensionless normalized stress σ^*, with the maximum tensile stresses as [1,54]:

$$\sigma_{ts} = \frac{\alpha E}{1-\nu}(T_0 - T_1)\,\sigma^*(B) = \frac{\alpha E}{1-\nu}\Delta T\,\sigma^*(B) \tag{20}$$

The Biot-modulus and the corresponding normalized stress σ^* depend on the geometry of the considered specimen. In *hard* thermal shock (*worst case* scenario), the assumed infinite *B* may result in a corresponding $\sigma^*(B)$ of 1, whereas in *soft* shocking conditions, both *B* and $\sigma^*(B)$ may be much smaller than 1 [54].

Therefore, the critical temperature difference ΔT_c where first cracking may occur can be expressed for perfect cooling conditions (*worst-case* thermal shock) as [1]:

$$\Delta T_c = \frac{\sigma_f(1-\nu)}{\alpha E} \equiv R \tag{21}$$

where σ_f is the strength prior to thermal shock. The critical temperature difference may be also denoted as the *first* thermal shock parameter *R* [1]. More information about the different thermal shock parameters for assessing the sensitivity of ceramics to thermal shock can be found in [53,55–57].

It is worth highlighting that for the accurate prediction of the critical temperature difference ΔT_c the heat transfer coefficient *h* has to be considered. However, *h* is strongly depending on the actual testing condition and difficult to determine [54].

Additionally, it is evident that the sample size (dimension) strongly affects the critical temperature difference ΔT_c. For instance, decreasing the dimension lead to larger ΔT_c of the same material, as experimentally validated in [58,59]. This fact should be considered by the engineers when designing with ceramics for applications where rapid temperature changes may arise.

2.2. Multi-material design concepts

In novel multi-material ceramics the positive aspects of (i) *architectural* designing by introducing alternating in plane residual stresses, together with the concept of (ii) *microstructure tailoring* have been effectively combined for significantly enhancing their overall (mechanical) properties, aiming to open new application fields in the future [8].

2.2.1. Architectural design

In case of architectural designing, layered ceramics can be distinguished in systems with (i) rather weak or (ii) strong interfaces of the adjacent layer regions [9]. The first concept is based on the work of Clegg et al. [60], where weak graphite interfaces have been introduced within silicon carbide ceramics with higher reported fracture energies. The so-called "graceful failure" is associated with deflection of the propagating crack along the interfaces (interface delamination) during the fracture process. Other studies have shown promising results in enhancing the fracture energies of structural ceramics by interface weakening of laminates through porous interlayers [61,62].

As second approach, layered ceramic architectures with strong interfaces and alternating ceramic/ceramic regions have been proven to be very effective for tailoring the mechanical and/or fracture resistance through the presence of in-plane compressive residual stresses. These residual stresses may be generated due to the strain mismatch of the adjacent layer regions caused by their different thermal expansion coefficients (CTE's) after cooling from sintering temperature [7]. Due to the relatively strong interfaces, alternating (in-plane) tensile and compressive residual stresses may develop within the layers of the ceramic laminate [63]. Based on the classical laminate theory [64,65], the magnitude of the residual stresses within each layer region ($\sigma_{\mathrm{res,i}}$) can be analytically estimated as [63,66]:

$$\sigma_{res,i} = \frac{E_i}{1-\nu_i}(\bar{\alpha} - \alpha_i)\Delta T \tag{22}$$

where E_i is the Young's modulus, α_i the CTE and ν_i the Poisson's ratio of each i$^{\mathrm{th}}$ layer region. The temperature difference, $\Delta T = T_0 - T_{\mathrm{ref}}$ can be calculated from the room temperature (T_0) and the reference temperature (T_{ref}). The corresponding reference temperature, also known as

so-called stress-free temperature above which the laminate may be considered as free of residual stresses, needs to be estimated for the specific materials system in advance. For instance, in case of alumina-based ceramic laminates T_{ref} has been determined in the work of Chlup et al. [67], as ~1470 °C. The average coefficient of thermal expansion can be calculated in the following [63,66]:

$$\bar{\alpha} = \left. \sum_{i=1}^{N} \frac{E_i t_i \alpha_i}{1-\nu_i} \middle/ \sum_{i=1}^{N} \frac{E_i t_i}{1-\nu_i} \right. \tag{23}$$

where t_i is the thickness of the ith layer and N the number of layers. Considering a ceramic laminate consisting of two alternating materials regions (i.e. material A and B), the magnitude of the (in-plane) residual stresses may depend on the materials properties (E_A, E_B, α_A, α_B) and the corresponding volume ratio (V_B/V_A). The volume ratio (V_B/V_A) can be also expressed as ratio of the total thicknesses ($T_B/T_A = \Sigma t_{B,i}/ \Sigma t_{A,i}$) of the contributing material regions, so that Eq. 22 can be written as [63]:

$$\sigma_{res,i} = f_i \left(\left. \sum_{j=1}^{n_B} t_{B,j} \middle/ \sum_{j=1}^{n_A} t_{A,j} \right. \right) = f_i \left(T_B / T_A \right) = f_i \left(V_B / V_A \right) \tag{24}$$

From this correlation, it is clear that the magnitude of the in-plane residual stresses does not depend on the individual layer thicknesses i; however, they can be tailored by their total layer thickness or volume ratio of material A to B, as it has been addressed in the work of Sestakova et al. [63].

In order to describe the crack propagation within layered ceramic architectures, theoretical models based on weight function approximation methods (or finite element analysis) have been provided in literature [63,66,68,69], explaining the shielding effect associated with the compressive residual stresses. The interpretation of these models plotting the "apparent fracture toughness" K_R as function of the crack lengths a for laminates with external as well as internal compressive residual stresses is well explained in the articles [8,9,63] and summarized in the following: In layered ceramics, the stress intensity factor at the crack tip (K_{tip}) can be defined

as the superposition of the external (applied) stress intensity factor (K_{appl}) and the stress intensity factor considering the contribution of the residual stresses (K_{res}) [8,9,63]:

$$K_{tip}(a) = K_{appl}(a) + K_{res}(a) \tag{25}$$

By assuming an external (applied) stress field σ_{appl}, the corresponding applied stress intensity factor K_{appl} can be written as [8,9,63]:

$$K_{appl}(a) = \sigma_{appl} Y \sqrt{\pi a} \tag{26}$$

where Y is the geometry factor depending on loading configuration as well as crack shape and a is the cack length. Considering Eq. 25 together with the Griffith/Irwin failure criterion [28,31] (see Section 2.1.1) leads to the condition [8,9,63]:

$$K_{appl}(a) \geq K_{Ic} - K_{res}(a) = K_R(a) \tag{27}$$

where K_{Ic} is the fracture toughness of the material. The "apparent fracture toughness" K_R can be calculated, for instance, using the Weight function approach as follows [9]:

$$K_R(a) = K_0 - \int_0^a h(x,a)\sigma_{res}(x)\,dx \tag{28}$$

with K_0 as the (intrinsic) fracture toughness of each layer region, $\sigma_{res}(x)$ as residual stress field at the distance x, a the crack depth and $h(x,a)$ as weight function [9]. The weight function $h(x,a)$ for propagating (surface) edge cracks within a bar can be found in [70,71].

As can be seen from the Eqs. 27 and 28, acting compressive residual stresses ($\sigma_{res} < 0 \rightarrow K_{res} < 0$) may lead to the condition $K_R(a) \geq K_{Ic}$, thus, proposing an increase in the R-curve (*shielding effect*), whereas tensile residual stresses ($\sigma_{res} > 0 \rightarrow K_{res} > 0$) may result in a decreasing of K_R with crack extension (*anti-shielding effect*) [8,9,63].

Depending on the location of the in-plane compressive residual stresses (external or internal), two main design approaches can be pursued, yielding either mechanical-resistant or damage-tolerant laminates [8,9].

Approach I – Layered architectures with external compressive residual stresses

In case of designing ceramic laminates with compressive residual stresses induced in the external (top surface) layers, the positive shielding effect [68,69] may yield a rise in the R (crack growth resistance [72])-curve within the first (top-surface) layer region [63]. Figure 3 illustrates a diagram where the apparent fracture toughness K_R as well as the applied stress intensity factor K_{appl} are plotted as function of the "crack length parameter" for laminates with external compressive residual stresses. To explain the effect of shielding, two laminates (ECS1 and ECS2) with different stress magnitude as well as layer thicknesses (distinct volume ratios) are compared in the following, as discussed in the works [9,63]: As schematically illustrated in Fig. 3, the outer layer region (yellow – A) (compressive residual stresses) of ECS1 may be thicker than that of the ECS2-laminate; however, the compressive residual stresses designed in the outer A-region of ECS1 are lower, yet showing significant rise of the curve (shielding effect) for both systems. The inner layer region (blue – B) of ECS1 is designed to be thinner than that of ECS2 with larger tensile residual stresses in the former. In the following, the different applied stresses (σ_{appl}), corresponding to the slopes of the grey lines 1–4, may result in different applied stress intensity factors (K_{appl}). Assuming cracks with the dimensions of those in the shaded bar, and at rather low applied stresses (i.e. line 1 and 2) the condition $K_{appl} < K_R$ might hold, so that the crack cannot extend in both systems ECS1 and ECS2. Considering the ECS1 laminate under higher applied stresses (i.e. line 3), it could be seen that the larger flaws within dashed bar may fulfil the condition $K_{appl} = K_R$, resulting in extension of the crack; however, for the smaller defects crack propagation might not occur. In case of ECS2, all cracks within the shaded bar are too small to favour the crack extension. An increase in the applied stresses (line 4) may yield crack propagation within ECS2 only for the largest flaw (i.e. right end of the shaded bar), corresponding to a crack depth of the size of the first layer region A (A/B-interface). It is

important to emphasize that the maximum shielding might be achieved at the A/B-interface depth with the highest peak in the apparent fracture toughness (K_{Rpeak}), indicating a so-called threshold strength (lower limit) for the laminates below failure might not occur. In contrast to that, the lowest strength of the monolithic ceramic correspond to the (intrinsic) fracture toughness K_{Ic} of the material where the defects are located (dashed grey line) [9,63]. As it has been concluded in the study of Sestakova et al. [63], the laminates with external compressive residual stresses have to be designed in a way that the first (top surface) outer layers are as thin as possible; however, thick enough to cover all possible processing flaws.

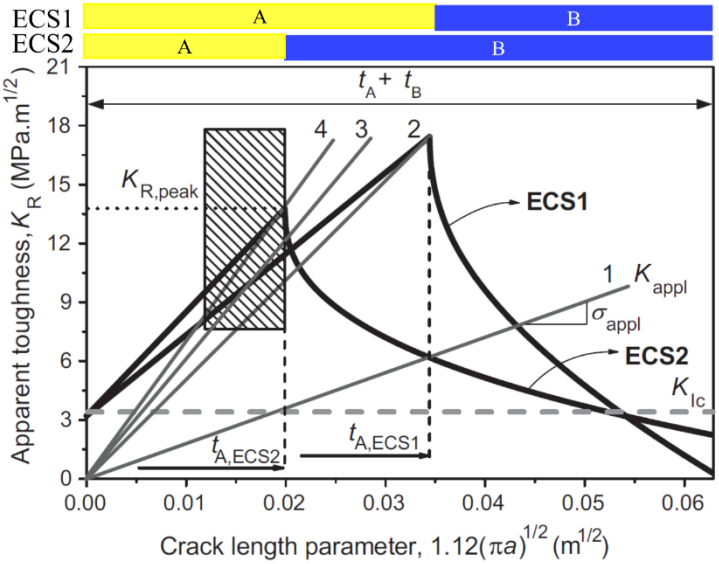

Fig. 3: Apparent fracture toughness of laminates with external (top surface) layers under compressive residual stresses [9,63]. Adapted from [9] with permission from Elsevier.

Approach II – Layered architectures with internal compressive residual stresses

The damage-tolerant design approach, where (protective) layers stresses are embedded within the ceramic architecture, has been proven to be very effective for acting against crack propagation ("crack arresting" phenomena) by taking advantage of the shielding effect [8,63,66,68,69] associated with the in-plane compressive residual stresses [63]. Figure 4a shows the model of the apparent fracture toughness K_R as well as the applied stress intensity factor K_{appl} as a function of crack length for a *periodic* (constant thickness of A and B-regions,

respectively) ceramic architecture with internal compressive layers. As explained in [8,9,63], it might be extracted from such diagrams whether a propagating crack may be arrested (stopped) or not within the internal compressive layers under certain conditions. For instance, assuming a layered ceramic architecture with an artificial pre-crack within the first (surface) A-layer (blue), unstable crack propagation (*pop-in* event) through this tensile-layer may be predicted as long as the condition K_{appl} (see dashed line) > K_R holds. After entering the embedded compressive layer region, the extending crack may be arrested (stopped) since the condition $K_{appl} < K_R$ is likely to be fulfilled (see second intersection of dashed line with the rising curve) [8,9,63]. The phenomena of crack arrest within laminates of the embedded compressive layers is associated with the shielding effect and has been experimentally proven in various works (see [14–16,73]). Further increase in the applied stresses (or K_{appl}) may lead to stable crack propagation up to the highest peak ($K_{R,\,max}$) where the bold line intersects this maximum point, followed by unstable extension until failure of the laminate. Therefore, the slope of the bold line might correspond to the threshold strength (lower bound) (σ_{min}) below failure does not occur. In this regard, the lower bound (σ_{min}) as well as the highest toughness ($K_{R,max}$) can be predicted from the apparent toughness over crack length parameter plot for each specific layered architectures with embedded compressive layer regions [8,9,63].

To achieve the highest toughness (maximum shielding effect) together with (optimum) threshold strengths, the layered *periodic* architecture may be designed with tailored volume ratios resulting in relatively high magnitudes of residual stresses. Following this approach may significantly affect the structural integrity of the layered ceramic architectures through cracking (i.e. tunnelling and/or edge cracks [74,75]) of layer regions, limiting the design optimizations by using periodic structures. *Non-periodic* (thickness of certain material regions are not constant) architectures have been demonstrated as effective design approach for achieving higher toughness as well as higher threshold strength than that of a periodic system with same volume ratio (cp. Fig. 4b) [8,9,63]. In order to optimize the non-periodic laminate designs with internal compressive layers, the first layer (tensile layer) might be selected relatively thin, whereas the embedded (compressive) layer regions is recommended to be made as thick as possible, as stated by Sestakova et al. [63].

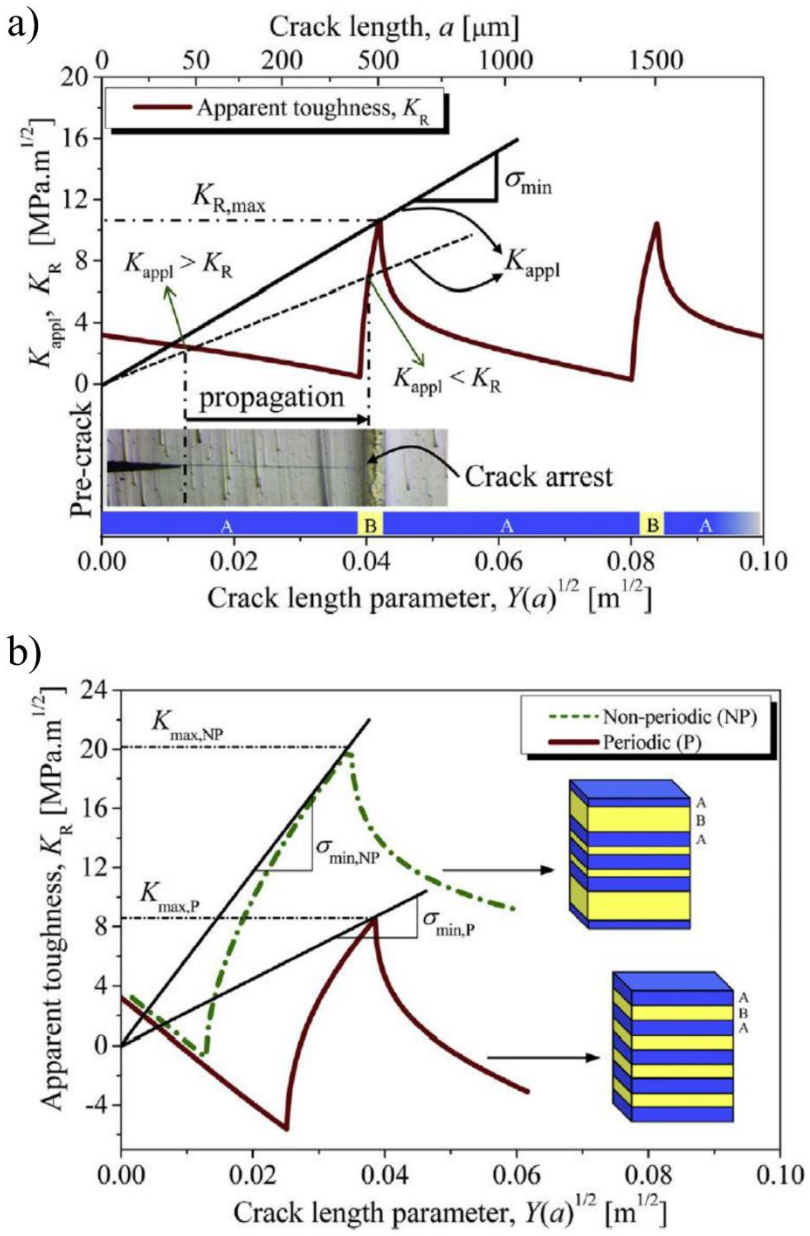

Fig. 4: Apparent fracture toughness of laminates with internal (embedded) layers under compressive residual stresses [8,63]. Reprinted from [8] with permission from Elsevier.

2.2.2. Tailoring of microstructure

In order to design layered ceramic architectures with improved damage tolerance and/or higher mechanical strength, the differences in the thermal expansion coefficient of the containing materials regions must be high enough to induce in-plane compressive residual stresses for the shielding effect; however, not too high to avoid cracking [74]. Therefore, it is from high importance to select proper materials systems which might be combined in a layered multi-

material architecture. Especially, alumina-zirconia-based systems have been exploited as effective combination of materials for ceramic laminates, guaranteeing a minimum (threshold) strength [76].

Another interesting approach to further enhance the fracture resistance of ceramic laminates can be achieved by "texturing" their embedded layer regions inspired from biological systems [8]. One outstanding material found in nature is nacre (or mother of pearl) containing of 95 vol.% aragonite ($CaCO_3$) and 5 vol.% organic phases. Due to their hierarchical architecture and the resulting toughening mechanisms acting over a wide length scale, nacre shows the optimum toughness-to-strength relationship among all materials [6].

Mimicking the "brick-mortar" structure of nacre (see Fig. 5a) may show high potentials for designing "tougher" ceramic systems, leading to the development of nacre-like alumina [4,6,77–79]. Such nacre-like ceramics fabricated through ice-templating, magnetically-assisted slip casting, etc., perfectly resemble the structure of mussels, where alumina may act as brick and the second phases (i.e. Poly(methyl methacrylate) (PMMA), graphene, Ni/NiO, among others) as mortar material [6]. In ceramic coatings, controlling the microstructure of alumina could be achieved through the nucleation process during Chemical Vapour Deposition (CVD) [80]. Besides that, orienting the microstructure ("texturing") along preferred crystal orientations during the sintering stage has been also established as promising "bio-inspired" design strategy by taking advantage of the templated grain growth (TGG) process [81–83]. The preferred alignment of high aspect-ratio platelets for the formation of textured alumina ceramics has been attempted through the application of strong magnetic fields [84,85] and most commonly through the gel/tape casting process [83,86]. During the TGG, oriented templates ("seeds") are favoured to grow under consumption of the finer surrounded particle matrix based on the effect of Ostwald ripening [87], yielding rather dense (alumina) ceramics with textured microstructures after sintering (Fig. 5b) [19,83]. It has been shown that in such textured alumina ceramics rather high "texture" degrees are achievable highlighting the success of the approach [88] .

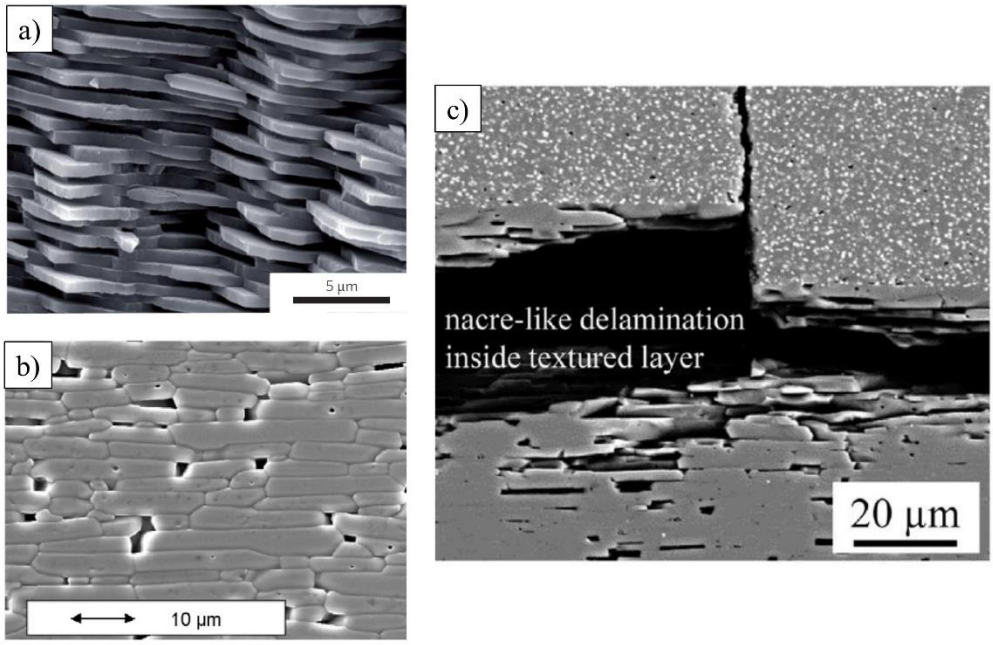

Fig. 5: (a) Fracture surface of nacre ("brick-mortar" structure). Reproduced with permission from Springer Nature [78]. (b) Microstructure of textured alumina. Adapted from [19] with permission from Elsevier. (c) Fracture behaviour of alumina-based laminates with internal textured layers [8,22]. Adapted from [8] with permission from Elsevier.

In recent research activities, the positive effect of microstructure texturing together with the concept of residual stresses have been combined in layered ceramic architectures, resulting in enhanced damage tolerances associated with favoured crack deflection mechanisms (see Fig. 5c) during the fracture process [8,19,22].

In order to assess whether a propagating crack may deflect or penetrate at the interface of dissimilar materials, predictions may be derived from the models of He, Hutchinson and Evans [89,90], where the maximum interfacial fracture resistance favouring crack deflection mechanisms may be correlated to the ratio of maximum critical energy release rate for deflection (G_d) to that for penetration (G_p). It has been demonstrated in the work of Pavlacka et al. [20] that the He-Hutchinson plot can be also applied on individual textured platelets within alumina composites. The adapted model (Fig. 6) predicts that cracks are favoured to deflect on the "basal" interfaces between two adjacent platelets as long as the ratio of its interfacial fracture resistance Γ_i to the fracture resistance of the single platelet (G_c) might be less than 25% ($\Gamma_i / G_c < 0.25$) [20,22].

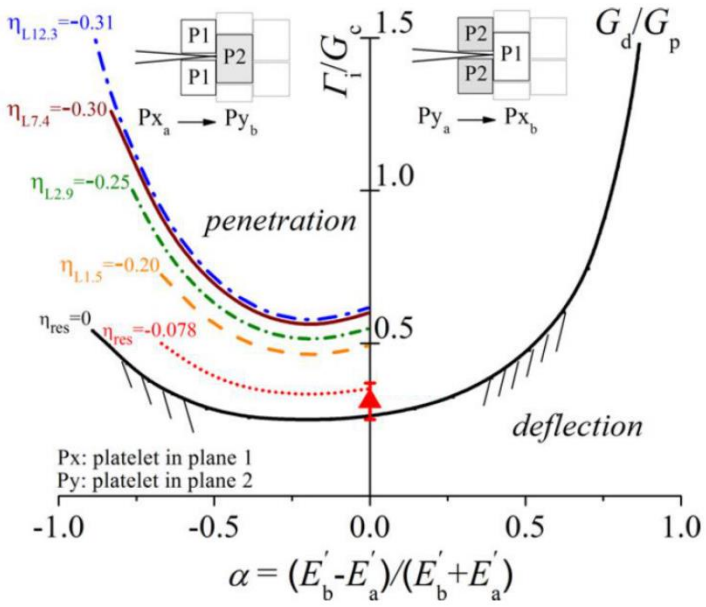

Fig. 6: He and Hutchinson plot of textured alumina platelets within ceramic laminates with and without residual stresses. Adapted from [22] with permission from Wiley.

The effect of the in-plane compressive residual stresses within the textured layer regions on the acting toughening mechanisms has been incorporated in the adapted He-Hutchinson plot by calculating the non-dimensional length parameters η_{res} [89], which may indicate a rather significant upwards shift of the G_d/G_p-curve depending on the magnitude of residual stresses, the fracture toughness of the platelets, etc. The upwards shift of G_d/G_p-curve associated with the internal compressive stresses may extend the "preferred" zone in the He-Hutchinson plot where the crack is favoured to deflect from its transverse propagation path, allowing to further enhance the fracture resistance of layered ceramic architectures with textured microstructures [20,22].

2.2.3. Fabrication of 2D and 3D layered ceramics

Nowadays, the tape casting technology is widely used to fabricate layered ceramics for various functional applications. In tape casting (Fig. 7a), the ceramic slurry poured within a reservoir is carefully spread using a gap adjusted by a doctor blade through carrier motion for casting thin foils (or films). The solvent content within the slurries can be evaporated by slowly moving the casted layer through a drying chamber [91,92]. Details about slurry preparation, the tape casting itself and the drying process may be found in literature [92]. Tape casting followed by stacking and lamination, debinding and sintering is so far the major approach for fabricating layered ceramics with tailored residual stresses and microstructures (even texturing). However, one limitation in tape casting ceramic laminates is the restriction in building-up more complex-shaped geometries, thus limiting the potential of multi-material-based components for novel structural applications.

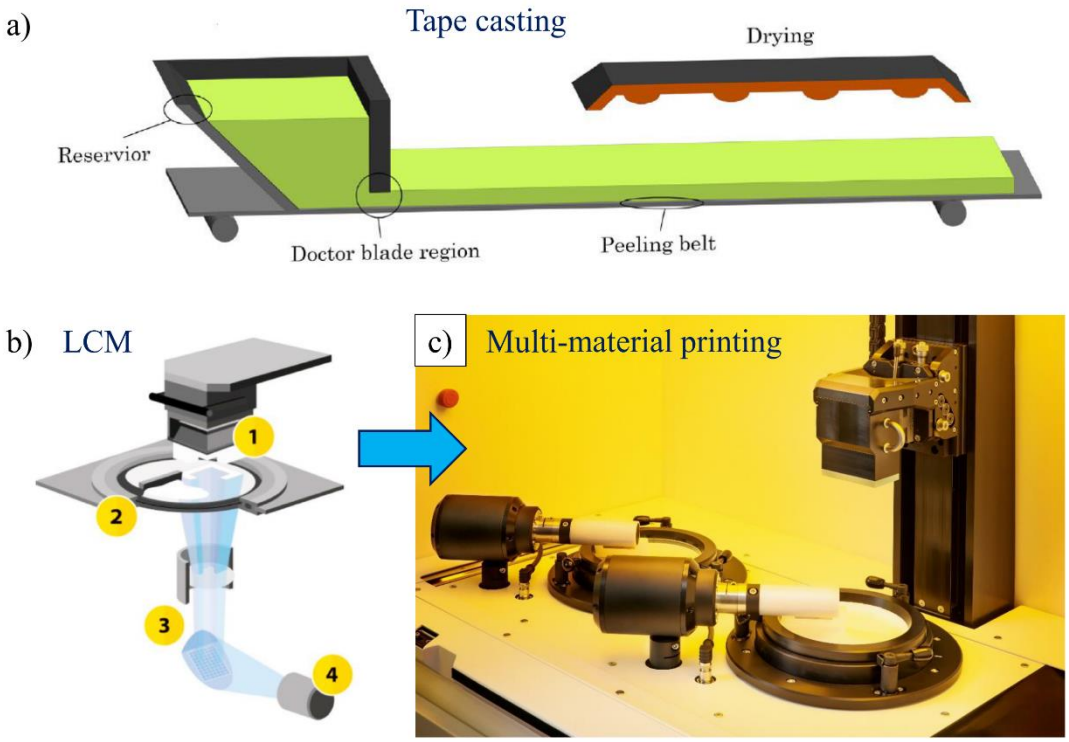

Fig. 7: (a) Schematic of the tape casting technology. Adapted from [91] with permission from Elsevier. (b) Principle of LCM-printing: (1) building platform, (2) vat, (3) optical system, (4) light engine. Adapted under the terms of the CC-BY license [93]. (c) Multi-material 3D-printing using the two-vat system (with courtesy of Lithoz GmbH) [94].

In recent years, additive manufacturing (or 3D-printing) has been established as promising technology for fabricating special components of highly-shaped complexities in the field of metals, polymers as well as ceramics [95]. In the sector of technical ceramics, additive manufacturing may provide many solutions for designing complex ceramic parts and components [96,97]. Especially, stereolithographic 3D-printing, such as the Lithography-based Ceramic Manufacturing (LCM) technology (Fig. 7b), has opened new pathways for developing (bulk) ceramic parts and components with sound mechanical properties [23].

The LCM-technology is based on the layer-by-layer photo-polymerisation of slurries composed of homogeneously-dispersed ceramic powders within a polymer matrix through digital light processing [23–25]. The schematic of the LCM-process is illustrated in Fig. 7b, where the building platform (1) is lowered into the photo-sensitive slurry to the distance of the desired (green) layer thickness from the bottom of a transparent rotating vat (2) and subsequently exposed by using light from below. The photo-polymerisation takes place using light with wavelength of ~460 nm emitted by a light engine (4) through a dynamic mask (optical system) (3), generating highly-resolved structures in a layer-by-layer curing process. After printing, the parts are removed from the building platform and carefully cleaned to remove the excess slurry. The cured polymer network within the part can be removed through a defined debinding (binder-burn out) stage. Finally, a sintering step takes place to achieve a highly-dense ceramic part or component with properties well-comparable with that fabricated by conventional methods [24,25,93]. More details about the LCM-process can be found in literature [23–25].

The influence of sintering parameters together with the consideration of surface conditions and testing configuration with respect to printing directions of 3D-printed (monolithic) alumina has been studied in a previous work [26]. Considering these aspects enabled the development of LCM-alumina with sound characteristic strength and relatively high Weibull-modulus. The feasibility of the LCM-process for printing bulk (monolithic) alumina ceramics with textured microstructure has been investigated in [98]. Beyond these advances, a two-vat multi-material LCM printing system [27] (see Fig. 7c) has been developed by Lithoz GmbH, which enables the successful printing of (i) novel porosity-graded ceramics [99,100] and might open a new way for designing as well as fabricating multi-material ceramic architectures with tailored residual stresses.

3. Materials of study and architectures

A brief overview of the designed layered 2D/3D architectures with tailored microstructures investigated in the **Publications A** [101], **B** [102], **C** [103], **D** [104], and **E** [105] is given in the following. The main processing of the designed architectures was conducted by co-authors listed in the corresponding publications. The reader is again cautioned that the term "*2D*-architectures" is corresponding to all samples fabricated by the "planar (2D)" tape-casting technology, whereas "*3D*-architectures" may belong to the samples as well as components printed by using the LCM-technology.

In case of the 2D-architectures, the investigated materials were (equiaxed) alumina (EA) and textured alumina (TA) with elongated grains oriented in [0001] (basal)-direction. The layered 2D-architectures are designed with alternating EA (tensile residual stresses) as well as TA (compressive residual stresses), as schematically illustrated in Fig. 8.

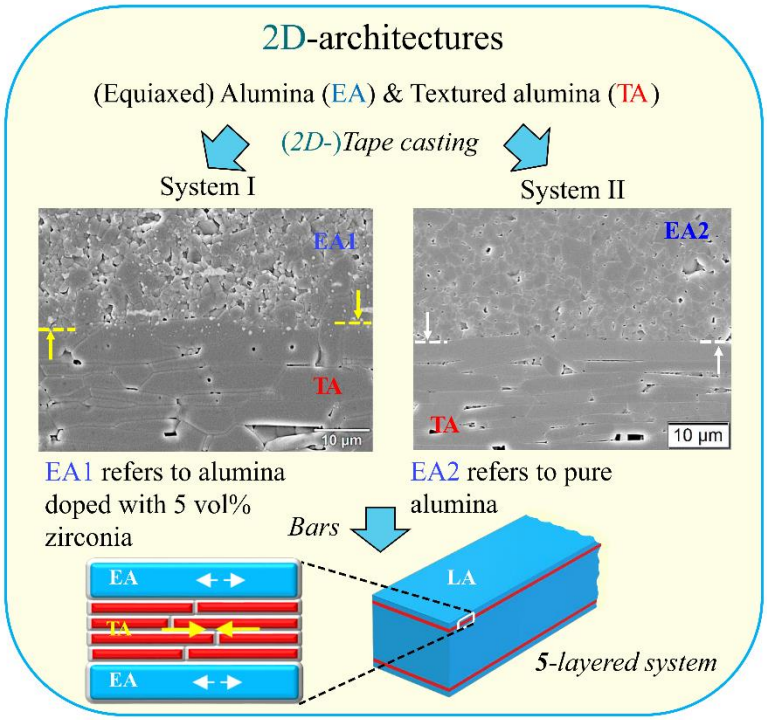

Fig. 8: Layered 2D-architectures with embedded textured microstructures. In case of the laminate designs, the textured material regions (compressive residual stresses) were embedded either between (equiaxed) alumina-zirconia (EA1) or (euqiaxed) pure alumina (EA2) regions (tensile residual stresses). Images were taken from own works under the terms of the CC-BY as well as the CC-BY-NC license [102,103].

In **Publication A** [101], notched micro-cantilevers located within single textured grains and along grain boundaries were tested. The material of study was textured alumina prepared from a slurry containing high-purity α-alumina powder. Single-crystal alumina platelets (templates) of high-aspect ratio as well as a small concentration of dopants ($CaO:SiO_2$ = 1:1) were added to the powder for favouring the TGG process. After tape casting, stacking, post-processing and sintering, a sample was prepared from the monolithic textured alumina plate. The microstructure of the textured alumina sample showed elongated grains with length of ~15 – 40 µm and a thickness of ~ 3 – 5 µm. The determined Lotgering factor (LF), which can be considered as a measure of the texture degree, was approx. 0.8. Details about the slurry as well as sample preparation are found in the corresponding article [101].

To study the Hertzian contact damage behaviour of layered alumina-based ceramics (**Publication B** [102]), three different designs, namely monolithic EA, monolithic TA as well as a layered architecture of alternating EA/TA regions were fabricated through the tape-casting technology. In case of monolithic EA as well as the EA-regions of the laminates, an alumina-based slurry of high-purity alumina powder was mainly used. Additionally, 5 vol% of 3 mol% yttria-stabilized zirconia particles were added to the alumina powder. The choice of the equiaxed alumina material doped with zirconia (EA1) allows the introduction of higher residual stresses in the laminate through the larger CTE mismatch and may also prevent abnormal grain growth in alumina. A layered *non-periodic* architecture of alternating EA/TA/EA/TA/EA regions of ~ 110 µm/300 µm/2520 µm/300 µm/110 µm with a volume ratio (V_{EA}/V_{TA}) of approx. 5 was designed (see System I in Fig. 8). In case of the TA-regions, similar slurry preparation (minor changes) was conducted as mentioned above. In the layered architectures, in-plane tensile residual stresses of ~ +50 MPa and in-plane compressive residual stresses of ~ −240 MPa were introduced within the EA- and TA-regions, respectively. Further information on sample fabrication and preparation for the Hertzian indentation tests are given in **Publication B** [102]. Details about slurry preparation can be also found in the work of Hofer et al. [106].

In **Publication C** [103] the high-temperature fracture behaviour of alumina laminates with embedded textured layer regions was explored. Tape casting was employed for fabricating the monolithic EA, TA as well as layered EA/TA system. The TA material was prepared in a similar way (only minor changes) as explained before; however, in case of the EA material a pure alumina slurry was used from the high-purity α-alumina powder without a content of zirconia particles (referred as EA2). The design of the *non-periodic* 5-layered architecture of volume

ratio V_{EA}/V_{TA} of ~ 8 was achieved by the sequence of layer regions EA/TA/EA/TA/EA of ~ 200 µm/160 µm/2240 µm/160 µm/200 µm. Figure 8 shows also a SEM microstructure image of the interface region of the laminate with alternating pure "EA2" and TA alumina layers (System II). The corresponding in-plane residual stresses at room temperature can be determined as ~ +25 MPa (tensile) within EA and −200 MPa (compressive) in the embedded TA-layer regions. It is worth highlighting that in the article the residual stresses within the layered system as a function of temperature is provided for better interpretations of the high-temperature bending tests. Details of materials processing as well as sample preparation can be found in **Publication C** [103].

In case of 3D-architectures, the materials of study were alumina (A) and alumina-zirconia (or zirconia-toughened alumina) with 80 vol. % alumina and 20 vol. % of 3 mol % yttria stabilized zirconia (ZTA). The layered architectures were designed with alternating A-regions (compressive residual stresses) and ZTA-layers (tensile residual stresses) following two main design strategies, as schematically illustrated in Fig. 9. Printing of the designs was performed by Lithoz GmbH.

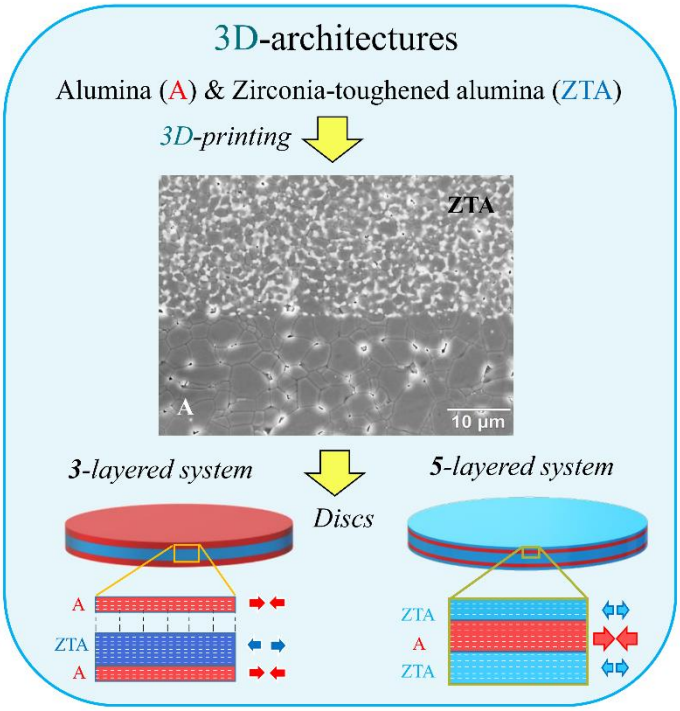

Fig. 9: Multi-material 3D-architectures designed with alternating alumina (A) (compressive residual stresses) and alumina-zirconia regions (ZTA) (tensile residual stresses). Images were taken from own works under the terms of the CC-BY license [104,105].

In **Publication D** [104], a strategy for significantly improving the strength of 3D-printed alumina is demonstrated, where a 3-layered alumina-based architecture composing of top surface pure alumina (A) layers with compressive residual stresses and an internal ZTA-region with tensile residual stresses was designed. The multi-material architectures as well as monolithic (reference) A disc-shaped specimens were fabricated by using the LCM-technology. After sintering a design with the sequence A/ZTA/A of ~ 75 µm/700 µm/60 µm was achieved, corresponding to the selected volume ratio V_{ZTA}/V_A of ~ 5. In the multi-material sample, the in-plane compressive residual stresses within the outer A-layers were estimated as ~ −320 MPa, whereas the tensile residual stresses induced in the internal ZTA-regions were only +60 MPa. Details about the printing and the sintering conditions can be found in the corresponding **Publications D** [104].

Publication E [105] demonstrates the feasibility of arresting thermal shock cracks by embedding internal A-layers with compressive residual stresses between ZTA-layer regions (tensile residual stresses). Monolithic A, ZTA as well as the multi-material system were 3D-printed through the LCM-technique. After sintering, the designed *non-periodic* multi-material architecture showed alternating ZTA/A/ZTA/A/ZTA layer regions of ~ 140 µm/210 µm/ 1040 µm/ 220 µm/ 110 µm with volume ratio V_{ZTA}/V_A of ~ 3. In such architectures, the in-plane compressive residual stresses (A-region) as well as the in-plane tensile residual stresses (ZTA-region) were calculated as ~ −300 MPa and +100 MPa, respectively. Based on this concept, the multi-material component was designed with 150 µm outer ZTA- and 200 µm embedded A-layer regions. For more details on the multi-material printing as well as the post-processing, the reader is referred to the corresponding article [105].

4. Experimental methods

In the following, selected (most important) methods of typical loading scenarios (i.e. bending, contact loading and thermal shock) used for mechanically characterizing the layered architectures are briefly discussed. Details and experimental descriptions of other materials characterization methods (microstructural characterization, elastic-modulus, CTE, etc.) examined in this thesis can be found in the **Publications A** [101], **B** [102], **C** [103], **D** [104] and **E** [105].

4.1. Loading scenario I – Bending

The experimental methods used in this work to evaluate the fracture toughness (micro- and macro-scale) as well as the strength of the investigated alumina-based ceramics are briefly explained in the following.

4.1.1. Micro-scale fracture toughness and macro-scale fracture resistance

The (fracture) toughness evaluation of layered alumina-based samples are crucial for understanding their fracture behaviour. At small scales, several methods such as micro-pillar splitting, nano-indentations as well as bending of notched micro-cantilevers are used to locally measure the fracture toughness of thin films, single grains, individual phases, etc. In the latter method, micro-cantilevers are prepared and notched by using the Focus-Ion beam technique (FIB) and subsequently tested through nano-indenters [107,108]. The local fracture toughness determination through micro-cantilever bending tests on ceramic grain and grain boundaries has been extensively studied in literature [77,109–112]. In case of brittle materials, the micro-scale fracture toughness K_{Ic} may be calculated from the testing data using the Griffith-Irwin criterion (Eq. 5), where the fracture stress σ_c for pentagonal-shaped cantilevers (see schematics in Fig. 10a) can be analytically calculated according to the Euler-Beam-theory as follows [113]:

$$\sigma_c = \frac{F_{max}(b - z_0)}{I_x}(L - x_2 - x_1) \tag{29}$$

with F_{max} as the maximum fracture load and *a, b*, m_a, *L*, x_1 and x_2, and α (notch depth) are the corresponding cantilever dimensions (see Fig. 10a). The distance z_0 and the second moment of area I_x for the pentagonal shape can be calculated as [113]:

$$z_0 = \frac{1}{b + \frac{m_a}{2}} \left(\frac{b^2}{2} - \frac{{m_a}^2}{6} \right) \tag{30}$$

and

$$I_x = \frac{ab^3}{3} + \frac{a{m_a}^3}{12} - a\left(b + \frac{m_a}{2}\right){z_0}^2, \tag{31}$$

respectively.

Due to the differences noticed between the shape-factor *Y* for pentagonal cantilevers stated by Chan [114] and that reported by Di Maio and Roberts [115], a new fitted polynomial factor as function of normalized crack lengths for the evaluation of K_{Ic} of the pentagonal-shaped (notched) cantilevers has been derived. Details about the testing procedure and evaluation are reported in **Publication A** [101].

On the macro-scale level, the concept of work of fracture [116,117] has been considered for the evaluation of the fracture resistance of textured alumina-based architectures tested over a wide temperature range (**Publication C** [103]). In this study, the area under the load-displacement curves was integrated with the fracture force as maximum limit and consequently divided by twice of the cross-area of the bending bars. As result, the inelastic work of fracture (plastic contribution) and the total work of fracture were calculated and the amount of plasticity expressed in the reported work of fracture ratios (*WOF*-ratio) for each layered system. This procedure has been conducted for the special case of (indented) textured ceramics, showing favoured inelastic contribution during the high-temperature bending.

For the basic materials characterization of 3D-printed alumina as well as alumina-zirconia (ZTA) in **Publication D** [104], fracture toughness measurements were performed on bars using the Single-Edge-V-Notched Beam (SEVNB-method). Details about the SEVNB–method can be found in the ISO 23146 standards [118].

4.1.2. Strength testing and evaluation

To evaluate the flexural strength, indentation strength or retained strength, either uniaxial or biaxial bending tests were performed on the multi-material as well as monolithic (reference) samples, respectively. In case of brittle materials, the most common standard testing configurations for measuring the uniaxial flexural strengths are either three-point bending or four-point bending [119]. A review on flexural bending tests may be found in the work of Quinn and Morrell [120].

In **Publication C** [103], (uniaxial) four-point bending tests (see Fig. 10b) are conducted at room temperature in air or at elevated temperatures (up to 1200 °C) in vacuum for the determination of the (indentation) strength of alumina-based ceramic laminates with embedded textured layers as well as the monolithic bars. The flexural strength (σ_f) using the four-point bending fixture can be calculated as [119]:

$$\sigma_f = \frac{3}{2} \frac{F(S_1 - S_2)}{bh^2}, \tag{32}$$

where F is the (maximum) fracture force, S_1 and S_2 are the outer and inner spans, b is the specimen width and h the height of the specimen. The corresponding flexural (outer fibre) strain (ε) in the 4-point bending loading configuration may be calculated from the registered displacements (δ) measured by using a three-point contact extensometer, as follows:

$$\varepsilon = \frac{4\delta h}{{S_2}^2}. \tag{33}$$

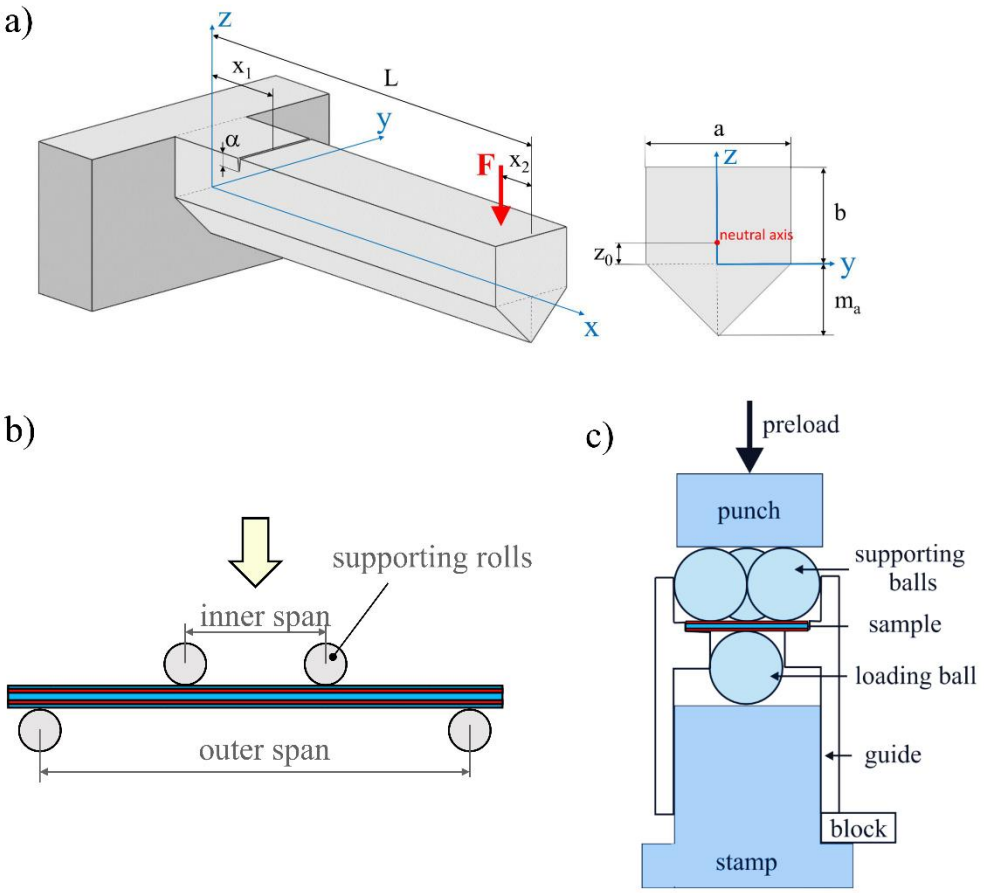

Fig. 10: (a) Illustration of the pentagonal-shaped micro-cantilevers used for fracture toughness evaluation of single grain and grain boundaries. Reprinted under the terms of the CC-BY license [101]. (b) Schematic of bars tested under four-point bending for evaluation of work of fractures and/or for indentation strength testing. (c) Schematic illustration of the B3B-Test used for biaxial strength measurements. The alternating blue/red layer regions refer to the layered designs of the laminate architectures. Adapted under the terms of the CC-BY [104].

In the praxis many ceramic components are loaded under biaxial stress conditions (i.e. thermal shock); therefore, biaxial bending methods are preferentially used for the strength testing of brittle materials [121]. Among all biaxial testing methods, the Ball-on-Three-Balls test (B3B) was used for measuring the strength on the 3D-printed multi-material as well as monolithic (reference) discs in **Publication D** [104] and **Publication E** [105]. It is worth highlighting that the main advantage of the B3B-setup is that only a small volume or surface is loaded in the specimen centre during testing, which may avoid influences from edge defects [122]. The

schematic of the B3B-test is shown in Fig. 10c, indicating the symmetrical support of the disc-shaped specimen by three balls during the central loading (opposite side) by a fourth ball. After a defined pre-load is applied, the block has to be removed through lowering the guide and the force can be increased until fracture will occur [123,124]. The maximum (biaxial) tensile stress at the centre of the specimen discs has been defined as strength σ_f and can be calculated as [123]:

$$\sigma_f = f \cdot \frac{F_{max}}{t^2}, \tag{34}$$

where F_{max} is the maximum fracture load, t the specimen thickness and f a dimensionless pre-factor. In case of monolithic discs, the factor f is mainly depending on the specimen geometry (t/R), the support geometry (R_a/R) and the Poisson's ratio (ν) of the material and was evaluated for a wide parameter set, so that $f = f(t/R, R_a/R, \nu)$, where R_a and R are the support ring as well as specimen radius [123]. In case of the multi-material discs, the effect of the elastic mismatch has been considered in the calculation; therefore, the factors for multi-materials architectures, $f = f(t/R, R_a/R, \nu_A, \nu_B, E_A, E_B)$, have been evaluated for each specific design, where E_A and E_B are the corresponding elastic moduli of each material regions of the multi-material architectures.

4.1.3. Fracture analysis

To analyse the micro- as well as macro-scale fracture surfaces of all architectures investigated in this work, scanning electron microscopy (SEM) was used. In this regard, the specimen surfaces were sputtered with gold in advance for guaranteeing appropriate imaging of the non-conducting samples. An excellent guidance for the interpretation of fracture is found in the work of Quinn [32].

4.2. Loading scenario II – Hertzian contact loading

In the last decades, Hertzian indentation tests have been conducted on many polycrystalline ceramics and glasses for investigating their contact damage resistance [125,126]. In this work (**Publication B** [102]), spherical indentation tests were performed on layered alumina-based laminates with embedded textured layer regions and on the corresponding monolithic (reference) samples. To investigate the effect of microstructure texturing on the contact damage behaviour of layered alumina-based architectures, the procedure schematically illustrated in Fig. 11 has been followed by combining *cross-sectioning* and *ion-slicing* techniques together with *acoustic* measurements during the indentation cycle.

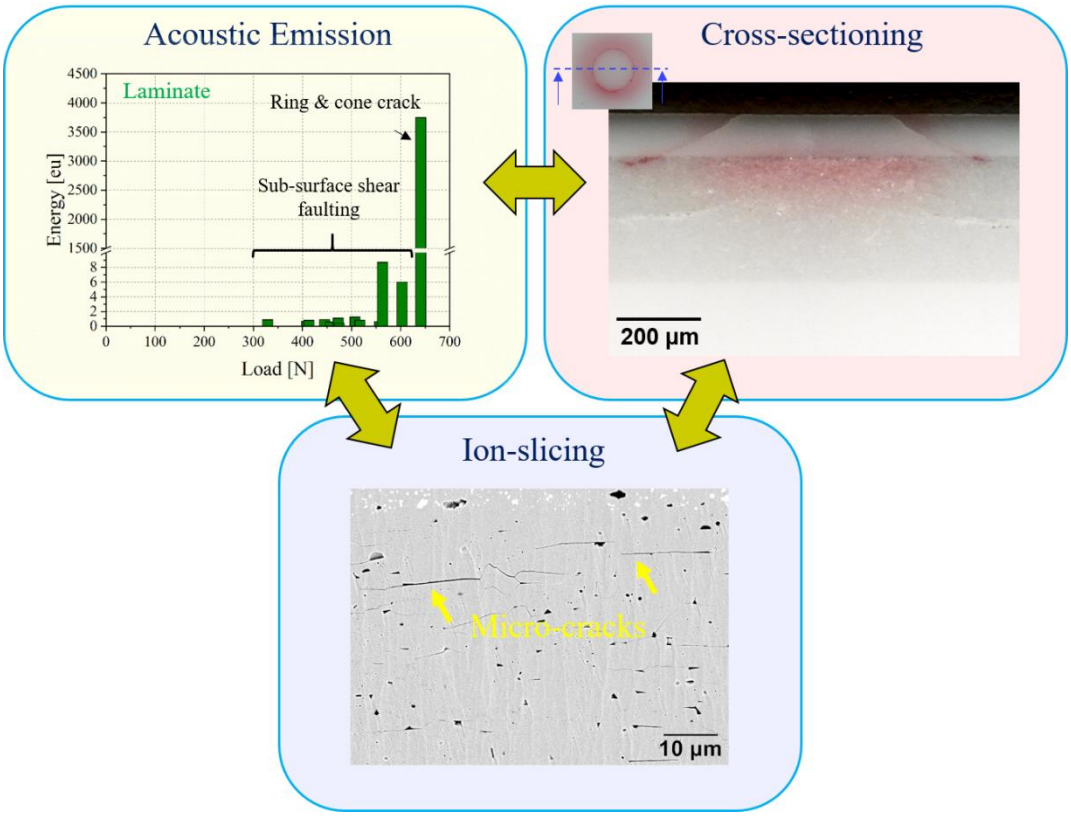

Fig. 11: Illustration of the Hertzian contact damage investigation combining cross-sectioning and the ion-slicing technique together with acoustic measurements. Images adapted from own work under the terms of CC-BY-NC license [102].

4.2.1. Acoustic emission for crack detection

Acoustic emission (AE) is an exceptional method for analysing the materials behaviour under different loading scenarios. For instance, crack propagation, fibre breakage and among others may send elastic waves detected by AE-sensors, resulting in a transfer of these AE-signals into electrical ones [127,128]. In our case, the AE events may be associated with the contact damage mechanism during the spherical indentation test. In this regard, the AE-system may allow the detection of critical forces of (first) Hertzian ring crack initiation. In AE-diagrams, the AE-signals can be expressed as energy units (eu), where it is noteworthy mentioning that 1 eu may corresponding to $10^{-14}V^2s$ [127]. In the resulting AE-diagrams of each individual Hertzian indentation tests, the energy units are plotted over the indentation load. The combination of cross-sectioning/ion slicing together with AE-diagrams may allow a classification of the damage mechanism. For instance, rather small energies have been correlated to the quasi-plastic response (micro-cracks) (< 100 eu) of the textured microstructure and relatively high peaks (above 1000 eu) can be associated with Hertzian ring and cone cracking on the surface regions. The reader is referred to **Publication B** [102] for more details.

4.2.2. Cross-sectioning and Ion-slicing

Revealing the sub-surface patterns of ceramics after indentation can be achieved by using the so-called “bonded interface” methods, where the specimen is cut in two pre-sections and subsequently bonded together before indenting. Afterwards, the sample surface can be indented directly at the interface bonding, allowing the identification of damage patterns on each half through microscopic techniques [41]. In literature, this procedure has been widely used to reveal the sub-surface damage after indentation ceramic materials [43–45,48].

In this work, a novel approach to assess the (sub-surface) damage mechanisms, either Hertzian ring and cone cracking or quasi-plastic formation, was followed by applying the combination of cross-sectioning (after the indentation) together with the ion-slicing technique. In quasi-plastic damage regions, grain pull-outs associated with the grinding and polishing treatment may not enable the identification of shear faulting cracks. After cross-sectioning of the side surfaces to the region of interests (centre of imprints), applying the ion-slicing technique could be used for revealing specific regions along the cross-sections and detecting micro-crack formations through scanning electron microscopy (SEM).

4.3. Loading scenario III – Rapid temperature changes (thermal shock)

4.3.1. Evaluation of strength degradation

In the works of Hasselman [56,129], the thermal shock crack initiation and the effect on the strength of ceramic materials has been theoretically predicted and experimentally validated on alumina rods. As long as the selected temperature difference (ΔT) is below the critical temperature difference (ΔT_c), $\Delta T < \Delta T_c$, no fracture nucleation and extension of the initial crack (i.e. defects described as short Griffith cracks) might occur so that the strength is not affected. The strength degradation of ceramic materials after critical thermal shock ($\Delta T_c' > \Delta T \geq \Delta T_c$) may follow a rather constant trend associated with the subcritical nature of the newly formed cracks with a certain depth. A significant increase in the thermal shock severity ($\Delta T \geq \Delta T_c'$), where $\Delta T_c'$ is a new critical thermal shock difference, may be required for further unstable crack growth yielding a gradual strength decrease [56,129]. It is worth highlighting that in the case of low strength ceramics only a gradual strength decrease above the critical temperature difference (ΔT_c) is expected [56], as could be experimentally shown for porous ceramics [130].

In this work (**Publication E** [105]), the thermal shock resistance of alumina-based multi-material ceramics and that of (reference) monolithic samples is investigated after performing water quench tests over a wide range of temperature differences (see Fig. 12, right side). The retained (biaxial) strength after thermal shock is determined using the evaluation (B3B) explained in Section 4.1.2.

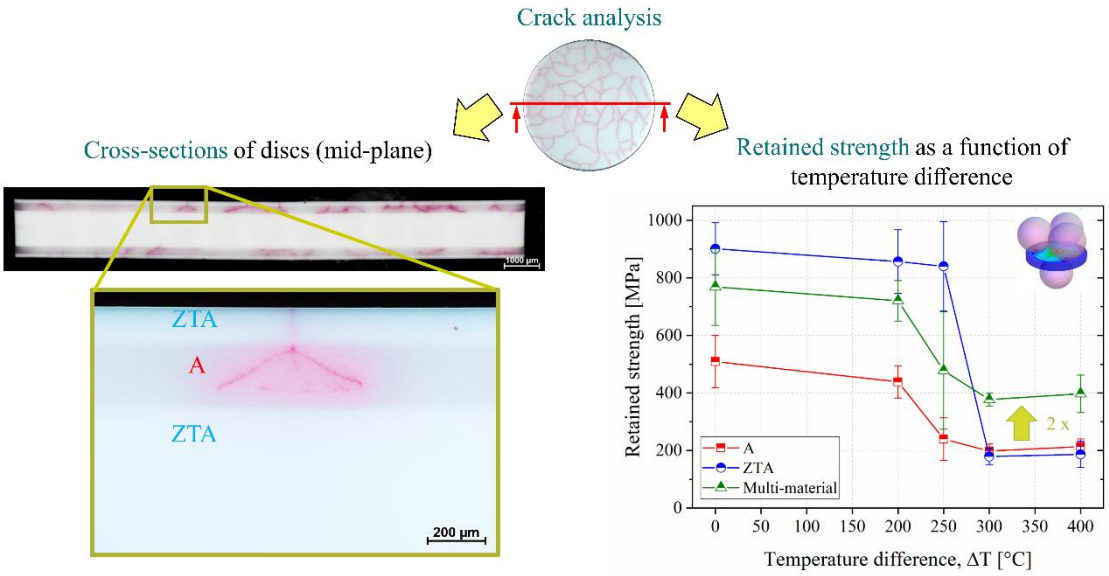

Fig. 12: Schematic procedure of the assessment of thermal shock resistance. Images adapted from own work under the terms of the CC-BY license [105].

4.3.2. Analysis of thermal shock cracks

To study surface patterns, the thermal shock cracks are analysed on the top sample surfaces by counting the intersected cracks along selected lines, which can be defined as crack densities. Although the crack density may be used to qualitatively estimate the sensitivity of materials to thermal shock, the strength degradation, or retained strength over temperature difference, may be correlated with the depths of thermal shock cracks after critical shocking (see Griffith-Irwin criterion, Eq. 5). In doing so, specimen discs can be treated with liquid dye penetrant after the water quenching tests and selected cross-sections in the region of interest (i.e. mid-plane of discs) are analysed by measuring the final depth of the propagated cracks. Cross-section analysis together with measuring the retained strength after critical thermal shocking are an exceptional strategy for quantitatively describing the thermal shock resistance of ceramic materials. More experimental details are found in **Publication E** [105].

5. Summary of publications

In this Chapter, a brief overview of the **Publications A** [101], **B** [102], **C** [103], **D** [104] and **E** [105] included in this doctoral thesis is given. The mechanical response as well as the fracture behaviour of layered alumina-based architectures with tailored microstructures under distinct loading conditions are discussed in detail. Design concepts for 3D-printing multi-material alumina-based ceramics with exceptional mechanical properties are presented.

5.1. Understanding fracture of layered ceramics with textured microstructure: From micro- to macro-scale

In recent years, the (macro-scale) fracture behaviour of alumina-based laminates with embedded textured layers has been extensively studied under uniaxial bending [20,22,106], where the combination of the textured microstructure together with compressive residual stresses has been proven as promising strategy for enhancing their fracture resistance. However, the underlying mechanisms during the (macro-scale) fracture process may be not fully understood yet. Especially the question arose, why the propagating (surface) crack during fracture may be favoured along the "basal" boundaries of the elongated "textured" grains. It was hypothesized that exploring the "micro-scale" fracture properties in the level of single grains might deliver some important insights of the fracture mechanisms and could be further used for optimizing the textured microstructure within novel ceramic architectures.

On the micro-scale level (**Publication A** [101]), pentagonal-shaped cantilevers were fabricated using the focus ion beam (FIB) technique, either within single textured alumina grains perpendicular to the (basal) [0001]-direction (c-axis of the crystal), or along multiple textured grains parallel to the c-axis, with artificial notches in one of the prismatic facets or directly at the basal grain boundaries (see Fig. 13). The FIB milling process was conducted by cutting the notches from the desired locations of the textured grains or directly at their boundaries, followed by coarse milling of the pentagonal-shaped cantilevers and the fine polishing to its final beam size. The bending tests on the micro-cantilevers were performed on a nanoindenter with a spherical tip by using a constant load rate until fracture. Afterwards, the fracture surfaces were analysed, and the notch depths were measured on the corresponding SEM images of the broken cantilevers. The micro-scale fracture toughness data (K_{Ic}) was evaluated using the Griffith-Irwin criterion [28,31] according to the Linear Elastic Fracture mechanics. The corresponding

fracture stress was evaluated based on the Euler-Bernoulli beam theory by using the equations for pentagonal-shaped cantilevers, as can be found in the work of Csanádi et al. [113] (see Section 4.1.1). An appropriate shape function (Y) for the pentagonal-shaped cantilevers was determined from Finite Element (FE) analysis. More details on the cantilever fabrication and testing as well as on the evaluation of the micro-scale fracture toughness values can be found in the author's **Publication A** [101].

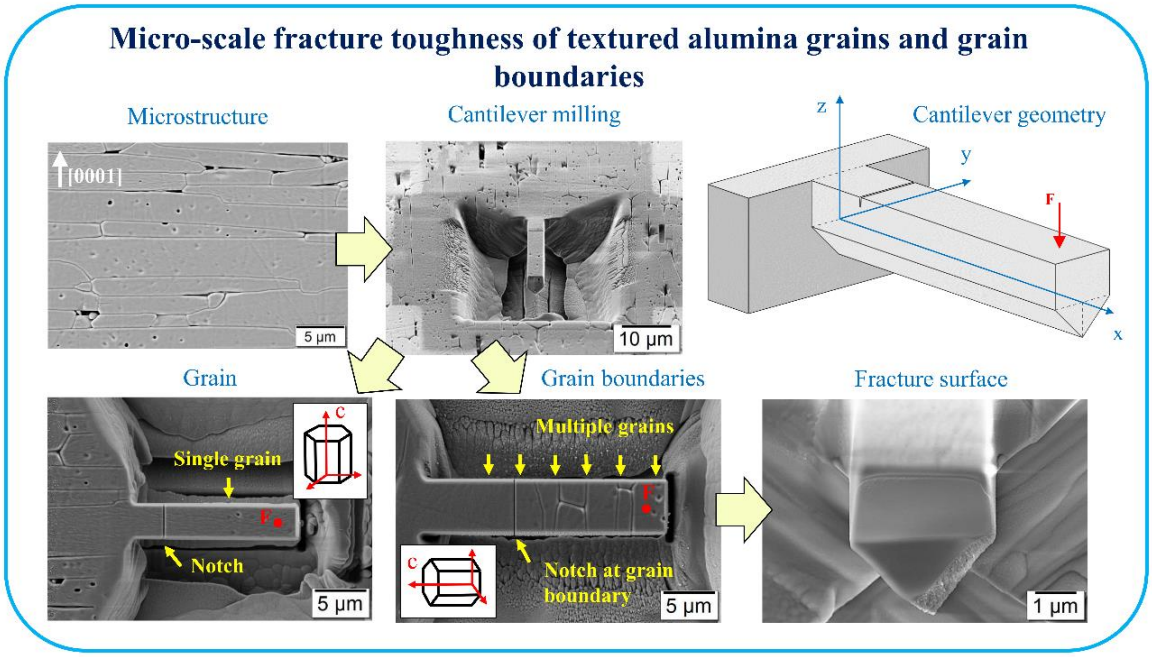

Fig. 13: Micro-scale bending experiments on pentagonal-shaped cantilevers notched within single textured grains and grain boundaries. Adapted under the terms of the CC-BY license [101]. Copyright 2023, The Authors. Published by Elsevier Ltd.

The micro-scale fracture toughness of individual textured grains fractured along one of the prismatic facets (m-, or a-plane) was 3.3 ± 0.2 MPa $m^{1/2}$, whereas that of the basal grain boundaries (c-plane) was determined as 2.3 ± 0.2 MPa $m^{1/2}$. It is worth highlighting that the rather smooth fracture surface of the cantilever tested directly at the grain boundaries (see **Publication A** [101] – Fig. 6b and d) confirms the preferred crack path along the intersection of the basal-boundaries, contrary to typical c-plane "step-like" fracture through the alumina basal-grains [110]. The (prismatic) fracture surfaces of the micro-cantilever tested within single textured grains followed also a rather smooth path (Fig. 13), which is agreement with the typical m- and a-plane fracture characteristics along the prismatic orientations [110].

The significant difference in the fracture toughness values might be from high relevance for the understanding of the macroscopic fracture of textured alumina ceramics. For instance, the macroscopic fracture toughness values of monolithic textured alumina [106] is about 30% higher than that measured on single textured grains in this work, with the difference corresponding to the additional energy-dissipating mechanism acting on the macro-level of microstructural features. The macroscopic fracture of (monolithic) textured alumina has been explored as rather inter-granular following a stepwise path, compared to that of monolithic equiaxed (non-textured) alumina [106]. In case of multi-material laminates, the crack deflection mechanisms favoured along the basal boundaries of the embedded textured layer region is significantly driven by the combined effect of the textured microstructure and the compressive residual stresses [8,20,22], resulting in long horizontal crack paths. To further enhance the damage tolerance of alumina-based laminates, microstructure tailoring using higher aspect ratios of textured alumina grains in combination with additional "weak" second phases should be pursued in order to increase the fracture energy of the material.

The significantly lower micro-scale fracture toughness (~30%) of the grain boundaries (2.3 ± 0.2 MPa $m^{1/2)}$ compared to that of the individual textured grains (3.3 ± 0.2 MPa $m^{1/2}$) may explain the favoured crack path along the rather weak basal grain boundaries of the textured grains during the fracture process of alumina-based ceramic laminates with embedded textured layer regions [101].

The results on the micro-scale level [101] may be also helpful in understanding of the underlying damage mechanisms within alumina-based laminates tested under other loading scenarios than bending (i.e. Hertzian indentation tests [41]). From fractographic analysis of ceramic components, it is widely known that most of the failure reasons can be associated with the unstable propagation of (surface) cracks initiated through thermal shock and/or contact loading scenarios [3]. In this regard, it was hypothesized that the combined effect of microstructure texturing together with introducing compressive residual stresses in a ceramic laminate may be also suitable for acting against the propagation of deleterious cone cracks initiated from the surface.

In **Publication B** [102], the potential of enhancing the contact damage tolerance by embedding textured regions in layered alumina-based architectures was explored under spherical loading scenario (see Fig. 14). In this regard, Hertzian indentation tests were performed on (i) monolithic equiaxed (non-textured) alumina, (ii) monolithic textured alumina, and (iii) an alumina-based laminate with embedded textured layers in a universal testing machine using a

tungsten-carbide sphere as indenter equipped with an Acoustic emission (AE) setup. The AE system was used for monitoring the indentation cycles, which enabled the determination of the "critical" crack initiation forces and the correlation of the underlying damage mechanisms with its AE-energies. The surface cracks were analysed under polarized microscopy as well as confocal microscopy. To investigating the underlying sub-surface damage pattern, cross-sectioning was conducted through polishing together with ion-slicing of the region of interest for selected indentation loads of each sample system.

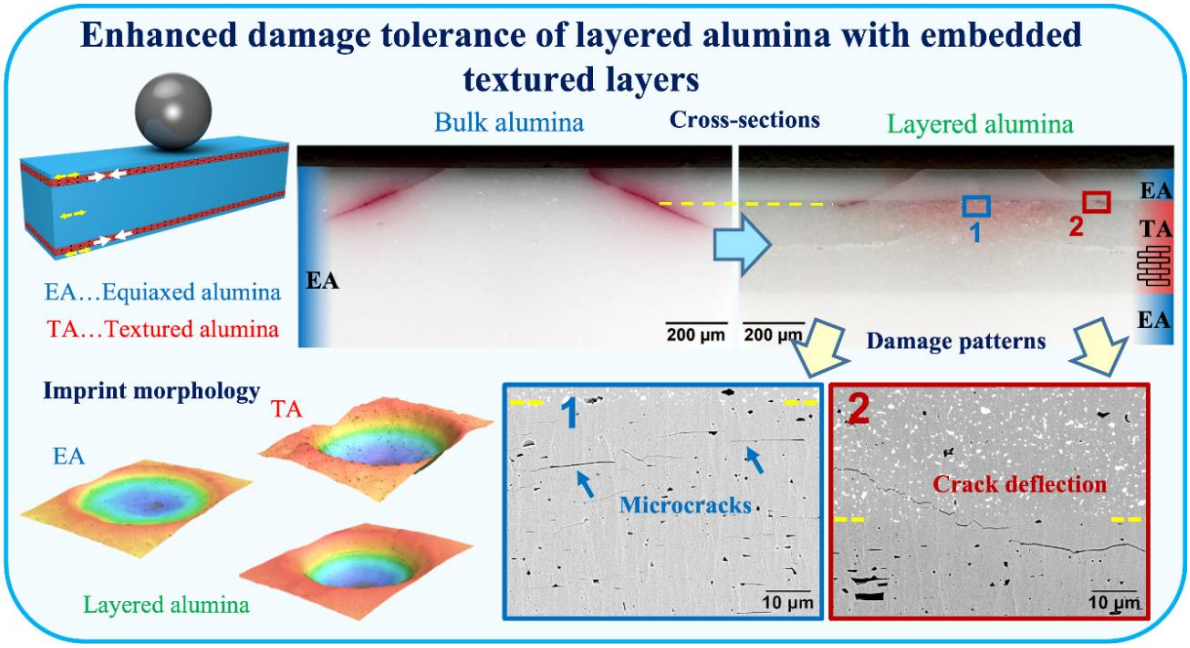

Fig. 14: Contact damage resistance of alumina-based layered ceramics with tailored microstructures and residual stresses. Graphical abstract reprinted under the terms of CC-BY-NC license [102]. Copyright 2022, The Authors. Published by Wiley Periodicals LLC on behalf of American Ceramic Society.

In case of the non-textured sample, classical ring and cone cracking [41,125,126] was observed with final crack depths of ~200 µm (Fig. 14) at the maximum selected load of 2000 N. The presence of ring and cone cracks were confirmed through optical (polarized) microscopy (top view) as well as on the corresponding cross-sections (Fig. 14), and can be correlated with rather high energy peaks emitted during the indentation cycle and detected by the AE system (see **Publication B** [102] – Fig. 10a). In case of the monolithic textured sample, surface depressions without any sign of ring cracks were found on the surface. Sub-surface polishing together with

ion-slicing technique revealed that a quasi-plastic deformation mode occurred within the textured sample tested under Hertzian contact loading, by an absence of the detrimental cone cracking. Controlling the microstructure as a prominent strategy for favouring quasi-plastic shear faulting within the sub-surface zone has been already reported in (i) ceramics with porous microstructures [45], (ii) on rather weak interfaces through the introduction of graphene nanofillers in silicon nitride [46], and mica-platelets in glass matrix [47], and at interface boundaries of heterogeneous alumina/calcium-hexaluminates [48,49]. In this work, micro-crack formation along the rather weak basal grain boundaries was found as nature of quasi-plasticity within the sub-surface-damage zone of the textured material (see **Publication B** [102] – Fig. 7c). A high number of low energy signals was found from the AE-measurements (see **Publication B** [102] – Fig. 10b) which may be associated with the sub-surface shear faulting during indentation, which allows the in-situ classification of the underlying damage mechanisms during spherical indentation.

In novel alumina-based layered ceramics with embedded textured layer regions, the effect of the in-plane compressive residual stresses together with microstructural deflections along the basal grain boundaries, could be used to design contact damage-tolerant systems, by limiting the detrimental cone crack growth from the surface (Fig. 14). For instance, the laminate tested with the indentation load of 2000 N showed a maximum depth of the cone crack of only 120 µm, whereas that of the monolithic equiaxed samples was about 200 µm. In the laminate design approach a combination of energy-dissipating mechanisms take place during spherical indentation. In the internal textured layer region energy is absorbed by quasi-plastic damage zone through the micro-crack formation along the basal grain boundaries. At the interface, the macroscopic deflection through the elastic mismatch leads to arrest by the crack deviation from the trajectory of the maximum stresses. Another damage mechanism is the microstructural deflections along the basal grain boundaries of textured alumina, favouring the crack propagation in a step-like manner (Fig. 14). The AE-signals showed both, low energy signals which may be correlated by micro-cracking in the internal textured region followed by high energy peaks associated with the brittle ring/cone cracking in the outer region (see **Publication B** [102]– Fig. 10c).

In particular, the sub-surface shear faulting through micro-crack formation and the deflection mechanism along the textured boundaries are typical effects which can be correlated to the weakness of the basal grain boundaries, as has been in discussed on the micro-scale level through the significant difference in the local fracture toughness values [101,102].

5.2. Effect of temperature on fracture behaviour of textured ceramic architectures

Layered alumina-based laminates with embedded textured layers have shown high potential for designing damage-tolerant ceramics based on a bio-inspired concept [8]. As discussed above, the mechanical behaviour of textured laminates was already studied under bending at room temperature, showing improved reliability compared to the monolithic systems [20,22]. However, the positive effect on the damage tolerance of ceramic laminates (without textured interlayers) may be reduced at elevated temperatures [131,132]. In this work (**Publication C** [103], it was hypothesized that although the magnitude of the in-plane compressive residual stresses shall be reduced at high temperatures, the positive effect from the textured microstructure may contribute to the fracture response.

The high-temperature fracture behaviour of layered alumina-based with textured microstructures was studied over a wide temperature range (Fig. 15). The mechanical response on (i) laminates with embedded textured interlayers and on monolithic samples with (ii) textured as well as (iii) equiaxed microstructures was explored under uniaxial bending in vacuum up to temperatures of 1200 °C [103].

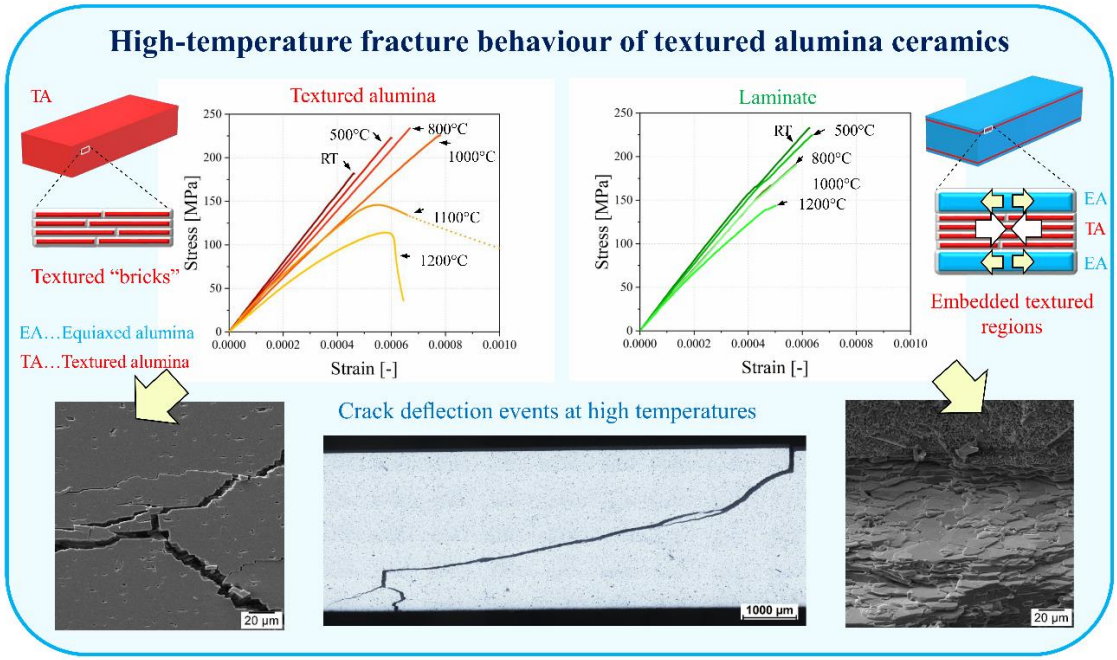

Fig. 15: High-temperature fracture behaviour of textured alumina ceramics. Adapted under the terms of the CC-BY license [103]. Copyright 2023, The Authors. Published by Elsevier Ltd.

All the uniaxial bending tests on bars with introduced artificial cracks (HV10) were performed using a 4-point testing fixture at elevated temperatures (500 °C – 1200°C) as well as room temperature (reference tests) within a built-in vacuum/inert atmosphere chamber under position control. The corresponding stress-strain curves were determined and the inelastic as well as total work of fractures were calculated. To assess the effect of the temperature on the residual stress recovery within the layered laminate, the thermo-elastic properties, namely elastic modulus as well as coefficient of thermal expansions, were determined from 20 °C to 1500 °C and the corresponding residual stress profiles were calculated. The high-temperature fracture behaviour was analysed and the fracture path was studied on the corresponding broken surfaces using a SEM.

The fully linear elastic stress-strain curves of the monolithic (reference) non-textured sample demonstrated typical brittle fracture behaviour independently on the tested temperatures. The corresponding inelastic work of fractures were only ~2% over the complete temperature range (RT – 1200 °C). In case of textured alumina, it was shown that a transition from brittle to a more ductile fracture behaviour occurred at testing temperature of ~800 °C (see Fig. 15), showing distinctive crack deflection events, which corresponded to additional weakening (softening) of the basal grain boundaries. It was hypothesized that this effect is associated to the softening of glassy phases (from processing), which is in good accordance with the reported glass-transition temperatures of glasses in literature [133]. The high-temperature damage tolerance of monolithic textured materials was quantified by considering the fracture energy, showing an amount of plasticity of almost 50% at the maximum temperature of 1200°C. In case of the textured laminates a loss of the in-plane compressive residual stresses with increasing temperatures was presented (see **Publication C** [103] – Fig. 4); however, the strong effect of texturing demonstrated favoured crack deflection events leading to an inelastic work of fracture (plastic contribution) of almost 25 % at 1200°C.

Post-mortem analysis of the (indented) equiaxed sample tested at 1200°C indicated a transition from trans- to inter-granular fracture (see **Publication C** [103]– Fig. 8), which could be related to the subcritical crack growth during the high-temperature testing [32]. Fractography of the monolithic textured samples tested up to 800 °C indicated an inter-granular fracture, where the crack may follow a rather straight path along the basal boundaries (stepwise) (Fig. 15), as it has been typically observed on textured materials after room temperature bending [21,106]. The fracture path of the textured samples tested between 800 °C and 1200 °C indicated rather strong

deflection events along the weak basal grain boundaries (Fig. 15) associated with the additional softening effects, leading to more ductile fracture behaviour. At room temperature, the laminate architecture showed promising crack arrest as well as deflection events within the internal textured layer related to the effect of in-plane compressive residual stresses and microstructure texturing [8,20,22]. Although at high temperatures (up to 1200°C), a significant loss of the residual stresses was observed, significant deflections along the embedded TA-region were found through post-mortem analysis (Fig. 15), highlighting the exceptional damage tolerance of the multi-material laminate.

In conclusion, it was shown that even under severe conditions up to 1200°C, the damage tolerance of alumina-based ceramics might be guaranteed by the positive effect of microstructure tailoring [103].

The design of textured architectures demonstrates that attractive mechanical properties are achievable from room temperature to elevated temperatures up to 1200°C. The understanding of the high-temperature fracture behaviour together with the new insights from the micro-scale level may be used to further optimize the design concepts on bio-inspired ceramic systems, which may have potential for the use as materials systems for high-temperature applications.

5.3. Potentials of additive manufacturing in the field of 3D-multi-material ceramics

In the sector of ceramic materials, the LCM-technique has provided new advances of fabricating complex-shaped components with mechanical properties well comparable with those of traditional manufactured ceramics [23]. Based on preliminary studies on (monolithic) LCM-alumina ceramics with sound strength [26], it was hypothesized that combining the multi-material printing process with the concept of residual stresses could be exploited for further enhancing their mechanical properties.

An important final goal of this thesis was to develop a first “demonstrator” 3D-printed component with complex-shape and enhanced damage tolerance through a multi-material design approach. The potential of the stereolithographic LCM 3D-printing technique to design novel alumina-based multi-material architectures with enhanced (i) mechanical resistance or (ii) damage tolerance was explored.

In the first design approach (**Publication D** [104]) alumina-zirconia layers (ZTA) were sandwiched between top surface alumina layers, aiming to introduce in-plane compressive residual stresses in the outer alumina region (see Fig. 16).

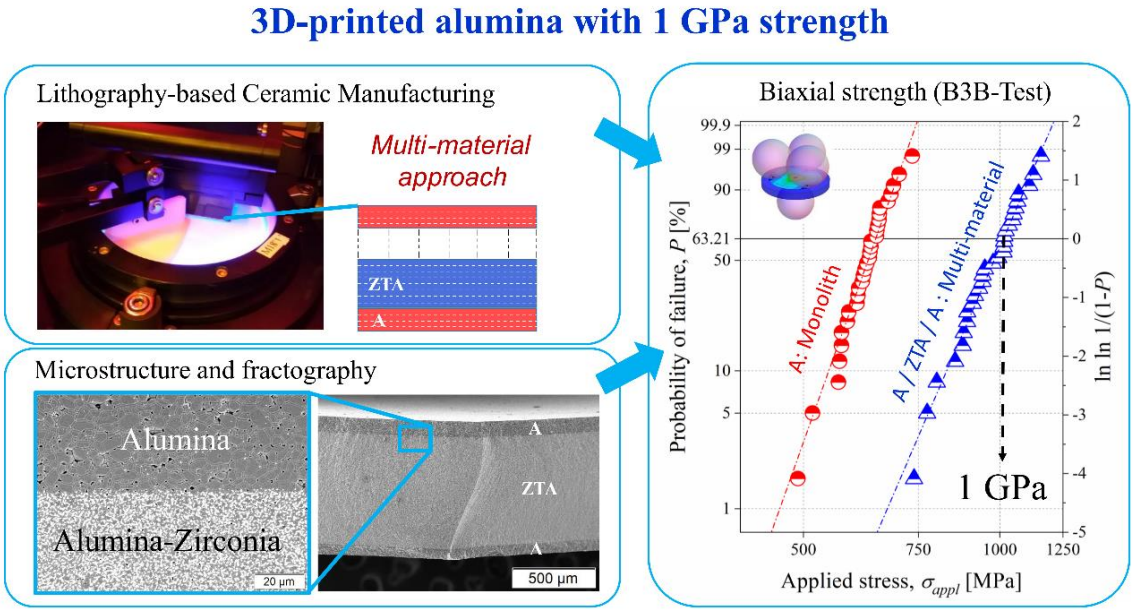

Fig. 16: Multi-material design approach for 3D-printed alumina with strength as high as 1GPa. Graphical abstract reprinted under the terms of the CC-BY license [104]. Copyright 2021, The Authors. Published by Elsevier Ltd on behalf of European Ceramic Society.

The disc-shaped specimens fabricated by using the LCM-technology of (monolithic) alumina and the multi-material design with outer alumina surface regions under compressive residual stresses were tested by using the B3B-test [123,124]. Basic material properties (i.e. fracture toughness, elastic modulus as well as coefficient of thermal expansions) were determined on monolithic bars of the ZTA and the alumina materials. Based on these properties, an appropriate pre-factor for strength determination considering also the elastic mismatch between the alternating layer regions was developed. The strength data was evaluated through 2-parameter as well as 3-parameter Weibull distributions. Supporting microstructural and fractographic analysis were carried out to assess the quality of the 3D-printed multi-material sample.

The shielding effect [68,69] on the top surface alumina region due to the in-plane compressive residual stresses, as first studied by Nordberg et al. [11] in strengthened glasses, was exploited for tailoring the mechanical strength of the multi-material system. The SEM microstructures

showed comparable grain sizes of both systems. Furthermore, it is worth noting that the alumina/ZTA interfaces within the multi-material architectures are rather sharp, indicating well densified ceramic parts (Fig. 16).

The (biaxial) characteristic strength of the multi-material design was as high as 1 GPa, compared to the ~650 MPa of the reference (pure alumina) sample (Fig. 14). The difference in the characteristic strength corresponded to the in-plane compressive residual stresses of about 320 MPa introduced in the external alumina-layers. To assess the potential as typical components with relatively high reliability, the third parameter of the 3-parameter Weibull distribution [35,37] was used, taking the calculated compressive residual stresses (~320 MPa) as the third parameter, allowing a stable fitting of the corresponding strength data [37]. These considerations (see **Publication D** [104] – Fig. 5) might suggest a "threshold strength" (equal to the compressive residual stress) at relatively low probabilities of failures (below 10^{-4} – 10^{-6}) below failure does not occur, similar as in other works on laminates with surface compressive stresses [12,13].

Fractography of the multi-material sample confirmed that failure occurred from the top surface alumina regions, indicating the similar fracture origin as in the monolithic alumina sample (i.e. larger alumina grains) (cp. **Publication D** [104] – Fig. 6). The finding is in good agreement with the comparable Weibull moduli of both systems, suggesting similar defect size distributions [36].

This report showed the effectiveness of the multi-material approach for enhancing the mechanical resistance of 3D-printed alumina, which might open new ways of designing structural ceramics [104].

In the second design approach (see **Publication E** [105]) alumina regions under compressive residual stresses were embedded between the ZTA-layer regions to act as barriers against crack propagation, as has been successfully exploited on traditional fabricated "planar" samples in literature [18]. The potentials of the LCM 3D-printing technique for developing multi-material designs from planar samples (discs) to more complex-shaped components (turbine blade) with enhanced damage tolerance against thermal shock cracks (Fig. 17) was assessed in this work.

Disc-shaped multi-layered laminates and monolithic alumina and ZTA (reference samples) manufactured by using LCM were thermal shocked at various temperature differences (200 °C – 400 °C) and the corresponding strength degradations were investigated. B3B-tests were

performed on the thermal shocked as well as non-shocked (reference) specimens and the retained strength as a function of temperature differences was determined for each sample system, respectively. The crack analysis was conducted on the top surfaces (crack density) as well as on the corresponding cross-sections (crack depths) of the discs. Microstructural characterization and fractography was carried out using a SEM. In case of the 3D-printed turbine blades, thermal shock tests were performed at the maximum temperature difference of 400 °C and the final thermal shock crack depths within the architecture were studied and compared to those of the (reference) monolithic ZTA-turbine blades.

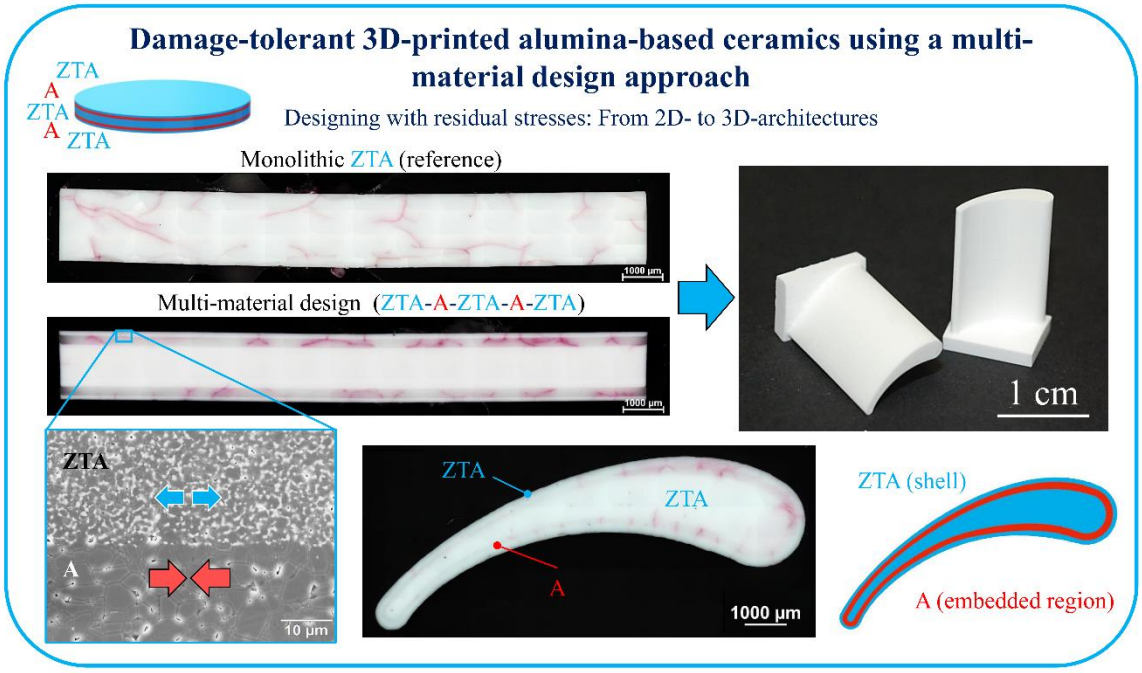

Fig. 17: Structural integrity of 3D-printed alumina-based multi-material ceramics: From discs to more complex components. Graphical abstract reprinted under the terms of the CC-BY license [105]. Copyright 2023, The Authors. Published by Elsevier Ltd.

The microstructures were well comparable with those of the previous work [104], showing similar grain sizes as well as rather dense and strong ZTA/alumina interfaces (Fig. 17) which might highlight the reproducibility of the multi-material printing process.

The analysis of crack patterns observed from the top surface of the samples showed that the monolithic alumina had first thermal shock cracks at a temperature difference of ~250 °C, whereas that of the monolithic ZTA sample was first cracked at ~300 °C. In case of the multi-

material sample with outer ZTA-layers, first thermal shock cracks were qualitatively observed at temperature differences of ~250 °C due to the effect of the tensile residual stresses (~ +100 MPa) (cp. **Publication E** [105] – Fig. 3). It could be seen that increasing temperature differences led to higher crack densities for all samples, similar as has been experimentally found in [134]. However, since the (retained) strength is compromised by the final thermal shock crack depths [28,31], cross-sections were analysed. For instance, the final crack depths for the monolithic alumina as well as the ZTA thermal shocked at ~400 °C were measured as ~500 µm and ~800 µm, respectively. The corresponding retained strength for both monolithic alumina and ZTA was approx. 200 MPa, indicating a rather high strength degradation especially for ZTA after thermal shock tests. The differences in the level of degradation could be related to the distinct materials properties, microstructures and the additional effect of low temperature degradation of ZTA [55,135,136].

In case of the multi-material sample, it was demonstrated that thermally induced cracks were bifurcated and arrested within the internal alumina layers due to the shielding effect [8,63,66,68,69] provided by the in-plane compressive residual stresses (~ −300 MPa). The final crack depth in the multi-material system could be limited by the internal layer thickness to only ~250 µm, whereas the monolithic (reference) counterparts are strongly degraded by the thermal shock cracks (Fig. 17). As a result, the corresponding (biaxial) retained strength plateau measured after critical thermal shocking of the multi-material system was twice (~400 MPa) as high as that of the monolithic reference samples. Fractography verified that the multi-material approach is a prominent strategy to protect the architectures from thermal shock cracks as well as processing-related (surface) defects (non-shocked discs) through the embedded compressive residual stresses.

A final 3D-printed multi-material turbine blade (Fig. 17) demonstrated that the concept of damage tolerance and the corresponding crack arrest capability may be also applicable for novel components in future applications, whereas the monolithic ZTA turbine blade was strongly degraded [105].

In conclusion, fundamental studies from *2D*- (in-plane) architectures to more complex-structured *3D*-printed components with enhanced mechanical properties have been presented within this doctoral thesis. The outcome should serve as input for further improvement in architectural and microstructural design on 3D-printed ceramic components.

6. Conclusion and outlook

In this doctoral thesis different alumina-based laminates were designed and mechanically characterized for assessing their potentials in novel future applications as structural component.

The textured alumina-based laminates showed enhanced contact damage resistance through the combined effect of microstructure texturing and the induced compressive residual stresses in the embedded protective regions. High-temperature uniaxial bending tests and the corresponding fracture analysis evidenced that crack deflections are favoured along the textured grain boundaries leading to improved work of fracture and damage tolerance, which may nominate them as possible high-temperature materials. The micro-scale fracture analysis explained the favoured energy-dissipating deflection mechanisms along the elongated grain boundaries within the textured region during the macro-scale fracture of alumina laminates. The fundamental research on the micro-scale level may be used for further optimizing the structural integrity of alumina laminates.

The investigations on the 3D-printed alumina-ZTA-multi-material ceramics have demonstrated that both design concepts show superior mechanical properties, either improved mechanical resistance or damage tolerance as compared to the reference monolithic counterparts, associated with the shielding effect due to the compressive residual stresses in the corresponding materials region. Based on these results, a first demonstrator component (i.e. multi-ceramic turbine blade) was designed, showing the capabilities of embedding protective “crack arresting” layer regions inside the complex-shaped multi-material architecture. The LCM-multi-material 3D-printing together with concept of residual stresses could be a new pathway of designing “damage-tolerant” components for special applications (i.e. medical sector, space applications), which might open new topics for future research.

Besides the introduced “demonstrator” multi-material turbine blades, damage-tolerant medical implants may be designed as possible structural ceramic parts. Further investigations as well as design optimizations must be carried out in future with the goal of an establishment of new multi-material components in the ceramic market (i.e. damage-tolerant hip-joints with embedded protective regions).

The development of novel ceramic architectures with different connectivity regions introduced within a 3D component could be also considered in further activities for tailoring its mechanical properties within the spatially resolved structures.

Based on the concept of layered ceramics with *weak* interfaces, ongoing research on the mechanical response of 3D-printed components with embedded porous interlayers and/or gradual porosity regions have shown first promising results for designing “light-weight” alumina ceramics with good thermal shock resistance. Based on this study, a first 3D-printed light-weight-alumina-component (i.e. ceramic nozzle) with embedded porous layer regions has already been designed. The introduction of spatially-tailored porosities within real parts or components might be another important topic for further investigations.

7. Publications

7.1. Included publications as first author

Publication A: J. Schlacher, T. Csanádi, M. Vojtko, R. Papšík, R. Bermejo, Micro-scale fracture toughness of textured alumina ceramics, J. Eur. Ceram. Soc. 43 (7) (2023) 2943–2950. https://doi.org/10.1016/j.jeurceramsoc.2022.06.028.

Publication B: J. Schlacher, A. Jabr, A.-K. Hofer, R. Bermejo, Contact damage tolerance of alumina-based layered ceramics with tailored microstructures, J. Am. Ceram. Soc. 105 (6) (2022) 4387–4399. https://doi.org/10.1111/jace.18389.

Publication C: J. Schlacher, Z. Chlup, A.-K. Hofer, R. Bermejo, High-temperature fracture behaviour of layered alumina ceramics with textured microstructure, J. Eur. Ceram. Soc. 43 (7) (2023) 2917–2927. https://doi.org/10.1016/j.jeurceramsoc.2022.11.046.

Publication D: J. Schlacher, A.-K. Hofer, S. Geier, I. Kraleva, R. Papšík, M. Schwentenwein, R. Bermejo, Additive manufacturing of high-strength alumina through a multi-material approach, Open Ceramics 5 (2021) 100082. https://doi.org/10.1016/j.oceram.2021.100082.

Publication E: J. Schlacher, S. Geier, M. Schwentenwein, R. Bermejo, Towards 3D-printed alumina-based multi-material components with enhanced thermal shock resistance, J. Eur. Ceram. Soc. 44 (4) (2024) 2294–2303. https://doi.org/10.1016/j.jeurceramsoc.2023.11.009.

7.2. Further publications related to the author

J. Schlacher, T. Lube, W. Harrer, G. Mitteramskogler, M. Schwentenwein, R. Danzer, R. Bermejo, Strength of additive manufactured alumina, J. Eur. Ceram. Soc. 40 (14) (2020) 4737–4745. https://doi.org/10.1016/j.jeurceramsoc.2020.03.073.

M. Staudacher, T. Lube, J. Schlacher, P. Supancic, Comparison of biaxial strength measured with the Ball-on-Three-Balls- and the Ring-on-Ring-test, Open Ceramics 6 (2021) 100101. https://doi.org/10.1016/j.oceram.2021.100101.

A.-K. Hofer, J. Rabitsch, D. Jutrzenka-Trzebiatowska, C. Hofstetter, I. Gavalda-Velasco, J. Schlacher, M. Schwentenwein, R. Bermejo, Effect of binder system on the thermophysical

properties of 3D-printed zirconia ceramics, Int. J. Appl. Ceram. Technol. 19 (1) (2022) 174–180. https://doi.org/10.1111/ijac.13806.

T. Lube, M. Staudacher, A.-K. Hofer, J. Schlacher, R. Bermejo, Stereolithographic 3D Printing of Ceramics: Challenges and Opportunities for Structural Integrity, Adv. Eng. Mater. 25 (7) (2023) 2200520. https://doi.org/10.1002/adem.202200520.

S. Nohut, J. Schlacher, I. Kraleva, M. Schwentenwein, R. Bermejo, 3D-printed alumina-based ceramics with spatially resolved porosity, Int. J. Appl. Ceram. Technol. 21 (1) (2024) 89–104. https://doi.org/10.1111/ijac.14512.

R. Papšík, O. Ševeček, J. Schlacher, R. Bermejo, Prediction of thermal shock induced cracking in multi-material ceramics using a stress-energy criterion, Eng. Fract. Mech. 303 (2024) 110121. https://doi.org/10.1016/j.engfracmech.2024.110121.

7.3. Contribution to the included publications

Publication A: Manuscript preparation, microstructure characterization, part of micromechanical testing, fracture toughness evaluation

Publication B: Manuscript preparation, design of the (contact) testing setup, supervising the spherical indention tests, parts of data evaluation

Publication C: Manuscript preparation, microstructure characterization, room and high-temperature testing, data evaluation, fractographic analysis and assessment of fracture resistance

Publication D: Manuscript preparation, thermo-physical characterisation, mechanical testing, strength evaluation, statistical analysis of strength distributions, part of the fractographic analysis

Publication E: Manuscript preparation, design of the component, microstructural analysis, part of thermal shock tests, analysis of thermal shock cracks, part of mechanical testing, strength evaluation, fractographic analysis

7.4. Supervised Bachelor's and Master's theses

A. Jabr, Contact Damage of Alumina-Based Layered Ceramics with Tailored Microstructure, Master's thesis, Montanuniversität Leoben, Austria (2021)

I. Gavalda-Velasco, Mechanical characterization of 3D-printed zirconia, Bachelor's thesis, Montanuniversität Leoben, Austria (2021)

L. Bastos Mateus, Thermal shock behaviour of 3D-printed alumina ceramics with spatially tailored porosity, Master's thesis, Montanuniversität Leoben, Austria (2023)

F. Stücklberger, Mechanical response of textured alumina-based ceramics after Hertzian contact damage, Master's thesis, Montanuniversität Leoben, Austria (2023)

8. References

[1] D. Munz, T. Fett, Ceramics: Mechanical Properties, Failure Behaviour, Materials Selection, Corr. second. print, Springer, Berlin, 2001.

[2] C.B. Carter, M.G. Norton, Ceramic Materials: Science and Engineering, Second edition, Springer, New York, 2013.

[3] R. Danzer, T. Lube, P. Supancic, R. Damani, Fracture of Ceramics, Adv. Eng. Mater. 10 (4) (2008). https://doi.org/10.1002/adem.200700347.

[4] U.G.K. Wegst, H. Bai, E. Saiz, A.P. Tomsia, R.O. Ritchie, Bioinspired structural materials, Nat. Mater. 14 (2015) 23–36.

[5] M.A. Meyers, P.-Y. Chen, A.Y.-M. Lin, Y. Seki, Biological materials: Structure and mechanical properties, Prog. Mater. Sci. 53 (2008) 1–206. https://doi.org/10.1016/j.pmatsci.2007.05.002.

[6] F. Bouville, Strong and tough nacre-like aluminas: Process–structure–performance relationships and position within the nacre-inspired composite landscape, J. Mater. Res. 35 (2020) 1076–1094. https://doi.org/10.1557/jmr.2019.418.

[7] L. Cheng, M. Sun, F. Ye, Y. Bai, M. Li, S. Fan, L. Zhang, Structure design, fabrication, properties of laminated ceramics: A review, Int. J. Lightweight Mater. Manuf. 1 (2018) 126–141. https://doi.org/10.1016/j.ijlmm.2018.08.002.

[8] R. Bermejo, "Toward seashells under stress": Bioinspired concepts to design tough layered ceramic composites, J. Eur. Ceram. Soc. 37 (13) (2017) 3823–3839. https://doi.org/10.1016/j.jeurceramsoc.2017.04.041.

[9] R. Bermejo, M. Deluca, Chapter 9.7 - Layered Ceramics, in: S. Somiya (Ed.), Handbook of Advanced Ceramics (Second Edition), Academic Press, Oxford, 2013, pp. 733–751.

[10] D.J. Green, R. Tandon, V.M. Sglavo, Crack arrest and multiple cracking in glass through the use of designed residual stress profiles, Science 283 (5406) (1999) 1295–1297.

[11] M.E. Nordberg, E.L. Mochel, H.M. Garfinkel, J.S. Olcott, Strengthening by Ion Exchange, J. Am. Ceram. Soc. 47 (5) (1964) 215–219. https://doi.org/10.1111/j.1151-2916.1964.tb14399.x.

[12] J. Pascual, T. Lube, R. Danzer, Fracture statistics of ceramic laminates strengthened by compressive residual stresses, J. Eur. Ceram. Soc. 28 (8) (2008) 1551–1556. https://doi.org/10.1016/j.jeurceramsoc.2007.10.005.

[13] C. Krautgasser, R. Danzer, M. Deluca, P. Supancic, F. Aldrian, R. Bermejo, Subcritical crack growth in multilayer Low Temperature Co-fired Ceramics designed with surface

compressive stresses, J. Eur. Ceram. Soc. 36 (16) (2016) 4095–4105. https://doi.org/10.1016/j.jeurceramsoc.2016.07.003.

[14] M. Rao, A. Sánchez-Herencia, G. Beltz, R.M. McMeeking, F.F. Lange, Laminar Ceramics That Exhibit a Threshold Strength, Science 286 (1999) 102–105.

[15] V.M. Sglavo, M. Paternoster, M. Bertoldi, Tailored Residual Stresses in High Reliability Alumina-Mullite Ceramic Laminates, J. Am. Ceram. Soc. 88 (10) (2005) 2826–2832. https://doi.org/10.1111/j.1551-2916.2005.00479.x.

[16] R. Bermejo, Y. Torres, A.J. Sánchez-Herencia, C. Baudín, M. Anglada, L. Llanes, Residual stresses, strength and toughness of laminates with different layer thickness ratios, Acta Mater. 54 (2006) 4745–4757. https://doi.org/10.1016/j.actamat.2006.06.008.

[17] V.M. Sglavo, F. de Genua, A. Molinari, F. Casari, Alumina/Silicon Carbide Laminated Composites by Spark Plasma Sintering, J. Am. Ceram. Soc. 92 (11) (2009) 2693–2697. https://doi.org/10.1111/j.1551-2916.2009.03247.x.

[18] Y. Chang, R. Bermejo, O. Ševeček, G.L. Messing, Design of alumina-zirconia composites with spatially tailored strength and toughness, J. Eur. Ceram. Soc. 35 (2) (2015) 631–640. https://doi.org/10.1016/j.jeurceramsoc.2014.09.017.

[19] R.J. Pavlacka, G.L. Messing, Processing and mechanical response of highly textured Al2O3, J. Eur. Ceram. Soc. 30 (14) (2010) 2917–2925. https://doi.org/10.1016/j.jeurceramsoc.2010.02.009.

[20] R. Pavlacka, R. Bermejo, Y. Chang, D.J. Green, G.L. Messing, Fracture Behavior of Layered Alumina Microstructural Composites with Highly Textured Layers, J. Am. Ceram. Soc. 96 (5) (2013) 1577–1585. https://doi.org/10.1111/jace.12292.

[21] P.W. Hall, J.S. Swinnea, D. Kovar, Fracture Resistance of Highly Textured Alumina, J. Am. Ceram. Soc. 84 (7) (2001) 1514–1520. https://doi.org/10.1111/j.1151-2916.2001.tb00870.x.

[22] Y. Chang, R. Bermejo, G. L. Messing, Improved Fracture Behavior of Alumina Microstructural Composites with Highly Textured Compressive Layers, J. Am. Ceram. Soc. 97 (11) (2014) 3643–3651. https://doi.org/10.1111/jace.13168.

[23] M. Schwentenwein, J. Homa, Additive Manufacturing of Dense Alumina Ceramics, Int. J. Appl. Ceram. Technol. 12 (1) (2015) 1–7. https://doi.org/10.1111/ijac.12319.

[24] A.D. Lantada, A. de Blas Romero, M. Schwentenwein, C. Jellinek, J. Homa, Lithography-based ceramic manufacture (LCM) of auxetic structures: Present capabilities and challenges, Smart Mater. Struct. 25 (5) (2016) 54015. https://doi.org/10.1088/0964-1726/25/5/054015.

[25] A. de Blas Romero, M. Pfaffinger, G. Mitteramskogler, M. Schwentenwein, C. Jellinek, J. Homa, A. Díaz Lantada, J. Stampfl, Lithography-based additive manufacture of ceramic biodevices with design-controlled surface topographies, Int. J. Adv. Manuf. Technol. 88 (5-8) (2017) 1547–1555. https://doi.org/10.1007/s00170-016-8856-1.

[26] J. Schlacher, T. Lube, W. Harrer, G. Mitteramskogler, M. Schwentenwein, R. Danzer, R. Bermejo, Strength of additive manufactured alumina, J. Eur. Ceram. Soc. 40 (14) (2020) 4737–4745. https://doi.org/10.1016/j.jeurceramsoc.2020.03.073.

[27] S. Geier, I. Potestio, 3D-Printing: From Multi-Material to Functionally-Graded Ceramic, Ceramic Applications 8 (2020) 32–35.

[28] A.A. Griffith, VI. The phenomena of rupture and flow in solids, Philos. Trans. R. Soc. 221 (1921) 163–198.

[29] J.B. Wachtman, M.J. Matthewson, W.R. Cannon, Mechanical Properties of Ceramics, Second edition, Wiley, Hoboken, New Jersey, 2009.

[30] R. Danzer, Fracture Mechanics of Ceramics - A Short Introduction, Key Eng. Mater. 333 (2007) 77–86. https://doi.org/10.4028/www.scientific.net/KEM.333.77.

[31] G.R. Irwin, Analysis of stresses and strains near the end of a crack traversing a plate, J. Appl. Mech. 24 (1957) 361–364.

[32] G. Quinn, Fractography of Ceramics and Glasses. NIST Special Publication 960-16, US Government Printing Office, Washington, 2016.

[33] R. Danzer, T. Lube, New Fracture Statistics for Brittle Materials, Fracture Mechanics of Ceramics (1996) 425–439.

[34] W. Weibull, A Statistical Theory of the Strength of Materials, Ingeniörsvetenskapsakademiens Handlingar (1939).

[35] W. Weibull, A Statistical Distribution Function of Wide Applicability, J. Appl. Mech. 18 (1951) 293–297.

[36] R. Danzer, A General Strength Distribution Function for Brittle Materials, J. Eur. Ceram. Soc. 10 (1992) 461–472.

[37] R. Danzer, P. Supancic, J. Pascual, T. Lube, Fracture statistics of ceramics – Weibull statistics and deviations from Weibull statistics, Eng. Fract. Mech. 74 (18) (2007) 2919–2932. https://doi.org/10.1016/j.engfracmech.2006.05.028.

[38] H. Hertz, Ueber die Berührung fester elastischer Körper, J. Reine Angew. Math. 1882 156–171.

[39] A.C. Fischer-Cripps, Introduction to Contact Mechanics, Springer Science+Business Media LLC, Boston, MA, 2007.

[40] K.L. Johnson, Contact mechanics, Cambridge University Press, Cambridge Cambridgeshire, New York, Port Melbourne, Madrid, Cape Town, 1985.

[41] B.R. Lawn, Indentation of Ceramics with Spheres: A Century after Hertz, J. Am. Ceram. Soc. 81 (8) (1998) 1977–1994. https://doi.org/10.1111/j.1151-2916.1998.tb02580.x.

[42] E. Jiménez-Piqué, L. Llanes, M. Anglada, 2.13 - Resistance to Contact Deformation and Damage of Hard Ceramics, in: V.K. Sarin (Ed.), Comprehensive Hard Materials, Elsevier, Oxford, 2014, pp. 367–383.

[43] F. Guiberteau, N.P. Padture, B.R. Lawn, Effect of Grain Size on Hertzian Contact Damage in Alumina, J. Am. Ceram. Soc. 77 (7) (1994) 1825–1831. https://doi.org/10.1111/j.1151-2916.1994.tb07057.x.

[44] S.K. Lee, S. Wuttiphan, B.R. Lawn, Role of Microstructure in Hertzian Contact Damage in Silicon Nitride: I, Mechanical Characterization, J. Am. Ceram. Soc. 80 (9) (1997) 2367–2381. https://doi.org/10.1111/j.1151-2916.1997.tb03129.x.

[45] B.A. Latella, B.H. OConnor, N.P. Padture, B.R. Lawn, Hertzian Contact Damage in Porous Alumina Ceramics, J. Am. Ceram. Soc. 80 (4) (1997) 1027–1031. https://doi.org/10.1111/j.1151-2916.1997.tb02940.x.

[46] M. Belmonte, P. Miranzo, M.I. Osendi, Contact damage resistant SiC/graphene nanofiller composites, J. Eur. Ceram. Soc. 38 (1) (2018) 41–45. https://doi.org/10.1016/j.jeurceramsoc.2017.08.009.

[47] H. Cai, S.M.A. Kalceff, B.R. Lawn, Deformation and fracture of mica-containing glass-ceramics in Hertzian contacts, J. Mater. Res. 9 (1994) 762–770. https://doi.org/10.1557/JMR.1994.0762.

[48] L. An, H.M. Chan, N.P. Padture, B.R. Lawn, Damage-resistant alumina-based layer composites, J. Mater. Res. 11 (1996) 204–210. https://doi.org/10.1557/JMR.1996.0025.

[49] H.-C. Ha, H.M. Chan, H.F. Nied, Hertzian contact behavior of alumina-based trilayer composites: experimental observation and FEM analysis, Acta Mater. 49 (2001) 2453–2461. https://doi.org/10.1016/S1359-6454(01)00151-3.

[50] P. Miranda, A. Pajares, F. Guiberteau, Y. Deng, B.R. Lawn, Designing damage-resistant brittle-coating structures: I. Bilayers, Acta Mater. 51 (2003) 4347–4356. https://doi.org/10.1016/S1359-6454(03)00290-8.

[51] P. Miranda, A. Pajares, F. Guiberteau, Y. Deng, H. Zhao, B.R. Lawn, Designing damage-resistant brittle-coating structures: II. Trilayers, Acta Mater. 51 (2003) 4357–4365. https://doi.org/10.1016/S1359-6454(03)00263-5.

[52] R. Danzer, Mechanical Failure of Advanced Ceramics: The Value of Fractography, Key Eng. Mater. 223 (2002) 1–18. https://doi.org/10.4028/www.scientific.net/KEM.223.1.

[53] W.D. Kingery, Factors Affecting Thermal Stress Resistance of Ceramic Materials, J. Am. Ceram. Soc. 38 (1) (1955) 3–15. https://doi.org/10.1111/j.1151-2916.1955.tb14545.x.

[54] M. Fellner, P. Supancic, Thermal Shock Failure of Brittle Materials, Key Eng. Mater. 223 (2002) 97–106. https://doi.org/10.4028/www.scientific.net/KEM.223.97.

[55] D.P.H. Hasselman, Elastic Energy at Fracture and Surface Energy as Design Criteria for Thermal Shock, J. Am. Ceram. Soc. 46 (11) (1963) 535–540. https://doi.org/10.1111/j.1151-2916.1963.tb14605.x.

[56] D.P.H. Hasselman, Unified Theory of Thermal Shock Fracture Initiation and Crack Propagation in Brittle Ceramics, J. Am. Ceram. Soc. 52 (11) (1969) 600–604. https://doi.org/10.1111/j.1151-2916.1969.tb15848.x.

[57] EN 820-3, Advanced technical ceramics - Monolithic ceramics - Thermomechanical properties - Part 3: Determination of resistance to thermal shock by water quenching, 1993.

[58] D. Sherman, D. Schlumm, Thickness effect in thermal shock of alumina ceramics, Scr. Mater. 42 (2000) 819–825. https://doi.org/10.1016/S1359-6462(99)00371-1.

[59] Z.-H. Jin, Y.-W. Mai, Effects of Damage on Thermal Shock Strength Behavior of Ceramics, J. Am. Ceram. Soc. 78 (7) (1995) 1873–1881. https://doi.org/10.1111/j.1151-2916.1995.tb08903.x.

[60] W. Clegg, K.K. Kendall, N.M. Alford, T.W. Button, J.D. Birchall, A Simple Way to Make Tough Ceramics, Nature 347 (1990) 455–457. https://doi.org/10.1038/347455a0.

[61] J.B. Davis, A. Kristoffersson, E. Carlström, W.J. Clegg, Fabrication and Crack Deflection in Ceramic Laminates with Porous Interlayers, J. Am. Ceram. Soc. 83 (10) (2000) 2369–2374. https://doi.org/10.1111/j.1151-2916.2000.tb01563.x.

[62] J. Ma, H. Wang, L. Weng, G.E.B. Tan, Effect of porous interlayers on crack deflection in ceramic laminates, J. Eur. Ceram. Soc. 24 (5) (2004) 825–831. https://doi.org/10.1016/S0955-2219(03)00338-8.

[63] L. Sestakova, R. Bermejo, Z. Chlup, R. Danzer, Strategies for fracture toughness, strength and reliability optimisation of ceramic-ceramic laminates, Int. J. Mater. Res. 102 (6) (2011) 613–626. https://doi.org/10.3139/146.110523.

[64] H.J. Oel, V.D. Fréchette, Stress Distribution in Multiphase Systems: I, Composites with Planar Interfaces, J. Am. Ceram. Soc. 50 (10) (1967) 542–549. https://doi.org/10.1111/j.1151-2916.1967.tb14992.x.

[65] D.J. Green, P.Z. Cai, G.L. Messing, Residual stresses in alumina–zirconia laminates, J. Eur. Ceram. Soc. 19 (13) (1999) 2511–2517. https://doi.org/10.1016/S0955-2219(99)00103-X.

[66] V.M. Sglavo, M. Bertoldi, Design and production of ceramic laminates with high mechanical resistance and reliability, Acta Mater. 54 (2006) 4929–4937. https://doi.org/10.1016/j.actamat.2006.06.019.

[67] Z. Chlup, H. Hadraba, D. Drdlik, K. Maca, I. Dlouhy, R. Bermejo, On the determination of the stress-free temperature for alumina–zirconia multilayer structures, Ceram. Int. 40 (4) (2014) 5787–5793. https://doi.org/10.1016/j.ceramint.2013.11.018.

[68] C.R. Chen, J. Pascual, F.D. Fischer, O. Kolednik, R. Danzer, Prediction of the fracture toughness of a ceramic multilayer composite – Modeling and experiments, Acta Mater. 55 (2007) 409–421. https://doi.org/10.1016/j.actamat.2006.07.046.

[69] M. Lugovy, V. Slyunyayev, N. Orlovskaya, G. Blugan, J. Kuebler, M. Lewis, Apparent fracture toughness of Si3N4-based laminates with residual compressive or tensile stresses in surface layers, Acta Mater. 53 (2005) 289–296. https://doi.org/10.1016/j.actamat.2004.09.022.

[70] T. Fett, Stress intensity factors and weight functions for the edge cracked plate calculated by the boundary collocation method, Kernforschungszentrum, 1990.

[71] T. Fett, D. Munz, Determination of Fracture Toughness at High Temperatures after Subcritical Crack Extension, J. Am. Ceram. Soc. 75 (11) (1992) 3133–3136. https://doi.org/10.1111/j.1151-2916.1992.tb04399.x.

[72] D. Munz, What Can We Learn from R-Curve Measurements?, J. Am. Ceram. Soc. 90 (1) (2007) 1–15. https://doi.org/10.1111/j.1551-2916.2006.01447.x.

[73] V.M. Sglavo, N. Bellettati, Ceramic laminates with improved mechanical reliability by tailoring the porosity of the constituting layers, J. Eur. Ceram. Soc. 37 (4) (2017) 1643–1650. https://doi.org/10.1016/j.jeurceramsoc.2016.11.022.

[74] C. Hillman, Z. Suo, F.F. Lange, Cracking of Laminates Subjected to Biaxial Tensile Stresses, J. Am. Ceram. Soc. 79 (8) (1996) 2127–2133. https://doi.org/10.1111/j.1151-2916.1996.tb08946.x.

[75] S. Ho, C. Hillman, F.F. Lange, Z. Suo, Surface Cracking in Layers Under Biaxial, Residual Compressive Stress, J. Am. Ceram. Soc. 78 (9) (1995) 2353–2359. https://doi.org/10.1111/j.1151-2916.1995.tb08668.x.

[76] M.G. Pontin, M.P. Rao, A.J. Sánchez-Herencia, F.F. Lange, Laminar Ceramics Utilizing the Zirconia Tetragonal-to-Monoclinic Phase Transformation to Obtain a Threshold Strength, J. Am. Ceram. Soc. 85 (12) (2002) 3041–3048. https://doi.org/10.1111/j.1151-2916.2002.tb00576.x.

[77] A. Wat, J. in Lee, C.W. Ryu, B. Gludovatz, J. Kim, A.P. Tomsia, T. Ishikawa, J. Schmitz, A. Meyer, M. Alfreider, D. Kiener, E.S. Park, R.O. Ritchie, Bioinspired nacre-like alumina with a bulk-metallic glass-forming alloy as a compliant phase, Nat. Commun. 10 (2019) 961. https://doi.org/10.1038/s41467-019-08753-6.

[78] R.O. Ritchie, The conflicts between strength and toughness, Nat. Mater. 10 (2011) 817–822. https://doi.org/10.1038/nmat3115.

[79] A.R. Studart, Towards High-Performance Bioinspired Composites, Advanced Materials 24 (2012) 1521–4095. https://doi.org/10.1002/adma.201201471.

[80] S. Ruppi, Deposition, microstructure and properties of texture-controlled CVD α-Al2O3 coatings, Int. J. Refract. Met. Hard Mater. 23 (2005) 306–316. https://doi.org/10.1016/j.ijrmhm.2005.05.004.

[81] G.L. Messing, S. Trolier-McKinstry, E.M. Sabolsky, C. Duran, S. Kwon, B. Brahmaroutu, P. Park, H. Yilmaz, P.W. Rehrig, K.B. Eitel, E. Suvaci, M. Seabaugh, K.S. Oh, Templated Grain Growth of Textured Piezoelectric Ceramics, Crit. Rev. Solid State Mater. Sci. 29 (2004) 45–96. https://doi.org/10.1080/10408430490490905.

[82] G.L. Messing, S. Poterala, Y. Chang, T. Frueh, E.R. Kupp, B.H. Watson, R.L. Walton, M.J. Brova, A.-K. Hofer, R. Bermejo, R.J. Meyer, Texture-engineered ceramics - Property enhancements through crystallographic tailoring, J. Mater. Res. 32 (2017) 3219–3241. https://doi.org/10.1557/jmr.2017.207.

[83] M.M. Seabaugh, I.H. Kerscht, G.L. Messing, Texture Development by Templated Grain Growth in Liquid-Phase-Sintered α-Alumina, J. Am. Ceram. Soc. 80 (5) (1997) 1181–1188. https://doi.org/10.1111/j.1151-2916.1997.tb02961.x.

[84] T.S. Suzuki, T. Uchikoshi, Y. Sakka, Control of texture in alumina by colloidal processing in a strong magnetic field, Sci. Technol. Adv. Mater. 7 (2006) 356–364. https://doi.org/10.1016/j.stam.2006.01.014.

[85] Z. Yang, J. Yu, C. Li, Y. Zhong, W. Xuan, Z. Ren, Q. Wang, Y. Dai, H. Wang, Preparation of textured porous Al2O3 ceramics by slip casting in a strong magnetic field

and its mechanical properties, Cryst. Res. Technol. 50 (2015) 645–653. https://doi.org/10.1002/crat.201500080.

[86] T. Carisey, A. Laugier-Werth, D.G. Brandon, Control of texture in Al2O3 by gel-casting, J. Eur. Ceram. Soc. 15 (1) (1995) 1–8. https://doi.org/10.1016/0955-2219(95)91293-W.

[87] M.N. Rahaman, Ceramic Processing, in: Kirk-Othmer Encyclopedia of Chemical Technology, 2014, pp. 1–98.

[88] M. Zhang, Y. Chang, R. Bermejo, G. Jiang, Y. Sun, J. Wu, B. Yang, W. Cao, Improved fracture behavior and mechanical properties of alumina textured ceramics, Mater. Lett. 221 (2018) 252–255. https://doi.org/10.1016/j.matlet.2018.03.123.

[89] M.Y. He, A.G. Evans, J.W. Hutchinson, Crack deflection at an interface between dissimilar elastic materials: Role of residual stresses, Int. J. Solids Struct. 31 (1994) 3443–3455. https://doi.org/10.1016/0020-7683(94)90025-6.

[90] H. Ming-Yuan, J.W. Hutchinson, Crack deflection at an interface between dissimilar elastic materials, Int. J. Solids Struct. 25 (1989) 1053–1067. https://doi.org/10.1016/0020-7683(89)90021-8.

[91] M. Jabbari, R. Bulatova, A.I.Y. Tok, C.R.H. Bahl, E. Mitsoulis, J.H. Hattel, Ceramic tape casting: A review of current methods and trends with emphasis on rheological behaviour and flow analysis, Materials Science and Engineering: B 212 (2016) 39–61. https://doi.org/10.1016/j.mseb.2016.07.011.

[92] R.E. Mistler, E.R. Twiname, Tape casting: Theory and practice, American Ceramic Society, Westerville, OH, 2000.

[93] A.A. Altun, F. Ertl, M. Marechal, A. Makaya, A. Sgambati, M. Schwentenwein, Additive manufacturing of lunar regolith structures, Open Ceramics 5 (2021) 100058. https://doi.org/10.1016/j.oceram.2021.100058.

[94] Lithoz GmbH, CeraFab Multi 2M30. https://lithoz.com/en/3d-printer/cerafab-multi/ (accessed 18 March 2024).

[95] M. Attaran, The rise of 3-D printing: The advantages of additive manufacturing over traditional manufacturing, Bus. Horiz. 60 (5) (2017) 677–688. https://doi.org/10.1016/j.bushor.2017.05.011.

[96] Z. Chen, Z. Li, J. Li, C. Liu, C. Lao, Y. Fu, C. Liu, Y. Li, P. Wang, Y. He, 3D printing of ceramics: A review, J. Eur. Ceram. Soc. 39 (4) (2019) 661–687. https://doi.org/10.1016/j.jeurceramsoc.2018.11.013.

[97] T. Chartier, C. Dupas, M. Lasgorceix, J. Brie, N. Delhote, C. Chaput, Additive Manufacturing to Produce Complex 3D Ceramic Parts, J. Ceram. Sci. Technol. 6 (2) (2014) 95–104. https://doi.org/10.4416/jcst2014-00040.

[98] A.-K. Hofer, I. Kraleva, R. Bermejo, Additive manufacturing of highly textured alumina ceramics, Open Ceramics 5 (2021) 100085. https://doi.org/10.1016/j.oceram.2021.100085.

[99] S. Nohut, S. Geier, I. Kraleva, M. Schwentenwein, R. Bermejo, Lithography-based additive manufacturing of porosity graded alumina, Addit. Manuf. Lett. 3 (2022) 100060. https://doi.org/10.1016/j.addlet.2022.100060.

[100] S. Nohut, J. Schlacher, I. Kraleva, M. Schwentenwein, R. Bermejo, 3D-printed alumina-based ceramics with spatially resolved porosity, Int. J. Appl. Ceram. Technol. 21 (1) (2024) 89–104. https://doi.org/10.1111/ijac.14512.

[101] J. Schlacher, T. Csanádi, M. Vojtko, R. Papšík, R. Bermejo, Micro-scale fracture toughness of textured alumina ceramics, J. Eur. Ceram. Soc. 43 (7) (2023) 2943–2950. https://doi.org/10.1016/j.jeurceramsoc.2022.06.028.

[102] J. Schlacher, A. Jabr, A.-K. Hofer, R. Bermejo, Contact damage tolerance of alumina-based layered ceramics with tailored microstructures, J. Am. Ceram. Soc. 105 (6) (2022) 4387–4399. https://doi.org/10.1111/jace.18389.

[103] J. Schlacher, Z. Chlup, A.-K. Hofer, R. Bermejo, High-temperature fracture behaviour of layered alumina ceramics with textured microstructure, J. Eur. Ceram. Soc. 43 (7) (2023) 2917–2927. https://doi.org/10.1016/j.jeurceramsoc.2022.11.046.

[104] J. Schlacher, A.-K. Hofer, S. Geier, I. Kraleva, R. Papšík, M. Schwentenwein, R. Bermejo, Additive manufacturing of high-strength alumina through a multi-material approach, Open Ceramics 5 (2021) 100082. https://doi.org/10.1016/j.oceram.2021.100082.

[105] J. Schlacher, S. Geier, M. Schwentenwein, R. Bermejo, Towards 3D-printed alumina-based multi-material components with enhanced thermal shock resistance, J. Eur. Ceram. Soc. 44 (4) (2024) 2294–2303. https://doi.org/10.1016/j.jeurceramsoc.2023.11.009.

[106] A.-K. Hofer, R. Walton, O. Ševeček, G.L. Messing, R. Bermejo, Design of damage tolerant and crack-free layered ceramics with textured microstructure, J. Eur. Ceram. Soc. 40 (2) (2020) 427–435. https://doi.org/10.1016/j.jeurceramsoc.2019.09.004.

[107] M. Sebastiani, K.E. Johanns, E.G. Herbert, G.M. Pharr, Measurement of fracture toughness by nanoindentation methods: Recent advances and future challenges, Current

Opinion in Solid State and Materials Science 19 (2015) 324–333. https://doi.org/10.1016/j.cossms.2015.04.003.

[108] J. Ast, M. Ghidelli, K. Durst, M. Göken, M. Sebastiani, A.M. Korsunsky, A review of experimental approaches to fracture toughness evaluation at the micro-scale, Materials & Design 173 (2019) 107762. https://doi.org/10.1016/j.matdes.2019.107762.

[109] R. Henry, T. Blay, T. Douillard, A. Descamps-Mandine, I. Zacharie-Aubrun, J.-M. Gatt, C. Langlois, S. Meille, Local fracture toughness measurements in polycrystalline cubic zirconia using micro-cantilever bending tests, Mechanics of Materials 136 (2019) 103086. https://doi.org/10.1016/j.mechmat.2019.103086.

[110] A.D. Norton, S. Falco, N. Young, J. Severs, R.I. Todd, Microcantilever investigation of fracture toughness and subcritical crack growth on the scale of the microstructure in Al2O3, J. Eur. Ceram. Soc. 35 (16) (2015) 4521–4533. https://doi.org/10.1016/j.jeurceramsoc.2015.08.023.

[111] M.G. Mueller, V. Pejchal, G. Žagar, A. Singh, M. Cantoni, A. Mortensen, Fracture toughness testing of nanocrystalline alumina and fused quartz using chevron-notched microbeams, Acta Mater. 86 (2015) 385–395. https://doi.org/10.1016/j.actamat.2014.12.016.

[112] L. Feng, R. Hao, J. Lambros, S.J. Dillon, The influence of dopants and complexion transitions on grain boundary fracture in alumina, Acta Mater. 142 (2018) 121–130. https://doi.org/10.1016/j.actamat.2017.09.002.

[113] T. Csanádi, M. Vojtko, J. Dusza, Deformation and fracture of WC grains and grain boundaries in a WC-Co hardmetal during microcantilever bending tests, Int. J. Refract. Met. Hard Mater. 87 (2020) 105163. https://doi.org/10.1016/j.ijrmhm.2019.105163.

[114] H. Chan, S.G. Roberts, J. Gong, Micro-scale fracture experiments on zirconium hydrides and phase boundaries, J. Nucl. Mater. 475 (2016) 105–112. https://doi.org/10.1016/j.jnucmat.2016.03.026.

[115] D. Di Maio, S.G. Roberts, Measuring fracture toughness of coatings using focused-ion-beam-machined microbeams, J. Mater. Res. 20 (2005) 299–302. https://doi.org/10.1557/JMR.2005.0048.

[116] J. Nakayama, Direct Measurement of Fracture Energies of Brittle Heterogeneous Materials, J. Am. Ceram. Soc. 48 (11) (1965) 583–587. https://doi.org/10.1111/j.1151-2916.1965.tb14677.x.

[117] R.O. Ritchie, K.J. Koester, S. Ionova, W. Yao, N.E. Lane, Ager, J W, 3rd, Measurement of the toughness of bone: a tutorial with special reference to small animal studies, Bone 43 (2008) 798–812. https://doi.org/10.1016/j.bone.2008.04.027.

[118] ISO/FDIS 23146, Fine ceramics (advanced ceramics, advanced technical ceramics) – Test methods for fracture toughness of monolithic ceramics – Single-edge V-notch beam (SEVNB) method, 2008.

[119] EN 843-1, Advanced technical ceramics - Monolithic ceramics- Mechanical properties at room temperature - Part 1: Determination of flexural strength, 1995.

[120] G.D. Quinn, R. Morrell, Design Data for Engineering Ceramics: A Review of the Flexure Test, J. Am. Ceram. Soc. 74 (9) (1991) 2037–2066. https://doi.org/10.1111/j.1151-2916.1991.tb08259.x.

[121] R. Morrell, N.J. McCormick, J. Bevan, M. Lodeiro, J. Margetson, Biaxial disc flexure – modulus and strength testing, British Ceramic Transactions 98 (1999) 234–240. https://doi.org/10.1179/096797899680507.

[122] W. Harrer, R. Danzer, P. Supancic, T. Lube, Influence of the Sample Size on the Results of B3B-Tests, Key Eng. Mater. 409 (409) (2009) 176–184. https://doi.org/10.4028/www.scientific.net/KEM.409.176.

[123] A. Börger, P. Supancic, R. Danzer, The ball on three balls test for strength testing of brittle discs: stress distribution in the disc, J. Eur. Ceram. Soc. 22 (9) (2002) 1425–1436. https://doi.org/10.1016/S0955-2219(01)00458-7.

[124] A. Börger, P. Supancic, R. Danzer, The ball on three balls test for strength testing of brittle discs: Part II: analysis of possible errors in the strength determination, J. Eur. Ceram. Soc. 24 (10-11) (2004) 2917–2928. https://doi.org/10.1016/j.jeurceramsoc.2003.10.035.

[125] J.P.A. Tillett, Fracture of Glass by Spherical Indenters, Proc. Phys. Soc. B 69 (1956) 47–54. https://doi.org/10.1088/0370-1301/69/1/306.

[126] A.A. Wereszczak, K.E. Johanns, O.M. Jadaan, Hertzian Ring Crack Initiation in Hot-Pressed Silicon Carbides, J. Am. Ceram. Soc. 92 (8) (2009) 1788–1795. https://doi.org/10.1111/j.1551-2916.2009.03146.x.

[127] Vallen Systeme GmbH, Acoustic Emission System AMSY-5 System Description. https://www.vallen.de/zdownload/pdf/y5sd0911.pdf (accessed 1 October 2021).

[128] S. Bouras, I. Zerizer, F. Gheldane, M.T. Bouazza, B. Bouzabata, Study of the resistance to crack propagation in alumina by acoustic emission, Ceram. Int. 34 (8) (2008) 1857–1865. https://doi.org/10.1016/j.ceramint.2007.06.015.

[129] D.P.H. Hasselman, Strength Behavior of Polycrystalline Alumina Subjected to Thermal Shock, J. Am. Ceram. Soc. 53 (9) (1970) 490–495. https://doi.org/10.1111/j.1151-2916.1970.tb15997.x.

[130] L. Shen, M. Liu, X. Liu, B. Li, Thermal shock resistance of the porous Al2O3/ZrO2 ceramics prepared by gelcasting, Mater. Res. Bull. 42 (2007) 2048–2056. https://doi.org/10.1016/j.materresbull.2007.02.001.

[131] E. Lara-Curzio, E. Cakmak, L. Lin, A.E. Marquez-Rossy, B. Armstrong, A. Flores-Betancourt, A. Macias, On the nonlinear temperature dependence of residual stresses in solid oxide fuel cells, J. Am. Ceram. Soc. 104 (2) (2021) 1014–1022. https://doi.org/10.1111/jace.17488.

[132] R. Bermejo, A.J. Sánchez-Herencia, L. Llanes, C. Baudín, High-temperature mechanical behaviour of flaw tolerant alumina–zirconia multilayered ceramics, Acta Mater. 55 (2007) 4891–4901. https://doi.org/10.1016/j.actamat.2007.05.005.

[133] U. Veit, C. Rüssel, Y. Houet, D. Laurent, Viscosity and Liquidus Temperature of Ternary Glasses Close to the Eutectic Composition in the CaO–Al2O3–SiO2 System, Int. J. Appl. Glass Sci. 7 (2016) 295–309. https://doi.org/10.1111/ijag.12191.

[134] J.H. Ainsworth, R.E. Moore, Fracture Behavior of Thermally Shocked Aluminum Oxide, J. Am. Ceram. Soc. 52 (11) (1969) 628–629. https://doi.org/10.1111/j.1151-2916.1969.tb15857.x.

[135] T.K. Gupta, Strength Degradation and Crack Propagation in Thermally Shocked Al2O3, J. Am. Ceram. Soc. 55 (5) (1972) 249–253. https://doi.org/10.1111/j.1151-2916.1972.tb11273.x.

[136] J. Chevalier, B. Cales, J.M. Drouin, Low-Temperature Aging of Y-TZP Ceramics, J. Am. Ceram. Soc. 82 (8) (1999) 2150–2154. https://doi.org/10.1111/j.1151-2916.1999.tb02055.x.

Publication Part

Publication A

Micro-scale fracture toughness of textured alumina ceramics

J. Schlacher, T. Csanádi, M. Vojtko, R. Papšík, R. Bermejo

J. Eur. Ceram. Soc. 43 (7) (2023) 2943–2950

https://doi.org/10.1016/j.jeurceramsoc.2022.06.028

Micro-scale fracture toughness of textured alumina ceramics

Josef Schlacher[1*], Tamás Csanádi[2], Marek Vojtko[2], Roman Papšík[1], Raul Bermejo[1]

[1] Department of Materials Science, Montanuniversitaet Leoben, Franz Josef-Strasse 18, A-8700, Leoben, Austria

[2] Institute of Materials Research, Slovak Academy of Sciences, Watsonova 47, 04353 Košice, Slovak Republic

*Corresponding author's email: josef.schlacher@unileoben.ac.at

Abstract

Enhanced fracture resistance of textured alumina is ascribed to crack deflection along grain boundaries. In this work, we quantify and compare the micro-scale fracture toughness of textured alumina grains and grain boundaries by micro-bending tests. Notched micro-cantilevers were milled from single alumina textured grains (perpendicular to the [0001] direction) and across several textured grains (along the [0001] direction), using a focused ion beam technique. Bending tests were performed with a nanoindenter. A shape function for notched pentagonal-shaped cantilevers was developed using finite element analysis. The critical stress intensity factor at the notch tip was determined based on the measured fracture loads. The micro-scale fracture toughness of the textured alumina grain boundaries (2.3 ± 0.2 MPa $m^{1/2}$) was about 30% lower than that of the grains (3.3 ± 0.2 MPa $m^{1/2}$). These findings at the micro-scale are paramount for understanding the macroscopic fracture behaviour of textured alumina ceramics.

Keywords: Textured alumina, micro-cantilever, fracture toughness, grains, grain boundaries

1. Introduction

Mimicking biological materials (e.g. mussels, bones, wood and among others) has been demonstrated as an effective approach for overcoming the lack of plasticity of ceramics, aiming to enhance their damage tolerance against external loading. The outstanding mechanical properties as well as the resistance to crack propagation of these biological materials are associated with their hierarchically arranged structures and the toughening mechanisms acting at different length scales [1,2]. Since the inherent toughness and strength of materials are generally mutually exclusive, many research areas have been focused on ceramic-based "bioinspired materials" with a remarkable strength to toughness ratio [3]. For instance,

mimicking the exceptional “damage tolerance” of nacre, has emerged as a novel concept for designing and fabricating tougher and more reliable ceramics [4–6].

The fabrication of “nacre-like” alumina ceramics with enhanced toughness has used processing routes such as through ice templating, magnetically-assisted slip casting and hot-pressing [5], based on the alignment of “template” particles, which resembles the structure of nacre. An alternative approach has focussed on ceramic multilayer architectures designed with strong interfaces and different ceramics constituents, aiming to tailor the alternating residual stresses caused by the different coefficients of thermal expansions within the layers [7]. Depending on the specific location of the compressive residual stresses, either within the embedded layers or in the outer layers, designs with enhanced damage tolerance [8–11] or mechanical resistance [12,13] have been achieved. The former (damage tolerant) design has been proven to be an effective way to introduce “barriers” against crack growth, which in some cases can even arrest the propagation of surface cracks [8,9]. Beyond this progress in architectural design, microstructural design has been pursued in multilayer ceramics to combine the “damage tolerant” effect of compressive residual stresses with the toughening capability of “hierarchical” microstructures, as found in nacre [9]. In this case, a “textured” microstructure is formed during the sintering step, associated with “template grain growth” (TGG) process, based on Ostwald ripening effect [14]. Orienting the grains (texturing) within the embedded compressive layers has proven to be very effective strategy to enhance the fracture energy of the system by guiding the crack along the basal interfaces of the textured grains [15–18]. Although experimental observations of different textured multilayer architectures are available, there is still a lack of understanding of the underlying mechanisms during the fracture process, especially at the micro-scale level.

The importance of determining the mechanical properties even at the micro-level are indisputable for optimizing “bioinspired” ceramic architectures with tailored microstructures. In this regard, the micro-scale data available on single alumina grains are rare. In the work of Feilden et al. [19], the strength of single alumina platelets was studied using micro-bending tests. Recently, the interface failure of nacre-alumina has been assessed and the micro-scale strength was determined at different interface angles with respect to the fixed end of the micro-cantilevers by Henry et al. [20]. They found that the apparent fracture stress determined is increasing with the corresponding interface angle. The fracture toughness of nanocrystalline alumina was studied by Mueller et al. [21] by using micro-scale testing of Chevron-notched cantilevers. The micro-scale fracture behaviour of single crystal, bi-crystal and polycrystalline

alumina was investigated by Norton et al. [22] by using micro-cantilever bending tests. In their work, sharp notches and rectangular artificial flaws were introduced by FIB milling to determine the apparent fracture toughness and the threshold stress intensity for subcritical crack growth of individual grains and grain boundaries. In the case of polycrystalline alumina grains and grain boundaries were evaluated by testing cantilevers crossing several grains and containing artificial flaws following the equations from Strobl et al. [23].

The objective of this work is to demonstrate for the first time the toughness difference between grains and grain boundaries within a tailored textured microstructure. To our best knowledge, the micro-scale fracture toughness of "as-sintered" individual grains and grain boundaries of a TGG "textured" alumina microstructure has not been quantified yet. It may be hypothesized that the exceptional damage tolerance in layered alumina ceramics is mainly attributed to crack deflection events along the (weak) basal-grain boundaries within the textured microstructure of the embedded "protective" layers. To verify this hypothesis, the micro-scale fracture toughness of individual textured alumina grains and grain boundaries has been measured through micro-cantilever bending.

2. Experimental

2.1. Sample preparation

Textured alumina was fabricated by using tape casting technology. High-purity α-Al_2O_3 powder (TM-DAR, Taimei Chemicals Co., Ltd., Tokyo, Japan) with a mean particle size of 200 nm was mainly used for the preparation of slurries. Single-crystal alumina platelets (Rona Flair® White Sapphire, EMD. Performance Materials Corp., Darmstadt, Germany) with average dimensions of ~ 3–10 µm in diameter and 0.1 µm in thickness were added to enhance TGG. A 0.25 wt% concentration of dopants ($CaO:SiO_2$=1:1) was added in respect to the alumina powder to favour liquid phase sintering. Especially the addition of these single-crystal alumina platelets with high-aspect ratios is paramount for establishing a high-quality texture in [0001]-direction (c-axis). This crystallographic direction is normal to the basal surfaces of the templates, aligned during the tape casting process.

Samples were fabricated by stacking dried tapes with dimensions of 30 × 30 mm^2 and warm-pressed with 20 MPa at 75 °C for 15 min. The thickness of the dried tapes was ~50 µm. Afterwards, isostatic lamination was performed at 20 MPa/75 °C for 30 min followed by binder burn out at 600 °C (2 h). Subsequently, the stacked plates were cold-isostatic pressed with

100 MPa for 15 min and sintered at 1550 °C for 2 h in order to achieve high relative density. The sample of study with the dimension of 11 × 3 × 1.2 mm^3 was prepared from one of the plates. Subsequently, the prismatic cross-section (11 mm × 1.2 mm) of the sample was polished to 0.25 µm mirror finish using a Struers RotoPol-25 equipment and thermally etched by 1450 °C for 5 min. A schematic of the surface of interest (prismatic cross-section) with the aligned textured bricks is shown schematically in Fig. 1.

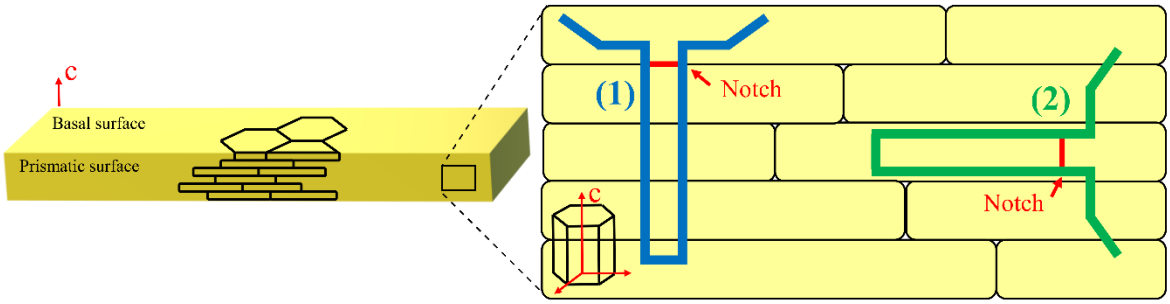

Fig. 1: Schematic of the textured sample with detail of the prismatic surface. The [0001]-direction, denoted as c-direction, is perpendicular to the basal surface of the sample (or grains). The inset shows the alignment of the notched microcantilevers FIB milled from several grains either (1) perpendicular to basal grain boundaries or (2) within a single alumina grain.

2.2. Microstructure and texture analysis

Prior to the measurements, both surfaces of textured samples (basal and prismatic surface) were inspected with an optical microscope. To investigate the textured microstructure, the thermally etched prismatic surface was coated with a thin gold layer and images were taken using Scanning electron microscopy (SEM) (Zeiss Auriga, Germany).

To assess the quality of texture, the X-ray diffraction (XRD) pattern of the basal-sample surface (perpendicular to [0001]-axis) was collected using the Θ-2Θ method with a scanning step size of 0.02° and time per step of 1.2 s. The Lotgering factor, LF, which is a measure for the texturing degree, was determined as [24]:

$$LF = \frac{\frac{\sum I^{T}_{(000l)}}{\sum I^{T}_{(hkil)}} - \frac{\sum I^{Ref.}_{(000l)}}{\sum I^{Ref.}_{(hkil)}}}{1 - \frac{\sum I^{Ref.}_{(000l)}}{\sum I^{Ref.}_{(hkil)}}} \quad (1)$$

where $\sum I^{T}_{(000l)}$ and $\sum I^{T}_{(hkil)}$ are the sum of peak intensities of (000*l*) and of all intensity peaks within the scan of the textured alumina, respectively. The sum of peak intensities of (000*l*), denoted as $\sum I^{Ref.}_{(000l)}$, and of all peaks ($\sum I^{Ref.}_{(hkil)}$) within the Θ-2Θ-scan were taken from a reference alumina material with non-textured microstructure. The reader is cautioned that LF of 1 represents a perfect texture and (000*l*) evidences the basal-planes (perpendicular to the c-axis) within the rhombohedral crystal structure of alumina.

2.3. Fabrication of microcantilevers

Testing specimens were fabricated by a focused ion beam (FIB) technique in a dual-beam FIB/SEM electron microscope (Zeiss Auriga, Germany) operated at 30 kV. Microcantilevers were cut both entirely from alumina grains with a beam surface perpendicular to the c-axis of the crystal, [0001] direction (see (2) in Fig. 1), and were FIB milled across the grain boundaries parallel with the c-axis, consisting of several grains (see (1) in Fig. 1). The FIB milling started with the making of notches and was followed by three consecutive steps, as described in [25]. First, long sharp notch of about 10 μm was FIB milled from the desired locations, using a low current of 50 pA for about 30 s, which resulted in a depth of about 100–600 nm. The FIB cut was performed either several microns apart from the designed fixed end of the cantilever beam inside the grains or at the grain boundaries depending on the beam orientation. This technique resulted in smaller rounding of the notches at the side of the final microcantilevers, due to the angle-dependent milling of Ga ions, compared to the case when the notches were induced in the last step. Second, coarse milling was applied to prepare trapezoid shape trenches at both sides of the cantilevers, and the material was also removed in front of the beams using a current of 20 nA. This resulted in rectangular columns, which were connected to the material along one side only. Third, cantilevers were cut to their designed size using a current of 2 nA, and the pentagonal cross-section (Fig. 2) was achieved by performing the milling in a tilt position of the sample at an opening angle of about 52° between the FIB gun and surface normal. Finally, a fine polishing was performed on the sides of the beams with a current of 500 pA to mill away

surface effects and to reach the final size of the specimen. A total of 16 cantilevers were FIB milled. The best 10 specimens (five for each orientation respectively) with lengths of $L \approx 10–20$ µm, widths of $a \approx 2–4$ µm and total thickness of $b+m_a \approx 3–4$ µm were selected and measured by SEM. Although the sample was covered with a 10–15 nm thin gold layer to minimize the surface charging during milling, a permanent drift made the milling process difficult and rather slow, having an average speed of one specimen per day.

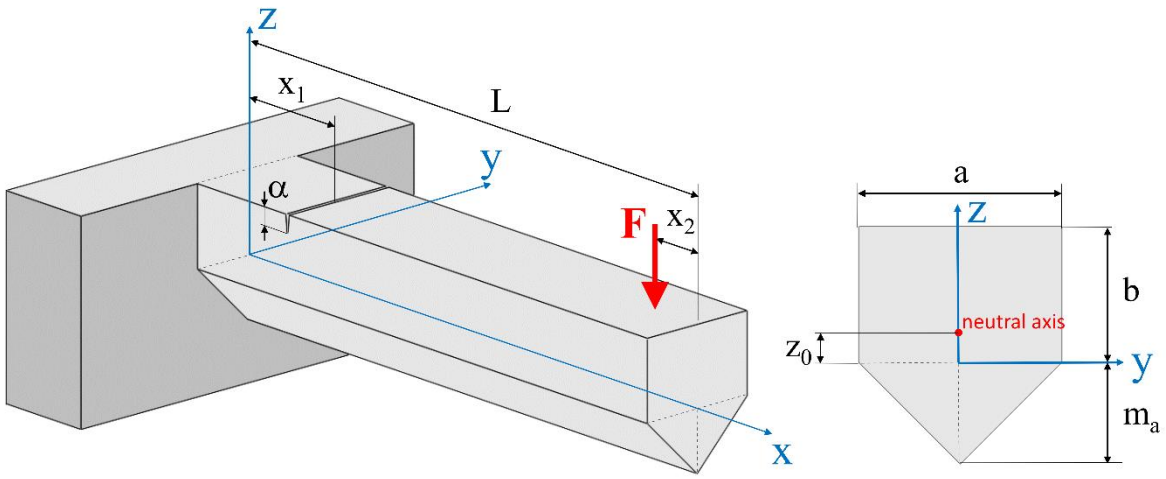

Fig. 2: Schematic of pentagonal-shaped notched cantilevers with all the indicated dimensions needed for calculation of the fracture toughness. The applied load F is represented by the red arrow.

2.4. Microcantilever bending tests

The bending tests of the microcantilevers were carried out on an Agilent G200 NanoIndenter equipped with a diamond spherical tip with a nominal radius of 1 µm, using a constant load rate of 0.015 mN/s. Based on preliminary tests, the maximum load was set to 6 mN, which was high enough to induce fracture in the microcantilevers. The loading process was carefully monitored and immediately interrupted manually after the fracture occurred (before reaching the maximum load) and then the testing process was followed by the unloading. Bending tests were started after reaching a predefined drift limit of 0.1 nm/s and each test was corrected for the drift rate measured at the end of the process. After the bending tests, a SEM (Zeiss Auriga, Germany) was used to inspect the broken microcantilevers and analyse the fracture surfaces of each specimen. Additionally, energy dispersive spectroscopy (EDS) measurements were carried out on the fracture surfaces at the grain boundaries to analyse the presence of Si and Ca dopants, as glass forming elements, using 20 kV in the SEM. The notch depth (α) was measured

on SEM images of the fracture surfaces. The dimensions of the beams and the fracture distance (x_1) in Fig. 2 were determined based on SEM micrographs. Followed by an appropriate microscope to indenter calibration on Agilent G200, the loading point (x_2) was measured based on the position of the cross-hair relative to the free end of the beam according to an optical micrograph of 2500x magnification acquired prior to each test using image processing software (Stream motion, Olympus). The accuracy of the positioning of the tip was about 0.2 µm, as determined in the earlier work of Csanádi et al. [26].

3. Evaluation of fracture toughness

According to Linear Elastic Fracture Mechanics, the fracture toughness K_{Ic} can be analytically calculated as follows:

$$K_{Ic} = \sigma_c \sqrt{\pi \alpha}\, Y(\tilde{\alpha}) \tag{2}$$

where α is the notch depth in Fig. 2, $Y(\tilde{\alpha})$ the corresponding shape factor as a function of the normalized notch length $\tilde{\alpha}$ and σ_c the fracture stress (see definitions below). Here, it is important to emphasize that σ_c in Eq. (2) denotes the nominal surface tensile stress at the location of the notch in the intact (unnotched) material; the influence of the notch on the stress field in its vicinity is considered to be comprised in the $Y(\tilde{\alpha})$ shape factor determined by FEM. Considering a small deflection of the beams, the fracture stress σ_c was calculated based on the Euler-Bernoulli beam theory using the formula derived for pentagonal-shaped cantilevers in the work of Csanádi et al. [26]:

$$\sigma_c = \frac{F_{max}(b - z_0)}{I_x}(L - x_2 - x_1) \tag{3}$$

where F_{max} is the maximum load at fracture, z_0 is the distance between the neutral axis and the X-Y plane of the coordinate system (Fig. 2):

$$z_0 = \frac{1}{b + \frac{m_a}{2}}\left(\frac{b^2}{2} - \frac{{m_a}^2}{6}\right) \tag{4}$$

and I_x is denoted as the second moment of area which is given for the pentagonal cross-section [26] as:

$$I_x = \frac{ab^3}{3} + \frac{am_a{}^3}{12} - a\left(b + \frac{m_a}{2}\right) z_0{}^2 \tag{5}$$

All the dimensions needed for the calculation (a, b, m_a, L, x_1 and x_2) are indicated in Fig. 2. In order to compare quantitatively the fracture behaviour of cantilevers with different sizes, the linear load (F)-displacement (h) data were converted to effective stress (σ)-strain (ε) curves, where σ is the effective stress calculated by Eq. (3) for the applied load F and ε is the corresponding effective strain, which is determined as follows [26]:

$$\varepsilon = \frac{3h(b - z_0)(L - x_2 - x_1)}{(L - x_2)^3} \tag{6}$$

It is important to note that the use of the above terminology (effective stress – effective strain) provides a quantitative comparison for the different beams but does not describe the actual stress-strain behaviour inside the cantilevers due to the presence of notches, which could significantly change their compliance. As a consequence, the ratio of the effective stress and strain values results in an effective Young's modulus of the notched beams ($E = \sigma/\varepsilon$) which is different from the Young's modulus of alumina material and, therefore, it was not analysed in the present work.

As described in Eq. (2), the determination of K_{Ic} requires the numerical calculation of the shape factor $Y(\tilde{\alpha})$ for pentagonal shape beam geometry. Such studies have already been performed in the literature for both rectangular and pentagonal shaped cantilevers, of which formulas were compared to each other in the work of Chan et al. [27]. However, due to a notable discrepancy between calculated dimensionless shape factors for pentagonal cantilevers proposed by Di Maio and Roberts [28] and the one calculated by Chan et al. [27], we performed new Finite Element (FE) analysis in this work to determine an appropriate shape factor for our investigated geometry, using the software ANSYS [29] as shown in Fig. 3. A material model with linear isotropic response was chosen. The typical macroscopic Young's modulus of ~380 GPa and Poisson's ratio of 0.22 for textured alumina were used in the FE-model [18]. The 3D model of the geometry was discretized by quadratic tetrahedral elements, exploiting the plane symmetry. The notch was assumed to be as a sharp discontinuity (i.e. crack) and the cantilever transitioned to the bulk material as shown in Fig. 3a. The displacement was fixed at (i) the back and (ii)

bottom face of the bulk as well as (iii) in the plane of symmetry. The simulation was conducted for various crack lengths ($100 \leq \alpha \leq 1000$ nm) with a fixed geometry of a = 3 µm in width and $b+ma$ = 3.5 µm in thickness using a load of 2 mN. The shape factors were determined for different crack lengths as the ratio of the numerically calculated stress intensity factor ($K_{I,FEM}$) using the J-Integral in the FE model and the analytical stress intensity factor ($\sigma\sqrt{\pi\alpha}$) according to the Euler-Bernoulli beam theory (Eq. (2)), where the stress values were calculated according to Eq. (3). The obtained data points were normalized ($\tilde{\alpha}$) and fitted by a polynomial function of 4th order in the interval of $0.035 \leq \tilde{\alpha} \leq 0.35$, as follows:

$$Y(\tilde{\alpha}) = 1.119 - 1.087\tilde{\alpha} + 5.224\tilde{\alpha}^2 - 8.082\tilde{\alpha}^3 + 8.821\tilde{\alpha}^4 \quad (7)$$

where the normalized notch length was calculated as:

$$\tilde{\alpha} = \frac{\alpha}{2(b - z_0)} \quad (8)$$

Our polynomial fit ($Y(\tilde{\alpha})$) is similar to the shape factor function proposed by Chan et al. [27].

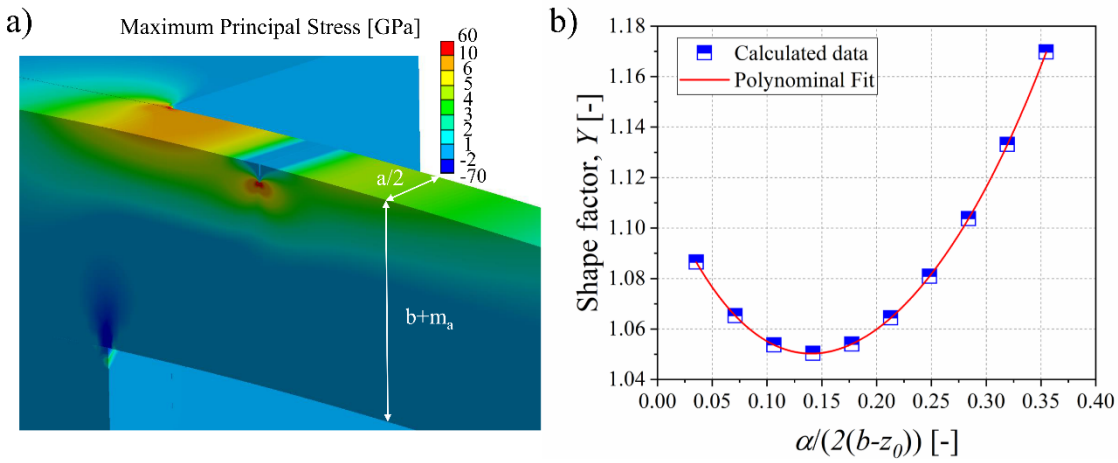

Fig. 3: (a) FE-model of the bent cantilever with the introduced sharp crack of 300 nm. The maximum principal stress is represented using a coloured scale. (b) Analytical fit of data points from FE-calculations used for the determination of the shape factor $Y(\tilde{\alpha})$.

4. Experimental results

Figure 4a illustrates the microstructure of the textured material (prismatic surface view), exhibiting highly-elongated grains with ~ 15–40 µm in length and ~ 3–5 µm in thickness. It can be observed that the level of porosity at the basal grain boundaries is rather low, showing only small pores within the grains. Figure 4b shows the XRD pattern measured on the textured alumina. Predominant (0006) and (00012) peaks were detected, corresponding to the [0001]-direction of the grains (c-axis), which agrees with the strong alignment of the textured microstructure, as seen in Fig. 4a. The relatively large Lotgering factor (LF ~ 0.8) confirms the high quality of the texture achieved with tape casting process, and is comparable to the texture degree reported for in alumina ceramics [18,30,31].

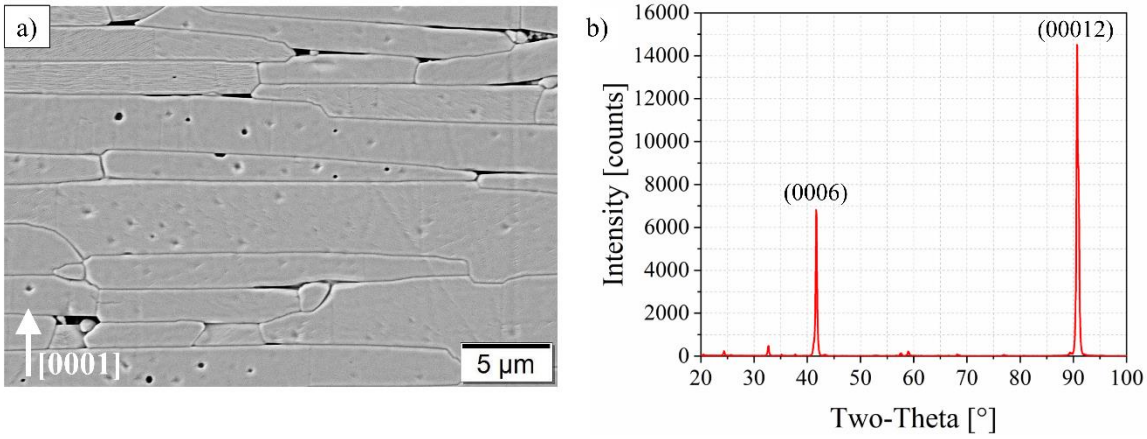

Fig. 4: (a) Microstructure and (b) corresponding XRD pattern of textured alumina, indicating the strong alignment of grains perpendicular to the [0001]-basal-direction. The dominant peaks of the (0006) and (00012) planes are indexed.

Figure 5 shows representative cantilevers in both directions, milled either (i) entirely from the textured grains with a beam direction perpendicular to the c-axis, or (ii) crossing several grains parallel with the c-axis ([0001] direction), respectively. Figure 5a shows a cantilever prepared within the grain and notched parallel to the c-axis (marked by a yellow arrow) to guarantee the fracture along with one of the prismatic facets of the alumina grain. Figure 5c shows the cantilever notched directly at the grain boundary (indicated with yellow arrows) with the c-axis perpendicular to the notch, in order to evaluate the fracture toughness of the boundary of the textured grains. It is worth noting that the grain boundary of the basal orientation is tested in this beam configuration. To illustrate the pentagonal cross-section of the cantilevers, an inclined

side view of its free end is represented in Fig. 5b and d for both configurations. The natural porosity of the textured alumina microstructure is clearly observable on these beam cross-sections.

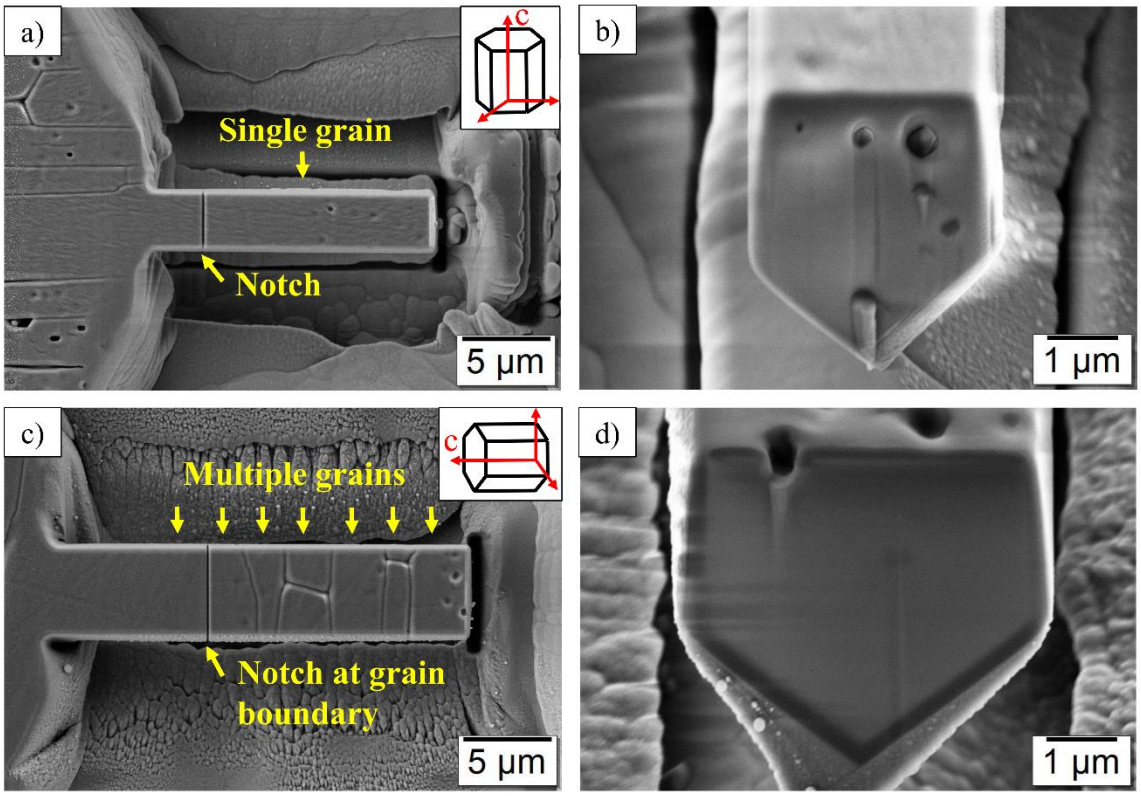

Fig. 5: The top views and the corresponding pentagonal-shaped cross-sections of the as-milled cantilever notched within textured grains (a, b) and in grain boundary direction (c, d) are represented.

The micro-scale fracture toughness of cantilevers milled entirely from single textured grains, fractured along prismatic facets, was 3.3 ± 0.2 MPa $m^{1/2}$, whereas that of the basal grain boundaries was 2.3 ± 0.2 MPa $m^{1/2}$. The specimen dimensions, the measured fracture forces as well as the results of the individual fracture toughness results of each tested cantilever are listed in a supplementary Table S1. The fracture toughness of the basal grain boundaries is about 30% lower than that of the grains, which may explain the preferred (macroscopic) crack propagation along the basal boundaries of textured alumina samples.

Figure 6 reports representative effective stress-strain curves of tested specimens notched either within the grain (Fig. 6a) or at grain boundaries (Fig. 6c, e). The fracture surfaces of the corresponding broken cantilevers are shown in Fig. 6b, d, and f, respectively.

All the curves follow a linear trend confirming the applicability of the linear elastic fracture mechanics for the evaluation of fracture toughness from the micro-cantilever experiments. The comparison of the representative stress-strain curves of beams (Fig. 6a, c, e) exhibit different slopes due to the different compliance of the microcantilevers. This is a combined effect of geometry (notch depth to total thickness ratio), elastic anisotropy of alumina grains and the presence of grain boundaries. Since it is a complex elastic problem out of focus of the present investigation, the deduction of Young's modulus values from the microcantilever bending experiments was not addressed in this work.

Figure 6b displays a representative fracture surface of a notched cantilever tested within the grain. The rather smooth fracture surface agrees with the expected brittle fracture along with one of the prismatic planes (i.e. m- or a-plane), as reported in [22]. Figure 6d shows the fracture of one representative cantilever notched directly at the basal grain boundary. The smooth and flat fracture surface is associated with the preferred crack path along the intersection of the grain boundaries in basal orientation. In Fig. 6f, another fracture surface of a cantilever notched at the grain boundary is depicted. The transition of the notch to the final fracture surface reveals a step-like area [22] (as typical for c-plane basal fracture), followed by a rather smooth fracture surface from the boundary intersection. We caution the reader that a slight deviation of the notch from the sides was observed in several cantilevers after post-mortem inspection. In such cases, the notch depth was corrected (based on six measurements along the cantilever width) prior fracture toughness evaluation. It is worth noting that all cantilevers exhibited typical "compression curls" in the last third of the specimen's thickness.

EDS analysis revealed that glass-forming elements of Si and Ca, which were added as dopants during processing, can be observed at the grain boundaries in some places in the amounts of ~0.4 at% and ~0.2 at%, respectively for Si and Ca; the measurement was performed perpendicular to the sample surface. However, these elements could not be detected on the fracture surface of microcantilevers at the grain boundaries. Regarding that the deposited thin Au layer (4–6 microns) exhibited an EDS signal of 0.7–1.0 at%, it can be concluded that only a very thin (few nanometres) glassy phase might have been present at the grain boundaries in the textured alumina sample but not as large amount as was reported for nacre-like alumina [20].

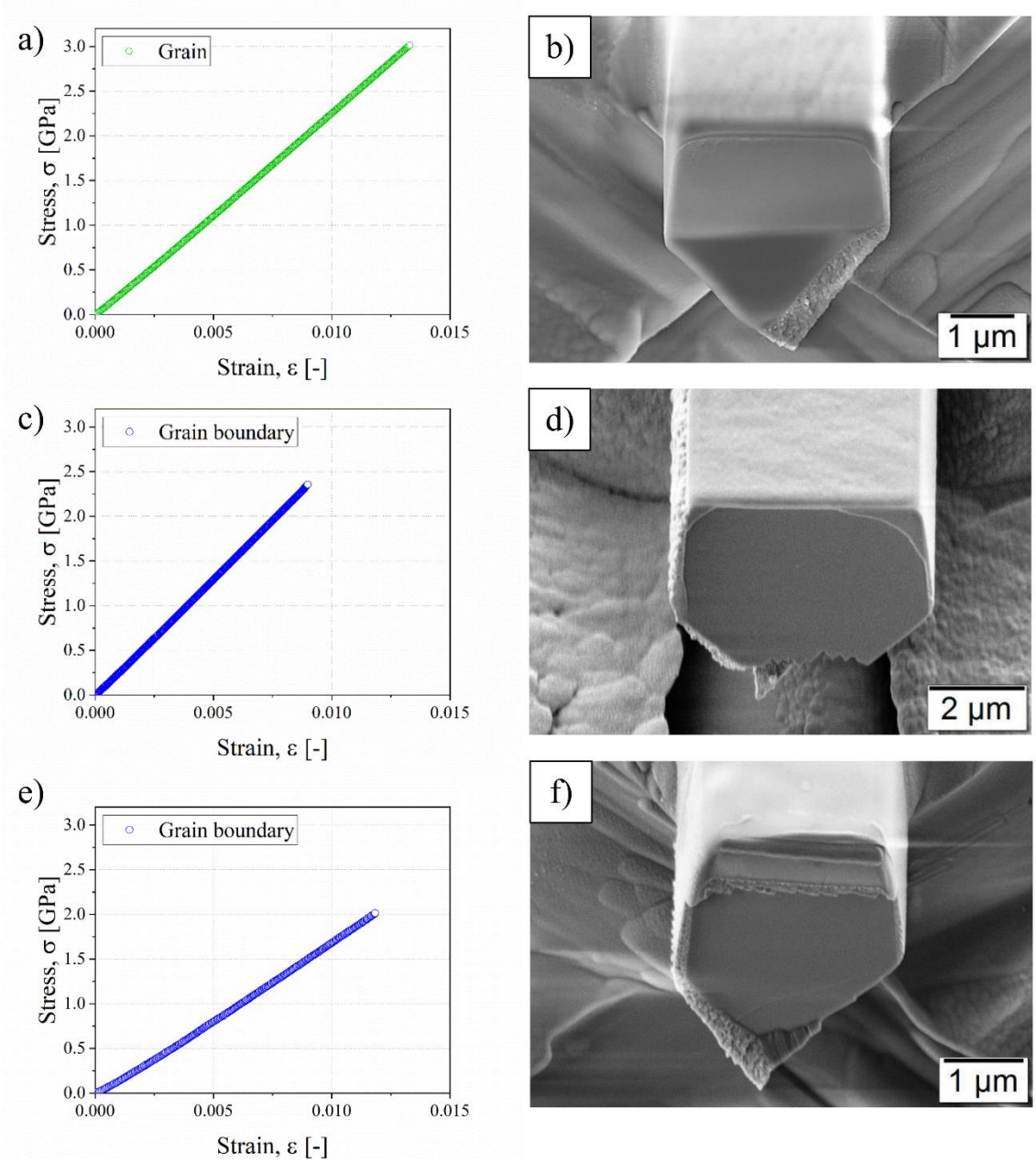

Fig. 6: The effective stress-strain curves of the microcantilever tested within the grains (a) as well as at the grain boundaries (c, e), respectively, together with the corresponding fracture surface of the beams at the notch (b,d,f).

5. Discussion

5.1. Reliability of the micro-scale testing method

In order to assess the reliability of micro-mechanical bending tests for the determination of the fracture toughness of textured alumina grains and grain boundaries, different aspects which may affect the results are considered. Norton et al. [22] claimed in their study that with

increasing notch tip radius, the fracture toughness determined on micro-cantilevers of sapphire (m- or c-fracture plane) is significantly overestimated. However, they showed that for the smallest tip blunting of ~15 nm the correction factor for the notch tip radius is only 0.9. In our case, by using pentagonal shaped cantilevers with a relatively sharp notch tip radius (measured on selected cantilevers as ~ 11 nm), this error may be negligible.

Best et al. [32] studied the influence of ion bombardment on the small-scale fracture toughness measurement by using xenon and helium- and conventional gallium-ion sources for milling of chromium nitride cantilevers. They showed differences in the fracture toughness depending on the amount of damage. It was concluded that there may be an influence of ion damage on the fracture toughness data [32]. As reported by Norton et al. [22], the gallium ion implantation during FIB milling may have an influence on the measurement of fracture toughness both inside the grains and at the grain boundaries: (i) directly due to material structure modification in the vicinity of the notch and/or (ii) indirectly associated with increased notch radius with increasing current. In light of these recommendations, a low milling current of ~50 pA was used in our work to minimize possible ion damage during notching. Our EDS analysis done on the fracture surfaces in the vicinity of the notches showed relatively low and similar values of Ga content (~1.0 at%) in both regions, indicating a negligible effect on the toughness measurements. The different K_{Ic} values obtained for the grains and grain boundaries are attributed to the weaker bonds between the adjacent grains compared to the grain interiors, in which a very thin glassy phase may play a role as described in the results part.

Furthermore, it is also worth noting that the accuracy in the measurement of the notch length after fracture has a significant influence on the calculated fracture toughness. For instance, a 10% inaccuracy in the measurement of the final notch length yields an error of about 5% in the fracture toughness value. To avoid errors in the calculations and to correct any deviations near the side surfaces of the notch front through the milling process of the cantilevers, the average notch length was taken from six measurements along the width of the cantilever.

Finally, the notch positioning and orientation with respect to the grain boundaries may also affect the measured fracture toughness. In the present work, only microcantilevers notched within a position accuracy of about 100 nm to grain boundaries were evaluated, which is similar to the width of trenches between the adjacent grains caused by thermal etching.

5.2. Orientation dependent micro-scale fracture toughness

In our work, the micro-scale fracture toughness of the individual textured grains (3.3 ± 0.2 MPa $m^{1/2}$) was found to be significantly higher than that of the textured grain boundaries (2.3 ± 0.2 MPa $m^{1/2}$). The micro-scale fracture toughness of the textured alumina grains with prismatic fracture planes (m or a-plane), is in good agreement with the reported values (3.9 ± 0.1 MPa $m^{1/2}$ and 3.8 ± 0.1 MPa $m^{1/2}$ for the m- and a-planes, respectively) of α-alumina grains grown by chemical vapour deposition by the study of Konstantiniuk et al. [33]. Furthermore, our results are in good agreement with the apparent stress intensity factors at fracture measured in polycrystalline alumina (cantilever tested with introduced artificial flaw) for transgranular fracture in grain (3.9 ± 0.2 MPa $m^{1/2}$) and intergranular fracture on grain boundaries (2.8 ± 0.2 MPa $m^{1/2}$) as well as with those of notched cantilevers on single crystals (3.7 ± 0.2 MPa $m^{1/2}$) and bicrystal grain boundaries (2.9 ± 0.2 MPa $m^{1/2}$) [22].

In the work of Iwasa and Bradt [34], macro-scale fracture toughness values of 3.1 ± 0.3 MPa $m^{1/2}$ (m-plane) and 2.4 ± 0.3 MPa $m^{1/2}$ (a-plane) were reported on single-crystal alumina tested at room temperature along prismatic planes, respectively. Furthermore, they showed that the lowest fracture toughness of the rhombohedral r-plane (2.4 ± 0.1 MPa $m^{1/2}$) may indicate its preferred cleavage. In their study, the highest macro-scale fracture toughness was found to be along the c-plane (4.5 ± 0.3 MPa $m^{1/2}$), similar to the trends evidenced in the work of Wiederhorn [35]. Due to the alignment of platelets in [0001]-direction during the tape casting process, cantilevers fractured within the textured grains may yield preferred fracture along with one of the prismatic planes. In our micro-scale experiments, fracture toughness of the grains (3.3 ± 0.2 MPa $m^{1/2}$) is well comparable with the macro-scale fracture along m-plane as stated above (3.1 ± 0.3 MPa $m^{1/2}$), with a difference of only ~6%. The micro-scale fracture toughness of the grains seems to be significantly higher than the macroscopic toughness in prismatic a- as well as rhombohedral r-plane. Regarding that the micro-scale fracture toughness of the m- and a-planes were reported to be equal within their scatters [22,33], the K_{Ic} measured for grains in this work is considered as an average of the prismatic planes despite that it fits quantitatively well with the macro-scale fracture along the m-plane [34]. The micro-scale fracture toughness of the basal-grain boundaries (2.3 ± 0.2 MPa $m^{1/2}$) shows a significantly lower value compared to the macro-scale c-plane fracture toughness, which may indicate the weakening effect of the grain boundary in basal orientation.

5.3. Relevance for the macroscopic fracture behaviour of textured alumina

The residual stresses in polycrystalline alumina samples may play an important role in their macro-scale fracture behaviour. Based on the literature, residual stresses are induced during processing due to the thermal expansion anisotropy and misorientation of adjacent grains, which was found to be lower for textured specimens compared with untextured alumina samples [36,37]. The magnitude of residual stresses for untextured alumina with grain size similar to our sample was measured to be ~200 MPa, which is compressive along the a-direction and tensile along the c-direction ([0001] direction) [36]. Thus, residual stresses may affect crack initiation and propagation, which in our case promotes cracking along the basal grain boundaries (c-planes). Additionally, it could result in the presence of separation of grains along the c-planes in the as-sintered samples, as can be seen in Fig. 4, favouring crack deflection in textured alumina at the macro-scale. However, at the level of microcantilevers, where the material was removed around the beams, these residual stresses both in the grains and at the boundaries may be considered negligible.

Hofer et al. [18] studied the fracture behaviour and the crack path of textured and non-textured alumina bulk materials. They showed that the fracture toughness of the textured material is about 10% higher (4.4 ± 0.2 MPa $m^{1/2}$ [18]) than that of the non-textured alumina (3.9 ± 0.4 MPa $m^{1/2}$ [18]), favoured by crack deflection mechanisms along the basal planes resulting in an intergranular and rather stepwise fracture mode. The macroscopic fracture toughness of textured alumina (4.4 ± 0.2 MPa $m^{1/2}$) is approx. 30% higher than that of one individual textured alumina grain (3.3 ± 0.2 MPa $m^{1/2}$) determined in this work. This significant difference may be explained by the additional energy-dissipating mechanisms (i.e. crack deflection, crack bridging) acting at the macro-scale level that can be further enhanced by an appropriate texture design, for example varying the length to thickness ratio of the alumina grains. Here it is important to emphasize that the knowledge of fracture toughness difference of grains and grain boundaries plays a fundamental role in such designs. This has been shown in the recent work of Schlacher and Jabr et al. [38], where the enhancement of the contact damage tolerance of layered alumina with embedded textured layers was associated with micro crack-formation (absorption of contact damage induced energy) and microstructural deflections along the basal grain boundaries within textured alumina. The significantly lower micro-scale fracture toughness of the grain boundaries (2.3 ± 0.2 MPa $m^{1/2}$) measured in this work, could elucidate the favoured crack path along the basal boundaries of elongated textured grains during crack

propagation. To the best of our knowledge, the present experimental findings are the first report demonstrating quantitatively the “weakness” of textured grain boundaries.

6. Conclusions

The micro-scale fracture toughness of individual grains along with prismatic facets and grain boundaries along the basal interfaces in a textured alumina sample was determined through micro-cantilever bending tests. It was found that the micro-scale fracture toughness of the grain boundaries along the basal interface is significantly lower (2.3 ± 0.2 MPa $m^{1/2}$) than that of the individual grains along with the prismatic facets in the textured microstructure (3.3 ± 0.2 MPa $m^{1/2}$). The demonstrated difference of approximately 30% in fracture toughness explains the favoured crack path along the basal-grain boundaries. This experimental finding is paramount for understanding the macroscopic fracture behaviour of layered alumina ceramics with embedded textured layers. Microstructure tailoring by applying grains with higher aspect ratios and additional interface weakening methods, such as introducing second phases, could further enhance the damage tolerance of layered alumina ceramics with textured microstructures.

Acknowledgements

Funding for this research was provided by the European Research Council (ERC) excellent science grant “CERATEXT” through the Horizon 2020 program under contract 817615. T. Csanádi is grateful for the support of a SAS-ERC Visiting Fellowship Grant of the Slovak Academy of Sciences via the project SAS-ERC/2020/941.C/HECERS. The authors gratefully acknowledge I. Kraleva (Department of Materials Science, Montanuniversität Leoben) for the support in sample polishing, A.-K. Hofer (Department of Materials Science, Montanuniversität Leoben) for performing the XRD-measurement and D. Kiener (Department of Materials Science, Montanuniversität Leoben) for the fruitful discussions on micro-scale testing.

References

[1] M.A. Meyers, P.-Y. Chen, A.Y.-M. Lin, Y. Seki, Biological materials: Structure and mechanical properties, Prog. Mater. Sci. 53 (2008) 1–206. https://doi.org/10.1016/j.pmatsci.2007.05.002.

[2] P. Fratzl, R. Weinkamer, Nature's hierarchical materials, Prog. Mater. Sci. 52 (2007) 1263–1334. https://doi.org/10.1016/j.pmatsci.2007.06.001.

[3] R.O. Ritchie, The conflicts between strength and toughness, Nat. Mater. 10 (2011) 817–822. https://doi.org/10.1038/nmat3115.

[4] U.G.K. Wegst, H. Bai, E. Saiz, A.P. Tomsia, R.O. Ritchie, Bioinspired structural materials, Nat. Mater. 14 (2015) 23–36.

[5] F. Bouville, Strong and tough nacre-like aluminas: Process–structure–performance relationships and position within the nacre-inspired composite landscape, J. Mater. Res. 35 (2020) 1076–1094. https://doi.org/10.1557/jmr.2019.418.

[6] A. Wat, J. in Lee, C.W. Ryu, B. Gludovatz, J. Kim, A.P. Tomsia, T. Ishikawa, J. Schmitz, A. Meyer, M. Alfreider, D. Kiener, E.S. Park, R.O. Ritchie, Bioinspired nacre-like alumina with a bulk-metallic glass-forming alloy as a compliant phase, Nat. Commun. 10 (2019) 961. https://doi.org/10.1038/s41467-019-08753-6.

[7] R. Bermejo, "Toward seashells under stress": Bioinspired concepts to design tough layered ceramic composites, J. Eur. Ceram. Soc. 37 (13) (2017) 3823–3839. https://doi.org/10.1016/j.jeurceramsoc.2017.04.041.

[8] M. Rao, J. Sanchez-Herencia, G. Beltz, R.M. McMeeking, F. Lange, Laminar ceramics that exhibit a threshold strength, Science 286 (1999) 102–105.

[9] Y. Chang, R. Bermejo, G. L. Messing, Improved Fracture Behavior of Alumina Microstructural Composites with Highly Textured Compressive Layers, J. Am. Ceram. Soc. 97 (11) (2014) 3643–3651. https://doi.org/10.1111/jace.13168.

[10] V.M. Sglavo, M. Paternoster, M. Bertoldi, Tailored Residual Stresses in High Reliability Alumina-Mullite Ceramic Laminates, J. Am. Ceram. Soc. 88 (10) (2005) 2826–2832. https://doi.org/10.1111/j.1551-2916.2005.00479.x.

[11] V.M. Sglavo, M. Bertoldi, Design and production of ceramic laminates with high mechanical resistance and reliability, Acta Mater. 54 (2006) 4929–4937. https://doi.org/10.1016/j.actamat.2006.06.019.

[12] M.E. Nordberg, E.L. Mochel, H.M. Garfinkel, J.S. Olcott, Strengthening by Ion Exchange, J. Am. Ceram. Soc. 47 (5) (1964) 215–219. https://doi.org/10.1111/j.1151-2916.1964.tb14399.x.

[13] D.J. Green, R. Tandon, V.M. Sglavo, Crack arrest and multiple cracking in glass through the use of designed residual stress profiles, Science 283 (5406) (1999) 1295–1297.

[14] M.N. Rahaman, Sintering of Ceramics, CRC Press, 2007.

[15] R. Pavlacka, R. Bermejo, Y. Chang, D.J. Green, G.L. Messing, Fracture Behavior of Layered Alumina Microstructural Composites with Highly Textured Layers, J. Am. Ceram. Soc. 96 (5) (2013) 1577–1585. https://doi.org/10.1111/jace.12292.

[16] R.J. Pavlacka, G.L. Messing, Processing and mechanical response of highly textured Al2O3, J. Eur. Ceram. Soc. 30 (14) (2010) 2917–2925. https://doi.org/10.1016/j.jeurceramsoc.2010.02.009.

[17] P.W. Hall, J.S. Swinnea, D. Kovar, Fracture Resistance of Highly Textured Alumina, J. Am. Ceram. Soc. 84 (7) (2001) 1514–1520. https://doi.org/10.1111/j.1151-2916.2001.tb00870.x.

[18] A.-K. Hofer, R. Walton, O. Ševeček, G.L. Messing, R. Bermejo, Design of damage tolerant and crack-free layered ceramics with textured microstructure, J. Eur. Ceram. Soc. 40 (2) (2020) 427–435. https://doi.org/10.1016/j.jeurceramsoc.2019.09.004.

[19] E. Feilden, T. Giovannini, N. Ni, C. Ferraro, E. Saiz, L. Vandeperre, F. Giuliani, Micromechanical strength of individual Al2O3 platelets, Scr. Mater. 131 (2017) 55–58. https://doi.org/10.1016/j.scriptamat.2017.01.008.

[20] R. Henry, H. Saad, A. Doitrand, S. Deville, S. Meille, Interface failure in nacre-like alumina, J. Eur. Ceram. Soc. 40 (13) (2020) 4694–4699. https://doi.org/10.1016/j.jeurceramsoc.2020.05.068.

[21] M.G. Mueller, V. Pejchal, G. Žagar, A. Singh, M. Cantoni, A. Mortensen, Fracture toughness testing of nanocrystalline alumina and fused quartz using chevron-notched microbeams, Acta Mater. 86 (2015) 385–395. https://doi.org/10.1016/j.actamat.2014.12.016.

[22] A.D. Norton, S. Falco, N. Young, J. Severs, R.I. Todd, Microcantilever investigation of fracture toughness and subcritical crack growth on the scale of the microstructure in Al_2O_3, J. Eur. Ceram. Soc. 35 (16) (2015) 4521–4533. https://doi.org/10.1016/j.jeurceramsoc.2015.08.023.

[23] S. Strobl, P. Supancic, T. Lube, R. Danzer, Surface crack in tension or in bending – A reassessment of the Newman and Raju formula in respect to fracture toughness measurements in brittle materials, J. Eur. Ceram. Soc. 32 (8) (2012) 1491–1501. https://doi.org/10.1016/j.jeurceramsoc.2012.01.011.

[24] F.K. Lotgering, Topotactical reactions with ferrimagnetic oxides having hexagonal crystal structures—I, J. Inorg. Nucl. Chem. 9 (1959) 113–123. https://doi.org/10.1016/0022-1902(59)80070-1.

[25] M. Lu, H. Russell, H. Huang, Fracture strength characterization of protective intermetallic coatings on AZ91E Mg alloys using FIB-machined microcantilever bending technique, J. Mater. Res. 30 (2015) 1678–1685. https://doi.org/10.1557/jmr.2015.104.

[26] T. Csanádi, M. Vojtko, J. Dusza, Deformation and fracture of WC grains and grain boundaries in a WC-Co hardmetal during microcantilever bending tests, Int. J. Refract. Met. Hard Mater. 87 (2020) 105163. https://doi.org/10.1016/j.ijrmhm.2019.105163.

[27] H. Chan, S.G. Roberts, J. Gong, Micro-scale fracture experiments on zirconium hydrides and phase boundaries, J. Nucl. Mater. 475 (2016) 105–112. https://doi.org/10.1016/j.jnucmat.2016.03.026.

[28] D. Di Maio, S.G. Roberts, Measuring fracture toughness of coatings using focused-ion-beam-machined microbeams, J. Mater. Res. 20 (2005) 299–302. https://doi.org/10.1557/JMR.2005.0048.

[29] https://www.ansys.com/ (accessed 26 May 2021).

[30] Y. Sun, H. Xie, L. Liu, Q. Kou, S. Zhang, B. Yang, W. Cao, Y. Chang, Enhanced mechanical properties in ceramic multilayer composites through integrating crystallographic texture and second-phase toughening, Ceram. Int. 47 (22) (2021) 31222–31228. https://doi.org/10.1016/j.ceramint.2021.07.298.

[31] M. Zhang, Y. Chang, R. Bermejo, G. Jiang, Y. Sun, J. Wu, B. Yang, W. Cao, Improved fracture behavior and mechanical properties of alumina textured ceramics, Mater. Lett. 221 (2018) 252–255. https://doi.org/10.1016/j.matlet.2018.03.123.

[32] J.P. Best, J. Zechner, I. Shorubalko, J.V. Oboňa, J. Wehrs, M. Morstein, J. Michler, A comparison of three different notching ions for small-scale fracture toughness measurement, Scr. Mater. 112 (2016) 71–74. https://doi.org/10.1016/j.scriptamat.2015.09.014.

[33] F. Konstantiniuk, M. Tkadletz, C. Kainz, C. Czettl, N. Schalk, Mechanical properties of single and polycrystalline α-Al_2O_3 coatings grown by chemical vapor deposition, Surf. Coat. Technol. 410 (2021) 126959. https://doi.org/10.1016/j.surfcoat.2021.126959.

[34] M. Iwasa, R.C. Bradt, Fracture toughness of single-crystal alumina, in: Advances in ceramics, pp. 767–779.

[35] S.M. Wiederhorn, Fracture of Sapphire, J. Am. Ceram. Soc. 52 (9) (1969) 485–491. https://doi.org/10.1111/j.1151-2916.1969.tb09199.x.

[36] Q. Ma, D.R. Clarke, Piezospectroscopic Determination of Residual Stresses in Polycrystalline Alumina, J. Am. Ceram. Soc. 77 (2) (1994) 298–302. https://doi.org/10.1111/j.1151-2916.1994.tb06996.x.

[37] V.R. Vedula, S.J. Glass, D.M. Saylor, G.S. Rohrer, W.C. Carter, S.A. Langer, E.R. Fuller Jr., Residual-Stress Predictions in Polycrystalline Alumina, J. Am. Ceram. Soc. 84 (12) (2001) 2947–2954. https://doi.org/10.1111/j.1151-2916.2001.tb01119.x.

[38] J. Schlacher, A. Jabr, A.-K. Hofer, R. Bermejo, Contact damage tolerance of alumina-based layered ceramics with tailored microstructures, J. Am. Ceram. Soc. 105 (6) (2022) 4387–4399. https://doi.org/10.1111/jace.18389.

Supplementary information

for

Micro-scale fracture toughness of textured alumina ceramics

Josef Schlacher[1*], Tamás Csanádi[2], Marek Vojtko[2], Roman Papšík[1], Raul Bermejo[1]

[1] Department of Materials Science, Montanuniversitaet Leoben, Franz Josef-Strasse 18, A-8700, Leoben, Austria

[2] Institute of Materials Research, Slovak Academy of Sciences, Watsonova 47, 04353 Košice, Slovak Republic

*Corresponding author's email: josef.schlacher@unileoben.ac.at

Supplementary Table S1: The geometrical parameters of the microcantilevers tested together with the measured load of fracture and calculated fracture toughness values for grains and grain boundaries, respectively.

Cantilever direction	Specimen	Cantilever dimensions (cp. Fig 2) [µm]							Fracture load, F_{max} [mN]	Fracture toughness, K_{Ic} [MPam$^{1/2}$]
		L	a	b	m_a	x_1	x_2	α		
Grain	1	15.80	3.24	2.31	1.37	2.81	1.70	0.32	1.41	3.20
	2	21.14	4.08	2.43	1.77	3.70	2.00	0.69	1.03	2.97
	3	18.98	4.49	2.31	1.74	3.67	2.20	0.59	1.60	3.56
	4	14.79	1.89	1.59	1.04	2.23	1.60	0.21	0.53	3.22
	5	16.20	2.67	2.40	1.12	3.87	1.80	0.23	1.46	3.35
Grain boundary	1	9.26	2.54	1.80	1.12	1.98	2.50	0.34	1.08	2.17
	2	9.11	1.62	1.31	1.03	2.18	1.60	0.32	0.46	2.57
	3	23.21	5.08	2.52	1.94	8.49	2.80	0.27	2.29	2.28
	4	12.41	3.50	2.02	1.38	0.89	2.00	0.39	0.85	1.98
	5	13.45	3.52	1.84	1.47	0.46	2.20	0.12	1.58	2.52

Publication B

Contact damage tolerance of alumina-based layered ceramics with tailored microstructures

J. Schlacher, A. Jabr, A.-K. Hofer, R. Bermejo

J. Am. Ceram. Soc. 105 (6) (2022) 4387–4399

https://doi.org/10.1111/jace.18389

Contact damage tolerance of alumina-based layered ceramics with tailored microstructures

Josef Schlacher[1], Abdullah Jabr[1], Anna-Katharina Hofer, Raul Bermejo[*]

Department of Materials Science, Montanuniversitaet Leoben, Franz Josef-Strasse 18, A-8700, Leoben, Austria

*Corresponding author's email: raul.bermejo@unileoben.ac.at

[1] Authors contributed equally to this work.

Abstract

This work demonstrates how to enhance contact damage resistance of alumina-based ceramics combining tailored microstructures in a multilayer architecture. The multilayer system designed with textured alumina layers under compressive residual stresses embedded between alumina-zirconia layers was investigated under Hertzian contact loading and compared to the corresponding monolithic reference materials. Critical forces for crack initiation under spherical contact were detected through an acoustic emission system. Damage was assessed by combining cross-section polishing and ion-slicing techniques. It was found that a textured microstructure can accommodate the damage below the surface by shear-driven, quasi-plastic deformation instead of the classical Hertzian cone cracking observed in equiaxed alumina. In the multilayer system, a combination of both mechanisms, namely Hertzian cone cracking on the top (equiaxed) surface layer and quasi-plastic deformation within the embedded textured layer, was identified. Further propagation of cone cracks at higher loads was hindered and/or deflected owed to the combined action of the textured microstructure and compressive residual stresses. These findings demonstrate the potential of embedding textured layers as a strategy to enhance the contact damage tolerance in alumina ceramics.

Keywords: Alumina; Multilayers; Hertzian indentation; Textured microstructure, Residual stresses

1. Introduction

Advanced ceramics have been established as materials of choice for many demanding applications. In comparison to metals and polymers, some advantageous properties of ceramics, such as oxidation and corrosion resistance, high temperature stability, high hardness and wear

resistance, stiffness, biocompatibility together with interesting functional properties, are the driving factors for the high interest in developing ceramic materials [1,2]. However, the inherent brittleness of ceramics (low fracture toughness) along with strength variability are major concerns for safety and reliability issues. Failure of ceramic parts is often associated with the (unstable) propagation of cracks, upon applied mechanical loading, initiated from microstructural defects distributed within or at the surface of components. These flaws may be introduced at the processing step (e.g. pores, agglomerates), during machining of the parts (surface roughness, scratches) or in service conditions during the lifetime of the component [3,4]. In this regard, many strategies have been adopted for controlling and reducing the size of critical defects in ceramics, using for instance colloidal processing [5], or eliminating critical flaws by means of proof testing [4]. However, avoiding failure related to post-processing defects during handling and in service remains a difficult challenge [6]. In this regard, a more prominent strategy has been attempted, which aims to control the propagation of cracks by taking advantage of energy-dissipating toughening mechanisms occurring during the crack propagation events. The so-called "damage tolerant" behavior has been reported in several alumina-based layered ceramic systems designed with embedded (protective) layers under in-plane compressive residual stress [7–12]. In addition, tailoring the microstructure of the protective layers (following the "brick-and-mortar" approach used in bio-inspired materials [13]) has significantly enhanced the fracture energy of the system. For instance, texturing the microstructure by aligning platelets parallel to the layer plane has proven to have a positive impact on the mechanical properties of layered ceramic architectures [14,15]. The effect of residual stresses, degree of texture, as well as layer distribution within the multilayer design on the damage tolerance of the ceramic parts has been thoroughly investigated under different loading conditions, such as bending, thermal shock or cycling loading [16]. An important question is how effective such layered design may be against contact loading.

Blunt contact loading, first studied by Hertz [17], is one of the main sources of failure in advanced ceramics during in-service conditions [3]. In some situations, sudden failure occurs due to the (unstable) propagation of contact cracks, and in some cases failure of ceramic components may also ensue as a consequence of the strength degradation caused by contact induced damage [18]. In homogeneous, polycrystalline fine-grained ceramics and in glasses, classical Hertzian ring and cone cracking is the typical damage pattern under spherical loading [19–21]. Due to the fact that such macroscopic cracking significantly impairs the strength of ceramic components, much research has been dedicated to restrict deleterious cone crack propagations for increasing their contact damage resistance. One strategy is to introduce "shear-sensitive" microstructural

elements within the ceramic material, so that the response of the material to the contact loading scenario leads to subsurface shear faulting rather than cone crack formation starting from the surface [19]. The successful transition from brittle cone cracking to the quasi-plastic damage mode has been reported in ceramics with controlled microstructures, i.e. grain coarsening [22,23] or increasing the level of porosity [24], as well as in heterogeneous ceramics containing second phases with weak interface boundaries. Few examples are (i) mica-platelets within a glass matrix [25], (ii) graphene nanofillers added to silicon carbide [26], (iii) layered heterogeneous alumina designed with calcium-hexaluminate interfaces [27,28], or (iv) layered brittle coating systems with enhanced fracture resistance [29,30].

In this work, we explore the contact damage resistance of novel layered ceramics designed with embedded layers with internal compressive stresses and textured microstructure. The aim of this work is to investigate the effect of texturing on the response of layered alumina ceramics under spherical contact loading scenario. It is hypothesized that the combination of shear-faulting driven micro-failures at the weak basal interfaces of the textured grains with the potential of the in-plane compressive stresses in arresting the propagation of cone cracks may significantly enhance the damage tolerance of the ceramic system. The contact damage behavior is first investigated and compared in monolithic alumina-based samples designed with and without textured microstructures, respectively. Initiation of ring crack is detected by using an acoustic emission system (AE) and confirmed by using polarized light microscopy. Moreover, the underlying damage mechanisms are explored by using cross-sectioning together with the ion-slicing techniques. AE is used for measuring the critical crack initiation forces and the data are analyzed and classified for the different damage mechanisms. The critical crack initiation forces as well as the calculated maximum tensile stresses are analyzed in the framework of Weibull statistics.

2. Experimental

2.1. Materials of study and samples

Three different samples were fabricated using the tape casting technique: (i) monolithic samples with equiaxed microstructure (EA) containing alumina and 5 vol.% tetragonal zirconia, (ii) monolithic textured alumina (TA) consisting of elongated alumina grains aligned in casting direction, and (iii) a multilayer architecture with alternating EA and TA-layers designed with tailored in-plane residual stresses.

The main powder used for fabrication of monolithic as well as multilayer composites was high-purity α-Al_2O_3 (AKP-50, Sumitomo Chemicals, Tokyo, Japan) with particle size distribution from 0.09 µm to 0.34 µm and a mean particle size of d_{50} = 0.20 µm. To prevent abnormal grain growth in EA, 5 vol% of 3 mol% yttria stabilized zirconia with a mean particle size of d_{50} = 0.04 µm was added to the alumina-powder. In the case of TA, 5 vol% single crystal alumina platelets (Rona Flair® White Sapphire, EMD Performance Materials Corp., Darmstadt, Germany) with a diameter of 5–16 µm and a thickness of ~0.1 µm were used as templates together with a 0.25 wt% dopant concentration in respect to the alumina powder ($CaO:SiO_2$ = 1:1) for enhancing the templated grain growth (TGG) [31]. All slurries contained an acrylic binder system. After slurry preparation and tape casting process, the specific tapes (EA and TA) were cut and stacked according to the desired design. Subsequently, uniaxial pressing (8 MPa), isostatic lamination (20 MPa), binder burn out (450 °C) and cold isostatic pressing (200 MPa) of the stacked plates were performed. Afterwards, the plates were sintered at 1550°C for 4 h and the samples of study were prepared for testing. More details about slurry compositions and the processing of the layered alumina architectures can be found in previous work [31].

To study the microstructure of the monolithic EA, TA and the laminate, the samples were polished on the side surface up to 1µm mirror finish using a Struers Pedemax-2 equipment (Struers Tech, DK2610 Copenhagen, Denmark) and thermally etched at 1450°C for 30 min. Subsequently, the polished side surfaces were gold-coated using an Agrar Sputter coater. The images of the microstructures taken using a scanning electron microscope (JEOL JCM-6000Plus, Neoscope™, JEOL Ltd., Tokyo, Japan) can be seen in Fig. 1. The microstructure of EA shows alumina grains with a size of ~2 µm and rather fine-grained zirconia (~0.5 µm) located at the triple points (see Fig. 1a). Figure 1b shows the TA microstructure composing highly elongated alumina grains with length of ~20 µm and thicknesses of ~5 µm. The multilayer sample exhibits a strong EA/TA interface, as illustrated in Fig. 1c.

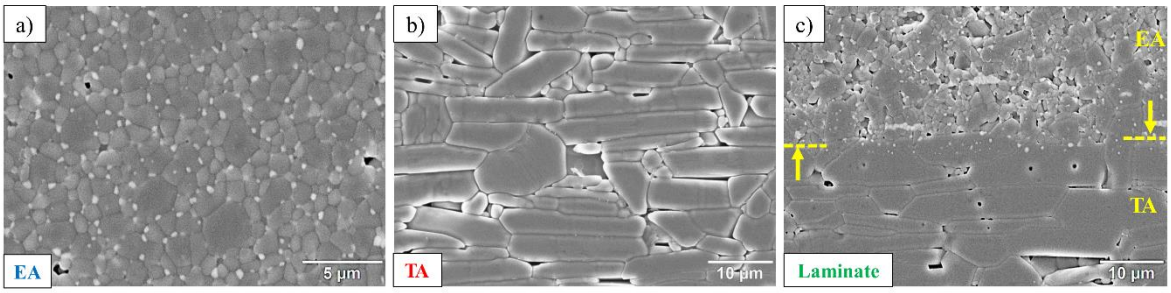

Fig. 1: Microstructure of (a) monolithic equiaxed microstructure (EA), (b) monolithic textured alumina (TA) and (c) multilayer composite samples. The strong EA/TA-interface of the laminate is indicated by yellow arrows.

The testing sample geometries of the prismatic bend bars prepared from the tapes were ~25 × 3 × 3 mm^3 for monolithic (EA, TA) and ~25 × 4 × 3.5 mm^3 for the layered architecture, respectively. The top surfaces were ground with D15 finish on both sides to guarantee fully flat samples for testing. Subsequently, the testing surface (one of the top surfaces) was polished up to 1 µm mirror finish using a Struers Pedemax-2 equipment.

The layered ceramic architecture consisted of two TA layers embedded within three EA alumina-zirconia layers following the sequence EA/TA/EA/TA/EA. After grinding and polishing of the outer-most EA layers, the final thickness of the individual layers was ~110 µm/300 µm/2520 µm/300 µm/110 µm, which corresponds to a volume ratio between the materials of V_{EA}/V_{TA} ~ 5.

The analytical estimation of the in-plane residual stresses within the alternating layers of the multilayer architecture can be obtained through the following equation [32]:

$$\sigma_{res,n} = \frac{E_n}{1-\nu_n}(\bar{\alpha} - \alpha_n)\Delta T \qquad (1)$$

where ν_n is the Poisson's ratio (~ 0.22 for EA and TA), E_n is the Young's modulus (~380 GPa for both EA and TA [31]), α_n is the coefficient of thermal expansion (8.2 × 10^{-6} K^{-1} and 7.8 × 10^{-6} K^{-1} for EA and TA, respectively [31]) of the n^{th} layer of each contributing material. The temperature difference is $\Delta T = T_0 - T_{ref}$, where T_0 is the room temperature and T_{ref} is the reference temperature, above which the material is assumed to be free of residual stresses (so-called stress-free temperature). In our work, T_{ref} is taken as ~1500°C, as estimated for alumina/zirconia ceramics elsewhere [33]. The average coefficient of thermal expansion for the layered system was calculated according to the following equation [32]:

$$\bar{\alpha} = \left. \sum_{n=1}^{N} \frac{E_n t_n \alpha_n}{1-\nu_n} \right/ \sum_{n=1}^{N} \frac{E_n t_n}{1-\nu_n} \tag{2}$$

where t_n is the corresponding nth layer thickness of the multilayer composite.

In the multilayer architecture of study, the in-plane residual stresses in the EA and TA layers resulted in ~ +50 MPa and ~ −240 MPa, respectively.

2.2. Testing procedure

Hertzian indentation tests were performed in ambient conditions (25°C and ~25% relative humidity) using a universal testing machine (MIDI 10-5/6x11, Messphysik, Fürstenfeld, Austria) with a load cell of 25 kN. A tungsten-carbide sphere (94WC-6Co, Kugel Pompel®, Austria) with a diameter of 4 mm was used as indenter. The EA, TA and multilayer prismatic bar-shaped samples are schematically represented in Fig. 2. We caution the reader that the contact region between sphere and specimen is approx. 10 times smaller than the width of the bar, and thus no influence of free edges on the contact stress distribution may be expected.

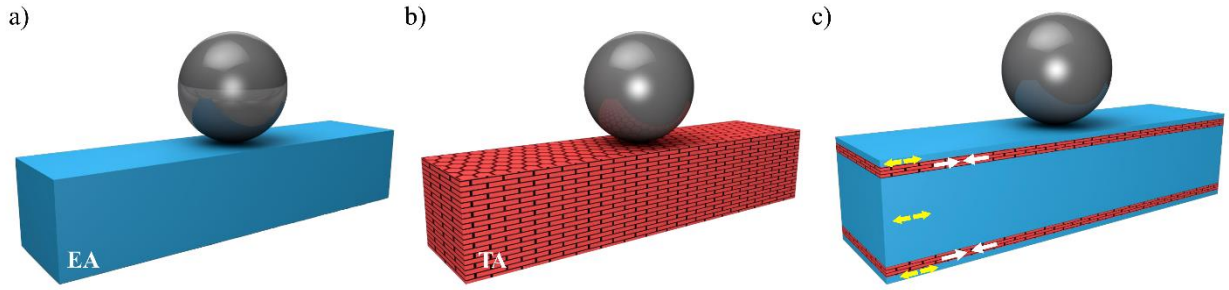

Fig. 2: Schematic of the contact testing setup for the three samples: (a) equiaxed microstructure (EA), (b) textured alumina (TA) and (c) multilayer. In the TA-specimens, the top surface under contact loading was set parallel to the basal planes of the textured microstructure (the textured grains are illustrated as "bricks"). In the multilayer architecture, the in-plane tensile and compressive residual stresses in the EA and TA regions are indicated by yellow and white arrows, respectively.

To detect acoustic events during the indentation cycle, AE sensors (VS150-M, Vallen Systeme GmbH, Germany) were attached onto the indenter as well as on the sample holder. This AE

system allowed the accurate determination of the critical forces responsible for the initiation event corresponding to the first crack. A threshold amplitude limit of 21.9 dB was found to be sufficient to eliminate background noise. All the contact tests were carried out using a pre-load of 10 N, a displacement rate of 0.01 mm/min and a dwell time of 10 s at the maximum load of the cycle. At least 20 spherical indentations per sample were performed to detect the crack initiation force. Depending on the type of tests, this maximum load was either deliberately selected as specific force (800, 1000, 1500 and 2000 N) for studying the crack propagation or limited by the crack initiation force as detected by the AE system to investigate the onset of cracking. In the latter case, the loading cycle was interrupted by the main unit of the AE system right after detecting the first crack initiation event. To avoid crack interactions, a distance of 2 mm between imprints within a sample was set by using a precision cross-head table. All the imprints were performed on the top surface of the stacked samples (see Fig. 2).

2.3. Damage observation

In order to study the surface damage, liquid dye penetrant (Diffu-Therm® red penetrant) was applied on all the tested sample surfaces for 24 h. The surface cracks were observed with an optical microscope (Nikon ECLIPSE LV100ND, Japan) under polarizing and non-polarizing mode. In particular, the polarizing light microscopy technique was exploited in this study for visualizing surface ring cracks at first formation stage, which otherwise would remain invisible in non-polarizing mode. To measure the depth profile of the indents as well as to visualize the corresponding surface depression in 3D, a laser scanning confocal microscope (Keyence VK-X1000, Belgium) was employed.

In the case of sub-surface damage investigations, the samples were cross-sectioned by grinding and polishing starting from a side surface to the region of interest (mid-plane of the indent). Subsurface damage was observed using the optical microscope with and without polarized light. Furthermore, to study the damage patterns in detail, while avoiding possible mechanically induced damage of the zones due to polishing, ion-Slicing technique (Hitachi ArBlade 5000) was employed and observations were conducted using scanning Electron Microscopy (Tescan Clara).

2.4. Evaluation of data

The critical forces for crack initiation as well as their corresponding maximum tensile stresses (first principal radial stress) were analyzed according to contact Hertzian theory, as follows [34]:

$$\sigma_{max} = (1 - 2\nu)\frac{P}{2\pi a^2} \tag{3}$$

where ν is the Poisson's ratio of the sample (~0.22 for alumina), P is the indentation load (measured crack initiation load) and a is the corresponding contact radius. This contact radius a is defined as [34]:

$$a = \left(\frac{3}{4}\frac{PR}{E^*}\right)^{1/3} \tag{4}$$

where R is the radius of the indenter sphere, and E^* is the combined elastic modulus, which is given as follows [34]:

$$\frac{1}{E^*} = \frac{1 - \nu^2}{E} + \frac{1 - \nu_i{}^2}{E_i} \tag{5}$$

In this relation, ν_i is the Poisson's ratio of the indenter (assumed to be 0.21), E and E_i are the Young's moduli of the sample (~380 GPa [31]) and the indenter (~650 GPa [35]), respectively.

The crack initiation forces and the corresponding crack initiation stresses were analyzed in the framework of Weibull statistics [36,37]. According to Equations (3) and (4), the maximum tensile stresses, σ_{max}, are in correlation with the indentation load, P, as $\sigma_{max} \propto P^{1/3}$.

3. Results and discussion

3.1. Identification of damage mechanisms

Figure 3 shows a Hertzian ring crack formed on the monolithic EA-system. Under an optical microscope with non-polarized mode the ring crack cannot be visualized (see Fig. 3a). However, using polarized light the formation of ring cracks can be clearly verified (see Fig. 3b). It may be hypothesized that at low ring crack initiation forces (RCIF) no debris on the crack after indentation occurs and the cracks opening remains rather closed, which makes it barely observable without using special optical techniques. The typical Hertzian full-ring crack (indicated by white arrows) on the EA-sample surface is associated with the first detected ring

crack formation signal, after which the loading cycle was interrupted. It is worth indicating that in some cases either partial ring cracking or even simultaneous formation of ring and cone cracking were observed at the RCIF.

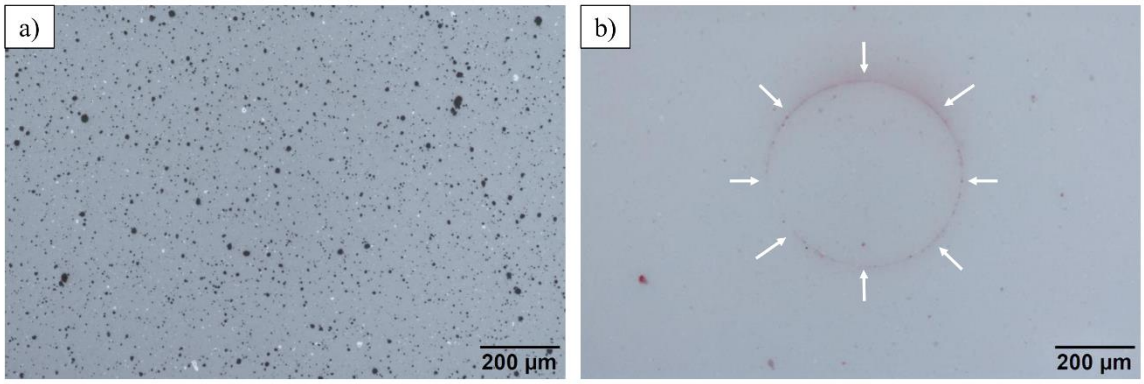

Fig. 3: Top view of a ring crack loaded until the first acoustic-emission signal (ring crack initiation force (RCIF) ~850 N) was recorded on an equiaxed microstructure (EA) sample in (a) non-polarized mode, where no ring crack is visible, and (b) polarized mode, where the crack (indicated by white arrows) is detectable.

Figure 4 shows observed surface damages on the different ceramic architectures after Hertzian indentation tests loaded at moderate loads (up to 1000 N). Figure 4a shows surface damage on EA after indenting at a maximum load of 800 N. As can be seen, the red halo-like reflection surrounding the ring crack (Fig. 4a, top) can be ascribed to the presence of cone crack as evidenced through cross-sectioning of the sample (see Fig 4a, bottom). It is thus demonstrated that damage initiation on the fine-grained polycrystalline EA material of study agrees with classical Hertzian cone cracking as has been observed in other glasses and ceramics [20,21,38]. It is worth emphasizing that this halo-like feature can only be observed due to the reflections of polarized light from the dye penetrant in shallow regions. Using the polarized-light technique is a novel way to make either ring cracks visible or even to prove whether cone cracks may be formed or not, without a further need of sample cross-sectioning.

Figure 4b shows a representative surface imprint on the TA material indented up to 1000 N. Apparently, no ring crack formation can be observed, what suggests a different damage mechanism during Hertzian indentation. In this regard, the image indicates a rather crater-like pattern (surface depression) after indenting associated with a quasi-plastic deformation behavior of the textured microstructure.

Figure 4c shows a representative surface imprint on the multilayer material (with the top EA indented layer). A concurrent ring and cone cracking formation at first detected RCIF (~645 N) is revealed on the multilayer architecture. Due to the fact that the outer region of the multilayer composite is EA, the damage pattern agrees with classical ring and cone cracking as found on the monolithic EA-specimens.

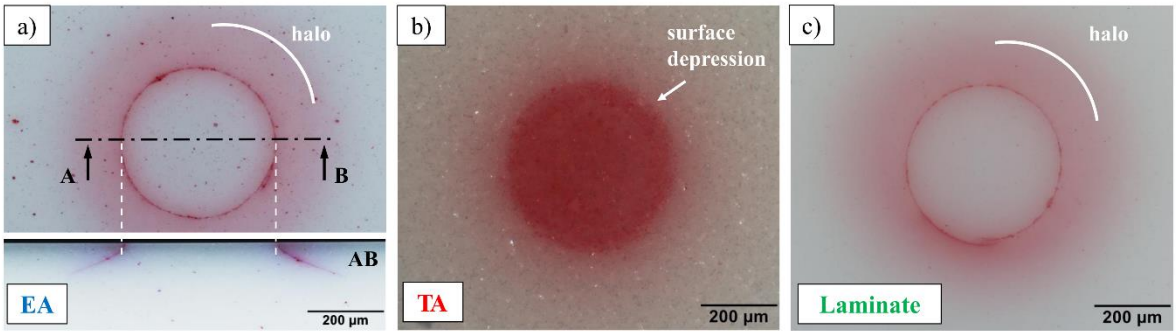

Fig. 4: Surface damages observed on different samples at moderate loads (up to 1000 N): (a) equiaxed microstructure (EA) – formation of ring and cone crack (top) together with section view (bottom), loaded until 800 N. It is observable that the red halo-like region in top view can be associated with the cone (section view). (b) Textured alumina (TA) – showing surface depression on basal surface after loading to 1000 N. (c) Laminate – concurrent formation of ring and cone cracks (ring crack initiation forces (RCIF) ~645 N); the cone crack is indicated by the surrounded halo-like region.

For a better understanding of the imprint morphology, confocal images were taken on selected imprints at higher loads. Figure 5 shows 3D confocal images of indents made with a maximum load of 2000 N on EA, TA and the laminate samples, together with their depth profiles.

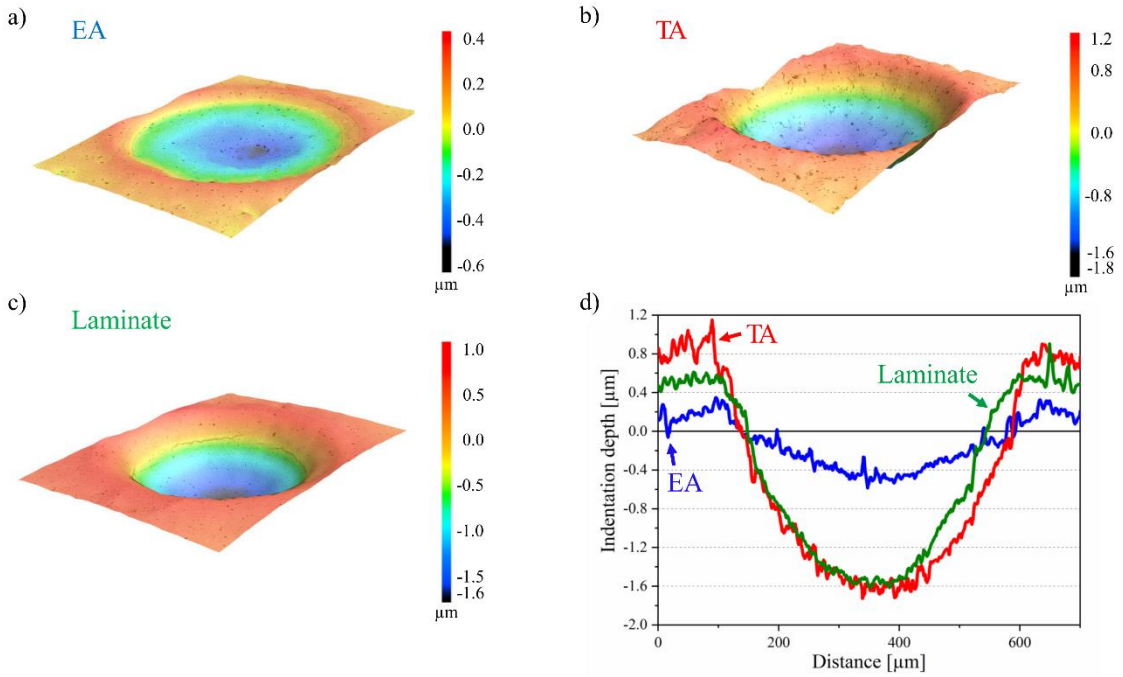

Fig. 5: 3D reconstructions from confocal measurements of imprints performed on (a) equiaxed microstructure (EA), (b) textured alumina (TA), and (c) laminate samples. (d) Depth profiles measured at the mid-plane of the indents. The indentations were made with a maximum load of 2000 N.

Comparison between the confocal image of EA (Fig. 5a) with those of TA (Fig. 5b) and the laminate sample (Fig. 5c) indicates that the textured microstructure of monolithic TA as well as the embedded TA regions within the laminate favors surface depression by its quasi-plastic response. The depth profile (Fig. 5d) reveals that in EA the surface depression is rather low with its maximum indentation depth of ~0.6 µm of the dale. Furthermore, it can be seen that only a relatively small pile-up of about 0.4 µm occurs. In contrast to that, TA shows large pile-ups (~0.8–1.2 µm) and a relatively high maximal indentation depth of ~1.7 µm. Interestingly, the laminate shows similar values of pile-up (0.6–0.9 µm) and maximal depth of surface depression (~1.6 µm), as compared to those of TA. Embedding of TA layers in the laminates may lead to the hypothesis of combined damage zones making the mechanisms more complicated to describe (combined classical Hertzian ring and cone cracking together with sub-surface shearing) by only showing surface damages. Therefore, cross-sectioning was used to reveal the subsurface damage zones of the monolithic as well as multilayer samples.

Figure 6 reveals typical subsurface damage zones of EA, TA and the multilayer after indentation with a maximum load of 1500 N, recorded in non-polarized (left) and polarized

mode (right). Figure 6a shows a well-developed cone crack found on the cross-section of the EA sample. Since the applied load of 1500 N is approx. 70% higher than the measured RCIF (~875 N for this indent), the extending cone crack shows a final depth of ~110 µm. In contrast to that, the cross-section view of TA shows no evidence of deleterious cone cracks (see Fig. 6b); however, a quasi-plastic damage zone is clearly visible. Especially, the cone cracks are best observable using polarized light microscopy, whereas the quasi-plastic deformation zones can be visualized using non-polarized light. Research done on the nature of quasi-plastic damage has reported the presence of distributed shear-fault cracks at the interface boundaries of heterogeneous alumina/calcium-hexaluminate [27,28] or at the weak interface between mica-platelets and glass-matrix [25]. Furthermore, the quasi-plastic damage modes can be controlled by using coarser microstructures [22,23] or higher amount of porosities [24] and by adding specific fillers, that is, graphene platelets to silicon carbide as in the study of Belmonte et. al. [26]. In our work, the subsurface quasi-plastic damage zones within TA are a result of shear-faulting driven micro-failures at the weak basal-interfaces of the textured microstructures. However, the cross-sectioning by using a polishing procedure leads to grain pull-outs and the subsurface damage zones are hardly observable. Most of the literature works mentioned above take advantage of the "bonded-interface" observations to reveal the origin of sub-surface damage zones [19,22–24,27]. In our work, a novel approach was attempted exposing ion-sliced regions aiming to explain the origin of quasi-plasticity within TA samples. As comparison, the ion-sliced image of the cone crack in the EA-sample is shown in Fig. 7a. Figure 7b shows an ion-sliced region of TA without the subsurface deformation zone (reference position). It can be seen that this region is free from micro-failures, showing only the natural porosity of TA. In contrast to that, Fig. 7c reveals the region where the maximum shear-sliding mechanisms take place. Micro-cracks extended along the weak basal planes of the textured grains (indicated by yellow arrows) are evident, consistent with the nature of quasi-plasticity prominent in the TA sample. The center of the quasi-plastic region (depth of ~100µm) is in agreement with the zone where the highest maximum shear stress occurs (~0.5 × a) [19]. Furthermore, a horizontal crack emanating from the elastic/plastic interface, induced during unloading, along the basal planes is visible (blue arrows in Fig. 6b).

As can be seen in Fig. 6c, both damage mechanisms, classical cone cracking in the outer EA-region and quasi-plastic deformation within the embedded TA-layer are conspicuous in the multilayer sample. The quasi-plastic deformation zone in the TA-layer is similar to that of the monolithic TA sample (see Fig. 6b), indicating the same damage mechanism of intergranular micro-failures. Furthermore, a notable deflection of the cone crack path at the interface EA/TA is paramount to mention, as shown in the work of Chlup et al. [39], where they studied the

deflection of Vickers-indentation cracks on dissimilar alumina-zirconia laminates. The crack deflection angles (measured in respect to the horizontal sample edge) at the interfaces of our multilayer systems were measured as <15°. Beside the crack deflection due to the dissimilar materials in the multilayer sample, further contribution from microstructural deflections along the weak basal-planes of the TA-grains is predominant. These effects cause the cone crack to deviate from maximum tensile stress trajectories induced during spherical indentation and thus limiting its maximal depth (~120 µm for this case). Again, horizontal cracks in the TA-region of the multilayer can be seen (indicated with yellow arrows in Fig. 6c).

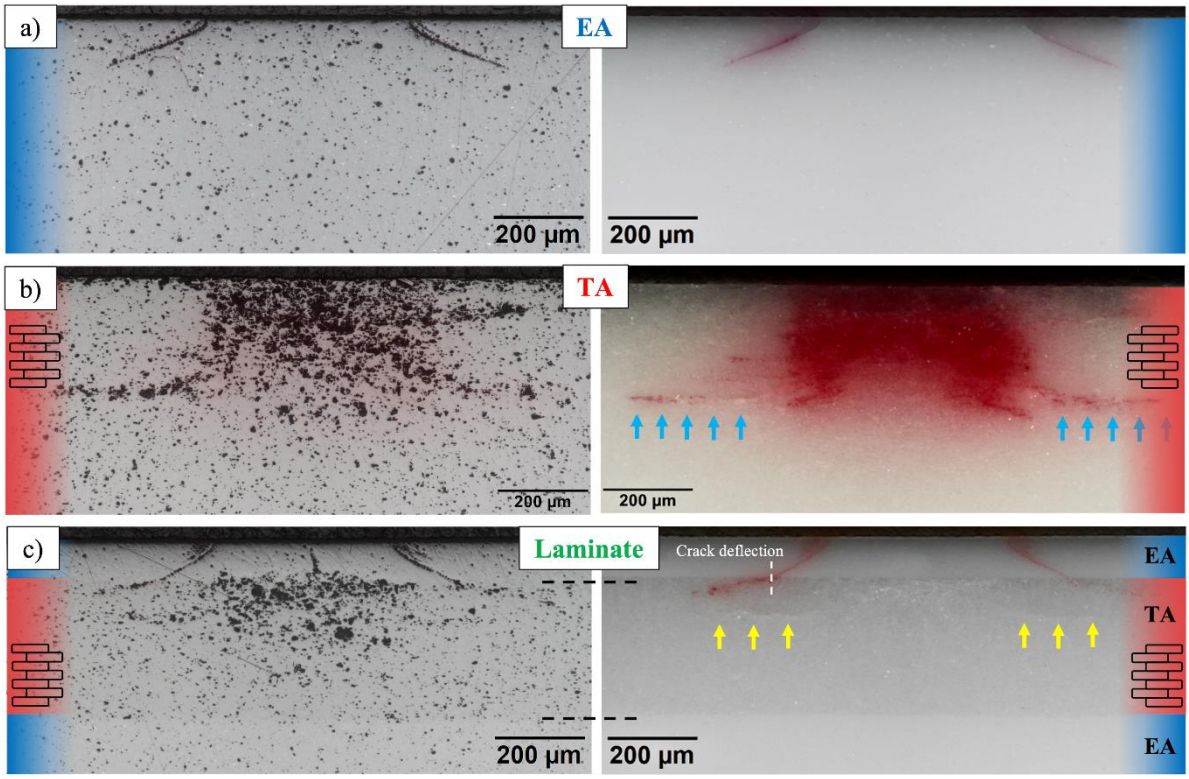

Fig. 6: Subsurface damage zones of (a) equiaxed microstructure (EA), (b) textured alumina (TA) and (c) multilayer architecture after indenting at a maximum load of 1500 N. The left and the right side show images taken in non-polarized and polarized mode, respectively. Arrows indicate horizontal cracks.

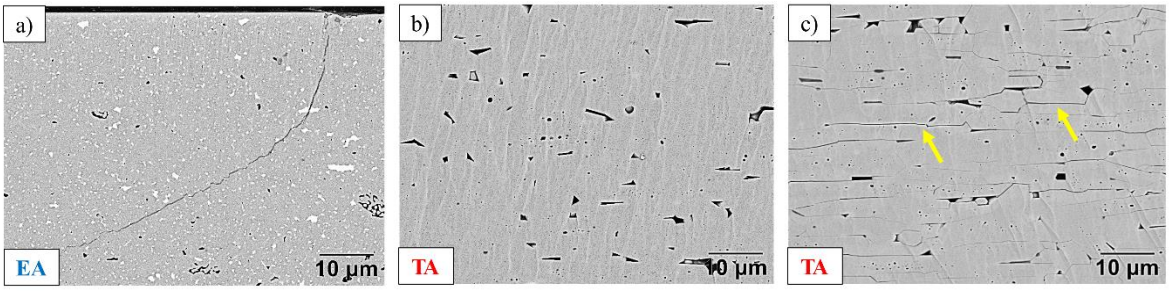

Fig. 7: Ion-sliced images of (a) cone crack in equiaxed microstructure (EA) (load of 1500 N), (b) damage-free zone in textured alumina (TA) (unloaded), and (c) quasi-plastic damage zone in TA (1500 N).

In order to study the propagation of cone cracks in the multilayer architecture, higher loads (2000 N) were applied in selected samples. Figure 8 shows the subsurface damage in the laminate, compared to the EA-sample. Both images were taken in polarizing-light mode in order to reveal the final crack depth after indenting. The final depth of the cone crack in EA loaded at 2000 N is ~200 µm (Fig. 8a), which is ~90 µm longer than the cone at 1500 N, indicating stable crack growth during loading.

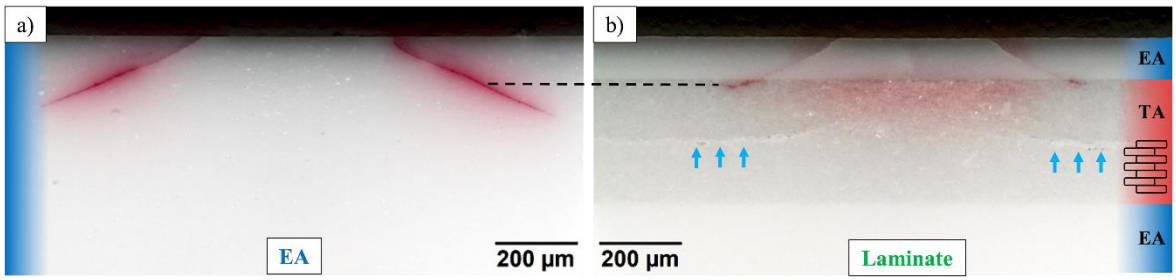

Fig. 8: Cross-sections of (a) equiaxed microstructure (EA) and (b) the multi-material system loaded with a maximum load of 2000 N. The dashed line indicates that the maximum depth of the cone crack in the EA sample is larger than that of the multilayer sample.

As can be seen in Fig. 8b, the quasi-plastic damage zone is expanded and the above-mentioned horizontal cracks within the TA-region are more extended (indicated by blue arrows). However, the final depth of the cone crack was measured again ~120 µm, indicating that the cone crack is not growing with increasing load which concurs with the explanation of cone-crack deviation from the trajectory of maximum stresses. Comparing the final cone crack length of ~200 µm

within the monolithic EA with that of ~120 µm within the EA-region of the multilayer architecture demonstrates the exceptional damage tolerance of multilayer systems with tailored microstructures. In our design approach three beneficial mechanisms can be achieved, as can be confirmed by exposing ion-sliced region within the multilayer sample (Fig. 9): (i) absorbing contact damage induced energy within the internal TA layer by micro-crack formation (Fig. 9c), (ii) deflection of the cone crack at the EA/TA interfaces, and (iii) microstructural crack deflection at the weak basal interfaces of the aligned textured grains, which favors the rather horizontally crack propagation in a step-like fashion through the embedded TA-region, as can be seen in Fig. 9b. The above-mentioned horizontal crack within the TA region is revealed in Fig. 9d. For the sake of comparison, the cone crack in the EA region of the laminate, similar to that in monolithic EA, is shown in Fig. 9a. The combination of these mechanisms may alleviate deleterious effects associated with cone cracking by limiting its final crack depth regardless of the indenting load.

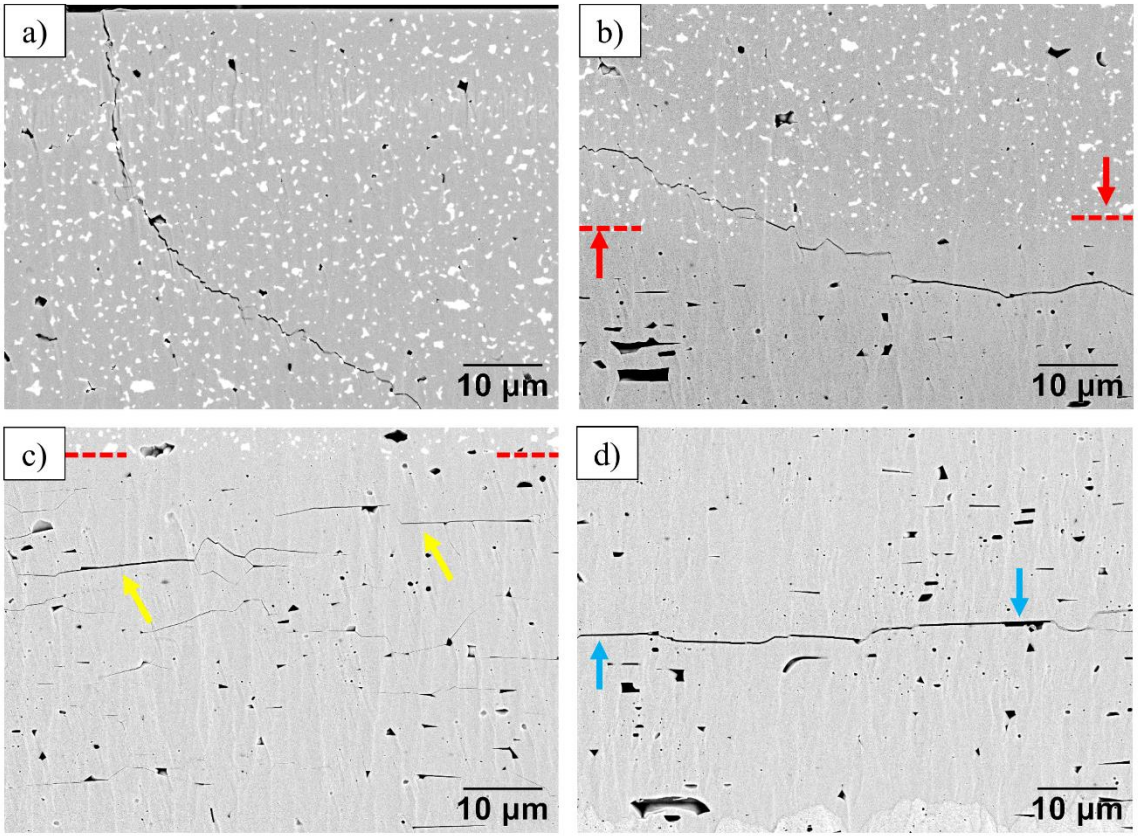

Fig. 9: Damage patterns of the laminate exposed by ion-slicing technique (loaded with 2000 N): (a) cone crack in the equiaxed microstructure (EA)-region, (b) deflection of the cone crack at the EA/textured alumina (TA)-interface (interface is indicated by red arrows), (c) quasi-plastic damage zone (micro-cracks are designated by yellow arrows), and (d) horizontal crack (indicated by blue arrows) in the TA-region of the multi-material system.

3.2 Assessment of damage

The measured ring crack radius, a_c, as well as the calculated contact radius a (evaluated according to Equation (4)), of the EA and the laminate system can be found in Table 1, respectively.

Table 1: Measured ring crack radius (a_c) as well as the calculated contact radius (a) for the equiaxed microstructure (EA) and the laminate, respectively.

Sample	Ring crack radius, a_c [µm]	Contact radius, a [µm]
EA	212 ± 16	164 ± 6
Multilayer	206 ± 17	159 ± 7

It can be seen that the ring crack radius, a_c, is for both systems approx. 30 % higher than the calculated contact radius, a, yielding to the observation that ring crack initiation takes place

outside of the contact circumference. The ratio a_c/a with the value of ~1.3 is in good agreement with the reported ones found in literature for different indented ceramics and glasses [20,21,40,41].

To study the influence of the tensile residual stresses in the EA-region of the multilayer on the cone crack angle, the angle (with respect to horizontal sample edge) was measured as ~27.2 ± 2.5° and 21.6 ± 0.5° on selected samples of the multilayer and the EA-monolith, respectively. This finding shows that tensile residual stresses of ~50 MPa in the surface EA-regions increase the cone crack angle by ~6°, which is consistent with the numerical predictions of Ceseracciu et. al. [42].

Figure 10 represents diagrams, where the energy of acoustic events is plotted versus the corresponding load during indentation, for one representative indent of EA, TA and the multilayer samples, respectively, measured under Hertzian indentation over a complete loading cycle. The energy is expressed in energy units (eu), where 1 eu corresponds to 10^{-14} V^2sec [43]. As can be seen in Fig. 10a, relatively high energies are emitted (>1000 eu) as long as classical Hertzian ring and/or cone cracking occurs during loading. For this representative measurement, it was found that the first acoustic event (E ~ 1620 eu) occurring at the RCIF (~875 N), was responsible for the formation of ring cracks. After the ring cracking event, even higher energy was measured (~53400 eu) at a load of approx. 1330 N. The second AE event corresponds to the pop-in of the cone crack. It is hypothesized that the third signal (E ~ 1735 eu) can be associated with stable crack growth of the cone crack at higher loads. However, the reader is cautioned that in EA, ring and cone cracking are not always considered to occur separately, but may also take place simultaneously as discussed in Section 3.1.

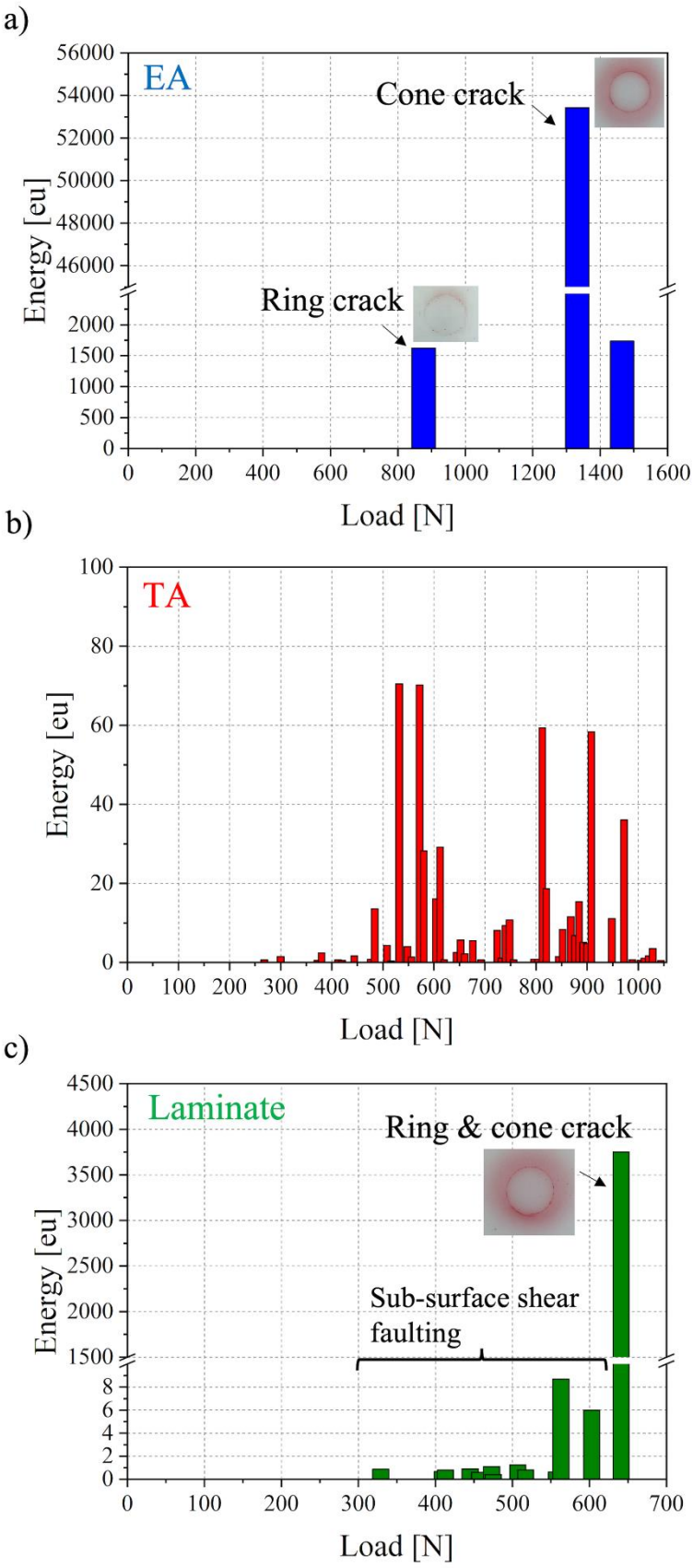

Fig. 10: Diagrams of the acoustic emission energies plotted versus the load from indentations made on (a) equiaxed microstructure (EA), (b) textured alumina (TA) and (c) laminate.

In contrast to that, Fig. 10b shows a high number of low-energy signals (<100 eu) starting at lower loads. The first signal at 260 N with an energy of ~1 eu could not be associated with surface damage. As the load is increased during the indentation cycle, low-energy signals are emitted in a frequent fashion. These low-energy patterns may indicate the formation of micro-cracks during subsurface shear faulting. The first higher peak of the low-energy signals (E ~ 70 eu) at the load of 570 N can be correlated with the start of a detectable surface impression on the surface of TA. To our best knowledge, this is the first report, showing the evidence of distinguishing the mechanisms of damage (classical ring/cone cracking or quasi-plastic deformation) by interpreting the AE signals. Fig. 10c reveals the detected energy signals versus load of the multilayer sample. Initially, low-energy signals (<10 eu) occur in a frequent manner comparable to the signals detected in TA (see Fig. 10b). The first detectable surface damage (ring and cone crack) was found at the load of approximately 650 N at the corresponding high-energy peak of ~3750 eu. As already discussed in Section 3.1, both damage zones are prominent in the multilayer sample after Hertzian contact testing; classical ring and cone cracks in the EA outer region and quasi-plastic subsurface damage in the embedded TA-regions. Due to the fact that the emitted signals at loads lower than ~600 N are similar to the energy values of TA, subsurface micro-cracking can be associated within this loading range. At higher loads, high-energy peaks of the laminate are found to be in the order of magnitude of energies detected in EA and are evident for being considered as RCIF. These findings show that subsurface damage mechanisms within the embedded TA layer is prior to classical ring crack initiation, as long as the maximum shear stress responsible for subsurface shear faulting lies within the TA layer and not in the EA layer. In the light of these results, it can be concluded that the response of the layered alumina architecture to contact loading may be controlled by designing the thickness of the outermost layer with respect to the depth of the shear stress field. This will be investigated in future work.

3.3 Evaluation of crack initiation stress

In order to discuss the influence of residual stresses on the data distributions, statistical analysis of the measured data was carried out. Figure 11a shows the RCIF distributions of the monolithic EA as well as the laminate system. In this Weibull diagram, the probability of failure is plotted versus the critical forces for ring crack initiation. In Fig. 11b, the corresponding ring crack initiation stress (RCIS) distributions are represented for both systems (EA and laminate). The probability of failure is plotted against the maximum tensile stresses as calculated according to Equation (3). The characteristic RCIF as well as the characteristic RCIS can be interpreted as

the critical force or stress where the probability of failure is ~63%. The Weibull modulus of the corresponding RCIF as well as RCIS data is a measure for the scatter and describes the width of the distributions. In both diagrams, the lines represent the best fits of the corresponding data sets according to the maximum-likelihood method. All the Weibull parameters are listed in Table 2.

Table 2: Characteristic ring crack initiation force (RCIF) (F_0), Characteristic ring crack initiation stress (RCIS) (σ_0), Weibull modulus (m) and the corresponding 90% confidence intervals of monolithic equiaxed microstructure (EA) and the laminate.

Sample	Characteristic RCIF, F_0 [N] and Weibull modulus m [-]	Characteristic RCIS, σ_0 [MPa] and Weibull modulus m [-]
EA	F_0 = 782 [751 – 814] m = 10 [7 – 13]	σ_0 = 2497 [2464 – 2531] m = 31 [22 – 39]
Laminate	F_0 = 719 [686 – 754] m = 9 [6 – 11]	σ_0 = 2428 [2391 – 2467] m = 26 [18 – 32]

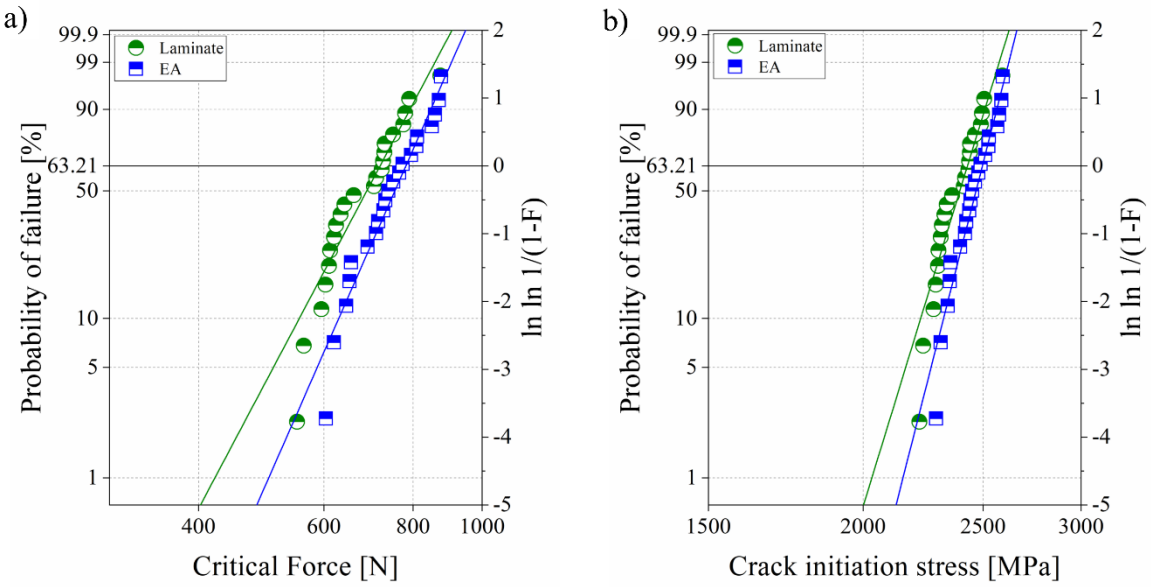

Fig. 11: (a) Ring crack initiation forces (RCIF) and (b) calculated RCIS distributions of equiaxed microstructure (EA) and the multilayer architecture. The lines represent the best fit according to the maximum-likelihood method.

The characteristic RCIF of EA is about 60 N higher than that of the laminate with comparable Weibull modulus. In the case of the RCIS distributions, it can be noticed that the characteristic RCIS of EA is ~70 MPa higher than that of the laminate, with the difference corresponding to the tensile residual stresses. The difference of ~70 MPa is well comparable with the estimated residual stresses according to Equation (1) (~50 MPa). These results indicate the high accuracy of the methodology employed and suggests the possibility of using spherical contact indentation techniques to estimate the residual stress state of ceramic-based components.

4. Conclusions

The contact damage behavior under spherical indentation of layered alumina architectures designed with embedded textured layers under in-plane compressive residual stresses was investigated. It is found that the quasi-plastic deformation associated with micro-cracking along basal planes within the embedded textured layer upon loading, enhances the capacity for damage absorption, compared to the reference bulk material with equiaxed microstructure. For higher applied loads, the cone cracks that extend from the surface ring crack can be deflected at the textured layer and guided parallel to the layer plane, thus preventing the multilayer architecture from catastrophic failure. The positive combined effect of textured architecture and compressive residual stress in subsurface layers shows the potential for the design of ceramic components with enhanced contact damage tolerance.

Acknowledgements

Funding for this research was provided by the European Research Council (ERC) excellent science grant “CERATEXT” through the Horizon 2020 program under contract 817615. We gratefully acknowledge G. Hawranek (Department of Materials Science, Montanuniversitaet Leoben) for the support with the ion-slicing technique and scanning electron microscopy analysis.

References

1. Munz D, Fett T. *Ceramics: Mechanical properties, failure behaviour, materials selection.* 2nd ed. Berlin: Springer; 2001.
2. Carter CB, Norton MG. *Ceramic materials: Science and engineering*. New York: Springer; 2013.
3. Danzer R, Lube T, Supancic P, Damani R. Fracture of ceramics. *Adv. Eng. Mater.* 2008;10.
4. Morrell R. *Fractography of brittle materials: Measurement good practice guide No. 15*. Teddington, UK; 1999.
5. Lange FF. Powder processing science and technology for increased reliability. *J. Am. Ceram. Soc.* 1989;72:3–15.
6. Lawn BR. *Fracture of brittle solids*. Cambridge: Cambridge University Press; 1993.
7. Rao M, Sanchez-Herencia J, Beltz G, McMeeking RM, Lange F. Laminar ceramics that exhibit a threshold strength. *Science*. 1999;286:102–5.
8. Bermejo R, Torres Y, Baudín C, Sánchez-Herencia AJ, Pascual J, et al. Threshold strength evaluation on an Al2O3–ZrO2 multilayered system. *J. Eur. Ceram. Soc.* 2007;27:1443–8.
9. Bermejo R, Torres Y, Sánchez-Herencia AJ, Baudín C, Anglada M, et al. Residual stresses, strength and toughness of laminates with different layer thickness ratios. *Acta Mater.* 2006;54:4745–57.
10. Sglavo VM, Paternoster M, Bertoldi M. Tailored residual stresses in high reliability alumina-mullite ceramic laminates. *J. Am. Ceram. Soc.* 2005;88:2826–32.
11. Costabile A, Sglavo VM. Influence of the architecture on the mechanical performances of alumina-zirconia-mullite ceramic laminates. *Adv. Sci. Technol.* 2006;45:1103–8.
12. Sglavo VM, Genua F de, Molinari A, Casari F. Alumina/silicon carbide laminated composites by spark plasma sintering. *J. Am. Ceram. Soc.* 2009;92:2693–7.
13. Wegst UGK, Bai H, Saiz E, Tomsia AP, Ritchie RO. Bioinspired structural materials. *Nat. Mater.* 2015;14:23–36.
14. Pavlacka RJ, Messing GL. Processing and mechanical response of highly textured Al2O3. *J. Eur. Ceram. Soc.* 2010;30:2917–25.
15. Chang Y, Bermejo R, L. Messing G. Improved fracture behavior of alumina microstructural composites with highly textured compressive layers. *J. Am. Ceram. Soc.* 2014;97:3643–51.
16. Bermejo R. “Toward seashells under stress”: Bioinspired concepts to design tough layered ceramic composites. *J. Eur. Ceram. Soc.* 2017;37:3823–39.

17. Hertz H. Ueber die Berührung fester elastischer Körper. *J. Reine Angew. Math;*1882:156–71.
18. Lawn BR, Wiederhorn SM, Johnson HH. Strength degradation of brittle surfaces: Blunt indenters. *J. Am. Ceram. Soc.* 1975;58:428–32.
19. Lawn BR. Indentation of ceramics with spheres: A century after Hertz. *J. Am. Ceram. Soc.* 1998;81:1977–94.
20. Tillett JPA. Fracture of glass by spherical indenters. *Proc. Phys. Soc. B*. 1956;69:47–54.
21. Wereszczak AA, Johanns KE, Jadaan OM. Hertzian ring crack initiation in hot-pressed silicon carbides. *J. Am. Ceram. Soc.* 2009;92:1788–95.
22. Lee SK, Wuttiphan S, Lawn BR. Role of microstructure in Hertzian contact damage in silicon nitride: I, Mechanical characterization. *J. Am. Ceram. Soc.* 1997;80:2367–81.
23. Guiberteau F, Padture NP, Lawn BR. Effect of grain size on Hertzian contact damage in alumina. *J. Am. Ceram. Soc.* 1994;77:1825–31.
24. Latella BA, OConnor BH, Padture NP, Lawn BR. Hertzian contact damage in porous alumina ceramics. *J. Am. Ceram. Soc.* 1997;80:1027–31.
25. Cai H, Kalceff SMA, Lawn BR. Deformation and fracture of mica-containing glass-ceramics in Hertzian contacts. *J. Mater. Res.* 1994;9:762–70.
26. Belmonte M, Miranzo P, Osendi MI. Contact damage resistant SiC/graphene nanofiller composites. *J. Eur. Ceram. Soc.* 2018;38:41–5.
27. An L, Chan HM, Padture NP, Lawn BR. Damage-resistant alumina-based layer composites. *J. Mater. Res.* 1996;11:204–10.
28. Ha H-C, Chan HM, Nied HF. Hertzian contact behavior of alumina-based trilayer composites: Experimental observation and FEM analysis. *Acta Mater.* 2001;49:2453–61.
29. Miranda P, Pajares A, Guiberteau F, Deng Y, Lawn BR. Designing damage-resistant brittle-coating structures: I. Bilayers. *Acta Mater.* 2003;51:4347–56.
30. Miranda P, Pajares A, Guiberteau F, Deng Y, Zhao H, et al. Designing damage-resistant brittle-coating structures: II. Trilayers. *Acta Mater.* 2003;51:4357–65.
31. Hofer A-K, Walton R, Ševeček O, Messing GL, Bermejo R. Design of damage tolerant and crack-free layered ceramics with textured microstructure. *J. Eur. Ceram. Soc.* 2020;40:427–35.
32. Sglavo VM, Bertoldi M. Design and production of ceramic laminates with high mechanical resistance and reliability. *Acta Mater.* 2006;54:4929–37.

33. Chlup Z, Hadraba H, Drdlik D, Maca K, Dlouhy I, et al. On the determination of the stress-free temperature for alumina–zirconia multilayer structures. *Ceram. Int.* 2014;40:5787–93.
34. Fischer-Cripps AC. *Introduction to contact mechanics*. Boston, MA: Springer Science+Business Media LLC; 2007.
35. Santhanam AT. Application of transition metal carbides and nitrides in industrial tools. In: Oyama ST, ed. *The chemistry of transition metal carbides and nitrides*. Dordrecht: Springer Netherlands; 1996:28–52.
36. Weibull W. A statistical distribution function of wide applicability. *J. Appl. Mech.* 1951;18:293–7.
37. EN 843-5. Advanced technical ceramics – Monolithic ceramics – Mechanical properties at room temperature – Part 5: Statistical analysis; 1996.
38. Wade J, Ghosh S, Claydon P, Wu H. Contact damage of silicon carbide ceramics with different grain structures measured by Hertzian and Vickers indentation. *J. Eur. Ceram. Soc.* 2015;35:1725–36.
39. Chlup Z, Novotná L, Šiška F, Drdlík D, Hadraba H. Effect of residual stresses to the crack path in alumina/zirconia laminates. *J. Eur. Ceram. Soc.* 2020;40:5810–8.
40. Marimuthu KP, Rickhey F, Lee JH, Lee H. Spherical indentation for brittle fracture toughness evaluation by considering kinked-cone-crack. *J. Eur. Ceram. Soc.* 2017;37:381–91.
41. Turner DN, Smith PD, Rotsey WB. Hertzian stress cracks in beryllia and glass. *J. Am. Ceram. Soc.* 1967;50:594–8.
42. Ceseracciu L, Anglada M, Jiménez-Piqué E. Hertzian cone crack propagation on polycrystalline materials: Role of R-curve and residual stresses. *Acta Mater.* 2008;56:265–73.
43. Vallen Systeme GmbH. Acoustic emission system AMSY-5 system description. Available at: https://www.vallen.de/zdownload/pdf/y5sd0911.pdf. Accessed October 1, 2021.

Publication C

High-temperature fracture behaviour of layered alumina ceramics with textured microstructure

J. Schlacher, Z. Chlup, A.-K. Hofer, R. Bermejo,

J. Eur. Ceram. Soc. 43 (7) (2023) 2917–2927

https://doi.org/10.1016/j.jeurceramsoc.2022.11.046

High-temperature fracture behaviour of layered alumina ceramics with textured microstructure

Josef Schlacher[1*], Zdeněk Chlup[2], Anna-Katharina Hofer[1], Raul Bermejo[1]

[1] Department of Materials Science, Montanuniversität Leoben, Franz Josef Strasse 18, A-8700, Leoben, Austria

[2] Institute of Physics of Materials, Czech Academy of Sciences, Zizkova 22, 616 62 Brno, Czech Republic

*Corresponding author's email: josef.schlacher@unileoben.ac.at

Abstract

Mimicking the damage tolerance of biological materials such as nacre has been realised in textured layered alumina ceramics, showing improved reliability as well as fracture resistance at room temperature. In this work, the fracture behaviour of alumina ceramics with textured microstructure and laminates with embedded textured layers are investigated under uniaxial bending tests at elevated temperatures (up to 1200°C). At temperatures higher than 800°C monolithic textured alumina favours crack deflection along the basal grain boundaries, corresponding to the transition from brittle to more ductile behaviour. In the case of laminates, the loss of compressive residual stresses is counterbalanced by the textured microstructure, effective up to 1200°C. This study demonstrates the potential of tailoring microstructure and architecture in ceramics to enhance damage tolerance within a wide range of temperatures.

Keywords: Alumina, textured microstructure, high-temperature properties, Laminate strategy, residual stresses

1. Introduction

Fracture resistance and mechanical reliability are key factors in the design of ceramics-based materials, especially for structural applications. Microstructure refinement and elimination of natural flaws have been established as successful approaches to increase strength and enhance reliability. New approaches to further increase fracture resistance and reliability in ceramics have been inspired by natural systems with outstanding properties, mainly based on the combination of microstructure and architecture. Some strategies involve metastable microstructures allowing phase transformation, combination of materials to induce internal

residual stresses, among others [1–3]. In this regard, extensive work has been devoted to combine ceramics in a layered structure to enhance strength and/or fracture resistance against propagation of natural flaws or artificial cracks. For instance, mismatch in the coefficients of thermal expansion and/or lattice transformation between layer materials have been employed to induce thermal strains into the microstructure during cooling down from the sintering temperature, with the corresponding residual stresses [3]. When improved mechanical strength is pursued, such layered ceramic architectures are designed with compressive residual stresses located in the top-surface layers [4,5], as utilized for instance in ion-exchanged glasses [6]. In case damage tolerance is sought, embedded layers with in-plane compressive residual stresses result in an effective barrier against crack propagation from surface flaws, providing in some cases a minimum threshold strength below which failure does not occur [7–12]. However, the benefits obtained in laminates with tailored residual stresses at room or moderate temperatures may vanish when loaded at elevated temperatures [13,14], thus reducing their field of application.

For high-temperature (HT) applications the use of composite materials reinforced by fibres has been extensively used, with the additional cost in terms of fabrication. Through tailoring the microstructure of the matrix and fibre interphases, significantly enhanced fracture resistance has been reported [15–18]. The use of monolithic bulk ceramics for HT has been dominated by silicon nitride, in particular through the combination of enlarged β-grains to reinforce the α-grain matrix [19]. An extension of this concept has been applied to alumina ceramics, aiming to induce a preferential orientation of grains (textured) [20]. Tape casting processing or more recently additive manufacturing processes [21] have been employed on alumina ceramics containing large-aspect ratio ”platelets” to align the microstructure. Several attempts have been made by applying a strong magnetic field [22,23], CVD deposition [24] and gel/tape casting [20,25,26]. In the case of alumina ceramics, templated grain growth (TGG) during sintering can develop a strong texture degree, as observed in the “brick-mortar” structure of nacre [27,28]. As a consequence, a significant increase in fracture toughness has been achieved. The question arises, whether the effect of texturing may be available also at high temperatures and how the combination of microstructure and residual stresses can affect the mechanical behaviour of the ceramic material.

This paper aims to investigate the fracture behaviour of layered ceramics over a wide range of temperatures, which combine non-textured (equiaxed) (EA) and textured (TA) material layers, with a special focus on fracture resistance and damage tolerance. High-temperature bending

tests were performed in the vacuum on EA-, TA- and laminate samples with artificial cracks to evaluate the indentation strength. Microstructural analysis, as well as X-ray diffraction (XRD) measurements, were carried out to study the quality of texture. The thermo-elastic materials properties were measured from room to elevated temperatures to estimate the residual stresses of the EA- as well as TA-regions within the laminate as a function of temperature. To better understand the fracture behaviour at high-temperatures, the crack paths were studied through a fractographic analysis. This work shows how textured materials employed as a monolith and/or embedded as a layer within ceramic composites may enhance the fracture resistance over a wide range of temperatures, extending their application as "damage tolerant" materials beyond room temperature.

2. Experimental

2.1. Processing of materials

Monolithic samples with non-textured (equiaxed (EA)) and textured (TA) microstructures as well as multi-layer samples of alternating EA/TA layers, were designed and fabricated by using the tape-casting process.

For all three systems, high-purity α-alumina powder (99.99% ultrafine α-Al_2O_3, TM-DAR, Taimei Chemicals Co. Ltd., Nagano, Japan) with a d_{50} particle size of ~0.3 μm was used for the slurry preparation. For the TA samples, 5 vol.% single crystal alumina platelets (Rona Flair© White Sapphire, EMD Performance Materials Corp., Darmstadt, Germany) of high aspect ratio with a diameter of ~ 5–16 μm and thickness of ~ 0.10 μm were added to the slurries. To enhance the template grain growth process (TGG) in TA, dopants ($CaO:SiO_2$ = 1:1, CaO in form of $Ca(NO_3)_2 \cdot 4H_2O$ (ThermoFischer GmbH, Kandel, Germany), SiO_2 in the form of $C_8H_{20}O_4Si$ (ThermoFischer GmbH, Kandel, Germany)) in a 0.10% wt. concentration to the alumina powder were added to the platelets. The slurries for the EA and TA tapes were prepared by powder ball milling using a Fisher Bottle/Tube roller (Fisherbrand™, Fisher Scientific GmbH, Vienna, Austria) with 5 mm alumina balls (rotational speed of 80 min^{-1}) for 24 h in a 1:1 xylene (Avantor Performance Materials Poland S.A., Gliwice, Poland) and ethanol (99%, Sigma-Aldrich, Darmstadt, Germany) solution with menhaden fish oil (Sigma-Aldrich GmbH, Vienna, Austria) as a dispersant. After the addition of a binder (Polyvinylbutyral, Sigma-Aldrich GmbH, Steinheim, Germany) and two plasticizers (Butylbenzyl Phthalate (Sigma-Aldrich GmbH, Steinheim, Germany); Dibutyl Sebacate (Sigma-Aldrich, Steinheim, Germany)) the slurry was ball milled for another 24 h. In the last step, the platelets were added to the slurry and ball milled

for another 30 min, followed by a de-airing process for 24 h. The casting of the EA and TA tapes followed a similar procedure as found in [29]. The prepared tapes (EA and TA) were cut to a size of 55 mm × 55 mm, stacked and warm-pressed with ~ 6 MPa at 75 °C for 15 min. Subsequently, isostatic lamination (20 MPa/75 °C/30 min) and binder burnout at 600 °C / 2 h were carried out. Sintering at 1550 °C for 2 h was chosen for all prepared plates to achieve fully-dense ceramic samples.

Several bend bars with dimensions of b ~ 4 mm, h ~ 3 mm and L ~50 mm were cut from the sintered plates. The monolithic EA, TA and the layered architecture of the laminate bend bars are schematically depicted in Fig. 1 (a). The side surfaces of the bars were ground using a diamond wheel. One side surface of each specimen was polished to a 1 µm mirror finish using a Tegramin-30 equipment (Struers, Denmark) to investigate the crack paths after testing. To avoid influences of edge defects on the strength results, both edges on the tensile sides (one top surface) of the bend bars were manually machined using SiC-paper with the grain size of 15 µm, resulting in ~50µm x 45° chamfers. Vickers indentations were placed on the tensile side of each specimen to generate artificial surface (starting) cracks for the indentation strength tests (Fig. 1b). In the case of the laminate, two textured (TA) layers were embedded between the EA-regions following the sequence EA/TA/EA/TA/EA with a final dimension after sintering of ~ 200 µm/160 µm/2240 µm/160 µm/200 µm, corresponding to a volume ratio V_{EA}/V_{TA} ~ 8.

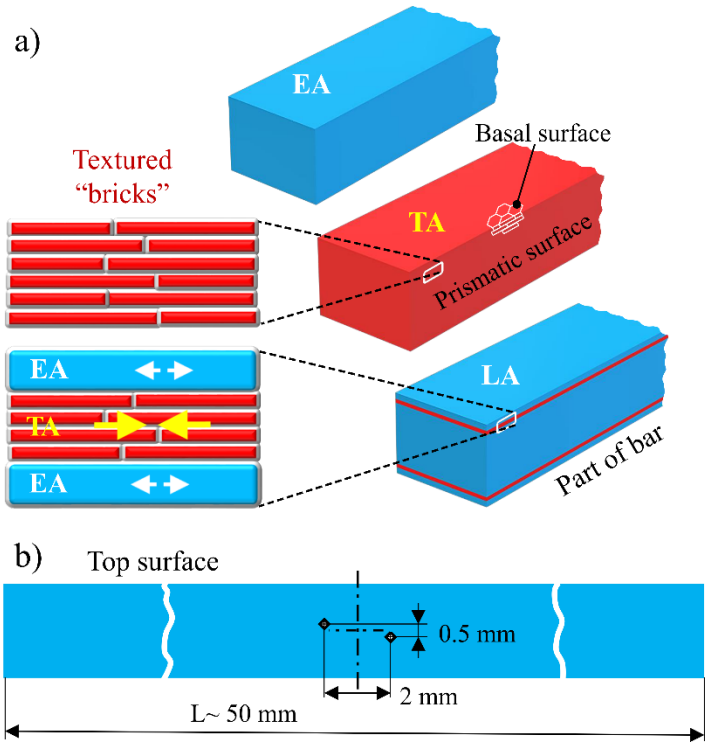

Fig. 1: (a) Schematic of monolithic EA, TA and laminate (LA). The close-ups indicate the textured microstructure as "bricks" for illustrative purposes. The in-plane tensile (EA-region), as well as compressive residual stresses (TA-region) within LA, are indicated as white and yellow arrows, respectively. (b) Top view of a bending bar indicating the locations of the Vickers indents. Two imprints were placed at a distance of ~2 mm and ~0.5 mm offset to avoid crack interactions during testing.

2.2 Microstructural analysis

Polished monolithic EA-, TA-, as well as the multilayer samples, were thermally etched at 1450 °C for 25 min. Afterwards, the polished side surfaces (1 µm) of the samples were gold-coated using an Agrar Sputter coater and observed under a scanning electron microscope (JEOL JCM-6000Plus, Neoscope^{TM}, JEOL LTd., Tokyo, Japan). Subsequently, several SEM images of the microstructures were taken and analysed to determine the grain size distributions using the line-intersection method [30].

To investigate the crystallographic orientation of the different microstructures, Electron backscatter diffraction (EBSD) was carried out using a SEM (LYRA 3 XMU, Tescan, Czech Republic) with EBSD camera Symmetry S2 (Oxford Instruments, UK). Prior to the EBSD

investigations, specimens were polished down to 0.25 μm using diamond paste and polishing equipment (LaboPol 25, Struers, Denmark).

For assessing the texture quality within the rhombohedral alumina crystal structure, XRD-patterns of the basal surface (perpendicular to the [0001]-direction) were obtained via the Θ-2Θ method using a scanning step size of 0.02° and step time of 1.2s. To quantify the degree of texture, the so-called Lotgering factor (LF) was evaluated as follows [31]:

$$LF = \frac{\frac{\sum I^{T}_{(000l)}}{\sum I^{T}_{(hkil)}} - \frac{\sum I^{E}_{(000l)}}{\sum I^{E}_{(hkil)}}}{1 - \frac{\sum I^{E}_{(000l)}}{\sum I^{E}_{(hkil)}}} \quad (1)$$

where $\Sigma I^{T}_{(hkil)}$ and $\Sigma I^{T}_{(000l)}$ are the total intensity peaks and the sum intensities of (000*l*) (all peaks of basal-planes perpendicular to the [0001] direction) within the Θ-2Θ-scan of monolithic textured alumina, respectively. In this regard, $\Sigma I^{E}_{(hkil)}$ as well as $\Sigma I^{E}_{(000l)}$ are denoted as intensities of all peaks and the sum of intensity peaks in (000*l*)-basal planes of the measured scan of monolithic alumina with equiaxed microstructure.

The density, ρ, of the monolithic (EA, TA) as well as laminate (LA) samples were measured according to EN623–2 standards [32] using the Archimedes method. The fact that both, EA as well as TA, show a similar theoretical density, ρ_{th}, of 3.986 g cm^{-3} (according to Taimei Chemicals Co. Ltd., Nagano, Japan), the corresponding laminate density can be calculated using the same theoretical density without considering any rule of mixture. For the monolithic as well as laminate samples, the relative densities, ρ_{rel}, were calculated as $\rho_{rel} = \rho/\rho_{th}$. The porosity was estimated from the relative density results, as residue to the theoretical density.

2.3 Thermo-elastic properties

The dependence of elastic modulus on temperature was determined by using the impulse excitation technique (IET) with a device IMCE RFDA 1600 (IMCE, Belgium) on polished prismatic bars resonating in the flexural mode according to ASTM E1876–15 [33]. The automatic excitation and consequent elastic properties determination was conducted in 30 s intervals with the heating and cooling rates set to 10 °C/min and dwell of 15 min at 1500 °C. The measured elastic moduli were compared with those determined from the linear part of loading curves of flexural indentation strength tests.

Dilatometric measurements of both materials were performed using a high-temperature dilatometer (L70/1700, Linseis, Germany) in the temperature range from 20 °C to 1500 °C. A heating and cooling rate of 1 °C/min was used. The cooling branches of the dilatometric curves were utilized to determine differences in coefficient of thermal expansion (CTE) between both materials, and allow the calculation of residual stresses in the laminated structure. The polynomic dependences of shrinkage on temperature were established according to the following equation:

$$\varepsilon = \frac{\Delta l}{l_0} = a_0 + a_1 T + a_2 T^2 + a_3 T^3 \quad (2)$$

The dependence of CTE with temperature was calculated as a derivation of Eq. (2), which along with the E-modulus (as a function of temperature) was employed to calculate the residual stress distribution in the laminate, as a function of temperature.

2.4 Vickers indentation

The indentation technique was employed for (i) hardness measurements and (ii) to introduce geometrically defined defects (cracks) onto the tensile surface of bending bars selected for the indentation strength tests. Indentations were done with a Vickers indenter implemented in a Zwick Z2.5 machine equipped with a fully instrumented ZHU0.2 indentation head (both Zwick/Roell, Germany). The obtained loading curves (force-indentation depth) were used to calculate hardness. The universal Martens hardness (HMs) and indentation hardness (H_{IT}) were determined instead of Vickers hardness due to difficulties (chipping) in the exact determination of indent diagonals in the case of textured materials. Indentation cracks larger than average natural (processing) flaws were introduced using 10 kg indent loads (HV10), to ensure fracture initiation from the indentation cracks during the bending tests. The Vickers crack lengths were measured on optical images taken with a confocal microscope (Olympus LEXT OLS 3100, Japan). The average crack lengths for EA, TA and LA were 396 ± 38 µm, 455 ± 43 µm and 477 ± 66 µm, respectively. The larger indentation crack length in LA, compared to EA, is associated with the effect of tensile residual stresses in the former.

2.5 Flexural strength and fracture resistance

To determine the effect of texture on the fracture resistance at elevated temperatures, flexural strength measurements of pre-indented specimens were performed. At least 3 specimens were tested for each material at elevated temperatures. Prismatic bars with cross-sections of ~ 3 × 4 mm^2 and a length of 50 mm were prepared introducing artificial flaws (see Fig. 1) to avoid crack initiation and fracture from existing natural flaws. The four-point loading configuration with spans of 40/20 mm and rollers of 5 mm in diameter was used for strength measurements. A universal testing machine Instron 8862 (Instron, USA) was employed for room temperature tests in the lab air environment. The experiments at elevated temperatures as well as for room temperature in a vacuum (~ 5×10^{-5} mbar) were conducted using Zwick/Kappa testing system (Zwick/Roell, Germany) with a built-in high-temperature vacuum/inert atmosphere chamber (Maytec, Germany). The flexural deformation, named as displacement (δ), was directly measured by a three-point contact extensometer (Maytec, Germany) placed inside the chamber. The loading mode was in position control with a crosshead speed of 0.1 mm/min. All specimens were preloaded to 20 N prior to testing. The indentation fracture strength, σ_f, for all three material systems under four-point bending was calculated using the following equation [34]:

$$\sigma_f = \frac{3}{2}\frac{F(S_1 - S_2)}{bh^2} \tag{3}$$

where F is the maximum fracture force, b the width of the specimen, h the specimen height, S_1 the outer span (40 mm) and S_2 the inner span (20 mm) of the loading configuration. Assuming the elastic mismatch of both "pure" alumina layers (EA and TA) within the laminate is rather small, Eq. (3) was also employed for the calculation of the maximum stress in LA material, without considering the classical laminate theory. To understand the flexural bending behaviour under high-temperature, the flexural stress (σ) – strain (ε) curves were built from the registered force (F) - displacement (δ) data (corrected by the pre-load), where the corresponding outer fibre strain ε was calculated as follows:

$$\varepsilon = \frac{4\delta h}{{S_2}^2} \tag{4}$$

The inelastic work of fracture (plastic contribution), as well as the total work of fracture (WOF), were calculated under consideration of the load-displacement curves up to the maximum of the loading force, where the first crack propagation or structural damage are expected. In this regard, the result of integrating the area under the load-displacement curves with the maximum fracture force as the upper integration limit was divided by twice the cross-area of the bend bars [35,36]. To interpret the fracture resistance of the systems, the inelastic WOF in respect to the total fracture was calculated as WOF-ratio.

Fractographical analyses were carried out on selected fracture surfaces of broken specimens. In this regard, the fracture surfaces were carbon coated by a sputter coater (Quantum Q150V Plus, Germany) and investigated by using a SEM (LYRA 3 XMU, Tescan, Czech Republic). To study the macroscopic fracture paths, images of the side surfaces of selected bending bars of EA, TA and LA for each testing temperature were taken using an optical microscope (Nikon ECLIPSE LV100ND, Japan). Furthermore, one TA-side surface was observed using SEM to study crack propagation along the textured grains during high-temperature bending tests.

3 Results and discussion

3.1 Microstructure and texture quality

Figure 2 shows SEM images of the microstructures of the monolithic EA, monolithic TA as well as the laminate LA together with XRD-patterns of the monoliths. The monolithic EA-sample (Fig. 2a) shows a rather fine-grained microstructure with a mean grain size d_{50}= 1.1 ± 0.6 µm. In Fig. 2b, the highly-textured microstructure with grains ranging from ~15–30 µm in prismatic direction (casting direction) and a mean grain size d_{50} of 2.1 ± 1.1 µm in basal direction is shown. In Fig. 2c the EA/TA interface region in the laminate is illustrated, exhibiting a relatively sharp interface. It is worth indicating that the grain size distributions of the EA- and TA-region of the laminated system with values of d_{50} = 1.7 ± 1.0 µm (EA) and as well as d_{50} = 2.2 ± 0.9 µm (TA, basal direction), respectively, are comparable to the above-mentioned mean grain sizes of the monolithic counterparts. The grains of TA in prismatic direction within the laminated architecture are also in the same range as those in monolithic TA.

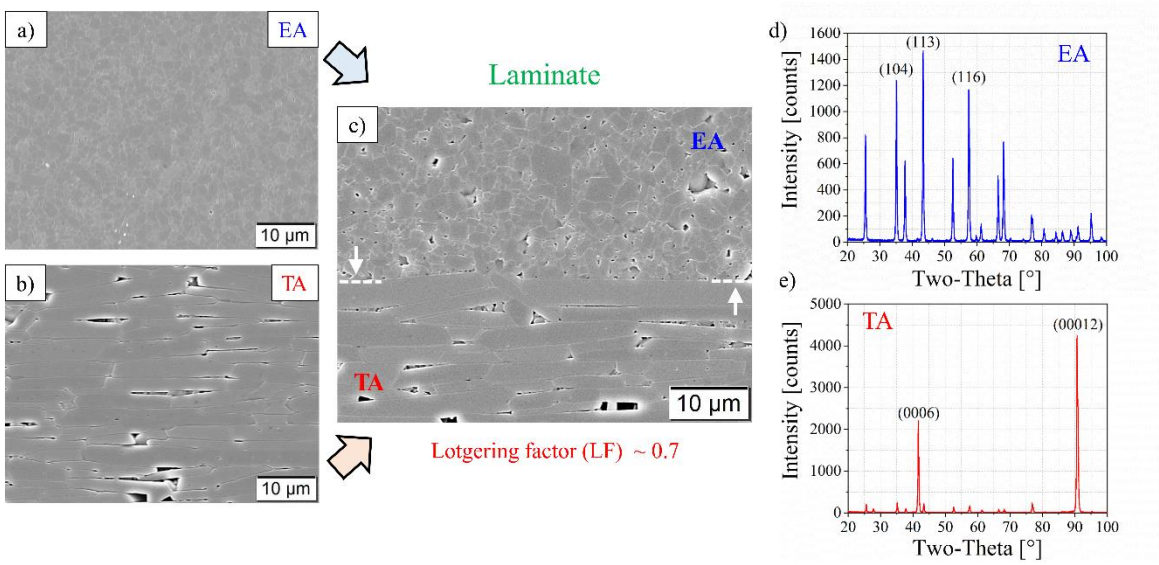

Fig.2: Microstructure and the corresponding measured XRD-pattern of (a, d) EA and (b, e) TA, respectively. The EA/TA interface region is indicated by white arrows in the SEM image of microstructure in the laminate sample (c).

Figures 2d and 2e show the collected XRD-patterns of monolithic EA and TA, respectively. The preferred orientation along the [0001]-directions is confirmed by the dominating peaks of (0006) as well as (00012) detected on textured alumina. These relatively high counts, corresponding to [0001]-direction of the grains, confirm the strong alignment of TA-platelets during the tape casting process. The LF of monolithic TA determined as ~ 0.7 is in good agreement with the stated texture degrees found in other works [29,37,38]. The monolithic EA shows rather low intensities in these specific orientations; however, significant counts of random prismatic peaks in (104), (113) and (116) were measured.

To highlight the degree of texture, EBSD-images of the monolithic TA- as well as laminate sample (interface region) are shown in Fig. 3.

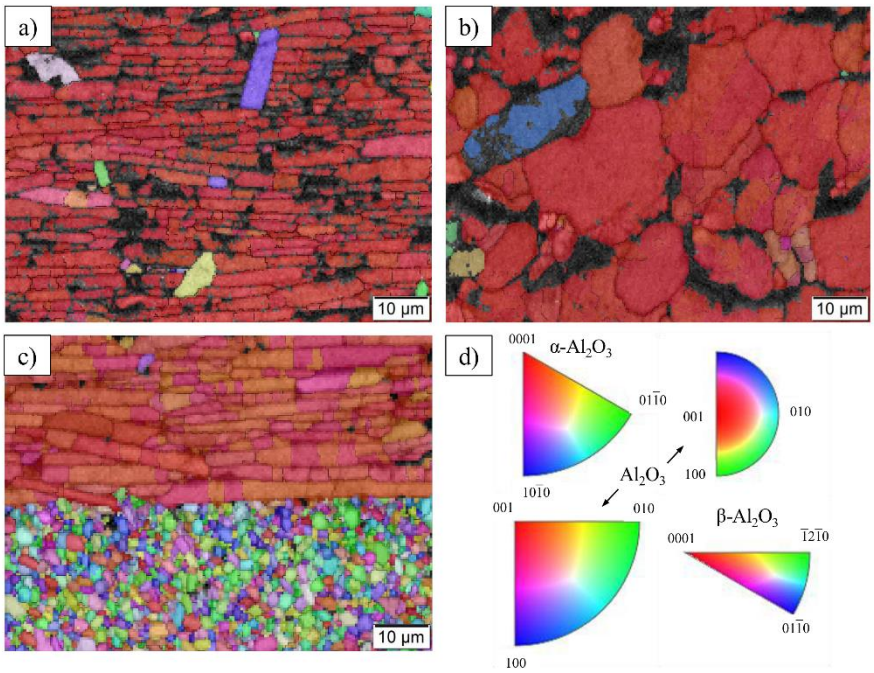

Fig. 3: Microstructure (EBSD) of (a) TA (prismatic surface), (b) TA (basal surface) and (c) the laminate (i.e, TA top and EA bottom). (d) Pole figures of the EBSD measurements.

In Fig 3a the microstructure on the prismatic side surface of the TA-sample is shown. The elongated grains are well aligned showing a preferred orientation in the basal direction (i.e., [0001]), corresponding to the axis perpendicular to the casting direction. Only a few grains are misaligned and depict different orientations in one of the prismatic planes. For the sake of comparison, the microstructure of TA on the basal surface is displayed in Fig 3b. This finding together with the above-stated LF of 0.7 indicate the relatively high degree of texture achieved during the tape casting process. Figure 3c illustrates the microstructure of the laminate, where the TA-region reveals a preferred orientation (basal) and the EA-region is randomly oriented in one of the prismatic crystallographic orientations.

The densities of the monolithic EA- and TA-samples were determined as 3.954 ± 0.005 g cm^{-3} and 3.857 ± 0.004 g cm^{-3}, respectively. The relative density of EA, ~99.2%, is slightly higher than that of the TA-sample (~96.8%). The density of the laminate was 3.930 ± 0.003 g cm^{-3}, which corresponds to a relative density of ~98.6%, in agreement with the calculated relative density applying the rule of mixture (~98.7%). The estimated amount of porosity present in the given microstructures is 0.8%, 3.2% and 1.4% for EA, TA and LA, respectively. The higher

porosity for TA is a consequence of the geometrically remaining spacing between stacked platelets. The slightly lower porosity on LA, compared to TA, may be associated with the effect of in-plane residual stresses in the former, favouring densification in the in-plane direction.

3.2 Thermo-elastic properties and residual stresses as a function of temperature

The elastic moduli data determined as a function of temperature by the IET method for EA and TA were fitted to a 2nd order polynomial. Values were compared to the elastic modulus estimated from the linear parts of the loading curves from bending experiments (see Fig. 4a). The corresponding polynomial fits for EA and TA are given as:

$$E_{EA}(T)[GPa] = 394.098 - 3.557 \times 10^{-2}T - 9.264 \times 10^{-6}T^2 \quad (5a)$$

$$E_{TA}(T)[GPa] = 398.250 - 2.963 \times 10^{-2}T - 9.136 \times 10^{-6}T^2 \quad (5b)$$

within the temperature interval of 20 °C ≤ T ≤ 1200 °C.

The elastic modulus of the monolithic TA is slightly higher than that of EA, over the complete temperature range. This difference may be explained by the effect of anisotropy in monolithic TA, where the majority of textured grains are aligned in [0001]-direction [39]. In the case of EA, the determined elastic moduli from the loading curves are in good agreement with the stated polynomial function. However, a notable difference is found for the TA material. This finding can be attributed to the fact that the linear fit of the loading curves for TA, especially at temperatures higher than 800°C, is affected by the plastic-behaviour associated with softening mechanisms of glassy phases and/or weakening of textured grain boundaries (as explained in the following sections). Therefore, only the data evaluation from the IET-measurement for the TA-material is considered for further analyses.

Determined coefficients of thermal expansions are in good agreement with literature data [40]. The slight difference between EA and TA materials (see Fig. 4b) is responsible for the formation of internal stresses between layers in the laminate. In the case of laminates, the CTE temperature dependence lays in between the two curves for EA and TA, being rather closer to EA, explained by the higher content of EA material (i.e., volume ratio of $V_{EA}/V_{TA} \sim 8$). The

polynomial fit 2nd order of the CTE's as a function of temperature for EA, TA and the laminate (LA) are given as:

$$\alpha_{EA}(T)[°C^{-1}] = 6.560 \times 10^{-6} + 4.452 \times 10^{-9}T - 1.106 \times 10^{-12}T^2 \quad (6a)$$

$$\alpha_{TA}(T)[°C^{-1}] = 6.257 \times 10^{-6} + 4.606 \times 10^{-9}T - 1.284 \times 10^{-12}T^2 \quad (6b)$$

$$\alpha_{LA}(T)[°C^{-1}] = 6.441 \times 10^{-6} + 4.659 \times 10^{-9}T - 1.266 \times 10^{-12}T^2 \quad (6c)$$

for the interval of 0 °C ≤ T ≤ 1500 °C, respectively.

To analytically estimate the in-plane residual stresses ($\sigma_{res,\,n}(T)$) within each layer region (EA and TA) in the laminate as a function of temperature, the following equation can be used:

$$\sigma_{res,n}(T) = \frac{E_n(T)}{1-\nu_n}\big(\bar{\alpha}(T) - \alpha_n(T)\big)\big(T - T_{ref}\big), \quad (7)$$

where α_n (T) is the coefficient of thermal expansion given as polynomial fit of 2nd order (CTE), E_n(T) the Young's modulus (determined by the IET-method and fitted by a polynomial function of 2nd order, see equation 5), and ν_n the Poisson's ratio (assumed to be ~0.22) of each n^{th} layer of the contributing materials (EA and TA), respectively. In this regard, $\Delta T = T - T_{ref}$, is known as temperature difference, where T is the given temperature and T_{ref} is the reference temperature. T_{ref}, also known as stress-free temperature, is the temperature above which the materials are stress-free and has been taken as ~1470 °C, as proposed in the work of Chlup et al. for alumina-based laminates [41]. The average coefficient of thermal expansion as a function of temperature, $\bar{\alpha}(T)$, can be calculated as follows:

$$\bar{\alpha}(T) = \sum_{n=1}^{N} \frac{E_n(T)t_n\alpha_n(T)}{1-\nu_n} \Big/ \sum_{n=1}^{N} \frac{E_n(T)t_n}{1-\nu_n}, \quad (8)$$

where t_n is considered as the n^{th} layer thickness of the laminate.

Figure 4c shows the in-plane residual stresses within the EA- (dashed line) as well as the TA- (full line) region of the laminate as a function of temperature. At room temperature, the in-plane tensile residual stresses in the EA-region and the in-plane compressive residual stresses in the embedded TA-layer regions within the laminate are calculated as + 24 MPa and − 197 MPa, respectively. During high-temperature bending of the laminate at 1200°C, the remaining in-plane tensile stress (in EA), as well as the in-plane compressive residual stresses (in TA), are only + 5 MPa and − 40 MPa, respectively, as indicated by the purple arrows in Fig. 4c. The ratio of residual stresses agrees with the volume ratio of V_{EA}/V_{TA}~8.

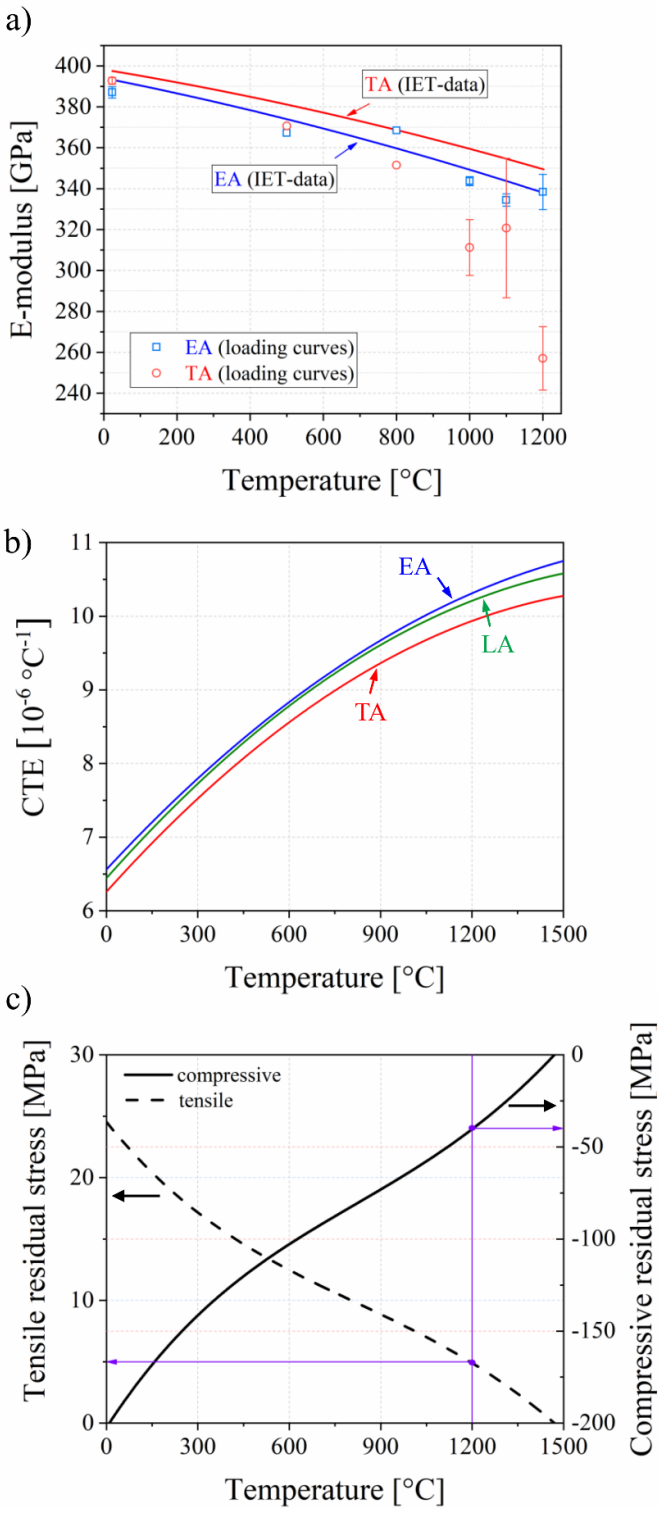

Fig. 4: (a) Dependence of elastic modulus determined by IET-method of monolithic EA- and TA- material on the testing temperature and the data points estimated from loading curves as a comparison. (b) CTE's as a function of temperature for EA, TA and the laminate, respectively. (c) The calculated tensile (EA-region) as well as compressive residual stresses (TA-region) within the layered architecture as a function of temperature.

3.3 Hardness

The measured Martens hardness of the EA, TA and laminate (HV10) was 10.7 ± 1.9 GPa, 8.1 ± 1.2 GPa and 10.9 ± 1.7 GPa, respectively. The indentation hardness, H_{IT}, was 18.5 ± 3.3 GPa (EA), 12.7 ± 1.9 GPa (TA) and 18.5 ± 3.2 GPa (LA – the top layer of EA). The hardness in EA and LA materials is almost identical. This experimental finding is in agreement with the layered design, where EA is in the outer-layer region (indenting surface). Furthermore, it can be noticed that the hardness of TA (basal) is slightly lower than the EA and the laminate counterparts.

3.4 Effect of temperature on the indentation flexural strength

Figure 5 shows the indentation strength results for the monolithic EA, TA and LA samples tested in a vacuum at different temperatures.

In monolithic EA, the strength determined from bending tests at room temperature was 143 ± 2 MPa. The bending strength exhibited slightly increased values at testing temperatures of 500 °C (174 MPa) and 800°C (176 MPa). At higher temperatures, the strength decreased to 155 ± 0.1 MPa for 1000°C and 146 ± 13 MPa for 1100°C. However, the bending strength at 1200 °C slightly increased again to a value of 165 ± 5 MPa.

In monolithic TA, the strength determined from bending tests at room temperature was 178 ± 6 MPa, which is approx. 25% higher than that of EA. At higher temperatures, a similar trend of increasing strength was observed, with a bending strength of 223 MPa and 234 MPa at temperatures of 500 °C and 800 °C, respectively (~30% higher than in EA). Beyond 800 °C the strength decrease is more pronounced than in EA. The corresponding strength of TA was 214 ± 16 MPa (at 1000 °C), 159 ± 16 MPa (at 1100 °C) and 123 ± 14 MPa (at 1200 °C), respectively. This may be explained by the sliding mechanisms of weak basal grains in the textured microstructure.

It is worth noting that in TA at testing temperatures 1000 °C and 1100 °C one out of three and at 1200 °C all three specimens were fractured at natural flaws. Since the dimension of natural flaws is in the range of the artificial Vickers cracks, the tests have been considered as valid.

The recognized increase in the indentation strength from room temperature to 800 °C for both EA and TA may be explained by crack blunting mechanisms acting at higher temperatures, as has been shown in alumina materials. The subsequent strength decrease after the highest peak may be associated with glass softening and plastic flow [42]. These effects in TA are connected to the content of the glassy phase (0.10 wt. %) from the slurry fabrication; however, in EA no additional glass-forming content was added, only very small Ca- (< 5 ppm), and Si-impurities (< 25 ppm) in the powder are listed in the data sheet [43]. The slight strength increase of EA at 1200 °C can be explained by "crack healing effects", as evidenced by SEM images (cp. Supplementary Fig. S1) by comparing the Vickers cracks prior to and after the testing condition (1200 °C/vacuum).

In laminate LA, the indentation strength at room temperature was 233 MPa, which is ~ 60 % and ~30 % higher than that measured in the monolithic EA and TA counterparts, respectively. The corresponding strength results obtained from bending tests performed at elevated temperatures indicate a decreasing trend, with values of ~ 225 MPa (at 500 °C), 215 MPa (at 800 °C), 183 ± 9 MPa (at 1000 °C) and 145 ± 1 MPa (at 1200 °C), respectively.

To study the effect of the atmosphere, the bending strength results for each system evaluated from tests conducted at room temperature in air, are depicted as references. The corresponding flexural strength for EA, TA and LA were 130 ± 2 MPa, 162 ± 10 MPa, and 218 MPa, respectively. These values obtained from air tests are approx. 10% lower than the one of the corresponding flexural strength values obtained from vacuum data for EA, TA and the laminate. This experimental finding may be subjected to subcritical crack growth, as has been observed for alumina in other works [44,45].

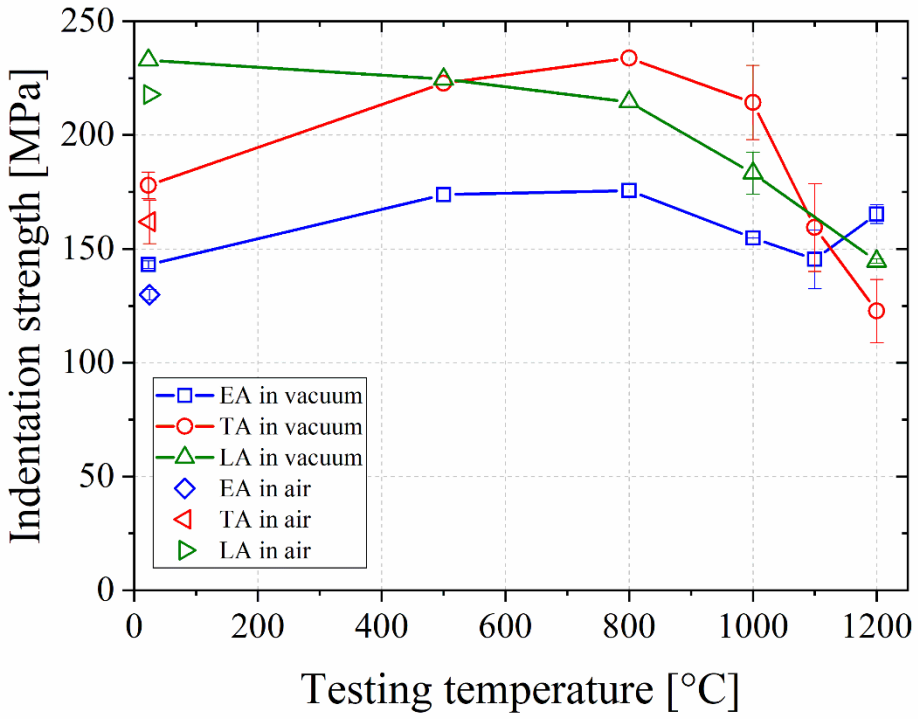

Fig. 5: Indentation flexural strength of pre-cracked EA, TA and LA samples as a function of the testing temperature. Symbols without scatter bars correspond to a single tested specimen with a defined crack size.

3.5. Analysis of stress-strain curves

Fig. 6 shows the converted stress-strain data of representative monolithic EA, TA and LA tested in a vacuum at different temperatures. The elastic moduli of all materials decreased with temperature (compare with Fig. 4a), as can be seen in the change of the slopes.

In the case of the EA samples, all the stress-strain curves show fully linear-elastic behaviour, before catastrophic failure. Interestingly, an increase in the strength from room temperature to higher temperatures is observable (Fig. 6a).

In the case of the TA samples, the stress-strain data indicate a transition at 800 °C from brittle "catastrophic" to more damage tolerant behaviour (Fig. 6c). The stress-strain curves show an increase in fracture strength up to a temperature of 800 °C, followed by a decrease up to 1200 °C. However, the fracture strain significantly increased between 800 °C to 1200 °C, which may be traced back to softening of the glassy phase (transition temperature). The glass

transition temperature for several glasses within the CaO-Al_2O_3-SiO_2 was found to be ~ 780 °C [46], which is in good agreement with the experimentally observed transition to a more ductile behaviour due to softening effects of the glassy phase within TA at 800 °C.

In the case of the LA samples, the maximum fracture stress decreased with the testing temperature (Fig. 6e). All the stress-strain curves show pop-in events at a stress-levels of ~160 MPa – 175 MPa from room temperature to 800 °C, associated with the (stable) growth of surface indentation cracks prior to failure. At these stress-levels, the propagation of the artificial surface cracks is limited to the first embedded TA layer, which acts as a barrier to crack propagation due to the presence of the in-plane compressive residual stresses. This well-known damage-tolerant behaviour of layered ceramics with tailored compressive residual stresses has been extensively studied at room temperature [7,8,47,48]. As it can be seen in Fig. 6, the pop-in stresses of the laminate are almost comparable with the maximum fracture stresses of the EA, the slight difference may be corresponding to the tensile residual stresses in the outer EA-layer of the multilayer. Furthermore, it is revealed that the maximum flexural stress of the tested laminates is significantly lower at 1200 °C as compared to low-temperature tests, which may be explained by the reduction of the magnitude of compressive residual stresses within the embedded layers (see Fig. 4c). Nevertheless, a change in slope can be observed at 1200 °C (see detail in Fig. 6e), which indicates the positive effect of the textured microstructure deflecting the crack. For a better understanding of these findings, the fracture behaviour, as well as fracture resistance of the different layered alumina architectures, is discussed in the following section.

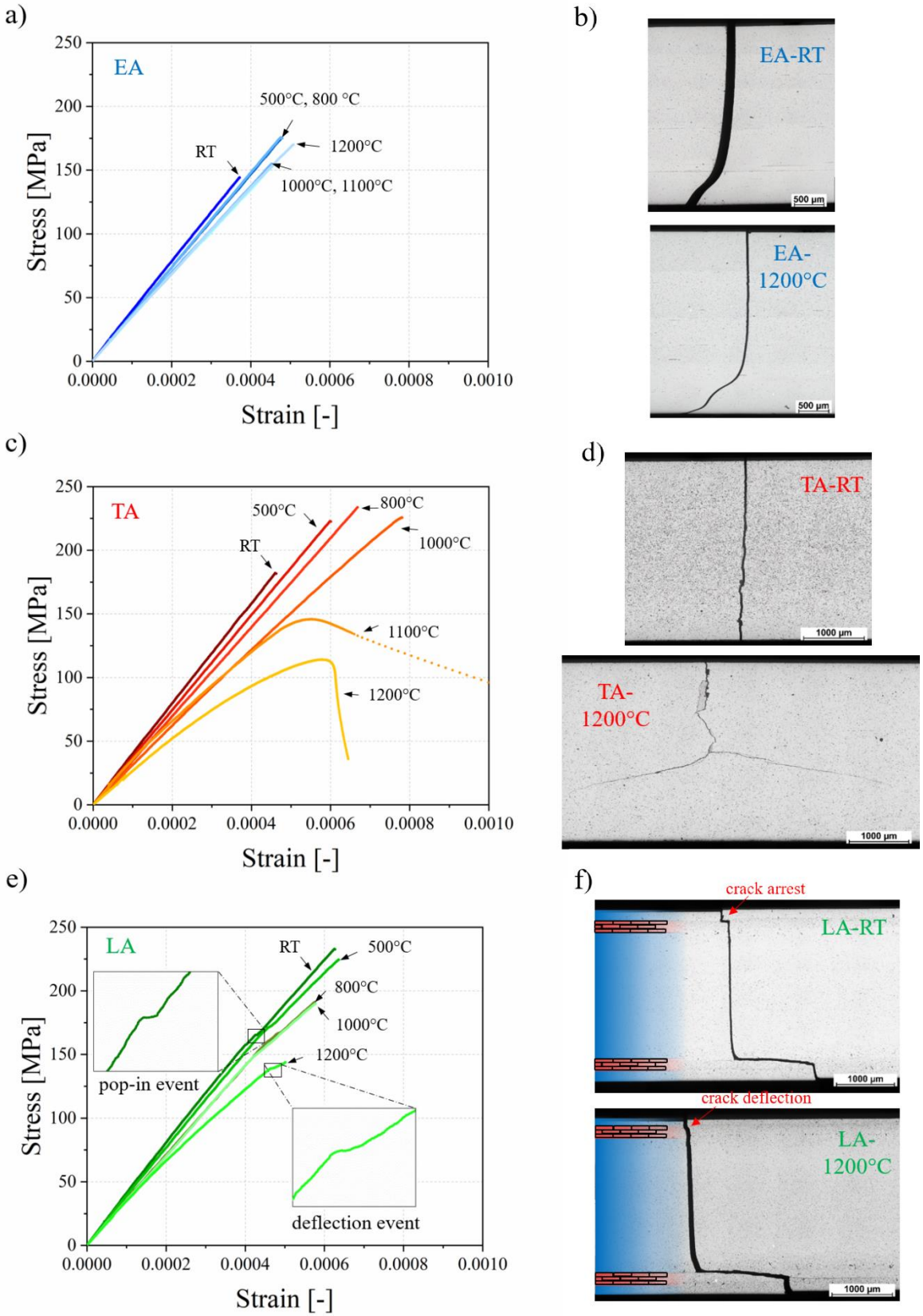

Fig. 6: Flexural stress – strain curves of 4-point bending test recorded from room temperature to 1200 °C and representative corresponding fracture paths for (a, b) EA, (c, d) TA and (e, f) the laminate.

3.6. Fracture behaviour

Fig. 7a shows the "inelastic" work of fracture (WOF) plotted over the temperature for EA, TA and LA samples. In order to evaluate the amount of plastic deformation during the fracture process, the inelastic WOF was normalized by the total fracture and is represented as the WOF ratio (in %) in Fig. 7b for all three systems as a function of the testing temperature.

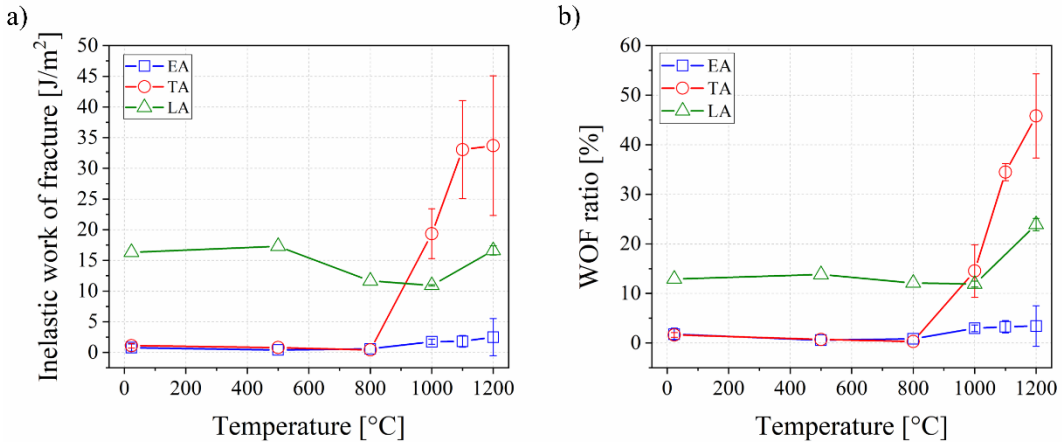

Fig. 7: (a) Inelastic work of fracture and (b) and WOF-ratio (Inelastic work of fracture in respect to total work of fracture) of the monoliths (EA, TA) and the laminate (LA), respectively.

In the case of monolithic EA, the inelastic work of fracture was determined as ~ 1 J/m^2, or as ~2% of the total work of fracture (WOF ratio), independently on the testing temperature. This finding explains well the brittle behaviour of the EA-monoliths with the absence of any significant plasticity even up to temperatures of 1200 °C.

The monolithic TA shows a similar trend up to temperatures of 800 °C with an inelastic work of fracture of only ~ 1 J/m^2, corresponding to a WOF-ratio of approx. 1%. However, at the transition temperature of 800 °C, a rising trend of the inelastic WOF, as well as the WOF ratio, can be observed, with a maximum at 1200 °C of ~ 34 ± 11 J/m^2 (i.e., 46 ± 8 %). The so-derived amount of plasticity of almost 50% confirms the damage-tolerant behaviour of TA during high-temperature testing conditions.

In the case of LA samples, the calculated inelastic WOF was ~ 15 J/m^2 over the entire tested temperature range. The corresponding WOF-ratio of the laminates tested from room temperature to 800 °C was ~13% and is significantly higher than that of the EA and TA counterparts. This finding can be explained by the existence of the compressive residual stresses within the embedded TA-layers, enhancing the fracture resistance of the laminate. At the highest temperature of 1200 °C, the WOF-ratio of the laminate is almost 25%, which could be related to the contribution of the quasi-plastic behaviour of the embedded TA-layers at high temperatures.

3.7 Fractographic analyses

Fracture in EA-specimens was initiated from artificially introduced surface cracks (Vickers imprints) over all testing temperatures. Figure 6b shows representative fracture paths of the monolithic EA samples, tested at RT and 1200°C respectively. The crack follows a rather straight path during the fracture process with only deviations at the compressive side (compressive curls). In this case, no differences in the fracture behaviour of EA at different testing temperatures are observable. A detailed analysis of the fracture surfaces shows a typical “half-penny” shaped Vickers crack of an EA-sample tested at 1200 °C (Fig. 8).

The initial surface crack from indenting is indicated by white arrows. Post-mortem analyses revealed that during high-temperature tests the initial surface crack extended during the test to its final critical length, associated with subcritical crack growth. The extended crack is designated by yellow arrows (Fig. 8). It may be noted that there is a transition from transgranular (indented at room temperature) to intergranular fracture during subcritical crack growth at high-temperature bending, as observed in other ceramic materials [49]. The transition zone is highlighted on the magnified image within the yellow window in Fig. 8.

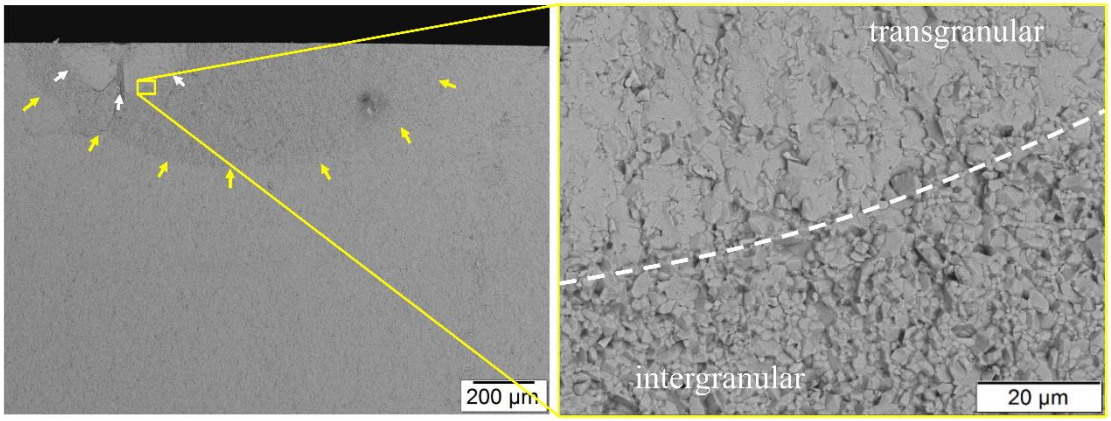

Fig. 8: Artificial crack as fracture origin within EA-sample tested at 1200 °C: The initial crack is indicated by white arrows and the extended one due to subcritical crack growth is marked by yellow arrows. The transition from transgranular to intergranular fracture is highlighted by the white dashed line within the yellow window.

The intergranular fracture pattern of the TA-sample during room temperature bending tests (see Fig. 6d top) follows a straight path in a step-like manner along the grain boundaries of the textured microstructure, as has already been discussed in other work [29,50]. Up to 800 °C, the fracture behaviour of TA-samples does not significantly change. Above this "transition" temperature of 800 °C, the crack is more favoured to propagate along the weak basal grain boundaries which result in deflections, and/or crack bifurcations, as can be seen on TA tested at 1200 °C (Fig. 6d bottom). Details on the fracture path are shown in Fig. 9, where the favoured crack path along weak basal grain boundaries is evident. These acting energy-dissipating mechanisms enhance significantly the fracture energy of TA at elevated temperatures, which agrees with the calculated work of fracture in Fig.7.

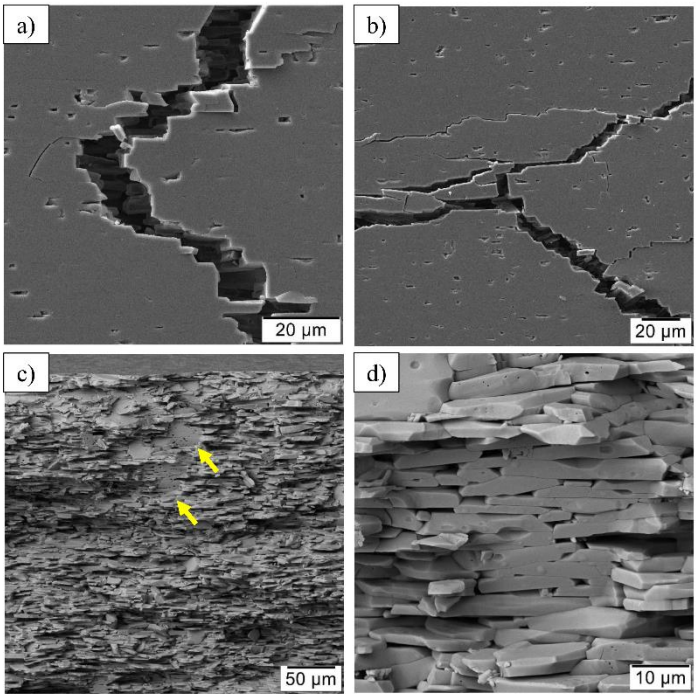

Fig. 9: (a, b) Favoured crack path along weak basal grain boundaries during high-temperature bending. (c) TA-sample tested at 1200 °C shows fracture at natural flaws (platelet sliding indicated with yellow origin) and (d) higher magnification of (c).

Some natural defects were identified as locations where several platelets may be oriented with the basal surface perpendicular to the applied stress field (see Fig. 9c). For instance, such a misaligned textured grain can be seen in the EBSD image of Fig. 3a (coloured as purple grain). During bending at high temperatures, the basal surfaces may be favoured due to softening or weakening of the grain boundaries for shear-sliding and as long as the total size of the cluster of misaligned platelets is in the order of the artificial defect size (or even higher), the fracture could also occur on such natural flaws. Fig. 9d shows clearly an area of missing platelets oriented with its [0001] direction perpendicular to the fracture surface. Furthermore, an intergranular fracture path along the textured grains can be seen on those fracture surfaces, which is commonly observed at low velocities of fracture as discussed in the work of Hall et. al. [50].

In contrast to that, the crack path of the laminate tested at room temperature indicates crack stop and deflection events at the EA/TA-interface as well as within the embedded TA-layer (see Fig. 6f top). These phenomena may be associated with a combined effect of compressive residual stresses and the textured microstructure, which is related to the above-mentioned pop-in events in the recorded stress – strain curves. The positive effect of texturing the microstructure has been evidenced in a recent work, where the micro-scale fracture toughness of basal grain

boundaries was ~30% lower than that of textured grains, explaining favoured microstructure-related deflection mechanisms during the fracture process [51]. Although a significant reduction of the compressive residual stresses has been proven at elevated temperature (Fig. 4c), deviations of the crack path within the TA-layers are visible (see Fig. 6f bottom). Therefore, it can be concluded that the deflection mechanisms acting at 1200 °C are the result of the textured microstructure, where the crack is favoured along the rather weak basal grain boundaries.

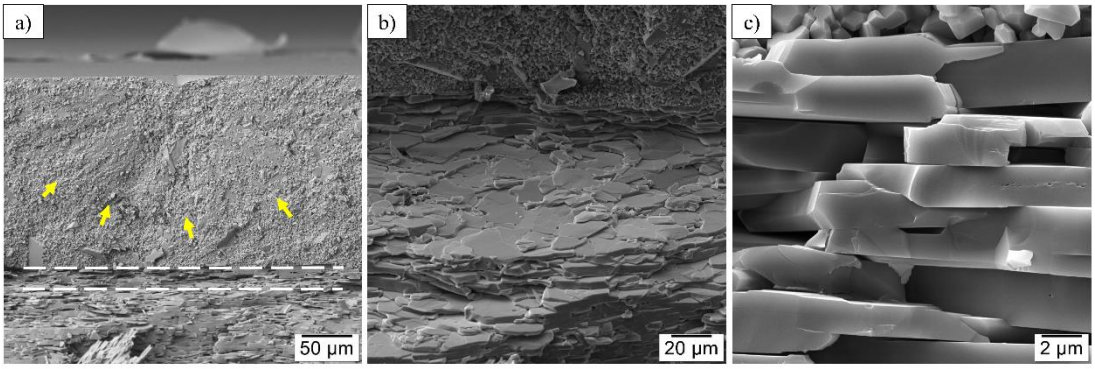

Fig. 10: Artificial Vickers crack as fracture origin in the laminate sample tested at 1200 °C: (a) The initial crack as well as the transition zone is indicated by yellow arrows and white dashed lines, respectively. (b) Tilted SEM images of the EA/TA interface region. (c) Textured grains within the transition zone.

Figure 10 shows a typical half-penny shaped Vickers crack introduced on the EA-outermost layer of the LA specimens tested at 1200 °C. The initial half-penny surface crack is indicated by yellow arrows in Fig. 10a. At high-temperature bending tests, the crack path is favoured to enter several microns into the EA/TA-interface (transition zone, see white dashed lines in Fig 10a) during the pop-in event prior to deflections along the basal grain boundaries of the textured platelets. Similar observations were found during room-temperature bending tests of laminates with embedded textured layers in the work of Pavlacka et al. [52]. Although the compressive residual stresses within the TA-layer may be negligible at 1200 °C, the fracture path is still likely to follow the basal boundaries of the textured grains (deflection mechanisms) after entering the interface. The contribution of the textured microstructure within laminates architectures for further enhancing the damage tolerance of ceramic systems is proven to be effective even under severe testing conditions (up to 1200 °C). Those dominating deflection mechanisms over several grains within the TA-region of the laminate are illustrated in Fig. 10b.

A high magnified micrograph of a few textured grains within the TA-region of the laminate is shown in Fig. 10c, which indicates the effect of the well-developed textured grains in deflecting the propagating crack.

4. Conclusions

The high-temperature fracture behaviour of monolithic samples with textured microstructure and a laminate design with embedded textured layers were investigated by 4-point bending tests at elevated temperatures and compared to the reference material with non-textured (equiaxed) microstructure. In the case of textured alumina, a transition from brittle to more reliable (damage-tolerant) behaviour was observed at high temperatures (> 800 °C), with increasing fracture energy up to a maximum at 1200 °C, associated with crack deflection events along weak boundaries of the textured grains. In laminates with embedded textured layers damage tolerance is achieved at room temperature due to the effect of compressive stresses, and for temperatures above 800 °C associated with the textured microstructure. The combination of different mechanisms acting at different temperatures may open new paths for designing ceramic systems for high-temperature applications.

Acknowledgements

Funding for this research was provided by the European Research Council (ERC) excellent science grant “CERATEXT” through the Horizon 2020 program under contract 817615.

References

[1] P.F. Becher, Microstructural Design of Toughened Ceramics, J. Am. Ceram. Soc. 74 (2) (1991) 255–269. https://doi.org/10.1111/j.1151-2916.1991.tb06872.x.

[2] R.C. Bradt, D. Munz, M. Sakai, K.W. White, Fracture Mechanics of Ceramics, Springer US, Boston, MA, 2005.

[3] L. Cheng, M. Sun, F. Ye, Y. Bai, M. Li, S. Fan, L. Zhang, Structure design, fabrication, properties of laminated ceramics: A review, Int. J. Lightweight Mater. Manuf. 1 (2018) 126–141. https://doi.org/10.1016/j.ijlmm.2018.08.002.

[4] D.J. Green, R. Tandon, V.M. Sglavo, Crack arrest and multiple cracking in glass through the use of designed residual stress profiles, Science 283 (5406) (1999) 1295–1297.

[5] J. Pascual, T. Lube, R. Danzer, Fracture statistics of ceramic laminates strengthened by compressive residual stresses, J. Eur. Ceram. Soc. 28 (8) (2008) 1551–1556. https://doi.org/10.1016/j.jeurceramsoc.2007.10.005.

[6] M.E. Nordberg, E.L. Mochel, H.M. Garfinkel, J.S. Olcott, Strengthening by Ion Exchange, J. Am. Ceram. Soc. 47 (5) (1964) 215–219. https://doi.org/10.1111/j.1151-2916.1964.tb14399.x.

[7] M. Rao, J. Sanchez-Herencia, G. Beltz, R.M. McMeeking, F. Lange, Laminar ceramics that exhibit a threshold strength, Science 286 (1999) 102–105.

[8] V.M. Sglavo, M. Paternoster, M. Bertoldi, Tailored Residual Stresses in High Reliability Alumina-Mullite Ceramic Laminates, J. Am. Ceram. Soc. 88 (10) (2005) 2826–2832. https://doi.org/10.1111/j.1551-2916.2005.00479.x.

[9] R. Bermejo, Y. Torres, C. Baudín, A.J. Sánchez-Herencia, J. Pascual, M. Anglada, L. Llanes, Threshold strength evaluation on an Al_2O_3–ZrO_2 multilayered system, J. Eur. Ceram. Soc. 27 (2) (2007) 1443–1448. https://doi.org/10.1016/j.jeurceramsoc.2006.05.037.

[10] A. Costabile, V.M. Sglavo, Influence of the Architecture on the Mechanical Performances of Alumina-Zirconia-Mullite Ceramic Laminates, Adv. Sci. Technol. 45 (2006) 1103–1108. https://doi.org/10.4028/www.scientific.net/AST.45.1103.

[11] V.M. Sglavo, F. de Genua, A. Molinari, F. Casari, Alumina/Silicon Carbide Laminated Composites by Spark Plasma Sintering, J. Am. Ceram. Soc. 92 (11) (2009) 2693–2697. https://doi.org/10.1111/j.1551-2916.2009.03247.x.

[12] R. Bermejo, Y. Torres, A.J. Sánchez-Herencia, C. Baudín, M. Anglada, L. Llanes, Residual stresses, strength and toughness of laminates with different layer thickness ratios, Acta Mater. 54 (2006) 4745–4757. https://doi.org/10.1016/j.actamat.2006.06.008.

[13] E. Lara-Curzio, E. Cakmak, L. Lin, A.E. Marquez-Rossy, B. Armstrong, A. Flores-Betancourt, A. Macias, On the nonlinear temperature dependence of residual stresses in solid oxide fuel cells, J. Am. Ceram. Soc. 104 (2) (2021) 1014–1022. https://doi.org/10.1111/jace.17488.

[14] R. Bermejo, A.J. Sánchez-Herencia, L. Llanes, C. Baudín, High-temperature mechanical behaviour of flaw tolerant alumina–zirconia multilayered ceramics, Acta Mater. 55 (2007) 4891–4901. https://doi.org/10.1016/j.actamat.2007.05.005.

[15] X. Chen, G. Bei, Toughening Mechanisms in Nanolayered MAX Phase Ceramics-A Review, Materials (Basel) 10 (2017). https://doi.org/10.3390/ma10040366.

[16] K.K. Chawla, Ceramic Matrix Composites: Second Edition, Springer US, Boston, MA, s.l., 2003.

[17] V. Fiore, T. Scalici, G. Di Bella, A. Valenza, A review on basalt fibre and its composites, Compos. B. Eng. 74 (2015) 74–94. https://doi.org/10.1016/j.compositesb.2014.12.034.

[18] L.M. Rueschhoff, C.M. Carney, Z.D. Apostolov, M.K. Cinibulk, Processing of fiber-reinforced ultra-high temperature ceramic composites: A review, Int. J. Ceramic Eng. Sci. 2 (2020) 22–37. https://doi.org/10.1002/ces2.10033.

[19] F.F. Lange, Relation Between Strength, Fracture Energy, and Microstructure of Hot-Pressed Si_3N_4, J. Am. Ceram. Soc. 56 (10) (1973) 518–522. https://doi.org/10.1111/j.1151-2916.1973.tb12401.x.

[20] R.J. Pavlacka, G.L. Messing, Processing and mechanical response of highly textured Al_2O_3, J. Eur. Ceram. Soc. 30 (14) (2010) 2917–2925. https://doi.org/10.1016/j.jeurceramsoc.2010.02.009.

[21] A.-K. Hofer, I. Kraleva, R. Bermejo, Additive manufacturing of highly textured alumina ceramics, Open Ceramics 5 (2021) 100085. https://doi.org/10.1016/j.oceram.2021.100085.

[22] T.S. Suzuki, T. Uchikoshi, Y. Sakka, Control of texture in alumina by colloidal processing in a strong magnetic field, Sci. Technol. Adv. Mater. 7 (2006) 356–364. https://doi.org/10.1016/j.stam.2006.01.014.

[23] Z. Yang, J. Yu, C. Li, Y. Zhong, W. Xuan, Z. Ren, Q. Wang, Y. Dai, H. Wang, Preparation of textured porous Al_2O_3 ceramics by slip casting in a strong magnetic field and its mechanical properties, Cryst. Res. Technol. 50 (2015) 645–653. https://doi.org/10.1002/crat.201500080.

[24] S. Ruppi, Deposition, microstructure and properties of texture-controlled CVD α-Al_2O_3 coatings, Int. J. Refract. Met. Hard Mater. 23 (2005) 306–316. https://doi.org/10.1016/j.ijrmhm.2005.05.004.

[25] T. Carisey, A. Laugier-Werth, D.G. Brandon, Control of texture in Al2O3 by gel-casting, J. Eur. Ceram. Soc. 15 (1) (1995) 1–8. https://doi.org/10.1016/0955-2219(95)91293-W.

[26] M.M. Seabaugh, I.H. Kerscht, G.L. Messing, Texture Development by Templated Grain Growth in Liquid-Phase-Sintered α-Alumina, J. Am. Ceram. Soc. 80 (5) (1997) 1181–1188. https://doi.org/10.1111/j.1151-2916.1997.tb02961.x.

[27] U.G.K. Wegst, H. Bai, E. Saiz, A.P. Tomsia, R.O. Ritchie, Bioinspired structural materials, Nat. Mater. 14 (2015) 23–36.

[28] R. Bermejo, "Toward seashells under stress": Bioinspired concepts to design tough layered ceramic composites, J. Eur. Ceram. Soc. 37 (13) (2017) 3823–3839. https://doi.org/10.1016/j.jeurceramsoc.2017.04.041.

[29] A.-K. Hofer, R. Walton, O. Ševeček, G.L. Messing, R. Bermejo, Design of damage tolerant and crack-free layered ceramics with textured microstructure, J. Eur. Ceram. Soc. 40 (2) (2020) 427–435. https://doi.org/10.1016/j.jeurceramsoc.2019.09.004.

[30] EN 623-3, Advanced technical ceramics - Monolithic ceramics - General and textural properties-Part 3: Determination of grain size, 1993.

[31] F.K. Lotgering, Topotactical reactions with ferrimagnetic oxides having hexagonal crystal structures—I, J. Inorg. Nucl. Chem. 9 (1959) 113–123. https://doi.org/10.1016/0022-1902(59)80070-1.

[32] EN 623-2, Advanced technical ceramics – Monolithic ceramics – General and textural properties – Part 2: Determination of density and porosity, 1993.

[33] ASTM E1876-15, Standard Test Method for Dynamic Young's Modulus, Shear Modulus, and Poisson's Ratio by Impulse Excitation of Vibration, 2015.

[34] EN 843-1, Advanced technical ceramics - Monolithic ceramics- Mechanical properties at room temperature - Part 1: Determination of flexural strength, 1995.

[35] J. Nakayama, Direct Measurement of Fracture Energies of Brittle Heterogeneous Materials, J. Am. Ceram. Soc. 48 (11) (1965) 583–587. https://doi.org/10.1111/j.1151-2916.1965.tb14677.x.

[36] R.O. Ritchie, K.J. Koester, S. Ionova, W. Yao, N.E. Lane, Ager, J W, 3rd, Measurement of the toughness of bone: a tutorial with special reference to small animal studies, Bone 43 (2008) 798–812. https://doi.org/10.1016/j.bone.2008.04.027.

[37] Y. Sun, H. Xie, L. Liu, Q. Kou, S. Zhang, B. Yang, W. Cao, Y. Chang, Enhanced mechanical properties in ceramic multilayer composites through integrating crystallographic texture and second-phase toughening, Ceram. Int. 47 (22) (2021) 31222–31228. https://doi.org/10.1016/j.ceramint.2021.07.298.

[38] M. Zhang, Y. Chang, R. Bermejo, G. Jiang, Y. Sun, J. Wu, B. Yang, W. Cao, Improved fracture behavior and mechanical properties of alumina textured ceramics, Mater. Lett. 221 (2018) 252–255. https://doi.org/10.1016/j.matlet.2018.03.123.

[39] J.B. Wachtman JR, W.E. Tefft, D.G. Lam JR, R.P. Stinchfield, Elastic Constants of Synthetic Single Crystal Corundum at Room Temperature, J. Res. Natl. Bur. Stand. A Phys. Chem. 64A (1960) 213–228. https://doi.org/10.6028/jres.064A.022.

[40] R.G. Munro, Evaluated Material Properties for a Sintered alpha-Alumina, J. Am. Ceram. Soc. 80 (8) (1997) 1919–1928. https://doi.org/10.1111/j.1151-2916.1997.tb03074.x.

[41] Z. Chlup, H. Hadraba, D. Drdlik, K. Maca, I. Dlouhy, R. Bermejo, On the determination of the stress-free temperature for alumina–zirconia multilayer structures, Ceram. Int. 40 (4) (2014) 5787–5793. https://doi.org/10.1016/j.ceramint.2013.11.018.

[42] R. Morrell, Handbook of properties of technical & engineering ceramics: An introduction for the engineer and designer, Reprinted with corrections, H.M.S.O, London, 1989.

[43] Product Description (Specification) − Aluminium oxide Taimicron TM-DAR, 2021.

[44] T. Fett, W. Hartlieb, K. Keller, B. Knecht, D. Münz, W. Rieger, Subcritical crack growth in high-grade alumina, J. Nucl. Mater. 184 (1991) 39–46. https://doi.org/10.1016/0022-3115(91)90530-K.

[45] J.E. Webb, K. Jakus, J.E. Ritter, R-curve and subcritical crack growth behavior at elevated temperatures in coarse grain alumina, Acta Mater. 44 (1996) 2259–2264. https://doi.org/10.1016/1359-6454(95)00361-4.

[46] U. Veit, C. Rüssel, Y. Houet, D. Laurent, Viscosity and Liquidus Temperature of Ternary Glasses Close to the Eutectic Composition in the CaO–Al2O3–SiO2 System, Int. J. Appl. Glass Sci. 7 (2016) 295–309. https://doi.org/10.1111/ijag.12191.

[47] V.M. Sglavo, N. Bellettati, Ceramic laminates with improved mechanical reliability by tailoring the porosity of the constituting layers, J. Eur. Ceram. Soc. 37 (4) (2017) 1643–1650. https://doi.org/10.1016/j.jeurceramsoc.2016.11.022.

[48] R. Bermejo Moratinos, Y. Torres, M. Anglada, L. Llanes, Fatigue Behavior of Alumina-Zirconia Multilayered Ceramics, J. Am. Ceram. Soc. 91 (2008) 1618–1625. https://doi.org/10.1111/j.1551-2916.2008.02336.x.

[49] G. Quinn, Fractography of Ceramics and Glasses. NIST Special Publication 960-16, US Government Printing Office, Washington, 2016.

[50] P.W. Hall, J.S. Swinnea, D. Kovar, Fracture Resistance of Highly Textured Alumina, J. Am. Ceram. Soc. 84 (7) (2001) 1514–1520. https://doi.org/10.1111/j.1151-2916.2001.tb00870.x.

[51] J. Schlacher, T. Csanádi, M. Vojtko, R. Papšík, R. Bermejo, Micro-scale fracture toughness of textured alumina ceramics, J. Eur. Ceram. Soc. (2022). https://doi.org/10.1016/j.jeurceramsoc.2022.06.028.

[52] R. Pavlacka, R. Bermejo, Y. Chang, D. Green, G. L. Messing, T. Parthasarathy, Fracture Behavior of Layered Alumina Microstructural Composites with Highly Textured Layers, J. Am. Ceram. Soc. 96 (2013). https://doi.org/10.1111/jace.12292.

Supplementary information

for

High-temperature fracture behaviour of layered alumina ceramics with textured microstructure

Josef Schlacher[1*], Zdeněk Chlup[2], Anna-Katharina Hofer[1], Raul Bermejo[1]

[1] Department of Materials Science, Montanuniversität Leoben, Franz Josef Strasse 18, A-8700, Leoben, Austria

[2] Institute of Physics of Materials, Czech Academy of Sciences, Zizkova 22, 616 62 Brno, Czech Republic

*Corresponding author's email: josef.schlacher@unileoben.ac.at

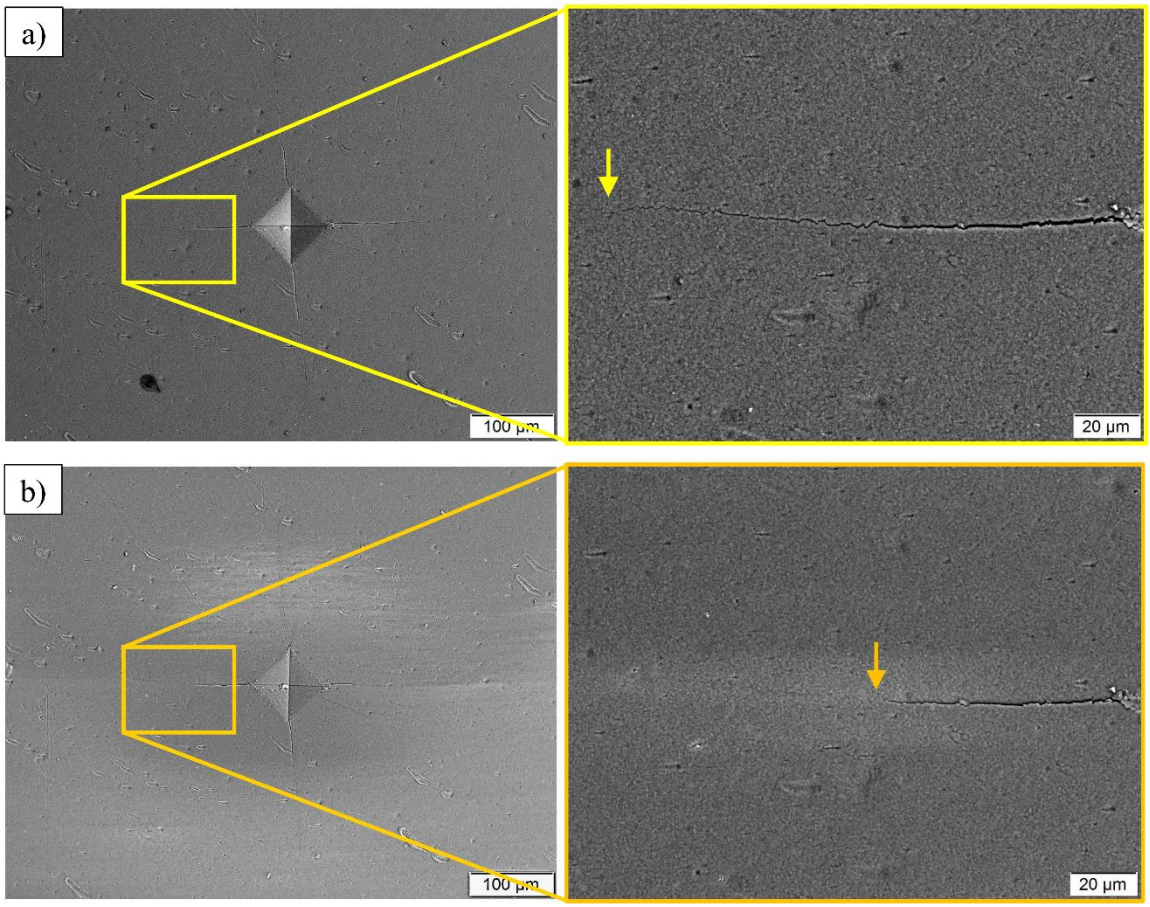

Supplementary Figure S1: The Vickers imprints (HV10) with emanating cracks is shown (a) prior and (b) after heat treatment at 1200°C for 1 h in vacuum. The crack tips are indicated by arrows.

Publication D

Additive manufacturing of high-strength alumina through a multi-material approach

J. Schlacher, A.-K. Hofer, S. Geier, I. Kraleva, R. Papšík, M. Schwentenwein, R. Bermejo,

Open Ceramics 5 (2021) 100082

https://doi.org/10.1016/j.oceram.2021.100082

Additive manufacturing of high-strength alumina through a multi-material approach

Josef Schlacher[1*], Anna-Katharina Hofer[1], Sebastian Geier[2], Irina Kraleva[1], Roman Papšík[1], Martin Schwentenwein[2], Raul Bermejo[1]

[1] Department of Materials Science, Montanuniversität Leoben, Franz Josef Strasse 18, A-8700 Leoben, Austria

[2] Lithoz GmbH, Mollardgasse 85a/2/64-69, A-1060 Wien, Austria

*Corresponding author's email: josef.schlacher@unileoben.ac.at

Abstract

This work demonstrates the use of additive manufacturing to design and fabricate alumina ceramics with strength as high as 1GPa. A multi-material approach is employed by embedding alumina-zirconia layers between outer pure alumina layers with significant compressive residual stresses. Biaxial bending is performed both on the 3D printed multi-material and monolithic alumina parts. Results are analysed in the framework of Weibull statistics. A characteristic biaxial strength higher than 1 GPa is measured on the multilayers, compared to 650 MPa in monolithic alumina, the difference corresponding to the magnitude of compressive residual stresses due to the thermal mismatch between material regions during cooling from sintering. This is the first report of employing additive manufacturing to tailor the strength of alumina ceramics, taking advantage of the layer-by-layer printing process. Designing complex-shaped ceramic architectures with residual stresses through additive manufacturing opens a new path for fabrication of technical ceramics with tailored mechanical properties.

Keywords: Additive manufacturing, Alumina, Strength, Multi-material, Residual Stress.

1. Introduction

The outstanding properties of ceramics, such as biocompatibility, resistance to oxidation and corrosion, high-temperature stability, wear resistance as well as special thermal, electrical and optical characteristics, nominate them as major candidates for demanding technical applications [1]. The fabrication of ceramics components begins with the processing of powders and sintering of the compound, aiming to achieve a final microstructure of the material, which shall govern the structural and/or functional behaviour of the final part. In many cases, a post-processing or final shaping of the sintered ceramics parts or components is necessary for the

end application. This often requires a relatively expensive and time consuming machining process using diamond tools [2]. In case the end part requires a complex shape or geometry, final shaping may not be possible, hindering possible applications of ceramics for structural or functional devices. In an attempt to overcome such difficulties and extend the ceramic market, additive manufacturing has been established as a promising technology to fabricate parts and components with almost no limitation in design-complexity. The latest advances in additive manufacturing of ceramics are discussed in the following works [3,4].

The recent progress in the field of stereolithographic 3D-printing techniques, in particular Lithography-based Ceramic Manufacturing technology (LCM), has led to major advances in fabricating bulk ceramic materials with mechanical properties comparable to those of ceramics manufactured through traditional routes [5]. This novel LCM-printing system consists of a building platform which is lowered into a transparent rotating vat, filled with a photosensitive ceramic-polymer slurry. During the layer-by-layer printing process, the slurry is exposed by light through a projection system from below (see Ref. [6] for more details). After printing, the ceramic green-bodies are removed from the building-platform. The post-processing includes cleaning of the part, binder burn-out and finally sintering to obtain a highly dense ceramic part [4,7–9]. Controlling powder characteristics, using appropriate binder systems, as well as tailoring and optimizing the sintering curves, have been key elements in the (rather fast) development of the LCM technology. An example of successful application of LCM technology has been demonstrated in alumina ceramics, where high mechanical strength with relatively low scatter has been measured [10]. This raises the question whether it may be possible to utilize the layer-by-layer deposition process to fabricate multi-material systems with enhanced mechanical properties.

In recent years, much effort has been directed to designing ceramic based multi-material architectures with improved strength and/or toughness, and in some cases enhanced reliability. The combination of layers containing different ceramic materials, connected with strong interfaces, has enabled tailoring alternating in-plane residual stresses (i.e. tensile and compressive), caused by different thermal strains in the layers during cooling down from the sintering temperature [11]. The location of the compressive stress layers, either at the surface layer or embedded in the architecture, has been associated with the final application, either to increase the mechanical strength [12,13] or enhance the resistance to fracture and/or crack propagation (so-called damage tolerance) [14–16]. The former approach is based on the outstanding results achieved in “strengthened glasses”, concept first studied by Nordberg et al.

[17], and technically exploited, for instance, as in Gorilla® glass [18]. It has been also demonstrated the feasibility of this approach to improve the mechanical strength and the insensitivity to subcritical crack growth [19].

The aim of this work is to demonstrate the capabilities of LCM technology to fabricate alumina ceramics with unprecedented high strength, based on a multi-material approach. Using a layer-by-layer deposition of different materials, tailored compressive residual stresses may be introduced in the surface layers, aiming to increase the strength and reliability of the ceramic material, compared to its bulk properties. Based on the progress and developments in the sector of stereolithographic printing techniques, a LCM-printer has been adapted by using a two vat system with separated filled slurries to enable the 3D-printing of alternated alumina and alumina-zirconia layers. Biaxial strength is measured on both monolithic and multilayer materials, and analysed within the framework of Weibull theory. Microstructural and fractographic analyses are performed to interpret the results. The consequence of introducing compressive stresses on the reliability of the ceramic parts is also discussed. It is shown how combining the advances of additive manufacturing and the multi-material ceramic approach can open a new pathway for designing complex 3D-printed ceramic systems.

2. Experimental

2.1. Materials of study and samples

In order to evaluate the strength under biaxial bending discs-shaped samples were fabricated by using the LCM-technology. The materials employed in this work were LithaLox MS548 (Lithoz GmbH, Austria), a photocurable suspension that is based on alumina (powder particle size, $d_{50} < 250$ nm), and LithaLox ZTA20 (Lithoz GmbH, Austria), a photocurable suspension (powder particle size, $d_{50} < 200$ nm) that is based on alumina and zirconia (3% mol. yttria stabilized zirconia) in a total ratio of 80%vol. alumina and 20%vol. zirconia. Bulk samples (both discs and prismatic bars) of alumina (A) and prismatic bars of alumina-zirconia (ZTA) were fabricated for characterization of material properties. Multilayer disc samples (A-ZTA-A) with ZTA layers embedded between the (A) surface layers, were fabricated for mechanical testing. Bulk materials were printed using a CeraFab 7500-printer (Lithoz GmbH, Vienna, Austria), whereas multilayers were manufactured employing a novel CeraFab Multi 2M30-printer (Lithoz GmbH, Vienna, Austria) [20]. Both the (A) and (ZTA) layers consist of several thin individual layers. The thickness of each printed layer was chosen to be approx. 25 µm in the green state. Both printer have a lateral resolution of 40 µm. During printing, each layer was

exposed with 180 mJ/cm^2 which corresponds to an exposure time of 2 s with a projector power of 90 mW/cm^2. All samples were sintered at 1600 °C for 2 h with a heating rate of 1 °C/min, respectively.

The building up of the multilayer as well as the monolithic samples can be seen schematically in Fig. 1 (a). Both types of samples were printed in "lying direction", where the printing direction is in the thickness direction of the discs. All the discs show a nominal sintered dimension of D ~10 mm in diameter and t ~0.8–1.0 mm in thickness. In the multilayers, the aimed total layer thickness after sintering was chosen to be 70 µm for the A-region (each side) and 700 µm for the ZTA-region, thus corresponding to a volume ratio V_A/V_{ZTA} of ~1/5.

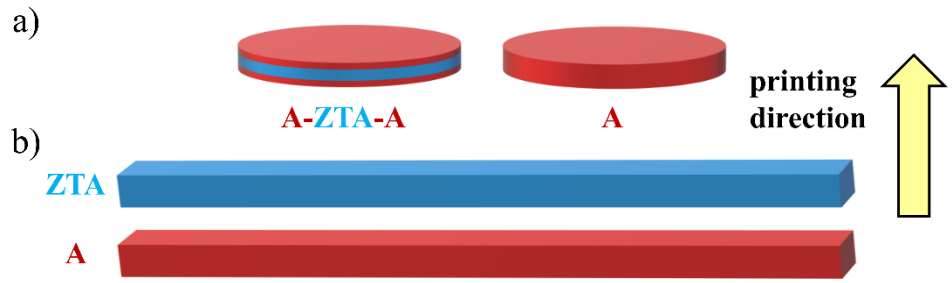

Fig. 1: Schematic of the 3D-printed a) A-ZTA-A-laminate (left) and the A-monolithic (right) disc-shaped samples as well as b) monolithic bars in respect to the printing direction (arrow).

Furthermore, monolithic bend bars with the dimensions of ~3 mm × 4 mm x 50 mm of both A and ZTA materials were also printed to measure thermal expansion coefficient, elastic modulus, and fracture toughness of the bulk materials. All bend bars were also printed in "lying" direction, as illustrated in Fig. 1 (b).

2.2. Microstructural analysis

In order to investigate the microstructure of the monolithic A- as well as multilayer A/ZTA/A-disc samples, cross-sections of the printed discs (perpendicular to the printing direction) were prepared and polished to 1 µm mirror finish using a Struers RotoForce4 equipment. After polishing samples were thermally etched at 1400 °C for 20 min. Subsequently, the cross-sections of the specimens were coated using an Agrar Sputter Coater and images were taken using a SEM Scanning electron microscope (JEOL JCM-6000Plus, Neoscope™, JEOL Ltd., Tokyo, Japan).

2.3. Materials properties

2.3.1. Density

The bulk densities of the monolithic as well as multilayer samples were determined using the Archimedes method according to EN623 - 2 [21]. The theoretical densities ρ_{th} of alumina and ZTA were $\rho_{th,A} = 3.986$ g/cm^3 and $\rho_{th,ZTA} = 4.39$ g/cm^3, as stated by the supplier, respectively. In the case of the A/ZTA/A-multilayer systems, the theoretical density was calculated using the rule of mixture, taking into account the volume ratio V_A/V_{ZTA} of ~0.2 of the layered composite. The corresponding relative densities ρ_{rel} of the monolithic and the multilayer systems were evaluated as $\rho_{rel} = \rho/\rho_{th}$.

2.3.2. Young's modulus

The measurement of the elastic moduli on the monolithic A- and ZTA-bars was performed under 3-point bending using a fixture with 40 mm outer span in a universal testing machine (Messphysik, Microstrain, Fürstenfeld, Austria) with a 100 N loading cell. All the tests were performed under displacement control using a crosshead speed of 0.5 mm/min in ambient conditions (24 °C and ~30 % relative humidity). Following the EN 843-2 standards [22], the load-displacement curves during alternate loading/unloading of 3 samples per material were registered by selecting a preload of 1 N and a maximum load of 15 N and 35 N for A- and ZTA-bars, respectively.

2.3.3. Coefficient of thermal expansion

In order to determine the coefficient of thermal expansion (CTE) of the monoliths, prismatic bars for each material (A and ZTA) with a standardized length of 25 mm were heated up from 30 °C to 900 °C using a dilatometer (Netzsch – Thermal Analysis, 95100 Selb, Germany). A heating rate of 5 °C/min, holding time of 1 h for each 100 °C segment and subsequently cooling rate of 5 °C/min was used. The change in length was registered during heating and cooling. For the CTE calculations, the room temperature (25 °C) was selected as reference temperature. Two bars were measured for each monolithic material.

2.3.4. Fracture Toughness

The fracture toughness of both monoliths, A and ZTA, was determined using the Single Edge V-Notched Beam (SEVNB)-method according to the ISO 23146 standards [23]. The notched specimens (8 per monolithic material) were tested using a 4-point bending fixture, with an outer span of 40 mm and an inner span of 20 mm, in a universal testing machine (Zwick 010,

Zwick/Roell Ulm, Germany) with a load cell of 200 N and a displacement rate of 0.5 mm/min at ambient conditions (24 °C and ~32% relative humidity).

2.4. Mechanical testing for the strength evaluation

All the monolithic as well as multi-material disc-shaped specimens were tested under biaxial bending using the Ball-on-Three-Balls (B3B)-test [24,25]. The testing setup can be schematically seen in Fig. 2. In B3B, one side of a disc (or plate)-shaped is symmetrically supported by three balls, the other side is loaded at the midpoint of the specimen through a fourth ball. During testing set-up, a defined pre-load is applied to guarantee contact between balls and specimen, and the "block" can be removed by lowering the "guide" (see schematic in Fig. 2). Subsequently, the applied force is constantly increased until fracture of the specimen is registered. Due to the fact that during the B3B-test only a small effective area or volume in the centre of the specimen is under biaxial stress, the influence of edge-defects could be neglected [26].

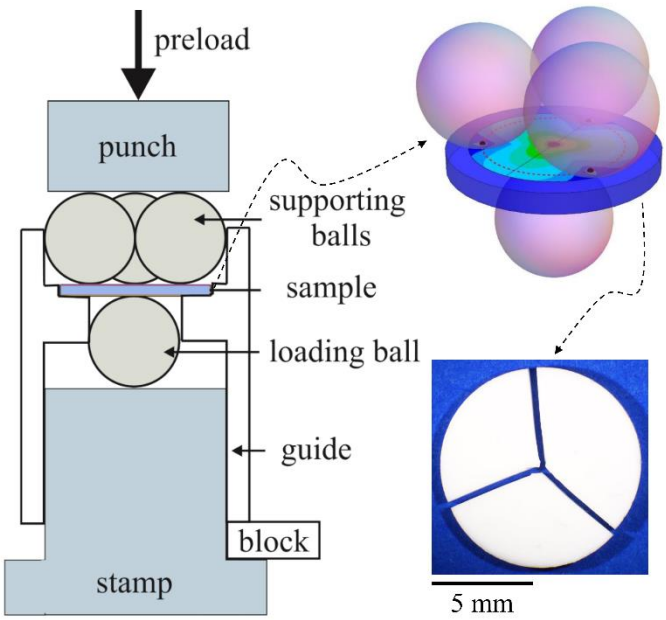

Fig. 2: Schematic of the B3B-testing setup.

All the B3B-tests were performed using a universal testing machine (Zwick 010, Zwick/Roell Ulm, Germany) with a load cell of 10 kN, a selected pre-load of 20 N and a displacement rate of 1 mm/min in ambient conditions (24 °C and ~25% relative humidity). The diameter of the

supporting balls as well as loading ball was chosen to be 6.35 mm. A total of 30 disc-shaped specimens per set (A and A/ZTA/A) were tested with the "as-printed" surface condition under tension.

2.5. Fractography

Identifying the critical size and location of failure origins is crucial to assess the potentials of the 3D-printing technique and can be done using fractographic analyses. Some recommendations and practice guides for fracture analysis are given in [27,28]. Selected fracture surfaces of the broken discs of A- and A/ZTA/A-discs were sputtered with gold using an Agrar Sputter Coater and investigated using a SEM (JEOL JCM-6000Plus, Neoscope^{TM}, JEOL Ltd., Tokyo, Japan). In the case of the multi-material sample, special attention was set to identifying the origin of failure, either at the surface or in the near region of the A/ZTA interface.

3. Results and discussion

3.1. Materials properties

The monolithic A- as well as ZTA-samples show a relative density of approx. 98%. The measured relative density of the multi-material A/ZTA/A-sample is approx. 99 %. Therefore, both monoliths and multilayers can be considered well-densified samples with relatively low amount of porosity, which is associated with the optimized sintering process. The thermo-elastic properties as well as the fracture toughness (K_{Ic}) of the monolithic A- and ZTA-ceramics are summarized in Table 1.

Table 1: Young's moduli (E), coefficient of thermal expansion (CTE) and fracture toughness (K_{Ic}) of the 3D-printed monolithic A- as well as ZTA-ceramic.

Monolith material	E-Modulus [GPa]	CTE (25 – 900 °C) [ppm/°C]	K_{Ic} [MPam$^{1/2}$]
A	367 ± 9	8.03 ± 0.06	3.13 ± 0.15
ZTA	333 ± 7	8.58 ± 0.02	4.02 ± 0.08

The Young's modulus of 367 GPa for monolithic alumina agrees with typical values for alumina as reported in literature, i.e. 320 GPa (95% relative density) – 410 GPa (fully dense) [1]. The ZTA-monolith shows a lower Young's modulus (i.e. 333 GPa) due to the addition of

20 vol.% zirconia (YTZP) having a lower elastic constant (i.e. 210 GPa) [29]. The experimentally determined E-modulus for ZTA is in good agreement with the calculated value according to the rule of mixture (i.e. $E_{ZTA,calc}$ = 334 GPa). The thermal expansion coefficients for both monolithic alumina and ZTA are in the typical range for alumina-zirconia ceramics. It is worth highlighting that the high accuracy of the measurements is crucial for a good estimation of residual stresses in the multi-material system.

The fracture toughness measured for the ZTA, ~4 $MPam^{1/2}$, is significantly higher than the one for the A material, ~3 MPa $m^{1/2}$. The higher fracture toughness in the former is associated with the stress-induced phase transformation in tetragonal-stabilized zirconia (toughening effect), as found in conventionally fabricated ZTA materials [29,30].

3.2. Microstructure

Fig. 3 shows SEM images of microstructures of the A monolithic as well as the multi-material A/ZTA/A sample. The microstructure of the bulk alumina sample (Fig. 3a) has a rather fine grain size distribution, with an average grain size of ~2 µm, containing very fine grains (down to 0.5µm) and larger grains (up to 10 µm). This microstructure seems very homogenous along the printing direction resulting in a low amount of porosity and a high densification of the individual layers (i.e. no boundaries between individual printed layers are visible). The low porosity observed in Fig. 3a agrees with the high relative density measured in the bulk material (i.e. ~98%). It is worth mentioning that selecting appropriate sintering curves is crucial to guaranteeing a homogenous and well densified 3D-printed alumina material [10].

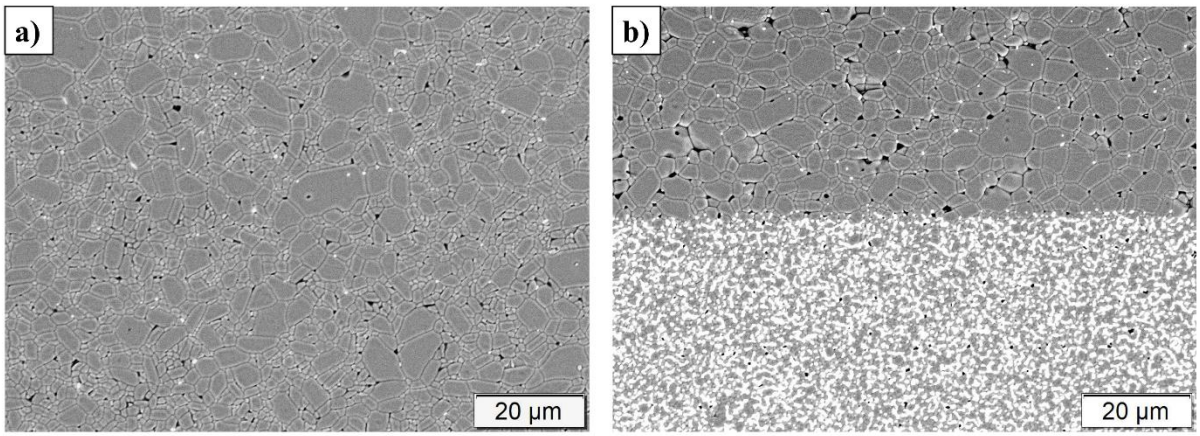

Fig. 3: Microstructure of (a) the monolithic A-sample and (b) the A/ZTA/A-multi-material system.

Fig. 3b shows the microstructure of the multi-material system, exhibiting a sharp interface between the A-region and the ZTA-region. Both microstructures are very homogeneous: this may be traced back to the appropriate choice of the sintering conditions (1600 °C, 2h) for these materials, and to the accuracy of the multi-material LCM-printing technique. The top alumina region shows a very similar grain size distribution as that of bulk alumina (Fig. 3a). The ZTA region contains very fine grains, with an average size of 1 µm. The homogeneous microstructure together with the low porosity of both regions agrees with the high relative density of ~99% measured in the A/ZTA/A multi-material sample. The final layer thicknesses (after sintering) of the different regions within the A/ZTA/A system were measured on selected SEM-images, resulting in ~75 µm/ 700 µm/ 60 µm, respectively[1], with a maximum of ±3% and ±1% deviation from the mean value for the A and ZTA layers, respectively.

3.3. Strength distributions in monoliths and multi-material samples

This section deals with the evaluation and interpretation of the strength data of multi-material sample in comparison to the monolithic alumina material. The elastic mismatch between the two materials, i.e. A and ZTA, must be taken into account for the correct evaluation of the strength for the multi-material architecture. In addition, the residual stresses acting within each region (A and ZTA) needs be estimated to interpret the strength results. Furthermore, the appropriate fracture statistics and its meaning for design reliability for multi-material ceramics with outside compressive residual stresses are also discussed.

3.3.1. Strength evaluation of monolithic discs

In the B3B-test, the strength of monoliths (applied stress) is defined as the maximum tensile stress at the centre of the specimen and can be calculated as [24]:

$$\sigma_A = f\left(\frac{t}{R}, \frac{R_a}{R}, \upsilon\right) \cdot \frac{F}{t^2} \tag{1}$$

where F is the maximum load at fracture in [N], and t is the thickness of the specimen in [mm]. In the case of "monolithic" disc shaped specimens, the dimensionless factor f has been evaluated for a wide parameter set and is only dependent on the support geometry (R_a/R), the specimen geometry (t/R) and the Poisson's ratio ν of the material [24]. Assuming a ν of ~0.23

[1] We caution the reader that, for the further discussion, all samples were tested with the thicker A-region under tension.

for alumina, the corresponding dimensionless factor was calculated to be approx. 1.8 for the monoliths, employing an interactive calculation tool [31].

3.3.2. Residual stresses in the multi-materials systems

The in-plane residual stresses $\sigma_{res,i}$ within each layer of the multi-materials system can be analytically estimated using the following equations [32]:

$$\sigma_{res,i} = \frac{E_i}{1-\nu_i}(\bar{\alpha} - \alpha_i)\Delta T \tag{2}$$

where E_i is the Young's modulus, ν_i the Poisson's ratio, α_i the Coefficient of thermal expansion (CTE) of each ith-layer and $\Delta T = T_0 - T_{ref}$ the temperature difference between the room temperature T_0, and a reference temperature T_{ref}, which is the temperature below which the material is assumed to be stress-free [32]. The stress-free reference temperature for alumina/zirconia laminates of similar composition was taken as ~1500 °C, as estimated by Chlup et al. [33].

The coefficient $\bar{\alpha}$ is the average coefficient of thermal expansion for the layered materials and can be calculated as follows [32]:

$$\bar{\alpha} = \left. \sum_{i=1}^{N} \frac{E_i t_i \alpha_i}{1-\nu_i} \middle/ \sum_{i=1}^{N} \frac{E_i t_i}{1-\nu_i} \right. \tag{3}$$

where t_i is the thickness of ith layer of the multilayer.

In the A/ZTA/A multilayer, the in-plane compressive residual stresses in the A-region (A-layers) and the tensile residual stresses in the ZTA-region (ZTA-layers) were calculated as −320 MPa and +60 MPa, respectively. Therefore, the near-surface region (A-region) of the multi-material system is shielded by the compressive stresses, which are ~5 times higher than the tensile residual stresses acting in the centre (ZTA-region). This is a consequence of the volume ratio between materials (i.e. V_{ZTA}/V_A ~5), as selected in the design of the multi-material sample [34].

3.3.3. Strength evaluation of multi-material ceramic discs

In the case of multi-material ceramic systems, the dimensionless factor *f* needs be corrected, since it is influenced by the elastic moduli of the different layers. Accordingly, the "total stress" of the laminate is a result of the "applied stress" shielded by the "compressive residual stress"

in the A-region ($\sigma_{res,}$). At the moment of fracture, the applied stress can be defined as the strength of the multi-material sample and is calculated according to:

$$\sigma_{A/ZTA/A} := f_{A/ZTA/A}\left(\frac{t}{R}, \frac{R_a}{R}, \upsilon_A, \upsilon_{ZTA}, E_A, E_{ZTA}\right) \cdot \frac{F}{t^2} = \sigma_A + \left|\sigma_{res,A}\right| \quad (4)$$

where F is the fracture force of the "shielded" multi-material specimen and t the thickness of the disc. The calculated strength of the multilayer system can be subdivided into the contribution of the "unshielded" alumina and the part of compressive residual stresses acting within the outer-most A layer of the laminate (see right side of the Eq. (4)). This holds under the assumption that both monolithic alumina and alumina region in the laminate obeys similar defect density functions (i.e. similar defect size distributions).

The dimensionless factor for the multilayer system (A/ZTA/A), i.e. $f_{A/ZTA/A}$, was evaluated for this specific multi-material system A/ZTA/A (~75 µm/ 700 µm/ 60 µm) using the FE-program ANSYS [35] by taken $\nu_A = 0.23$, $\nu_{ZTA} = 0.24$ and the Young's moduli of A and ZTA (E_A and E_{ZTA}) from Table 1. For this specific A/ZTA/A multi-material system and the given geometry a pre-factor of $f_{A/ZTA/A}$ ~2.0 was calculated.

3.3.4. Strength distributions

Figure 4 represents the conventional 2-parameter stress distributions of the A and A/ZTA/A samples in a Weibull diagram, where the probability of failure, P, is plotted versus the "applied" failure stress, σ_{appl}. The (applied) failure stress for the monolithic A-specimens (σ_A) and multi-material A/ZTA/A-specimens ($\sigma_{A/ZTA/A}$) was calculated according to Eqs. (1) and (4), respectively.

The strength data measured for the A-monoliths as well as the A/ZTA/A-system were evaluated in the framework of the Weibull statistics [36,37], following the EN-843-5 standards [38]. The probability of failure as a function of the applied stress can be described using a 2-parameter Weibull distribution, as according to:

$$P(\sigma_{appl}) = 1 - exp\left[-\left(\frac{\sigma_{appl}}{\sigma_0}\right)^m\right] \quad (5)$$

The characteristic strength, σ_0, represents the applied stress associated with a ~63% probability of failure. The Weibull modulus, m, describes the width of the strength distribution and indicates the scatter of the size of the critical defects in the sample. The dashed lines in Fig. 4

represent the best fit of the strength data sets, for both samples, according to the maximum-likelihood method. The corresponding Weibull parameters are given in Table 2.

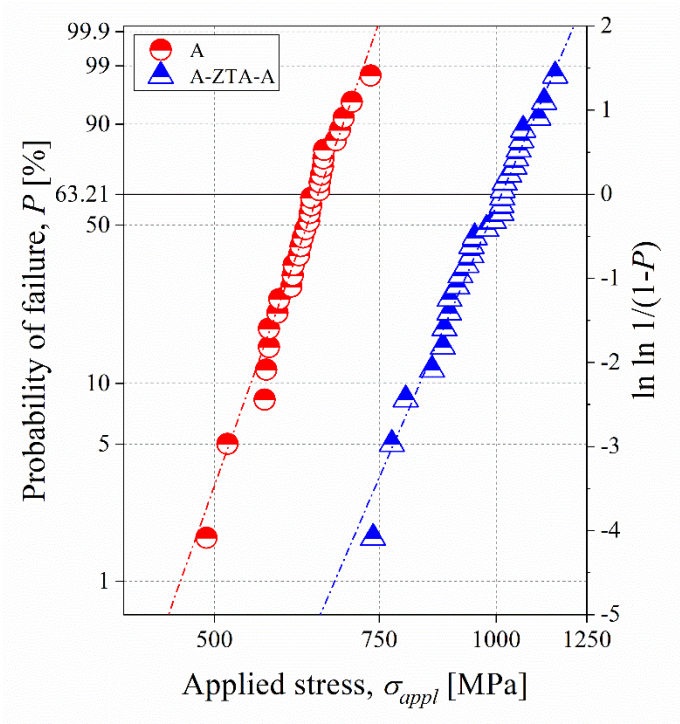

Fig. 4: 2-parameter strength distributions of the monolithic A- and A/ZTA/A-ceramic samples. The dashed lines represent the best fit of a 2 parameter Weibull distribution.

The characteristic strength of the A/ZTA/A multi-material sample (σ_0 = 1013 MPa), is significantly higher than that of the A monolithic sample (σ_0 = 645 MPa). To our best knowledge, this is the first time that a characteristic strength as high as 1 GPa has been measured in a 3D-printed alumina ceramic. The significant higher strength of the multi-material sample can be explained by the shielding effect of the compressive residual stresses (σ_{res}) in the A region (outside alumina layers). This approach was first studied in ion-strengthened glasses by Nordberg et al. [17], and has been successfully applied to other glass and ceramic systems. The difference of the applied characteristic strength of approx. −370 MPa agrees with the estimated compressive residual stresses, i.e. −320 MPa. The difference of ca. 50 MPa may be associated with the chosen reference temperature of 1500 °C. Considering the sintering temperature of 1600 °C, as set in this study, the reference temperature might be higher, resulting in slightly higher residual stresses.

In the case of multilayer systems with external compressive stresses, the total stress state σ_{tot} can be interpreted as the superposition of the applied stress (σ_{appl}) and the residual stress (σ_{res}) acting in the region where fracture occurs (i.e. $\sigma_{tot} = \sigma_{appl} + \sigma_{res}$). Accordingly, the 2-parameter distribution described in Eq. (5) may be replaced by a 3-parameter Weibull distribution [37], with the third parameter corresponding to the compressive residual stress. The fracture probability function, *P,* using a 3-parameter Weibull distribution may be given as follows:

$$P(\sigma_{appl}) = 1 - \exp\left[-\left(\frac{\sigma_{appl} + \sigma_{res}}{\sigma_0{}^*}\right)^{m^*}\right] \quad (6)$$

with

$$\sigma \rightarrow \sigma_{tot} = \sigma_{appl} + \sigma_{res} \quad (7)$$

where m^* represents the Weibull modulus and $\sigma_0{}^*$ the scale parameter in 3-parameter distributions, which may be interpreted as $\sigma_0{}^* = \sigma_0 + \sigma_{res}$.

In the general case where the third parameter (i.e. σ_{res}) is unknown, fitting of the 3-parameter distribution (especially for sets with low number of tested specimens) may result in unstable fitting values for $\sigma_0{}^*$ and m^*, as described in the work of Danzer et al. [39]. In our case, however, since the residual stresses within the compressive layers can be accurately estimated (i.e. $\sigma_{res} \sim -320$ MPa), the strength data can be successfully fitted using the 3-parameter approach. Further considerations on 3-parameter Weibull distributions on multi-material systems with residual stresses can be found in the literature [12,19]. The strength parameters: characteristic strength (σ_0) as well as the scale parameter for the 3-parameter distribution ($\sigma_0{}^*$), the Weibull moduli (m or m^*), and their corresponding 90%-confidence intervals of the different specimen sets (A and A/ZTA/A) are listed in Table 2.

Table 2: Characteristic strength (σ_0), scale parameter for 3-parameter distribution ($\sigma_0{}^*$), Weibull modulus (m or m^*) and the corresponding 90%-confidence intervals of the different specimen sets (A, A/ZTA/A).

Set	Characteristic strength, σ_0 or scale parameter, $\sigma_0{}^*$ [MPa]	Weibull modulus, m or m^*[-]
A (2-parameter form)	645 [630 – 662]	13.6 [10.2 – 16.6]
A/ZTA/A	1013 [983 – 1044]	11.2 [8.4 – 13.7]

(2-parameter form)		
A/ZTA/A (3-parameter form)	691 [661 – 723]	7.6 [5.7 – 9.2]

In order to explain the relevance of introducing compressive residual stresses in terms of design, the strength data for the monolithic alumina (fitted with a 2-parameter distribution) as well as the A/ZTA/A-system (fitted both with a 2- and 3-parameter distribution) are represented in Fig. 5. As it can clearly be seen, in the technical relevant range of probabilities (green upper window) and based on the relatively small number of tested specimens, both distributions (2- and 3-parameter) may seem appropriate to fit the data. However, in case of ceramic applications that require relatively high mechanical reliability (i.e. probability of failure below 10^{-4} – 10^{-6}) a significant difference can be observed between 2- and 3-parameter distributions. For such low failure probabilities, the curve tends asymptotically to a minimum strength, corresponding to the compressive stresses in the outer region. This stress value can be interpreted as a "threshold strength", below which no failure will occur. In case a 2-parameter distribution may be employed, the probability of failure for a given applied stress would be overestimated.

The scale parameter resulting from the 3-parameter Weibull distribution for the A/ZTA/A-system, σ_0^*, is defined as the characteristic strength σ_0 plus the residual compressive stress (i.e. $\sigma_0^* = \sigma_0 + \sigma_{res}$). The resulting 3-parameter Weibull-modulus m^* is slightly lower and strongly depending on the sample size. Hence, we caution the reader that the interpretation of the Weibull parameters resulting from the 3 parameter distribution (σ_0^*, m^*) is different. Therefore, the Weibull parameters from a 3-parameter distribution may not be directly comparable to the Weibull parameters from the 2-paramter fit (σ_0, m).

When comparing the 2-paramteter fit for both monolith and multilayer samples, a direct consequence of the compressive residual stresses, namely an increase in strength, can be observed. In case a 3-parameter distribution is favoured, a minimum strength (threshold strength) for the ceramic material can be estimated, thus significantly enhancing the material reliability. This aspect should be considered in the design of ceramic systems, especially for demanding applications that require very low probability of failure strength (e.g. bioceramic implants, space applications).

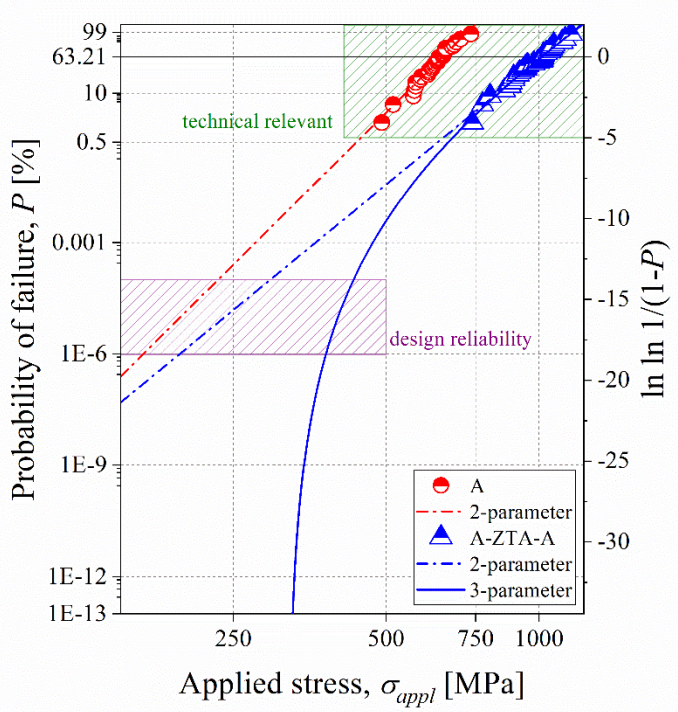

Fig. 5: Probability of failure plotted vs. (applied) failure stress. The dashed lines show the 2-parameter fit of the distributions for monolithic A- and the A/ZTA/A-system. The full line represents the 3-parameter fit of the A/ZTA/A-strength data.

3.4. Failure analysis

In order to estimate the critical defect sizes, a_c, which are responsible for failure, the Griffith criterion [40] based on Linear Elastic Fracture Mechanics was used:

$$a_c = \frac{1}{\pi}\left(\frac{K_{Ic}}{Y\,\sigma_f}\right)^2 \tag{8}$$

where σ_F is the fracture strength, K_{Ic} the fracture toughness and Y a geometry factor depending on the testing configuration and defect shape. For this analysis, the fracture toughness was taken from Table 1. The geometry factor was set as $Y = 2/\pi$ for penny-shaped volume defects and $Y = 1.12$ for semi-elliptical surface flaws [27]. In order to estimate an average critical flaw size, the fracture strength, σ_F, was taken as the characteristic strength σ_0 for A and $\sigma_0 + \sigma_{res}$ for A/ZTA/A, respectively. As a result, typical critical flaw sizes of ~6 µm for surface defects and 18 µm for near-surface and/or volume defects were calculated for both alumina monoliths and A/ZTA/A multilayers.

Fig. 6a and b show typical fracture surfaces and defect populations that cause failure in the 3D-printed A- and A/ZTA/A-discs investigated. Since the strength of the A- as well as A/ZTA/A-sample is relatively high, fragmentation during fracture impeded identification of clear fracture origins in many specimens. However, representative defects in the outer-most layers were identified as failure origins for both A monolith and A/ZTA/A multilayers. In the monolithic A sample, relatively large grains located either near the surface or directly at the surface (see Fig. 6a, arrows) were identified as fracture origins. In the A/ZTA/A multilayer, typical flaws were sub-surface (see Fig 6b, dashed circle) or surface-located larger grains. It is worth highlighting that all defects encountered in the A/ZTA/A multilayer were found in the A region (close to the surface), and not in the ZTA internal region. The similar Weibull moduli of the 2-parameter distributions, m ~14 and m ~11, for A- and A/ZTA/A samples, indicates that the underlying defect size density function in both materials follows almost the same inverse power law of the form $g(a)=g_0 \cdot (a)^{-r}$, with $m = 2(r\text{-}1)$ [41].

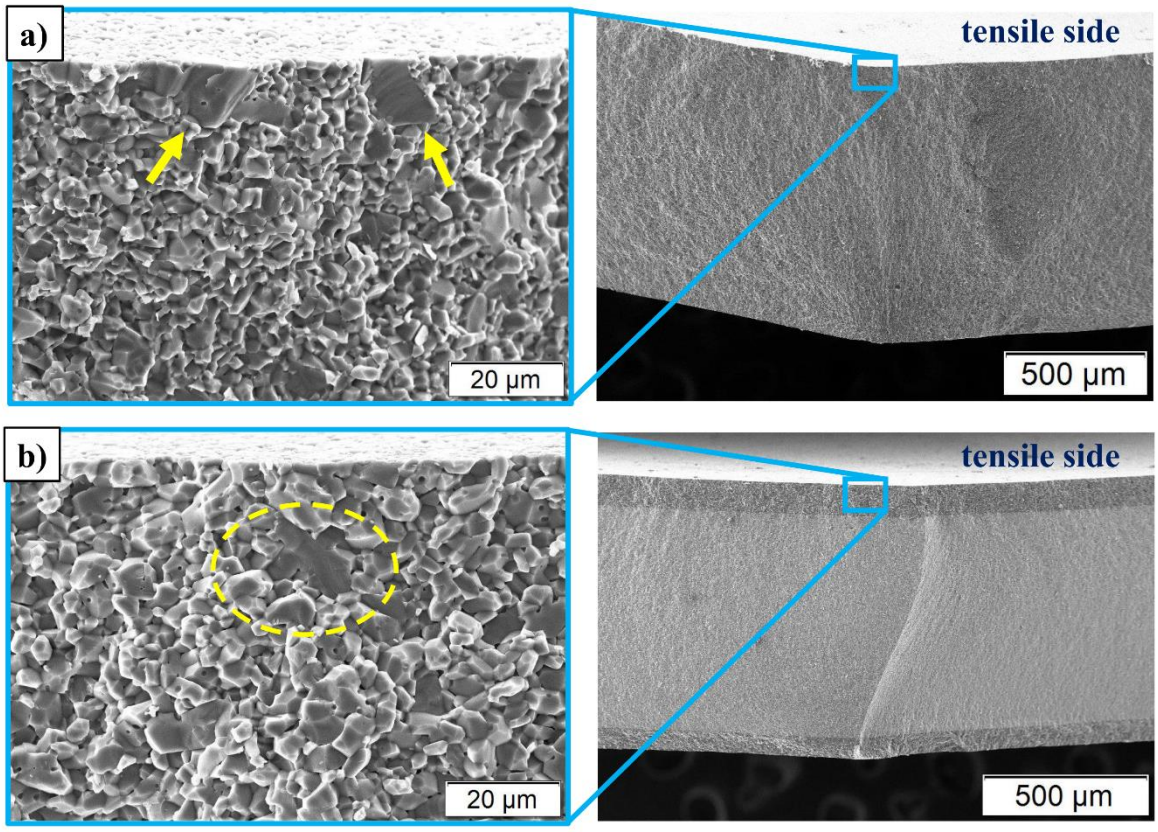

Fig. 6: (a) Two larger grains located at the as-printed surface as typical flaws in the alumina monolithic sample (see arrows), and (b) larger sub-surface grain (dashed line) as critical defect in the A-layer of the A/ZTA/A multi-material sample.

It is worth pointing out that all failure origins were found at or very near to the surface under tension, for both monolithic and laminates. However, there exists the possibility of activating defects in the ZTA material (central layer) during biaxial loading. Whether failure will start at the surface or at the interface A/ZTA may depend on the thickness of the outer layer as well as on the strength of the ZTA material. For instance, if the outer layer were too thin, high stresses would occur at the top region of the ZTA central layer during loading, thus raising the probability of failure of the laminate structure starting at the ZTA layer. In case the ZTA material may have lower strength, risk of failure would even increase. In this regard, preliminary B3B tests on the ZTA bulk material employed in this investigation resulted in strength values ranging between ~800 MPa and ~1000 MPa. This finding, along with the relatively high K_{Ic} of ZTA (i.e. ~4 MPa $m^{1/2}$), indicates rather low probability of activating a defect in the ZTA layer. Different 3D designs, which may employ low strength materials should take into account these considerations.

4. Conclusion

Additive manufactured alumina with outstanding biaxial strength was designed and fabricated, utilizing the “layer-by-layer” capability of the Lithography-based Ceramic Manufacturing technology. A multi-material approach allowed the combination of alumina-zirconia layers sandwiched between pure alumina layers, thus introducing significant compressive residual stresses in the latter. A characteristic strength higher than 1 GPa was measured on the alumina multi-material system, compared to ~650 MPa in monolithic alumina, taken as a reference. This is the first report of employing additive manufacturing to tailor the strength of alumina ceramics, taking advantage of the layer-by-layer printing process. Combining this multi-material approach with the design capabilities of the 3D-printing technique could be a new pathway for designing complex parts with outstanding mechanical strength and reliability.

Acknowledgement

Funding for this research was provided by the European Research Council (ERC) excellent science grant “CERATEXT” through the Horizon 2020 program under contract 817615.

References

[1] D. Munz, T. Fett, Ceramics: Mechanical Properties, Failure Behaviour, Materials Selection, Corr. second. print, Springer, Berlin, 2001.

[2] F. Klocke, Modern approaches for the production of ceramic components, J. Eur. Ceram. Soc. 17 (2) (1997) 457–465. https://doi.org/10.1016/s0955-2219(96)00163-x.

[3] Z. Chen, Z. Li, J. Li, C. Liu, C. Lao, Y. Fu, C. Liu, Y. Li, P. Wang, Y. He, 3D printing of ceramics: A review, J. Eur. Ceram. Soc. 39 (4) (2019) 661–687. https://doi.org/10.1016/j.jeurceramsoc.2018.11.013.

[4] T. Chartier, C. Dupas, M. Lasgorceix, J. Brie, N. Delhote, C. Chaput, Additive Manufacturing to Produce Complex 3D Ceramic Parts, J. Ceram. Sci. Technol. 6 (2) (2014) 95–104. https://doi.org/10.4416/jcst2014-00040.

[5] M. Schwentenwein, J. Homa, Additive Manufacturing of Dense Alumina Ceramics, Int. J. Appl. Ceram. Technol. 12 (1) (2015) 1–7. https://doi.org/10.1111/ijac.12319.

[6] https://www.lithoz.com/ (accessed 21 December 2020).

[7] N. Travitzky, A. Bonet, B. Dermeik, T. Fey, I. Filbert-Demut, L. Schlier, T. Schlordt, P. Greil, Additive Manufacturing of Ceramic-Based Materials, Adv. Eng. Mater. 16 (6) (2014) 729–754. https://doi.org/10.1002/adem.201400097.

[8] A.D. Lantada, A. de Blas Romero, M. Schwentenwein, C. Jellinek, J. Homa, Lithography-based ceramic manufacture (LCM) of auxetic structures: Present capabilities and challenges, Smart Mater. Struct. 25 (5) (2016) 54015. https://doi.org/10.1088/0964-1726/25/5/054015.

[9] A. de Blas Romero, M. Pfaffinger, G. Mitteramskogler, M. Schwentenwein, C. Jellinek, J. Homa, A. Díaz Lantada, J. Stampfl, Lithography-based additive manufacture of ceramic biodevices with design-controlled surface topographies, Int. J. Adv. Manuf. Technol. 88 (5-8) (2017) 1547–1555. https://doi.org/10.1007/s00170-016-8856-1.

[10] J. Schlacher, T. Lube, W. Harrer, G. Mitteramskogler, M. Schwentenwein, R. Danzer, R. Bermejo, Strength of additive manufactured alumina, J. Eur. Ceram. Soc. 40 (14) (2020) 4737–4745. https://doi.org/10.1016/j.jeurceramsoc.2020.03.073.

[11] C. Hillman, Z. Suo, F.F. Lange, Cracking of Laminates Subjected to Biaxial Tensile Stresses, J. Am. Ceram. Soc. 79 (8) (1996) 2127–2133. https://doi.org/10.1111/j.1151-2916.1996.tb08946.x.

[12] J. Pascual, T. Lube, R. Danzer, Fracture statistics of ceramic laminates strengthened by compressive residual stresses, J. Eur. Ceram. Soc. 28 (8) (2008) 1551–1556. https://doi.org/10.1016/j.jeurceramsoc.2007.10.005.

[13] D.J. Green, R. Tandon, V.M. Sglavo, Crack arrest and multiple cracking in glass through the use of designed residual stress profiles, Science 283 (5406) (1999) 1295–1297.

[14] M. Rao, J. Sanchez-Herencia, G. Beltz, R.M. McMeeking, F. Lange, Laminar ceramics that exhibit a threshold strength, Science 286 (1999) 102–105.

[15] R. Bermejo, "Toward seashells under stress": Bioinspired concepts to design tough layered ceramic composites, J. Eur. Ceram. Soc. 37 (13) (2017) 3823–3839. https://doi.org/10.1016/j.jeurceramsoc.2017.04.041.

[16] Y. Chang, R. Bermejo, G. L. Messing, Improved Fracture Behavior of Alumina Microstructural Composites with Highly Textured Compressive Layers, J. Am. Ceram. Soc. 97 (11) (2014) 3643–3651. https://doi.org/10.1111/jace.13168.

[17] M.E. Nordberg, E.L. Mochel, H.M. Garfinkel, J.S. Olcott, Strengthening by Ion Exchange, J. Am. Ceram. Soc. 47 (5) (1964) 215–219. https://doi.org/10.1111/j.1151-2916.1964.tb14399.x.

[18] https://www.corning.com/worldwide/en.html (accessed 21 December 2020).

[19] C. Krautgasser, R. Danzer, M. Deluca, P. Supancic, F. Aldrian, R. Bermejo, Subcritical crack growth in multilayer Low Temperature Co-fired Ceramics designed with surface compressive stresses, J. Eur. Ceram. Soc. 36 (16) (2016) 4095–4105. https://doi.org/10.1016/j.jeurceramsoc.2016.07.003.

[20] S. Geier, I. Potestio, 3D-Printing: From Multi-Material to Functionally-Graded Ceramic, Ceramic Applications 8 (2020) 32–35.

[21] EN 623-2, Advanced technical ceramics – Monolithic ceramics – General and textural properties – Part 2: Determination of density and porosity, 1993.

[22] EN 843-2, Advanced technical ceramics – Mechanical properties of monolithic ceramics at room temperature – Part 2: Determination of Young's modulus, shear modulus and Poisson's ratio, 2006.

[23] ISO/FDIS 23146, Fine ceramics (advanced ceramics, advanced technical ceramics) – Test methods for fracture toughness of monolithic ceramics – Single-edge V-notch beam (SEVNB) method, 2008.

[24] A. Börger, P. Supancic, R. Danzer, The ball on three balls test for strength testing of brittle discs: stress distribution in the disc, J. Eur. Ceram. Soc. 22 (9) (2002) 1425–1436. https://doi.org/10.1016/S0955-2219(01)00458-7.

[25] A. Börger, P. Supancic, R. Danzer, The ball on three balls test for strength testing of brittle discs: Part II: analysis of possible errors in the strength determination, J. Eur.

Ceram. Soc. 24 (10-11) (2004) 2917–2928. https://doi.org/10.1016/j.jeurceramsoc.2003.10.035.

[26] W. Harrer, R. Danzer, P. Supancic, T. Lube, Influence of the sample size on the results of B3B-tests, Key Eng. Mater. 409 (2009). https://doi.org/10.4028/www.scientific.net/KEM.409.176.

[27] G. Quinn, Fractography of Ceramics and Glasses. NIST Special Publication 960-16, US Government Printing Office, Washington, 2016.

[28] R. Morrell, Fractography of Brittle Materials: Measurement Good Practice Guide No. 15, Teddington, UK, 1999.

[29] C. Piconi, G. Maccauro, Zirconia as a ceramic biomaterial, Biomaterials 20 (1999) 1–25. https://doi.org/10.1016/S0142-9612(98)00010-6.

[30] P.F. Becher, Toughening behavior in ceramics associated with the transformation of tetragonal ZrO2, Acta Metall. 34 (10) (1986) 1885–1891. https://doi.org/10.1016/0001-6160(86)90246-4.

[31] https://www.isfk.at/interaktive-berechnungstools/b3b-strength-test (accessed 9 December 2020).

[32] V.M. Sglavo, M. Bertoldi, Design and Production of Ceramic Laminates with High Mechanical Reliability, Compos. Part B 37 (2006) 481–489.

[33] Z. Chlup, H. Hadraba, D. Drdlik, K. Maca, I. Dlouhy, R. Bermejo, On the determination of the stress-free temperature for alumina–zirconia multilayer structures, Ceram. Int. 40 (4) (2014) 5787–5793. https://doi.org/10.1016/j.ceramint.2013.11.018.

[34] L. Sestakova, R. Bermejo, Z. Chlup, R. Danzer, Strategies for fracture toughness, strength and reliability optimisation of ceramic-ceramic laminates, Int. J. Mater. Res. 102 (6) (2011) 613–626. https://doi.org/10.3139/146.110523.

[35] https://www.ansys.com/ (accessed 23 December 2020).

[36] W. Weibull, A Statistical Theory of the Strength of Materials, Ingeniörsvetenskapsakademiens Handlingar (1939).

[37] W. Weibull, A Statistical Distribution Function of Wide Applicability, J. Appl. Mech. 18 (1951) 293–297.

[38] EN 843-5, Advanced technical ceramics – Monolithic ceramics – Mechanical tests at room temperature – Part 5: Statistical analysis, 1996.

[39] R. Danzer, P. Supancic, J. Pascual, T. Lube, Fracture statistics of ceramics – Weibull statistics and deviations from Weibull statistics, Eng. Fract. Mech. 74 (18) (2007) 2919–2932. https://doi.org/10.1016/j.engfracmech.2006.05.028.

[40] A.A. Griffith, VI. The phenomena of rupture and flow in solids, Philos. Trans. R. Soc. 221 (1921) 163–198.

[41] R. Danzer, A General Strength Distribution Function for Brittle Materials, J. Eur. Ceram. Soc. 10 (1992) 461–472.

Publication E

Towards 3D-printed alumina-based multi-material components with enhanced thermal shock resistance

J. Schlacher, S. Geier, M. Schwentenwein, R. Bermejo

J. Eur. Ceram. Soc. 44 (2024) 2294–2303

https://doi.org/10.1016/j.jeurceramsoc.2023.11.009

Towards 3D-printed alumina-based multi-material components with enhanced thermal shock resistance

Josef Schlacher[1], Sebastian Geier[2], Martin Schwentenwein[2], Raul Bermejo[1,*]

[1] Department of Materials Science, Montanuniversität Leoben, Franz Josef Strasse 18, A-8700 Leoben, Austria

[2] Lithoz GmbH, Mollardgasse 85a/2/64-69, A-1060 Wien, Austria

*Corresponding author's email: raul.bermejo@unileoben.ac.at

Abstract

A novel architectural design is introduced which utilizes the layer-by-layer capabilities of the vat photopolymerization 3D printing process to fabricate multi-material ceramic components with improved thermal shock resistance. The combination of 3D-printed alumina-zirconia (ZTA) with alumina (A) layers generates compressive residual stresses in the embedded alumina regions during cooling down from sintering. Thermal shock tests in water are performed on samples at different maximum temperatures and the strength degradation of the multi-material design is investigated and compared to the reference monoliths. Experimental results show that the retained strength of the multi-material ceramic after thermal shock is twice as high as that of the monoliths, associated with the crack arrest capability of the embedded layers. The concept is demonstrated on 3D-printed multi-ceramic blades for potential high temperature applications, showing enhanced "damage-tolerance" against thermal shock cracks. These findings open the path for fabricating reliable ceramic components using the vat photopolymerization process.

Keywords: Additive manufacturing, Multi-material, Vat photopolymerization, Thermal shock, Residual stresses.

1. Introduction

The outstanding high-temperature resistance and chemical stability together with the high stiffness-to-weight ratio nominates ceramics as material of choice for demanding technical applications [1,2]. An example is yttria-stabilized zirconia ceramics employed in thermal barrier coatings for protecting super-alloy turbine blades from the severe heat transfer [3].

However, the use of bulk ceramics is often compromised by their inherent brittleness, which is still one of the largest limiting factors for using ceramic components in high temperature applications. In particular, during rapid temperature changes, thermal shock cracks may initiate at the surface, leading in most cases to catastrophic failure of the ceramic component [4].

Damage tolerant ceramic materials are required when reliability and safety are sought. A strategy to increase the fracture resistance in ceramics is to design (multi-material) layered ceramics with strong interfaces. The differential dimensional change of the dissimilar materials (strain mismatch) during cooling down from the sintering temperature may induce significant residual stresses [5]. They may be intrinsically generated due to (i) strain mismatch in materials with different coefficient of thermal expansion (CTE's), (ii) through phase transformations [6,7], or (iii) chemical reactions [8,9]. The magnitude and distribution of the residual stresses can be tailored by the volume ratio between materials (see more details in [10]). Depending on the application, the location of the compressive residual stresses can play a crucial role for the final design of layered ceramics. For instance, in order to enhance the mechanical resistance, in-plane compressive residual stresses are induced in the top-layer region of the laminates, based on the concept of surface strengthening in glasses [8]. This design approach allows a significant increase in the (characteristic) strength of ceramic systems [11–13], and guarantees a minimum strength (threshold strength), below which the material does not fail. Another concept to reduce significantly the strength variability and enhance the fracture resistance of ceramics uses embedding (protective) layers to arrest the propagation of surface defects. In this "damage tolerant" design, the in-plane residual stresses in the embedded layers provide an effective barrier against crack propagation [14–18]. Since more than 30% of failure of ceramic parts and components can be traced back to surface cracks caused by contact loading or thermal shock [4], designing ceramic components in a multilayer architecture may provide enhanced resistance to failure as well as high reliability. The improved thermal shock resistance of laminated alumina-based ceramics has been reported in literature [19–21]. However, beyond the major advances in the field of ceramic laminates, the transfer from (tape-casted) 2D-systems to highly-complex-structured 3D-architectures may be the last important step to increase the use of ceramic components for structural applications in the ceramic market. In this regard, stereolithographic 3D-printing technology such as Lithography-based Ceramic Manufacturing (LCM) [22] can combine the high printing resolution (in the micrometre-range) with the possibility of fabricating multi-material architectures, aiming to enhance the mechanical response.

LCM is based on the layer-by-layer photo-polymerisation technique, where a photosensitive ceramic-polymer slurry within a transparent vat is cured through exposing light from below. During the LCM-process, the slurry is adjusted by using a doctor blade, and the layers are subsequently printed on a building platform lowered within the vat system. After the printing of the green body, a cleaning step, debinding procedure as well as the sintering to a fully-dense ceramic part is conducted (post-processing). More details on the LCM-process can be found elsewhere [23–25]. The recent progress of the LCM-technology allows the combination of a two-vat multi-material printing system, developed by Lithoz GmbH [26], for the fabrication of porosity graded as well as multi-material ceramic parts [27,28].

In a previous work the capabilities of the LCM-method to fabricate alumina-based multi-material ceramics with (biaxial) strength as high as 1GPa were demonstrated [28]. In this design approach, (in-plane) compressive residual stresses were introduced within the outer alumina regions of an 3D-printed alumina/alumina-zirconia (ZTA) laminate, by taking advantage of the shielding effect. Based on this study, the question may arise whether it is possible to combine the damage-tolerant design concept (with embedded compressive layers) together with advances of the LCM-technique for improving the resistance to thermal shock of 3D-printed alumina-based components.

In this work, the thermal shock resistance of a 3D-printed multi-material design was investigated. The combination of alumina-zirconia (ZTA) with embedded alumina (A) layers with in-plane compressive residual stresses, associated with the different shrinkage of the combined materials during cooling down from sintering, was employed as strategy to provide resistance against propagation of (surface) cracks. In a first step, a simple 5-layered multi-material design (ZTA/A/ZTA/A/ZTA) with a disc geometry was investigated and compared to the monolithic reference samples (A, ZTA). All the samples were fabricated by using the LCM-technique. Thermal shock tests with temperature differences ranging from 200 °C to 400 °C were performed and the corresponding strength degradation of the multi-material design was evaluated and compared to the reference A and ZTA monolithic samples. The propagation of thermally-induced (surface) cracks was studied by cross-section polishing. Fractography was conducted to verify the results from strength testing. In a second step, the thermal-shock resistance of the multi-material samples was assessed on 3D-printed alumina-based components. Using the multi-material design approach on a ceramic turbine blade “demonstrator” opens new possibilities of printing “damage-tolerant” systems of complex-shapes.

2. Experimental

2.1. Materials of study and designs

Disc-shaped samples were fabricated by using the LCM-technology to evaluate the thermal shock behaviour of alumina-based materials. The materials of study were (i) an alumina-based photocurable suspension LithaLox MS548-D (Lithoz GmbH, Vienna, Austria) with d_{50} < 250 nm and (ii) LithaLox ZTA20 (Lithoz GmbH, Vienna, Austria), a suspension based on alumina and 3 mol% yttria stabilized zirconia (d_{50} < 200 nm) in a total ratio of 80 vol% alumina and 20 vol% zirconia [28]. These suspensions are based on reactive monomers using acrylate and methacrylate chemistry that can be cross-linked by radical photopolymerization. A CeraFab 7500-printer (Lithoz GmbH, Vienna, Austria) was employed for fabricating alumina (A) and alumina-zirconia (ZTA) monoliths, taken as a reference, as schematically illustrated in Fig. 1a (left). To manufacture the multi-material design (Fig. 1a right), a CeraFab Multi 2M30-printer (Lithoz GmbH, Vienna, Austria) [26] was employed. The detailed design and fabrication of complex multi-material components (Fig. 1b) is discussed in Section 3.5.

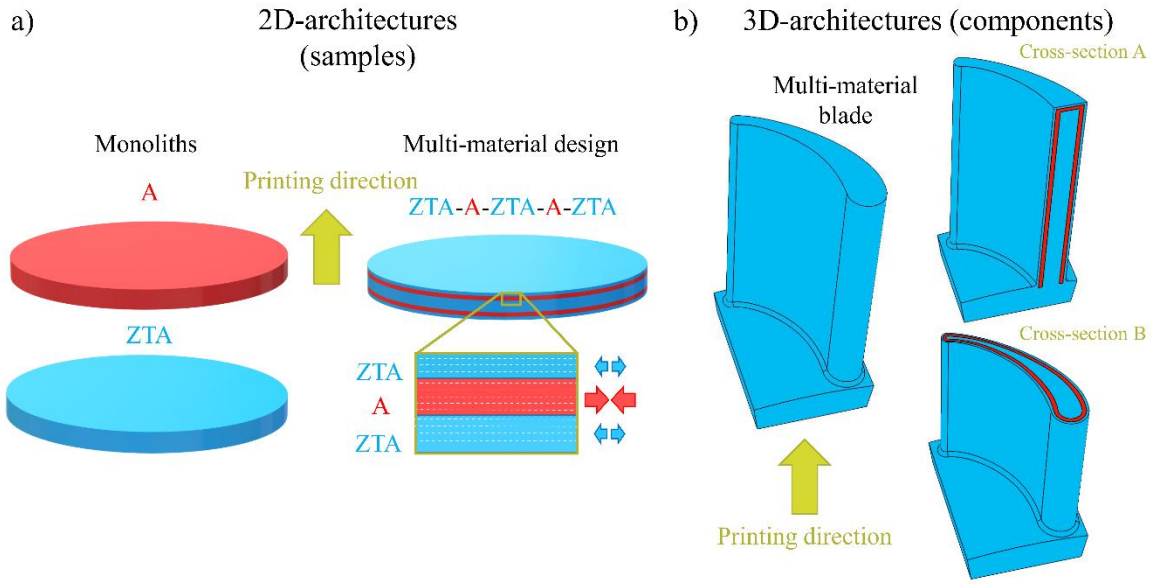

Fig. 1: (a) Schematic of the 3D-printed A- and ZTA-monoliths (left) as well as the multi-material design (right) in respect to the printing direction. The in-plane tensile (ZTA-region) as well as the compressive residual stresses (A-region) are indicated by blue and red arrows within the close-up of the multi-material design, respectively. (b) Schematic of the 3D-printed multi-material component in respect to the printing direction. The red layer indicates the embedded alumina (A) region, whereas the blue shell refers to the ZTA-region.

All samples were printed in thickness direction of the discs, as indicated by the gold arrow in Fig. 1, and designed with the final dimensions after sintering of D~15 mm in diameter and ~1.8 mm in thickness. The chosen layer thickness in the green state was ~25 µm. The monolithic A and ZTA samples were exposed with energies of 200 mJ/cm^2 and 280 mJ/cm^2, respectively. In the case of the multi-material samples, each individual layer was printed by using an exposure energy of 180 mJ/cm^2, corresponding to an exposure time of 3.6 s with a projector power of 50 mW/cm^2. All samples were sintered at 1600 °C for 2 h with a heating rate of 1 °C/min [28].

The multi-material sample was designed as non-periodic laminate with maximum shielding in the internal protective layer by following the guidelines as reported in [10]. For the multi-material design, the selected volume ratio was V_A/V_{ZTA} ~ 1/3, which agrees with the final (measured) individual layer ZTA regions with embedded A-layers ZTA/A/ZTA/A/ZTA of ~ 140 µm/210 µm/1040 µm/220 µm/110 µm after sintering. The final thickness of the layer regions was ±5% of the designed values for ZTA and A, respectively.

The corresponding in-plane residual stresses within each layer region (ZTA and A-layers) of the alternating multi-material system (ZTA/A/ZTA/A/ZTA) can be estimated according to [29]:

$$\sigma_{res,i} = \frac{E_i}{1-\nu_i}(\bar{\alpha} - \alpha_i)\Delta T \tag{1}$$

where ν_i is the Poisson's ratio (ν_{ZTA} ~0.24 and ν_A ~0.23), E_i is the Youngs' modulus (E_{ZTA}~333 GPa and E_A~367 GPa [28]) and α_i the coefficient of thermal expansion (α_{ZTA} = 8.58 × 10^{-6} K^{-1} and α_A = 8.03 × 10^{-6} K^{-1} [28] for ZTA and A, respectively) of each ith-layer region. In this relation $\Delta T = T_{ref} - T_0$ is known as the temperature difference, with T_0 as room temperature and T_{ref} as reference temperature. It is important to emphasize that T_{ref} is considered as the temperature where the ceramic material is free of internal residual stresses. In this regard, T_{ref} was selected as ~1500 °C, as it was determined for alumina-based ceramics as those employed in this study [30]. The average coefficient of thermal expansion ($\bar{\alpha}$) was calculated using the following equation, with t_i being the thickness of each individual *i*-layer [29]:

$$\bar{\alpha} = \left. \sum_{i=1}^{N} \frac{E_i t_i \alpha_i}{1-\nu_i} \right/ \sum_{i=1}^{N} \frac{E_i t_i}{1-\nu_i} \quad (2)$$

The corresponding in-plane compressive residual stresses within the embedded A-region and the tensile residual stresses in the ZTA-region were calculated according to Eq. (1), resulting in approx. − 300 MPa and + 100 MPa for the A and ZTA material, respectively.

2.2. Microstructural analysis

To investigate the microstructure of the monolithic A- and ZTA-, as well as the multi-material samples, cross-sections of the discs were polished (perpendicular to the printing direction) up to 1 µm mirror finish by using a Struers Tegramin-30 equipment. In the case of the multi-material sample, the exact layer thicknesses were measured on different locations along the specimen width using an optical microscope (Olympus BX50) and the image processing software (Stream motion, Olympus), respectively. The polished specimens were thermally etched at 1400 °C for 20 min. Subsequently, the polished cross-sections were gold coated using an Agrar Sputter coater and images were taken using a scanning electron microscope (SEM) (JEOL JCM-6000Plus, Neoscope™, JEOL Ltd., Tokyo, Japan). Subsequently, the mean grain size (d_{50}) of each sample system was determined from several SEM microstructures by using the line-intersection method [31].

2.3. Thermal shock tests and analysis

All thermal shock tests were performed on 6 specimens per temperature step and design (A, ZTA, and multi-material design) according to the EN820–3 standards [32]. The specimens of study were placed inside a vertical tubular furnace (HTM Reetz GmbH, Berlin, Germany) installed with a temperature regulator Eurotherm® (Typ2416/CP) and heated to 20 °C below to the selected maximum temperature (T_{max}) with a heating rate of 5 °C/min. Subsequently, the heating rate was switched to 2.5 °C/min until reaching T_{max}. After a holding time of about 15 min the specimens of study were quenched into water (T_w = 20 °C). The temperature difference, ΔT, can be calculated as $T_{max} - T_w$, which for thermal shock was set to ΔT = 200 °C, 250 °C, 300 °C and 400 °C.

To prove whether the critical temperature for crack formation has been reached, red liquid dye penetrant (Diffu-Therm® red penetrant) was applied on all quenched specimen for ~30 min. Images of surface cracks were taken with a stereo-microscope system (Olympus SZH10 (microscope) and KL2500 LCD (light source)). To analyse the surface crack patterns, the crack density of each sample was determined by counting the number of cracks intersecting certain lines along the specimen diameter. One specimen per sample and temperature step was prepared for cross-section polishing (perpendicular to the printing direction). The cross-sections of these samples were polished to 1 µm mirror finish using a Struers Tegramin-30 equipment, and analysed using an optical microscope (Nikon ECLIPSE LV100ND, Japan) under polarized light. The mean crack depths were determined from different regions along the diameter of the specimen cross-section measured perpendicular to the surface, using an image processing software (NIS-Elements, Nikon).

2.4. Strength evaluation

The retained (biaxial) strength after quenching at each temperature difference ΔT of the monoliths (A and ZTA) as well as the multi-material samples was determined on 5 specimens, respectively. All the specimens were tested under biaxial bending using the Ball-on-three-balls (B3B) testing fixture [33,34]. The B3B-tests were conducted on a universal testing machine (Zwick 010, Zwick/Roell Ulm, Germany) using a load cell of 10 kN under ambient conditions (~24 °C and ~32% relative humidity). A pre-load of 20 N and a cross-head testing speed of 1.5 mm/min were chosen. After reaching the pre-load, the disc (D ~ 15 mm, t ~ 1.8 mm) supported by 3 balls was loaded by a fourth ball of 11 mm diameter until fracture.

In the case of monoliths, the following relationship was used to calculate the maximum (biaxial) tensile stress at the centre of the specimen discs [33]:

$$\sigma_f = f\left(\frac{t}{R}, \frac{R_a}{R}, \upsilon\right) \cdot \frac{F_{max}}{t^2} \tag{3}$$

where t is the specimen thickness, F_{max} the maximum fracture load and f a dimensionless pre-factor, which takes into account the Poisson's ratio ν of the tested material, the specimen- (t/R) as well as the support geometry (R_a/R) of the setup. In this regard, R is the specimen- and R_a the

support ring radius [33]. For both monolithic materials (A and ZTA) with a Poisson's ratio of $\nu_{ZTA} \sim 0.24$ and $\nu_A \sim 0.23$, a pre-factor of ~ 1.8 is obtained.

For the multilayer case [28], the dimensionless pre-factor has to be corrected under consideration of the elastic mismatch between the layer regions within the multi-material disc. Therefore, the factor was evaluated for the ZTA/A/ZTA/A/ZTA laminate using the FE-software ANSYS [35]. The E-modulus of $E_{ZTA} \sim 333$ GPa and $E_A \sim 367$ GPa and Poisson's ratios of $\nu_{ZTA} \sim 0.24$ and $\nu_A \sim 0.23$ were used for the FE-model for ZTA and A, respectively [28]. The corresponding corrected pre-factor $f_{multi} = f(t/R,\ R_a/R,\ \nu_{ZTA},\ \nu_A,\ E_{ZTA},\ E_A)$ for our specific materials system resulted in ~ 1.8, with a relative difference of only ~ 2% to the monolithic system. This can be explained by the similar E-moduli of ZTA and A-layer regions and the rather small volume ratio of the system (V_A / $V_{ZTA} \sim 1/3$).

2.5. Fractography

To identify the origin for failure (i.e. natural defects and final crack depth induced after thermal shock tests), fracture analysis on broken discs (after B3B-tests) was performed. The samples were gold coated with an Agrar Sputter coater and the fracture surfaces were observed using a SEM (JEOL JCM-6000Plus, Neoscope™, JEOL LTd., Tokyo, Japan).

3. Results and discussion

3.1. Microstructure

Figure 2 shows the microstructure of the monolithic ZTA (Fig. 2a), monolithic A (Fig. 2b) and the multi-material sample (Fig. 2c). The mean grain size d_{50} of monolithic A was approx. 2.0 ± 1.6 µm. The level of porosity seems to be slightly higher than reported in the previous work for the same materials [28]. The measured Archimedes density of ~ 95% correlates well with the porosity level. In the case of monolithic ZTA, the microstructure is very homogenous with relatively fine grains ($d_{50} \sim 0.8 \pm 0.3$ µm (alumina grains) and $d_{50} \sim 0.5 \pm 0.2$ µm (zirconia grains)) and low porosity, resulting in a relative density of ~ 99%. The multi-material sample exhibits a sharp interface between the ZTA- and the A-region, consisting of a homogenous microstructure with relatively low amount of porosity. The corresponding average grain sizes of the ZTA- region were $d_{50} \sim 1.0 \pm 0.5$ µm (alumina grains) and $d_{50} \sim 0.5 \pm 0.2$ µm (zirconia grains), respectively. The d_{50} of the A-region of the multi-material sample was ~ 2.7 ± 1.5 µm. The grain size values are well comparable with those of the monolithic A and ZTA materials,

which can be explained by the same sintering condition. The Archimedes density of the multi-material was estimated as ~ 99 % according to the rule of mixture. In summary, the microstructural features are comparable with those of a previous work, where samples were fabricated with different dimensions yet using same sintering conditions (1600 °C, 2 h) [28], thus demonstrating the reproducibility of the 3D-printing process.

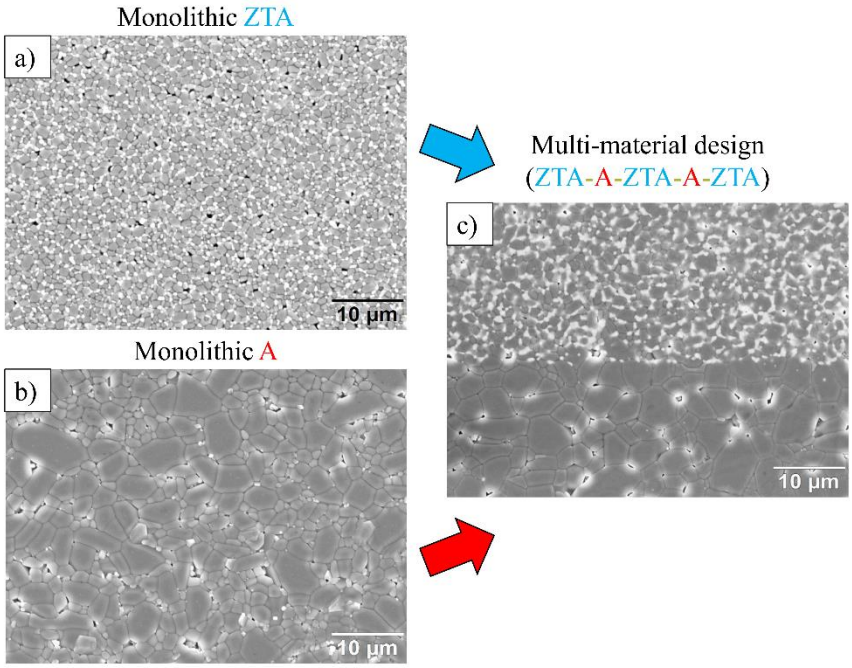

Fig. 2: Microstructure of (a) monolithic ZTA, (b) monolithic A and (c) the multi-material sample.

3.2. Thermal shock crack analysis

Figure 3 shows typical crack patterns in monolithic A, monolithic ZTA as well as the multi-material system thermal shocked at temperature differences, ΔT, of 250 °C, 300 °C and 400 °C, respectively. In the case of A-samples, the first observed crack pattern occurred at a temperature difference of ~ 250 °C (Fig. 3a). The crack density, defined as number of cracks per unit length, of A shows an increasing trend with higher temperature difference with values of 5.1 ± 1.2 cm^{-1} (at $\Delta T \sim 250$ °C), 9.3 ± 1.9 cm^{-1} (at $\Delta T \sim 300$ °C) and 14.9 ± 1.4 cm^{-1} (at $\Delta T \sim 400$ °C), respectively (see Supplementary Fig. S1). This experimental finding is in agreement with the trend reported in [36]. In the case of ZTA-samples, first thermal shock cracks were found at a temperature difference of 300 °C, with a finer network at 400 °C (Fig. 3e and f). The

corresponding crack density was 3.5 ± 1.3 cm^{-1} and 7.4 ± 1.3 cm^{-1} for $\Delta T \sim 300$ °C and $T \sim 400$ °C, respectively. In the multi-material system, first cracking was observed at $\Delta T \sim 250$ °C (Fig 3g). The lower ΔT for the latter can be explained by the in-plane tensile residual stresses of ~ + 100 MPa in the ZTA layers, which makes the multi-material system slightly more sensitive to thermal shock at the surface. With increasing temperature difference, the cracks patterns show higher density (finer network), similar to the monoliths, with crack densities of 1.5 ± 0.5 cm^{-1} (at $\Delta T \sim 250$ °C), 4.6 ± 1.3 cm^{-1} (at $\Delta T \sim 300$ °C) and 9.8 ± 2.1 cm^{-1} (at $\Delta T \sim 400$ °C), respectively. Comparing the crack densities of all systems (Supplementary Fig. S1), it may be seen that the monolithic A sample shows a significantly finer crack network for each temperature difference, whereas the differences between monolithic ZTA and the multi-material are only marginal. It is worth noting that the temperature upon which cracks are first observed corresponds to an upper bound of the critical temperature difference. Thus, a slightly lower critical temperature difference may be expected.

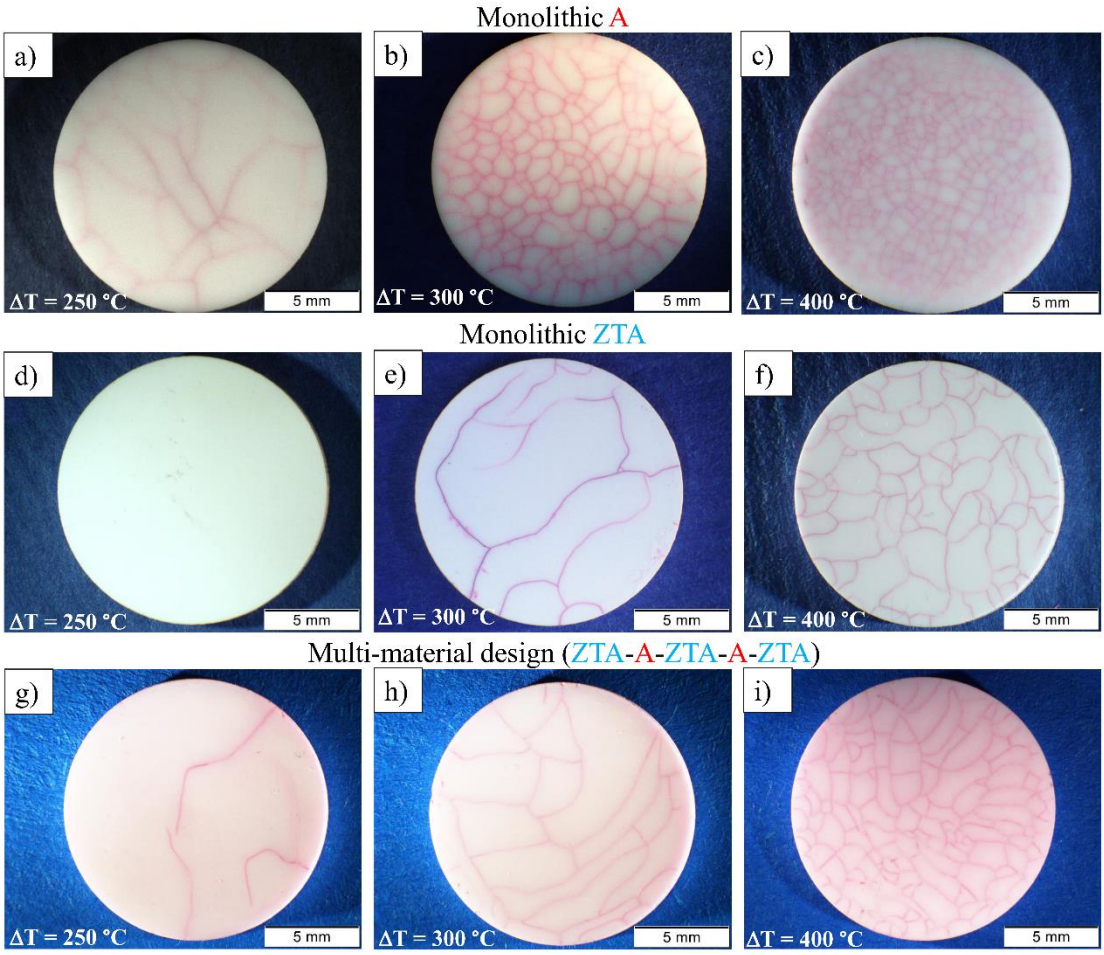

Fig. 3: Crack pattern induced through the thermal shock quench test at different temperature differences (250 °C, 300 °C and 400 °C) for monolithic A (a, b and c), monolithic ZTA (d, e and f) and laminate (g, h and i), respectively.

Regarding crack initiation due to thermal shock, the monolithic ZTA seems to be more resistant, which may be explained by a higher toughness of the ZTA material, associated with the toughening effect of tetragonal stabilized zirconia [37]. Another additional aspect are the distinct thermo-physical properties of ZTA such as thermal diffusivity, thermal expansion and elastic modulus, which may influence the thermal shock stresses [38].

The question arises how deep the initial thermal shock cracks propagate into the A and ZTA monolithic samples, compared to the multi-material design. Therefore, cross-sectioning (sub-surface observations) was performed in selected specimens. Fig. 4 depicts the sub-surface damage of the A-, ZTA- and multi-material samples thermally shocked at a temperature difference of 400 °C.

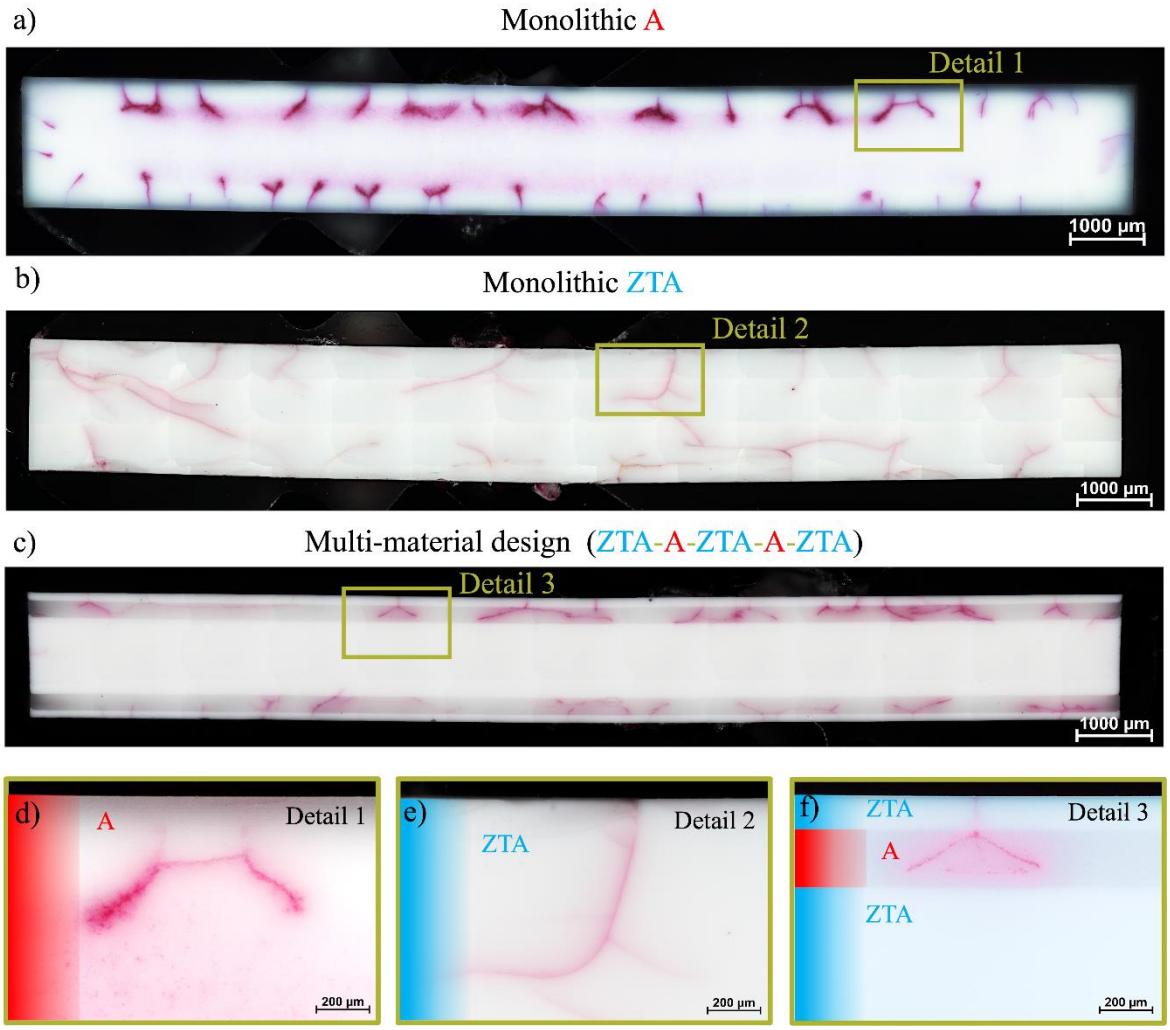

Fig. 4: Cross-sections of (a) monolithic A, (b) monolithic ZTA and (c) multi-material samples shocked at a temperature difference of ~ 400 °C. Representative regions of each system showing the final crack depths are illustrated in (d), (e) and (f).

In order to explain crack propagation, the Griffith-Irwin criterion (based on linear elastic fracture mechanics) [39,40] may be used to describe the relationship between strength, fracture toughness and defect size, according to the relation:

$$\sigma_f = \frac{K_{Ic}}{Y\sqrt{\pi a_c}} \tag{4}$$

where σ_f is the stress at fracture (strength), K_{Ic} is the fracture toughness, a_c is the critical defect size and Y is the geometry factor taking into account the defect shape as well as the loading configuration.

In case of monolithic A, the induced surface cracks propagate to a final depth of ~ 470 ± 63 µm (Fig. 4a). As discussed before, the ZTA-monolith is more resistant to crack initiation compared to monolithic A. However, the final crack depth is rather larger (786 ± 274 µm) (Fig. 4b), which according to Griffith-Irwin criterion (Eq. 4) may compromise the retained strength. In the case of the multi-material sample, the corresponding final crack depth is ~ 278 ± 41 µm (Fig. 4c). Due to the rather high in-plane compressive residual stresses in A (i.e. −300 MPa) the thermal shock cracks are deflected/bifurcated when entering the A first layer (Fig. 4c). The shielding effect associated with in-plane compressive stresses has been described in the literature [18,29,41,42], and is explained by the increase in the "apparent fracture resistance" of the laminate with the crack length in the A region. In some cases, crack bifurcation may also take place, especially in laminates containing relatively thick layers and/or large compressive residual stresses (see more details in [43–45]). As a consequence, the introduced artificial cracks cannot reach the second A/ZTA interface, demonstrating the capability of the multi-material design to enhance the damage tolerance of the ceramic part. To quantify these experimental observations, the retained thermal shock biaxial strength of the monolithic and multi-material samples as a function of temperature difference was measured. The results are represented in Fig. 5. A comparison between samples is discussed in the next section with respect to reference strength values (without thermal shock).

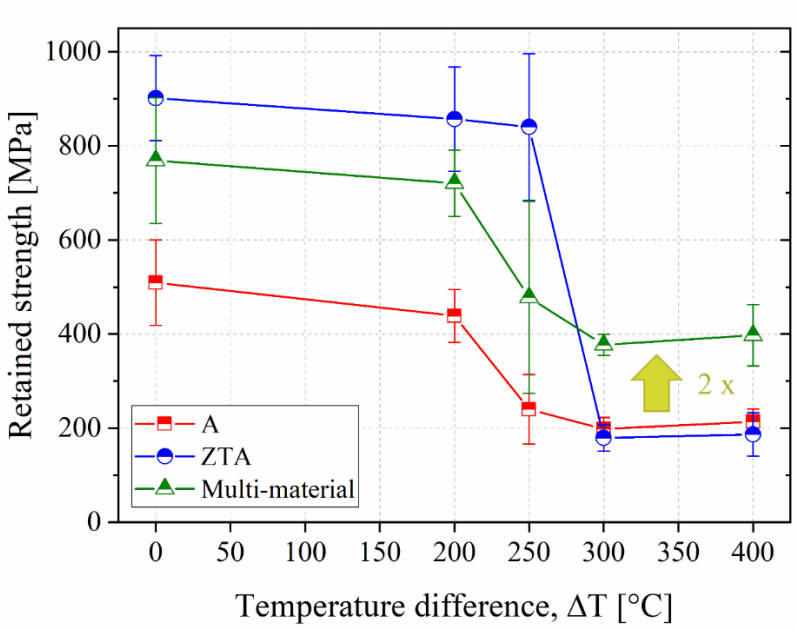

Fig. 5: Retained strength of the monoliths A and ZTA, as well as the multi-material design as a function of the temperature difference. The arrow indicates the increase in retained strength in the multi-material compared to bulk samples.

3.3. Assessment of thermal shock resistance

In the case of monolithic A, the reference strength (without thermal shock) was 509 ± 91 MPa. Up to a temperature difference ΔT of ~ 200 °C, the strength of A is on the same level as the non-shocked sample (439 ± 56 MPa), which suggests that the same defect population is responsible for failure (natural flaws). However, in the case of the A-sample shocked at 250 °C, a significant strength drop in correlation with the first induced surface cracks is observed (Fig. 3a). The corresponding retained strength of 240 ± 74 MPa is about 50% lower as the level of non-shocked A. The retained strength of A shocked at ΔT of 300 °C as well as 400 °C was 198 ± 25 MPa and 214 ± 27 MPa, respectively. The almost constant retained strength level over a certain range beyond the critical temperature difference is characteristic for thermal shocked alumina-based ceramics, and is in agreement with the predictions as well as experimental observations in [46,47].

In the case of monolithic ZTA, the reference strength was 902 ± 91 MPa, which is significantly higher (~ 77%) than that of monolithic A (509 ± 91 MPa). The obtained (biaxial) strength of 3D-printed ZTA is well comparable to the strength of conventional fabricated ZTA-ceramics [48]. Samples thermally shocked at the temperature differences of 200 °C and 250 °C, show

strength values of 857 ± 111 MPa and 840 ± 155 MPa, without any sign of crack initiation (Fig. 3d). However, increasing the temperature difference to 300 °C led to significant strength degradation (179 ± 28 MPa), being more than 4 times lower than the reference strength (non-shocked sample). This significant strength drop can be traced back to the relatively long thermal shock cracks (~ 600 – 900 µm), as shown in Fig. 4b. The lower crack density of monolithic ZTA compared to A measured on the sample surfaces (see Supplementary Fig. S1) may explain the higher strength decrease in the former. The relatively small number of thermal shock cracks extend deeper into the specimen, yielding a larger crack size and thus lower retained strength [1,49]. The corresponding strength at ΔT = 400 °C was 187± 46 MPa.

In light of these results it can be concluded that the strength of 3D-printed monolithic ZTA (non-shocked) is significantly higher than that of monolithic A. However, after crack initiation through thermal-mechanical loading the remaining strength is drastically decreased to the same level of thermal shocked alumina (i.e. ~ 200 MPa). The differences in the thermal shock strength degradation between monolithic ZTA and A may be explained by their different elastic properties, grain size and/or initial strength, as investigated in [49,50]. In addition, the phase present in the ZTA material during thermal shock (i.e. tetragonal versus monoclinic) may also affect the retained strength, especially for elevated temperatures, where zirconia may have suffered from low temperature degradation [51].

In the case of the multi-material sample, the reference strength was 769 ± 134 MPa, only 15% lower than that of the monolithic ZTA. The relative difference of ~ 130 MPa agrees with the in-plane tensile residual stresses in the top surface ZTA-region of the multi-material sample (~ 100 MPa). At ΔT = 200 °C the strength was 721 ± 70 MPa, not statistically different to the reference strength. Increasing the ΔT to ~ 250 °C significantly decreases the strength (~ 478 ± 204 MPa); the rather high scatter may be related to the fact that few of the specimens revealed cracks, whereas others remained non-cracked. Nevertheless, the ΔT of ~ 250 °C may be considered as the critical temperature difference, ΔT_c. It is important to emphasize that the mechanical strength of the multi-material sample at ΔT below 300 °C is slightly lower than that of the ZTA-counterpart, associated with the tensile residual stresses in the former. The retained strength for 300 °C and 400 °C were 377 ± 23 MPa and 397 ± 65 MPa, respectively. The retained strength of ~ 400 MPa is twice as high as that of the monolithic A- as well as the ZTA counterparts (~ 200 MPa). The relatively high retained strength in the multi-layer sample can be related to the crack arrest at the embedded layers under in-plane compressive residual

stresses, as evidenced in Fig. 4c. To our best knowledge, this is the highest reported thermal shock strength of 3D-printed alumina-based ceramics so far.

3.4. Fracture analysis

To verify the above-mentioned observations, fractographic analysis on selected monolithic A, ZTA as well as the multi-material samples tested at room temperature and after the thermal shock test at $\Delta T \sim 400$ °C was conducted (Fig. 6).

In case of alumina, only several larger grains (~ 10 µm) were responsible for failure (see Fig. 6a, yellow arrows). The 3D-printed monolithic ZTA as well as the multi-material specimen (with ZTA outer region) show typical surface artefacts and/or pores in the range of 10 – 20 µm as fracture origins (Fig. 6c and e). These processing defects were only found on the weakest specimens of each sample set. It is worth indicating that in the case of the multi-material disc fracture originates in the outer ZTA-region, and the design may be protected from such processing-related defects (i.e. pores or surface artefacts) by the embedded A-layer region under compressive residual stresses. In comparison, the SEM images of the crack fronts of thermally shocked ($\Delta T \sim 400$ °C) monolithic A-, ZTA as well as multi-material samples are represented in Fig. 6b, d and f. Rather deep cracks are observed on the fracture surfaces of monolithic A- and ZTA-samples, as discussed in Section 3.2. Only the thermally induced crack within the laminate is trapped within the embedded A-region. For instance, Fig. 6f shows the bifurcated crack within the ZTA/A-interface region; the propagated crack follows a rather intergranular fracture path, as indicated by the yellow arrows in the close-up of Fig. 6f.

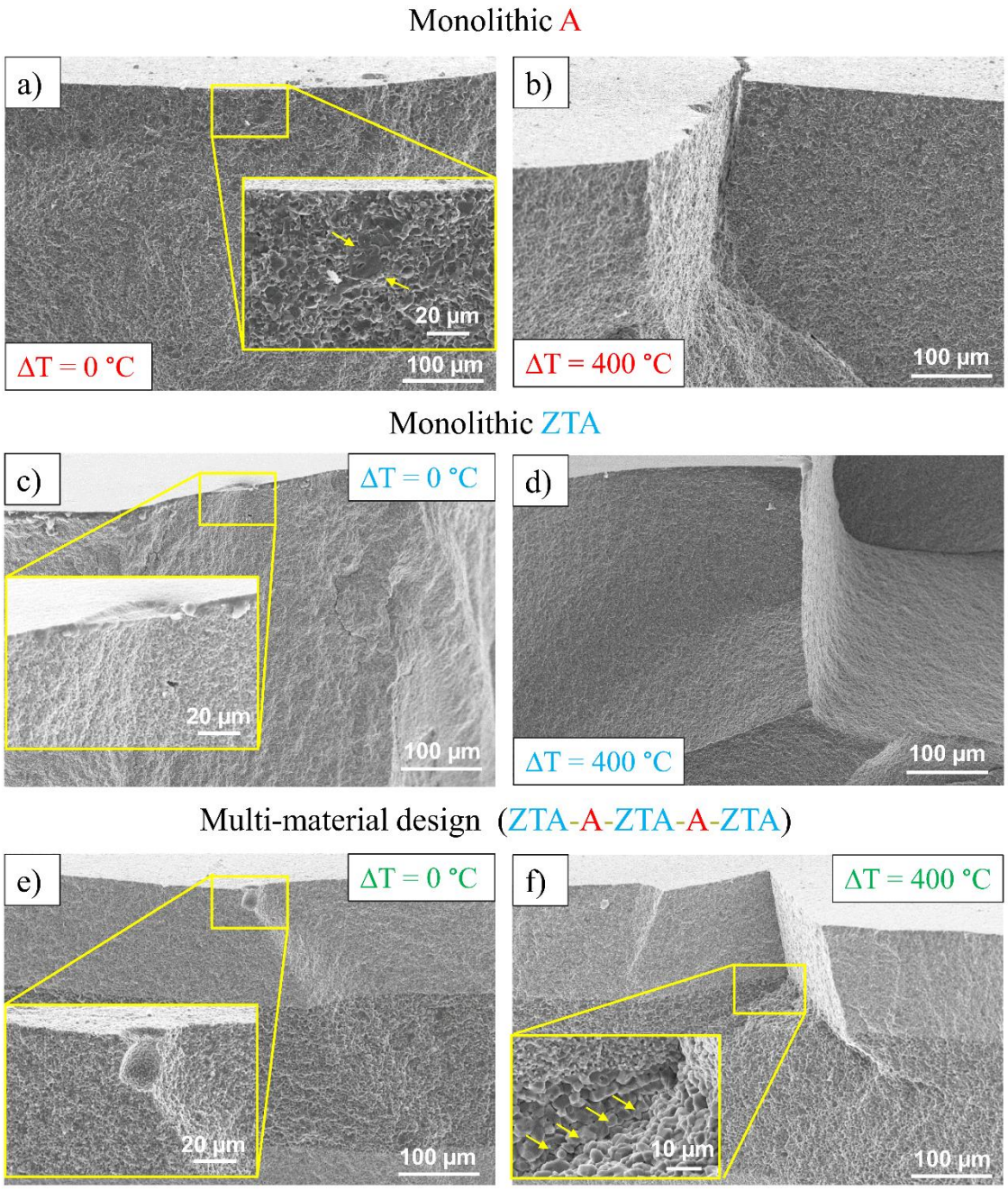

Fig. 6: Fracture surfaces of non-shocked ($\Delta T = 0$ °C) as well as thermal shocked ($\Delta T = 400$ °C) specimens: (a, b) monolithic A, (c, d) monolithic ZTA, (e, f) multi-material design. The window in Fig. 6f shows higher magnification of the intergranular crack path (indicated by yellow arrows).

3.5. Application to complex 3D-printed multi-material components

To assess the feasibility of 3D-printing complex alumina-based parts with enhanced damage tolerance, a turbine blade (ZTA/A/ZTA/A/ZTA) was designed by using the multi-material

design approach (see Fig. 1b, and Fig. 7a). In this regard, the shell (blue) indicate the ZTA-region (~ 150 µm) under in-plane tensile residual stresses. The embedded alumina (A) layer region (~ 200 µm) with tailored compressive residual stresses may be used as barrier against propagation from (surface) cracks. As reference parts, a pure ZTA turbine blade was also printed. The multi material as well as the pure ZTA-blades were fabricated using the same procedure as described in Section 2.1. It is worth noting that in the case of the multi-material turbine blade a thickness of 50 µm of the printed layer (green state) was selected for the suitability of the printing process, which corresponds to approx. 40 µm layers after sintering. The obtained microstructures of both pure and multi-material turbine blade samples can be seen in Supplementary Fig. S2, with comparable grain size and strong interfaces as in the corresponding disc-shaped specimens. The thermal shock tests in the turbine blades were performed setting the samples oriented such that the entry direction for both discs and turbine blades was in the "printing direction".

Figure 7b shows the crack patterns of the designed turbine blades of monolithic ZTA as well as the multi-material system thermal shocked at ΔT = 400 °C. Similar to the observations from the disc-shaped samples, the crack network of the multi-material design seems to be denser than that of the monolithic ZTA counterpart. The corresponding crack density of the monolithic ZTA-blade was 13.2 ± 3.5 cm^{-1}, whereas that of the multi-material blade was approx. 28.1 ± 2.5 cm^{-1} (measured in printing direction) and 12.0 ± 2.9 cm^{-1} (perpendicular to the printing direction). This can be explained by the induced (biaxial) tensile residual stresses on the ZTA "shell" of the layered turbine blade. To verify that the embedded internal A-layer within the 3D complex multi-material part may act as barrier against crack propagation, as observed in the 2D-laminated systems, the demonstrator parts were cross-sectioned from the top (see cross-section B, in Fig. 1b).

Figure 7c shows the crack deflection/bifurcation capability of the multi-material design of the turbine blade after thermal shock compared to the ZTA counterpart. In case of the monolithic ZTA the surface cracks propagated to a depth of ~ 550 ± 186 µm. However, in case of multi-material samples, surface cracks were limited to depths of ~ 315 ± 66 µm, associated with the effect of the in-plane compressive residual stresses in the embedded A-layers. Although most of the cracks stopped within the embedded layers, a few cracks at specific locations could enter the second ZTA region of the complex-3D-part (see Fig. 7c), which may be related to the different (biaxial) stress field in the non-uniform layer regions within the highly-complex shape of the part. For ideal elastic materials the in-plane residual stresses can be analytically

calculated for an infinite plate using the classical laminate theory according to Eq. (1) [52,53]; in case of the 3D-printed turbine vane-shape a FE-analysis should be carried out for calculating the residual stress field within the part. On the thin side of the turbine vane, both monolithic ZTA as well as the multi-material part are almost free from thermal shock cracks. It may be related to the fact that the critical temperature difference increases with decreasing sample size (dimension), as discussed in literature [54,55]. The concept of “damage tolerance” of the 3D-printed multi-material component has been proven at temperature differences up to 400 °C, whereas the ZTA counterpart is strongly degraded by the thermally induced cracks.

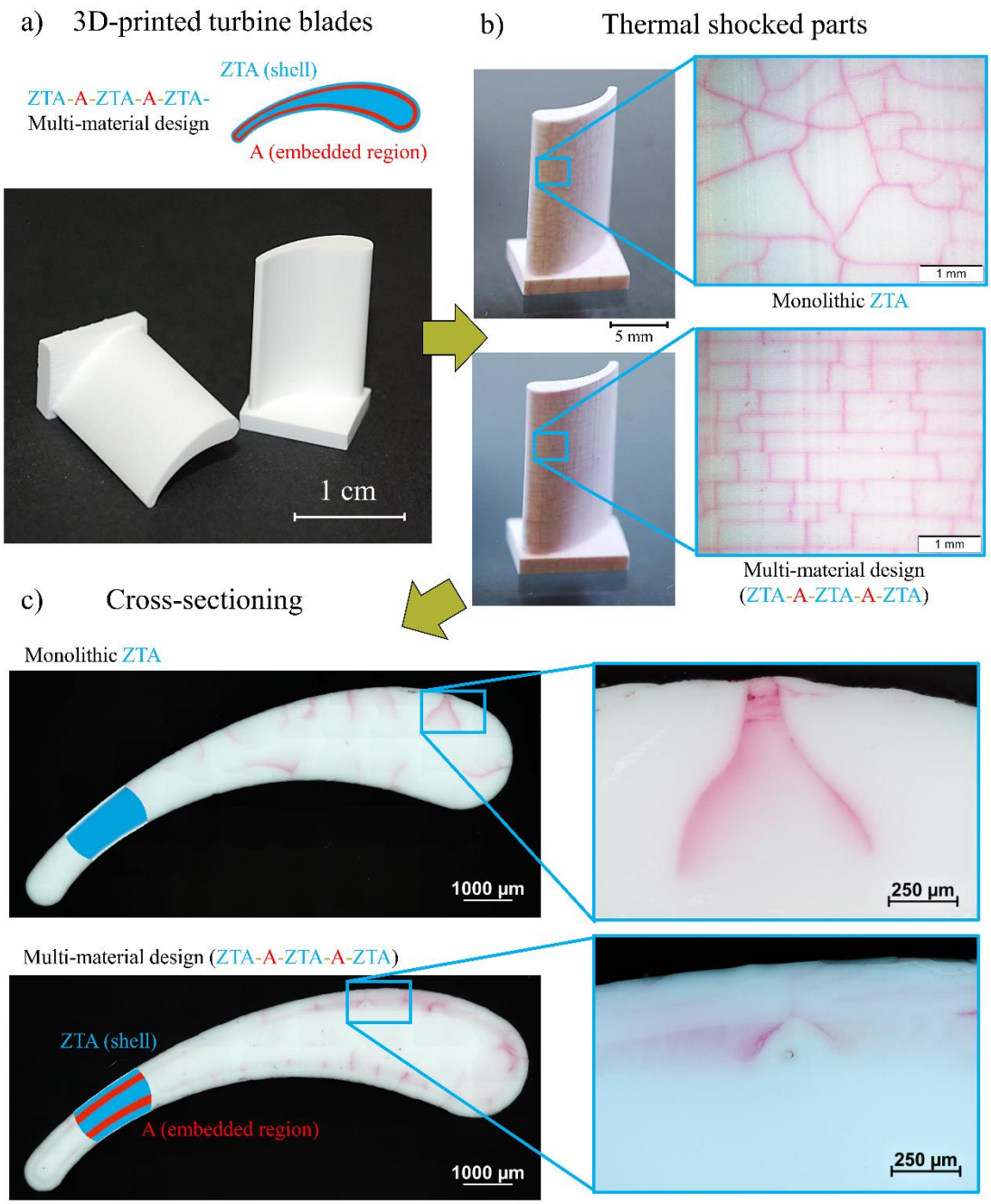

Fig. 7: (a) Image of the 3D-printed turbine blades. (b) Typical crack pattern induced through the thermal shock quench test at $\Delta T = 400$ °C for monolithic ZTA (top) and the multi-material turbine blade (bottom), respectively. (c) Polished cross-section of both ZTA blades (top) and multi-material blade (bottom), respectively. The close-ups indicate the final crack depths.

4. Conclusions

The potential of the LCM-method for designing damage-tolerant alumina-based multi-material components has been demonstrated. Thermal shock experiments were performed on 3D-printed multi-material of alumina-zirconia (ZTA) with compressive residual stresses in the embedded alumina (A) regions (protective layers) as well as on the monolithic reference A and ZTA samples. It was shown that the thermally induced cracks on the surface of the multi-material samples can be bifurcated and arrested within the embedded alumina layers, limiting its final depth, whereas the reference samples are strongly degraded. The corresponding retained (biaxial) strength after thermal shock at critical temperature differences of the multi-material sample is twice as high as those of the reference counterpart. The feasibility of 3D-printing more complex-shaped parts with embedded protective regions was proven on a demonstrator (turbine blades). This work demonstrated for the first time that the damage-tolerant design approach may be also applicable on 3D-printed complex-shaped parts, which could open novel application fields in the future.

Acknowledgements

Funding for this research was provided by the European Research Council (ERC) excellent science grant “CERATEXT” through the Horizon 2020 program under contract 817615. The authors gratefully acknowledge A.-K. Hofer (Department of Materials Science, Montanuniversität Leoben) for 3D-printing the monolithic reference samples, I. Kraleva (Department of Materials Science, Montanuniversität Leoben) for the support in sample cross-sectioning and microscopy analysis and L. Bastos Mateus (Department of Materials Science, Montanuniversität Leoben) for assistance in performing the thermal shock tests.

References

[1] D. Munz, T. Fett, Ceramics: Mechanical Properties, Failure Behaviour, Materials Selection, Corr. second. print, Springer, Berlin, 2001.

[2] C.B. Carter, M.G. Norton, Ceramic Materials: Science and Engineering, Second edition, Springer, New York, 2013.

[3] C. Kluthe, W. Kollenberg, Thermal shock behaviour of paper-derived alumina ceramics, Mat.-wiss. u. Werkstofftech. 44 (2013) 997–1004. https://doi.org/10.1002/mawe.201300131.

[4] R. Danzer, T. Lube, P. Supancic, R. Damani, Fracture of Ceramics, Adv. Eng. Mater. 10 (4) (2008). https://doi.org/10.1002/adem.200700347.

[5] L. Cheng, M. Sun, F. Ye, Y. Bai, M. Li, S. Fan, L. Zhang, Structure design, fabrication, properties of laminated ceramics: A review, Int. J. Lightweight Mater. Manuf. 1 (2018) 126–141. https://doi.org/10.1016/j.ijlmm.2018.08.002.

[6] A.V. Virkar, J.L.W. Huang, R.A. Cutler, Strengthening of Oxide Ceramics by Transformation-Induced Stress, J. Am. Ceram. Soc. 70 (3) (1987) 164–170. https://doi.org/10.1111/j.1151-2916.1987.tb04952.x.

[7] M.G. Pontin, M.P. Rao, A.J. Sánchez-Herencia, F.F. Lange, Laminar Ceramics Utilizing the Zirconia Tetragonal-to-Monoclinic Phase Transformation to Obtain a Threshold Strength, J. Am. Ceram. Soc. 85 (12) (2002) 3041–3048. https://doi.org/10.1111/j.1151-2916.2002.tb00576.x.

[8] M.E. Nordberg, E.L. Mochel, H.M. Garfinkel, J.S. Olcott, Strengthening by Ion Exchange, J. Am. Ceram. Soc. 47 (5) (1964) 215–219. https://doi.org/10.1111/j.1151-2916.1964.tb14399.x.

[9] R. Krishnamurthy, B.W. Sheldon, Stresses due to oxygen potential gradients in non-stoichiometric oxides, Acta Mater. 52 (2004) 1807–1822. https://doi.org/10.1016/j.actamat.2003.12.020.

[10] L. Sestakova, R. Bermejo, Z. Chlup, R. Danzer, Strategies for fracture toughness, strength and reliability optimisation of ceramic-ceramic laminates, Int. J. Mater. Res. 102 (6) (2011) 613–626. https://doi.org/10.3139/146.110523.

[11] D.J. Green, R. Tandon, V.M. Sglavo, Crack arrest and multiple cracking in glass through the use of designed residual stress profiles, Science 283 (5406) (1999) 1295–1297.

[12] J. Pascual, T. Lube, R. Danzer, Fracture statistics of ceramic laminates strengthened by compressive residual stresses, J. Eur. Ceram. Soc. 28 (8) (2008) 1551–1556. https://doi.org/10.1016/j.jeurceramsoc.2007.10.005.

[13] C. Krautgasser, R. Danzer, M. Deluca, P. Supancic, F. Aldrian, R. Bermejo, Subcritical crack growth in multilayer Low Temperature Co-fired Ceramics designed with surface compressive stresses, J. Eur. Ceram. Soc. 36 (16) (2016) 4095–4105. https://doi.org/10.1016/j.jeurceramsoc.2016.07.003.

[14] M. Rao, A. Sánchez-Herencia, G. Beltz, R.M. McMeeking, F.F. Lange, Laminar Ceramics That Exhibit a Threshold Strength, Science 286 (1999) 102–105.

[15] V.M. Sglavo, M. Paternoster, M. Bertoldi, Tailored Residual Stresses in High Reliability Alumina-Mullite Ceramic Laminates, J. Am. Ceram. Soc. 88 (10) (2005) 2826–2832. https://doi.org/10.1111/j.1551-2916.2005.00479.x.

[16] R. Bermejo, Y. Torres, A.J. Sánchez-Herencia, C. Baudín, M. Anglada, L. Llanes, Residual stresses, strength and toughness of laminates with different layer thickness ratios, Acta Mater. 54 (2006) 4745–4757. https://doi.org/10.1016/j.actamat.2006.06.008.

[17] V.M. Sglavo, F. de Genua, A. Molinari, F. Casari, Alumina/Silicon Carbide Laminated Composites by Spark Plasma Sintering, J. Am. Ceram. Soc. 92 (11) (2009) 2693–2697. https://doi.org/10.1111/j.1551-2916.2009.03247.x.

[18] R. Bermejo, "Toward seashells under stress": Bioinspired concepts to design tough layered ceramic composites, J. Eur. Ceram. Soc. 37 (13) (2017) 3823–3839. https://doi.org/10.1016/j.jeurceramsoc.2017.04.041.

[19] Z. Chen, J.J. Mecholsky, Damage-tolerant laminated composites in thermal shock, J. Mater. Sci. 28 (1993) 6365–6370. https://doi.org/10.1007/BF01352199.

[20] P. Hvizdoš, D. Jonsson, M. Anglada, G. Anné, O. van der Biest, Mechanical properties and thermal shock behaviour of an alumina/zirconia functionally graded material prepared by electrophoretic deposition, J. Eur. Ceram. Soc. 27 (2) (2007) 1365–1371. https://doi.org/10.1016/j.jeurceramsoc.2006.05.030.

[21] D. Jakobsen, W. Zhang, N. Doynov, A. Böhm, J. Malzbender, V. Michailov, A. Roosen, Thermal shock behaviour of laminated multilayer refractories for steel casting applications reinforced by residual stresses, Ceram. Int. 42 (12) (2016) 13562–13571. https://doi.org/10.1016/j.ceramint.2016.05.149.

[22] https://www.lithoz.com/ (accessed 7 December 2022).

[23] M. Schwentenwein, J. Homa, Additive Manufacturing of Dense Alumina Ceramics, Int. J. Appl. Ceram. Technol. 12 (1) (2015) 1–7. https://doi.org/10.1111/ijac.12319.

[24] A. de Blas Romero, M. Pfaffinger, G. Mitteramskogler, M. Schwentenwein, C. Jellinek, J. Homa, A. Díaz Lantada, J. Stampfl, Lithography-based additive manufacture of ceramic biodevices with design-controlled surface topographies, Int. J. Adv. Manuf. Technol. 88 (5-8) (2017) 1547–1555. https://doi.org/10.1007/s00170-016-8856-1.

[25] A.D. Lantada, A. de Blas Romero, M. Schwentenwein, C. Jellinek, J. Homa, Lithography-based ceramic manufacture (LCM) of auxetic structures: Present

capabilities and challenges, Smart Mater. Struct. 25 (5) (2016) 54015. https://doi.org/10.1088/0964-1726/25/5/054015.

[26] S. Geier, I. Potestio, 3D-Printing: From Multi-Material to Functionally-Graded Ceramic, Ceramic Applications 8 (2020) 32–35.

[27] S. Nohut, S. Geier, I. Kraleva, M. Schwentenwein, R. Bermejo, Lithography-based additive manufacturing of porosity graded alumina, Addit. Manuf. Lett. 3 (2022) 100060. https://doi.org/10.1016/j.addlet.2022.100060.

[28] J. Schlacher, A.-K. Hofer, S. Geier, I. Kraleva, R. Papšík, M. Schwentenwein, R. Bermejo, Additive manufacturing of high-strength alumina through a multi-material approach, Open Ceramics 5 (2021) 100082. https://doi.org/10.1016/j.oceram.2021.100082.

[29] V.M. Sglavo, M. Bertoldi, Design and production of ceramic laminates with high mechanical resistance and reliability, Acta Mater. 54 (2006) 4929–4937. https://doi.org/10.1016/j.actamat.2006.06.019.

[30] Z. Chlup, H. Hadraba, D. Drdlik, K. Maca, I. Dlouhy, R. Bermejo, On the determination of the stress-free temperature for alumina–zirconia multilayer structures, Ceram. Int. 40 (4) (2014) 5787–5793. https://doi.org/10.1016/j.ceramint.2013.11.018.

[31] EN 623-3, Advanced technical ceramics - Monolithic ceramics - General and textural properties-Part 3: Determination of grain size, 1993.

[32] EN 820-3, Advanced technical ceramics - Monolithic ceramics - Thermomechanical properties - Part 3: Determination of resistance to thermal shock by water quenching, 1993.

[33] A. Börger, P. Supancic, R. Danzer, The ball on three balls test for strength testing of brittle discs: stress distribution in the disc, J. Eur. Ceram. Soc. 22 (9) (2002) 1425–1436. https://doi.org/10.1016/S0955-2219(01)00458-7.

[34] A. Börger, P. Supancic, R. Danzer, The ball on three balls test for strength testing of brittle discs: Part II: analysis of possible errors in the strength determination, J. Eur. Ceram. Soc. 24 (10-11) (2004) 2917–2928. https://doi.org/10.1016/j.jeurceramsoc.2003.10.035.

[35] https://www.ansys.com/ (accessed 20 February 2023).

[36] J.H. Ainsworth, R.E. Moore, Fracture Behavior of Thermally Shocked Aluminum Oxide, J. Am. Ceram. Soc. 52 (11) (1969) 628–629. https://doi.org/10.1111/j.1151-2916.1969.tb15857.x.

[37] P.F. Becher, Toughening behavior in ceramics associated with the transformation of tetragonal ZrO2, Acta Metall. 34 (10) (1986) 1885–1891.

[38] W.D. Kingery, Factors Affecting Thermal Stress Resistance of Ceramic Materials, J. Am. Ceram. Soc. 38 (1) (1955) 3–15. https://doi.org/10.1111/j.1151-2916.1955.tb14545.x.

[39] A.A. Griffith, VI. The phenomena of rupture and flow in solids, Philos. Trans. R. Soc. 221 (1921) 163–198.

[40] G.R. Irwin, Analysis of stresses and strains near the end of a crack traversing a plate, J. Appl. Mech. 24 (1957) 361–364.

[41] M. Lugovy, V. Slyunyayev, N. Orlovskaya, G. Blugan, J. Kuebler, M. Lewis, Apparent fracture toughness of Si3N4-based laminates with residual compressive or tensile stresses in surface layers, Acta Mater. 53 (2005) 289–296. https://doi.org/10.1016/j.actamat.2004.09.022.

[42] C.R. Chen, J. Pascual, F.D. Fischer, O. Kolednik, R. Danzer, Prediction of the fracture toughness of a ceramic multilayer composite – Modeling and experiments, Acta Mater. 55 (2007) 409–421. https://doi.org/10.1016/j.actamat.2006.07.046.

[43] K. Hbaieb, R.M. McMeeking, F.F. Lange, Crack bifurcation in laminar ceramics having large compressive stress, Int. J. Solids Struct. 44 (2007) 3328–3343. https://doi.org/10.1016/j.ijsolstr.2006.09.023.

[44] M.P. Rao, F.F. Lange, Factors Affecting Threshold Strength in Laminar Ceramics Containing Thin Compressive Layers, J. Am. Ceram. Soc. 85 (5) (2002) 1222–1228. https://doi.org/10.1111/j.1151-2916.2002.tb00249.x.

[45] M. Oechsner, C. Hillman, F.F. Lange, Crack Bifurcation in Laminar Ceramic Composites, J. Am. Ceram. Soc. 79 (7) (1996) 1834–1838. https://doi.org/10.1111/j.1151-2916.1996.tb08003.x.

[46] D.P.H. Hasselman, Unified Theory of Thermal Shock Fracture Initiation and Crack Propagation in Brittle Ceramics, J. Am. Ceram. Soc. 52 (11) (1969) 600–604. https://doi.org/10.1111/j.1151-2916.1969.tb15848.x.

[47] D.P.H. Hasselman, Strength Behavior of Polycrystalline Alumina Subjected to Thermal Shock, J. Am. Ceram. Soc. 53 (9) (1970) 490–495. https://doi.org/10.1111/j.1151-2916.1970.tb15997.x.

[48] D. Tang, H.-B. Lim, K.-J. Lee, C.-H. Lee, W.-S. Cho, Evaluation of mechanical reliability of zirconia-toughened alumina composites for dental implants, Ceram. Int. 38 (3) (2012) 2429–2436. https://doi.org/10.1016/j.ceramint.2011.11.009.

[49] D.P.H. Hasselman, Elastic Energy at Fracture and Surface Energy as Design Criteria for Thermal Shock, J. Am. Ceram. Soc. 46 (11) (1963) 535–540. https://doi.org/10.1111/j.1151-2916.1963.tb14605.x.

[50] T.K. Gupta, Strength Degradation and Crack Propagation in Thermally Shocked Al2O3, J. Am. Ceram. Soc. 55 (5) (1972) 249–253. https://doi.org/10.1111/j.1151-2916.1972.tb11273.x.

[51] J. Chevalier, B. Cales, J.M. Drouin, Low-Temperature Aging of Y-TZP Ceramics, J. Am. Ceram. Soc. 82 (8) (1999) 2150–2154. https://doi.org/10.1111/j.1151-2916.1999.tb02055.x.

[52] H.J. Oel, V.D. Fréchette, Stress Distribution in Multiphase Systems: I, Composites with Planar Interfaces, J. Am. Ceram. Soc. 50 (10) (1967) 542–549. https://doi.org/10.1111/j.1151-2916.1967.tb14992.x.

[53] D.J. Green, P.Z. Cai, G.L. Messing, Residual stresses in alumina–zirconia laminates, J. Eur. Ceram. Soc. 19 (13) (1999) 2511–2517. https://doi.org/10.1016/S0955-2219(99)00103-X.

[54] D. Sherman, D. Schlumm, Thickness effect in thermal shock of alumina ceramics, Scr. Mater. 42 (2000) 819–825. https://doi.org/10.1016/S1359-6462(99)00371-1.

[55] Z.-H. Jin, Y.-W. Mai, Effects of Damage on Thermal Shock Strength Behavior of Ceramics, J. Am. Ceram. Soc. 78 (7) (1995) 1873–1881. https://doi.org/10.1111/j.1151-2916.1995.tb08903.x.

Supplementary information

for

Towards 3D-printed alumina-based multi-material components with enhanced thermal shock resistance

Josef Schlacher[1], Sebastian Geier[2], Martin Schwentenwein[2], Raul Bermejo[1,*]

[1] Department of Materials Science, Montanuniversität Leoben, Franz Josef Strasse 18, A-8700 Leoben, Austria

[2] Lithoz GmbH, Mollardgasse 85a/2/64-69, A-1060 Wien, Austria

*Corresponding author's email: raul.bermejo@unileoben.ac.at

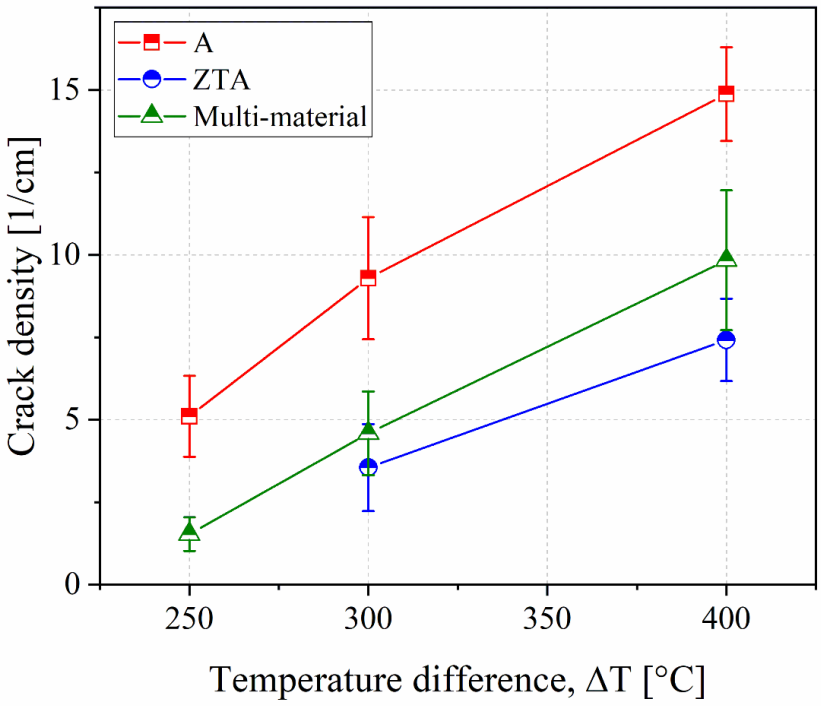

Supplementary Figure S1: Crack density of the monoliths A and ZTA, as well as the multi-material design as a function of the temperature difference, respectively.

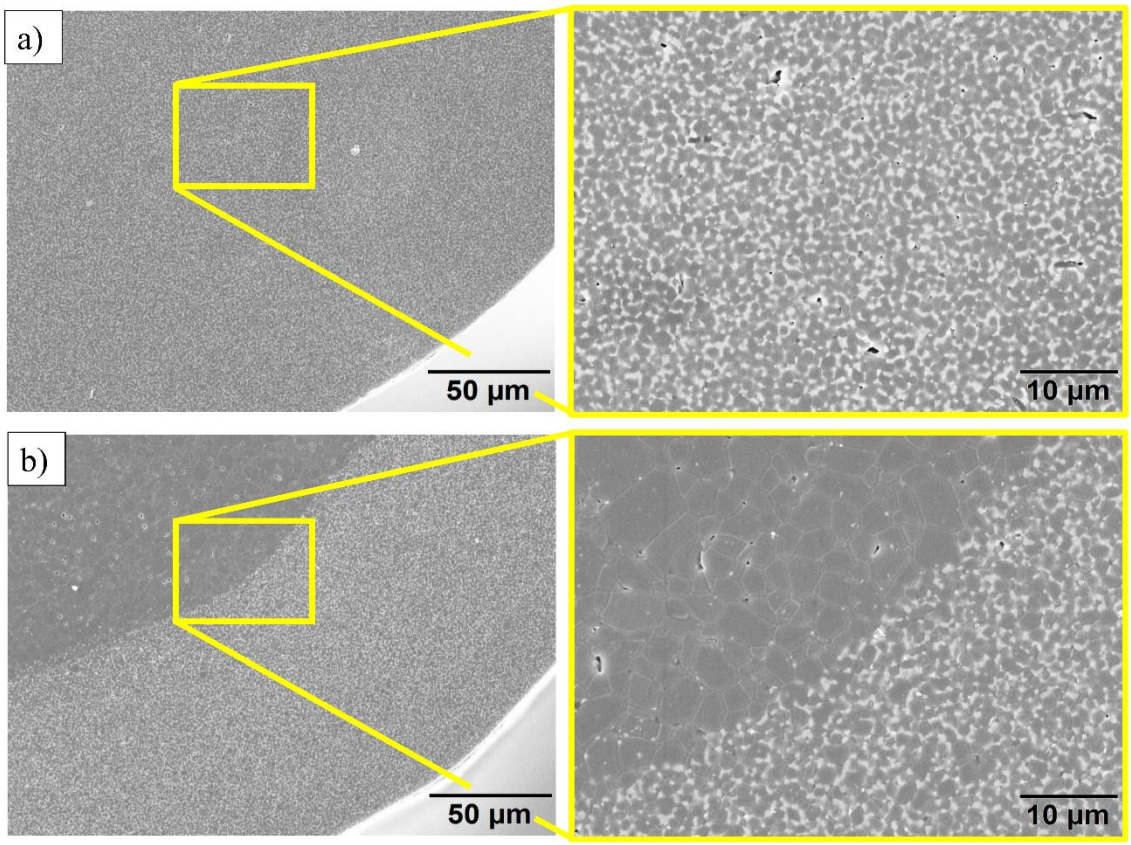

Supplementary Figure S2: Microstructure along the curved shape of (a) the monolithic ZTA- and (b) the multi-material blade.